Nonlinear Optical Frequency Conversion of Mode-locked All-Solid-State Lasers

Gail McConnell

Department of Physics and Applied Physics
University of Strathclyde

A thesis submitted in fulfilment of the requirements for the degree of Ph.D.

December 2001

Abstract

The work contained in this thesis concerns the design, development and implementation of robust diode-pumped solid-state mode-locked lasers as a platform for nonlinear optical frequency conversion experiments. One objective is to create an ultrashort-pulsed source that is tunable between $\lambda = 600\text{nm}$ and $\lambda = 700\text{nm}$, since currently no other laser gain media exists that covers this region of the electromagnetic spectrum. This novel source is intended for application to multi-photon imaging.

The first demonstration of additive pulse mode-locking of a diode-pumped $Nd^{3+}:YVO_4$ laser operating in the near-infrared is presented and the source characteristics compared to a similar system that is mode-locked using a saturable Bragg reflector. Although the additive-pulsed mode-locked laser demonstrates higher peak power, it is observed to be less robust due to vibrational intolerance. Therefore, the saturable Bragg reflector mode-locked laser is chosen as the basis for frequency conversion experiments.

This source is used to develop an efficient picosecond-pulsed ultraviolet laser that is intended to pump an optical parametric oscillator to realise tunable visible radiation in the wavelength region of interest. Using a resonant enhancement method to generate the third harmonic of the near-infrared laser, an average power of 320mW at $\lambda = 355\text{nm}$ is measured, with a peak power of approximately 68W. However, experiment and calculation proves this to be insufficient to reach the oscillation threshold of the proposed optical parametric oscillator to realise a visible tunable source.

The near-infrared laser is also used to obtain mid-infrared radiation by use of a quasi-phase-matched optical parametric oscillator. An average power of 1W tunable from $\lambda = 1460 - 1601\text{nm}$ is achieved. This is mixed with some fundamental radiation in a nonlinear medium to generate radiation that is tunable from $\lambda = 610$ to 650nm. This system is presented with emphasis on suitability for multi-photon imaging.

Acknowledgements

I would like to thank my supervisor, Prof. Allister Ferguson, for giving me the opportunity to work with such an expert. His constant enthusiasm and motivation for this research were often marvelled but always appreciated.

Also, thanks go to the other members of the Photonics Group with whom I've had the pleasure of working, namely Thomas Graf, Nigel Langford, Arkady Major and Stephen Lee. Notable mentions go to Grant Shepherd, Greg Dudziak and for preserving their sanity, and Firuz Torabi-Goudarzi and Michael Troebs for interesting conversations. A big thank you (and apology) also goes to Paul Barton for reading this thesis, and to everyone else in Photonics for keeping out of my way when I was writing it!

Thanks must also go to the staff at the Institute of Photonics for helpful discussions and use of their SBRs, as well as Robert Wylie and Ewan McLaggan of the technical workshop. Their expertise has enabled me to retain the use of my fingers, whilst providing simple mechanical solutions. I would also like to thank Jean Lindores and the rest of Admin. who know all there is to know about red-tape and shopping.

After being at Strathclyde for so long, there are countless people I'd like to thank. I would like to thank Madeleine White, who has been instrumental in this research in providing countless tea and gossip sessions, extreme toilet-humour and most importantly friendship, sometimes all at once. I must apologise to the other folks on Level 2 for the associated noise incurred. Thanks also go to Carol Trager-Cowan for an endless supply of novels and chat on the train.

I must also thank Gordon Fischbacher, Stuart Loch, David Smith, Jo Beswick, John Jeffers and countless others, who provided much entertainment and a new unit of time. I know you'd all take the million!

I must thank my Mum and Gran, who have been extremely supportive throughout my studies. I am in their debt, although I promise that I'll get a job soon... Thank you for your love and three-way conversations.

Lastly, I must thank Davie for all the love, support and encouragement, as well as being exceptionally helpful and caring. Most importantly, I'd like to thank him for all the fun that we've shared – thank you, for everything.

Contents

5. Nonlinear Optical Frequency Conversion

6. Singly Resonant Third Harmonic Generation

Chapter One

Introduction

1.1. Introduction

This chapter provides the background and motivation for the research presented in this thesis, with reference to existing applications and possible improvements. An overview of the strategy adopted to fulfil the project aims is presented. This is followed by a brief synopsis of the structure of each chapter and the principal arguments and results.

1.2. Technological background

Since the first demonstration in the 1960's [1, 2], the laser has undoubtedly become one of the most significant developments in optical technology. With progress of materials and methods, the versatility of the laser leads to an increasingly attractive device for many applications due to reliability, efficiency, flexibility and cost. For example, coherent photonic solid-state devices and optical fibre technology have revolutionised the telecommunications industry by the introduction of low-cost, high-bandwidth solutions [3]. Another example of the use of solid-state lasers is in high-density data storage, where devices such as the CD-RW have led to compact, reliable and rapid means to access and record information [4].

However, many applications call for laser sources with strict requirements for optimum performance, such as pulsed emission or a system that generates radiation at a particular wavelength. Neither of these problems are trivial. For example, a sizeable majority of all-solid-state lasers presently emit in the near-infrared region of

the electromagnetic spectrum [5], yet sources that operate at other wavelengths are desirable for a number of applications. For instance, it is well known that the ideal operational wavelength of optical systems for telecommunications systems is 1.55μm to minimise dispersion [6], but few laser gain materials emit at this wavelength [5]. A similar problem exists for data storage. The quantity of information that may be stored optically may be increased by use of a shorter-wavelength coherent source to read and write data. Although semiconductor laser diodes that emit red light are currently used, the capacity of an optical disk could be increased significantly by the use of an ultraviolet source [7]. Therefore, there is presently much research into new laser gain materials and methods to reach wavelengths not covered by existing media.

One of the characteristics of a laser source is the high magnitude of electric field exhibited. When such a source is incident on matter, the atomic response can no longer be described linearly and nonlinear effects are evident. This effect is enhanced significantly by use of an ultra-short (<ns) pulsed laser to pump the nonlinear optical material, due to the high peak electric fields exhibited by such a source. By exploiting this electric field, nonlinear optical devices that emit at wavelengths outside of the near-infrared wavelength regime have been demonstrated when pumped with a mode-locked near-infrared laser [8, 9]. Such nonlinear optical frequency converted lasers may be designed to yield a fixed or tunable wavelength coherent source of ultra-short pulses.

Advances in nonlinear optical materials and their pump sources has enabled the introduction of efficient frequency converted sources which generate over 1W of average output power [10] and sources which are widely tunable over the ultraviolet [11], visible [12] and infrared regimes [13]. It is these developments which have led to the motivation of this research.

1.3. Motivation

The research described in this thesis is concerned with the design and development of efficient and ultrafast all-solid-state laser sources that operate in wavelength regions not covered by conventional crystalline laser gain materials, with emphasis on a tunable source that emits from $\lambda = 600\text{nm}$ to 700nm. This wavelength region is of interest as it is not covered by solid-state gain media but has applications for multi-photon imaging.

This is achieved by first developing a robust picosecond-pulsed diode-pumped $Nd^{3+}:YVO_4$ high-power laser which serves as a pump to nonlinear optical media. By using lithium triborate and periodically poled lithium niobate crystals respectively, nonlinear optical frequency conversion via sum-frequency mixing and optical parametric oscillation generates two unique sources that operate in the ultraviolet and mid-infrared wavelength regimes. Further sum-frequency mixing experiments are then employed to generate radiation that is tunable between $\lambda = 615\text{nm}$ and $\lambda = 640\text{nm}$.

1.4. Thesis outline

In Chapter Two, an overview of mode-locking of diode-pumped solid-state lasers is given. A discussion of resonator design and pump schemes is presented. A synopsis of crystalline gain medium properties is given, with an emphasis on the characteristics of $Nd^{3+}:YVO_4$. An introduction to mode-locking is also presented, along with the advantages of developing such a source for nonlinear optical frequency conversion experiments.

Chapter Three describes a diode-pumped $Nd^{3+}:YVO_4$ laser, mode-locked using an additive-pulse method. An overview of additive pulse mode-locking is presented with an historical background of the technique. Using a 17W semiconductor diode laser bar as the pump source for a $Nd^{3+}:YVO_4$ crystal, average output powers of

1.1W were observed at the emission wavelength of $\lambda = 1064$nm, with a repetition frequency of 90.7MHz. Pulses of 2.7ps duration were obtained using the additive pulse mode-locking technique. This pulse duration corresponds to a peak power of 4.5kW. Mode-locking stability and mechanical sensitivity of the laser are also discussed, with reference to the system requirements for ensuing nonlinear optical frequency conversion experiments.

Chapter Four concerns the mode-locking of a diode-pumped $Nd^{3+}:YVO_4$ laser using a saturable Bragg reflector (SBR). An overview of semiconductor saturable absorbing mirrors with emphasis on the SBR is given, along with the fundamental principals of operation. Experimental results are also presented. Using a semiconductor diode laser bar of 17W average power to side-pump a $Nd^{3+}:YVO_4$ crystal, average output powers of 4.4W were observed at a repetition rate of 235MHz, at $\lambda = 1064$nm. With inclusion of the SBR, pulses of 33ps duration were measured using a second-harmonic autocorrelator. The attributes of the laser correspond to a 567W peak power. A brief comparison between the characteristics of the APM laser described in the previous chapter and SBR mode-locked laser is presented, and the consequence of using each laser for nonlinear optical frequency conversion experiments is discussed.

Chapter Five is an overview of nonlinear optical frequency conversion. The fundamental theory is described, as are methods of increasing conversion efficiency. This chapter ends with a discussion of the properties desired of nonlinear materials for optical frequency conversion.

Chapter Six involves the mathematical model of singly resonant enhancement cavities, specifically for second and third harmonic generation. The treatment includes a brief review of resonant nonlinear optical frequency conversion and related design considerations when applied to a real pump source. Using the SBR mode-locked laser outlined in Chapter Four as a pump source, theoretical conversion efficiencies of 30% are predicted when utilising a two-crystal singly resonant enhancement cavity to generate the third harmonic at $\lambda = 355$nm. This is greatly

increased over the calculated conversion efficiency for single-pass third harmonic generation, which, for the same materials, is significantly less than 5%. The simulation of the two-crystal resonant enhancement cavity is also realised experimentally. A discussion is presented on the nonlinear materials used, and specific model parameters for the experimental configuration are considered. Conversion efficiencies >11% were measured in a generated average power of 0.5W. With the pulse duration estimated at 20ps duration which, given a repetition rate of 235MHz, corresponds to a peak power of 68W. The application of this ultraviolet source as the pump to a BaB_2O_4 optical parametric oscillator is also considered in this chapter.

Chapter Seven considers a periodically-poled lithium niobate (PPLN) optical parametric oscillator (OPO), synchronously pumped by the SBR mode-locked laser described in Chapter Four. A background of OPO theory with a brief introduction to quasi-phase-matching is presented, with further investigation on the properties and fabrication of PPLN. Experimentally, 1W of average output power was observed at the signal wavelength, which was tunable via temperature controlling from 1.4-1.6μm. Given a measured pulse duration of 34ps duration at a repetition rate of 235MHz, this corresponds to a peak power of 125W. The signal output from the OPO is then mixed with some radiation at the fundamental wavelength in nonlinear potassium titanyl arsenate (KTA) to generate tunable light from $\lambda = 615\text{nm}$ to $\lambda = 640\text{nm}$.

Chapter Eight presents the conclusions of the work presented, along with a summary of the principal results.

1.5. References

[1] T.H. Maiman, "Stimulated optical radiation in ruby", Nature, Vol. 187, 1960 (pp493-494).

[2] T.H. Maiman, "Optical and microwave-optical experiments in ruby", Physical Review Letters, Vol. 4, No. 11, 1960 (pp564-566).

[3] A. Lowery, O. Lenzmann and I. Koltchanov *et al.*, "Multiple signal representation of photonic devices, systems and networks", IEEE Journal of Selected Topics in Quantum Optics, Vol. 6, No. 2, 2000 (pp282-296).

[4] Y.Y. Chang and L.H. Chou, "Erasing mechanisms of Ag-In-Sb-Te compact disk (CD)-Rewritable", Japanese Journal of Applied Physics, Vol. 2, No. 39 (4A), 2000 (ppL294-L296).

[5] A.A. Kaminskii, "Laser crystals – their physics and properties (2^{nd} Edition)", Springer-Verlag, (ISBN 0-387-52026-0) 1990.

[6] J. Wilson and J.F.B. Hawkes, "Lasers, principles and applications", (ISBN 0135236975) 1998.

[7] D. Day and M. Gu, "Use of two-photon excitation for erasable-rewritable three-dimensional bit optical data storage in a photorefractive polymer", Optics Letters, Vol. 24, No. 14, 1999 (pp948-950).

[8] N. Bloembergen, "Nonlinear optics: past, present and future", IEEE Journal of Selected Topics in Quantum Optics, Vol. 6, No. 6, 2000 (pp876-880).

[9] L. Lefort, K. Puech and S.D. Butterworth *et al.*, "Efficient, low-threshold synchronously-pumped parametric oscillation in periodically-poled lithium niobate over the 1.3μm to 5.3μm range", Optics Communications, Vol. 152, No. 1-3, 1998 (pp55-58).

[10] D.R. Suhre and L.H. Taylor, "Six-Watt mid-infrared laser using harmonic generation with Tl_3AsSe_3", Applied Physics B, Vol. 63, No. 3, 1996 (pp225-228).

[11] G.C. Bhar, P. Kumbhakar and U. Chatterjee *et al.*, "Widely tunable deep ultraviolet generation in CLBO", Optics Communications, Vol. 176, No. 1-3, 2000 (pp199-205).

[12] S. French, M. Ebrahimzadeh and A. Miller, "High-power, high-repetition-rate picosecond optical parametric oscillator tunable in the visible", Optics Letters, Vol. 21, No. 13, 1996 (pp976-978).

[13] P. Losa-Alvarez, C.T.A. Brown and D.T. Reid *et al.*, "High-repetition-rate ultrashort-pulse optical parametric oscillator continuously tunable from 2.8 to 6.8 μm", Optics Letters, Vol. 24, No. 21, 1999 (pp1523-1525).

Chapter Two

Mode-locked Diode-pumped Solid-state Lasers

2.1. Introduction

The solid-state laser was first demonstrated by Maiman in 1960. By using active chromium ions implanted into a sapphire crystal that was placed between two mirrors to create a feedback loop, emission of coherent infrared radiation was observed when the crystal was optically pumped [1]. However, the first laser source was not truly all-solid-state, as the gain medium was excited using a flash-lamp.

The notion of an all-solid-state laser was reported by Newman in 1963. He proposed the use of a GaAs p-n junction to optically pump crystalline Nd^{3+}:$CaWO_4$ [2]. At this time, semiconductor diode lasers were of little interest, exhibiting poor beam quality and pedestrian output powers, often operating at cryogenic temperatures. However, given significant developments in this research area, semiconductor diode lasers with average output powers in excess of 600W at room temperature are now commercially available [3]. These high-power, high-brightness solid-state lasers are ideal sources to optically excite solid-state gain media due to their directional and quasi-monochromatic nature. Using such a configuration has resulted in robust and reliable all-solid-state lasers which exhibit long (>10^5 hours) lifetimes and good mechanical stability.

This chapter presents the background to the technology and techniques involved in the design of all-solid-state lasers. A brief outline of active gain media is presented, followed by a synopsis of the advantages of crystalline gain medium excitation via semiconductor diode lasers. A description of pump geometries and resonator stability is also given. The properties of one gain medium, Nd^{3+}:YVO_4, are

described with a discussion on the suitability of this medium for mode-locked operation. An outline of the principles behind mode-locking are also presented, along with the motivation for using an ultrafast-pulsed laser.

2.1.1. Solid-state lasers

The gain medium in solid-state lasers is a crystalline dielectric host material, doped with active ions. This gain crystal is generally optically pumped and, for a truly solid-state system, is performed by a semiconductor diode laser. The advantages of the solid-state gain medium over the fluidic alternatives focus on their low-maintenance nature due to increased mechanical and vibrational stability.

The active ions implanted into the crystalline host are generally rare-earth, such as neodymium or erbium, or transition metals, such as titanium or chromium. The rare-earth elements possess an electronic structure of the form $4f^N5s^25p^65d^06s^2$, where N depends on the element. When the rare-earth element is introduced to the host medium, the two 6s electrons and one of the 4f electrons are used for ionic binding. Due to screening effects from the $5s^2$ and $5p^6$ electrons, the electron-phonon coupling is very weak. This results in very sharp transition lines.

The opposite is true for transition metal based gain media. The electronic structure of the transition metals, unlike the rare-earth elements, allows the 3d states to interact strongly with the crystal field of the host material. This results in broad absorption and emission bands, the latter giving rise to laser sources emitting tunable radiation.

The absorption and emission properties of crystalline gain media, as described above, are also dependent on the host material chosen. This is reflected by analysis of different materials as shown in table 1. For example, neodymium when implanted into $Y_3Al_5O_{12}$ (YAG) has different absorption and emission properties than when implanted into $YLiF_4$ (YLF). The choice of gain medium is then dependent on the application.

The defining properties of the host material must also be considered in the design process of the laser system. For example, oxide materials have a tendency to be harder whereas glass hosts have poor thermal properties [4]. This may influence the choice of material and pump source. For example, a glass host material would be unsuitable for a high-power application since it cannot withstand high pump powers.

Material	Absorption Wavelength (nm)	Emission Wavelength (nm)	Pump diode material
Nd^{3+}:YAG [5,6]	808	1064	GaAs/AlGaAs
Nd^{3+}:YLF [5]	793, 797	$\pi = 1.047$ $\sigma = 1.053$	GaAs/AlGaAs
Nd^{3+}:YVO_4 [6]	808	1064	GaAs/AlGaAs
Yb^{3+}:YAG [7,8]	940	1030	InGaAs

Table 1. Wavelength properties of laser gain materials and the associated semiconductor diode laser pump materials.

2.2. Method of excitation

Pumping of gain media is usually performed by two means – optical or electrical. Electrical pumping involves current flow in the gain medium and is most suitable for semiconductor materials. Optical pumping makes use of a continuous wave or pulsed light source to excite the gain material. The pump radiation may also be either coherent or incoherent. Incoherent pumping uses output from a high power lamp source to excite the atoms from the ground state. However, such sources have several disadvantages over coherent pumping. Coherent pumping utilises another laser to create a population inversion within the gain medium. With semiconductor lasers becoming increasingly available at high powers with continuous wave, room temperature operation, these devices are preferable to the alternative incoherent sources used in optical excitation.

Incoherent pump sources typically operate over a wide wavelength range (>10^3 nm). This leads to many undesirable effects. Typically, a gain material will only absorb over a narrow wavelength region compared with the emission of the incoherent source. This leads to absorption of unwanted radiation within the crystal, which may contribute to heating effects such as thermal lensing. In comparison, diode lasers have a narrow linewidth and many are operational at a wavelength matching that of the crystal absorption.

Brightness, defined as the power per unit area per unit solid angle, is also an advantage of coherent pump sources. Due to the highly directional nature of a laser beam, the peak intensity of a focussed beam is several orders of magnitude greater than that of an incoherent source of the same average power.

Diode lasers covering wavelength regions of $\lambda = 405$nm to $\lambda = 10\mu$m are commercially available [9, 10]. However, many diodes in this region have no application as pump sources due to poor optical properties or no crystalline media with absorption bands at these wavelengths. Generally, laser diodes for optical pumping fall between $\lambda = 650$nm and $\lambda = 980$nm, which provides the semiconductor industry with impetus to provide high-power, high-brightness lasers at these wavelengths.

Laser diodes also provide flexibility. Emission wavelength can be altered by changing the diode material, but also by temperature controlling, albeit to a lesser degree. For GaAs/AlGaAs devices, the wavelength varies as approximately 0.3nm/°C [11]. Temperature stabilisation (and cooling) generally ensures a longer operational lifetime of the diode under manufacturer specified limits.

2.2.1. Diode Pumping

Semiconductor diode laser pumping has been shown to be a high efficiency means of excitation. However, the diode laser type employed is dependent on the gain

medium and laser requirements. Wavelength, as described by table 1, and brightness are obvious requirements, but power is also a factor. Five main types of pump diodes currently exist: single stripe, diode array, diode bar, stacked bar and fibre coupled.

The diode bar is the basis of the most powerful semiconductor lasers, with output powers in excess of 15W. In this device, many arrays of "stripes" form the active region. This device is typically 1cm long, emitting in a fast-diverging elliptical beam. This structure is the foundation for the diode stack. An array of diode bars forms a large emitting region that may generate over 600W of average power [3]. Such structures are ideal for transverse pumping, which will be described in § 2.3.2.

A variation of the diode bar is the fibre-coupled device. These devices are based on the high-power diodes as described, but the output is coupled into fibre optic cables. The main disadvantages of these devices are power limitations and poor beam quality through highly divergent output. Output powers typically do not exceed 50W for this reason. They do, however, permit flexibility within pump schemes and are best suited to longitudinal pump geometries, as described in § 2.3.1.

2.3. Pump Schemes

One of the most fundamental considerations in the design of an efficient optically pumped laser is to ensure a good overlap between the pump and oscillating modes within the gain medium. Therefore, to make full use of the output from the devices described previously, the output must be used in conjunction with appropriate pump geometry to ensure a good match with the cavity mode. Again, this depends on the gain medium geometry and system requirements.

Two types of optical pumping configurations exist: longitudinal (or end) pumping and transverse (or side) pumping.

2.3.1. Longitudinal Pumping

Longitudinal pumping involves tight focussing of the pump radiation into one end of the gain medium to excite the lowest-order mode. This is described in figure 1 by use of a simple two-mirror resonator around a crystalline gain medium. Most frequently, a single pump beam is collimated using an external element and directed into the end of a laser rod through a cavity mirror, as shown. Output from diode bars and stacks are difficult to use in this geometry, owing to their large beam diameter and associated difficulties in obtaining a focussed beam over the length of the gain medium. Fibre-coupled devices are most suited to this application.

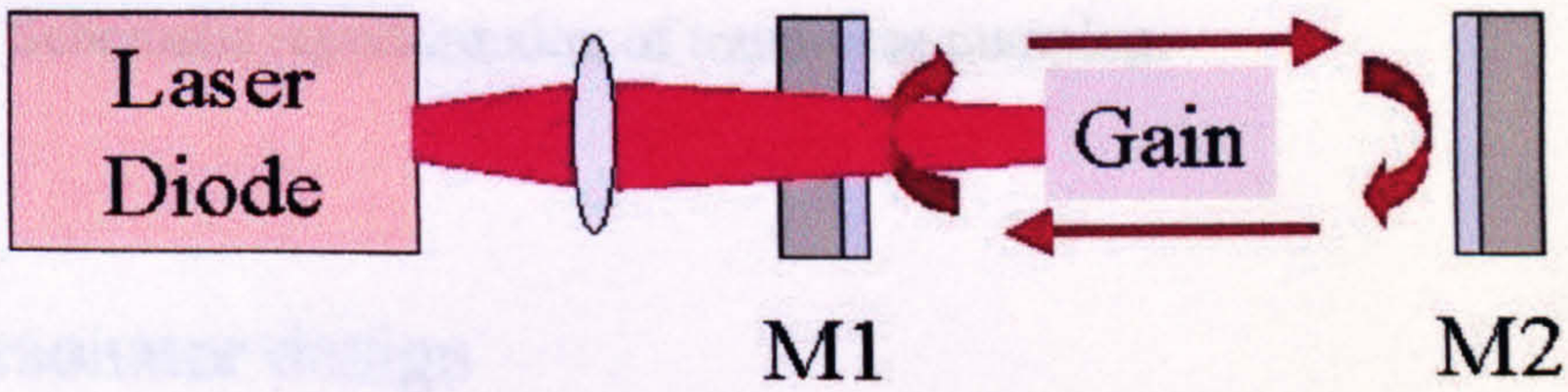

Figure 1. Schematic representation of longitudinal pumping of a crystalline gain medium. More than one focussing element may be used to focus the pump radiation into the end of the gain material.

Fibre-coupled devices have large divergences, but may be compensated by using a spherical focussing element when the gain medium is short, such as thin disk lasers [12]. The elliptical output from the diode array and single stripe structures may be corrected to a circular beam by use of cylindrical lenses or anamorphic prisms.

2.3.2. Transverse pumping

Transverse pumping is most frequently applied to slab and thick rod (>1mm) lasers and most often uses diode bars and stacks to generate high power lasers. The advantages of this system is the ease of power scaling by adding more diode lasers,

efficient coupling of the pump mode into the laser mode and reduction of localised heating within the gain material through less stringent focussing requirements.

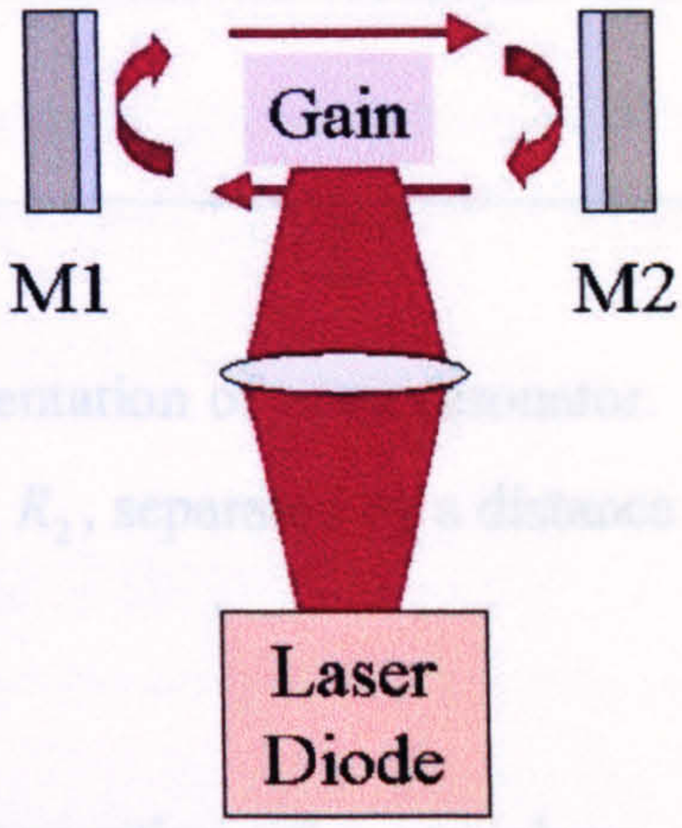

Figure 2. Schematic representation of transverse pumping.

2.4. Resonator design

The simplest resonator design comprises of two plane mirrors that reflect the stimulated emission from the gain medium and create a feedback loop. Such a basic cavity is widely used with various gain media but in reality more than two mirrors is common practice to create a good overlap between the pump and cavity modes, or allow for the introduction of additional elements into the cavity. The resonator design depends on the system requirements, pump geometry and laser operation. It is vital, however, that a stable resonator is created to ensure a high efficiency process.

The general structure assumed for an open resonator is two spherical mirrors separated by a distance L, as shown in figure 3. Using a ray transfer matrix approach, a condition for the cavity stability may be calculated.

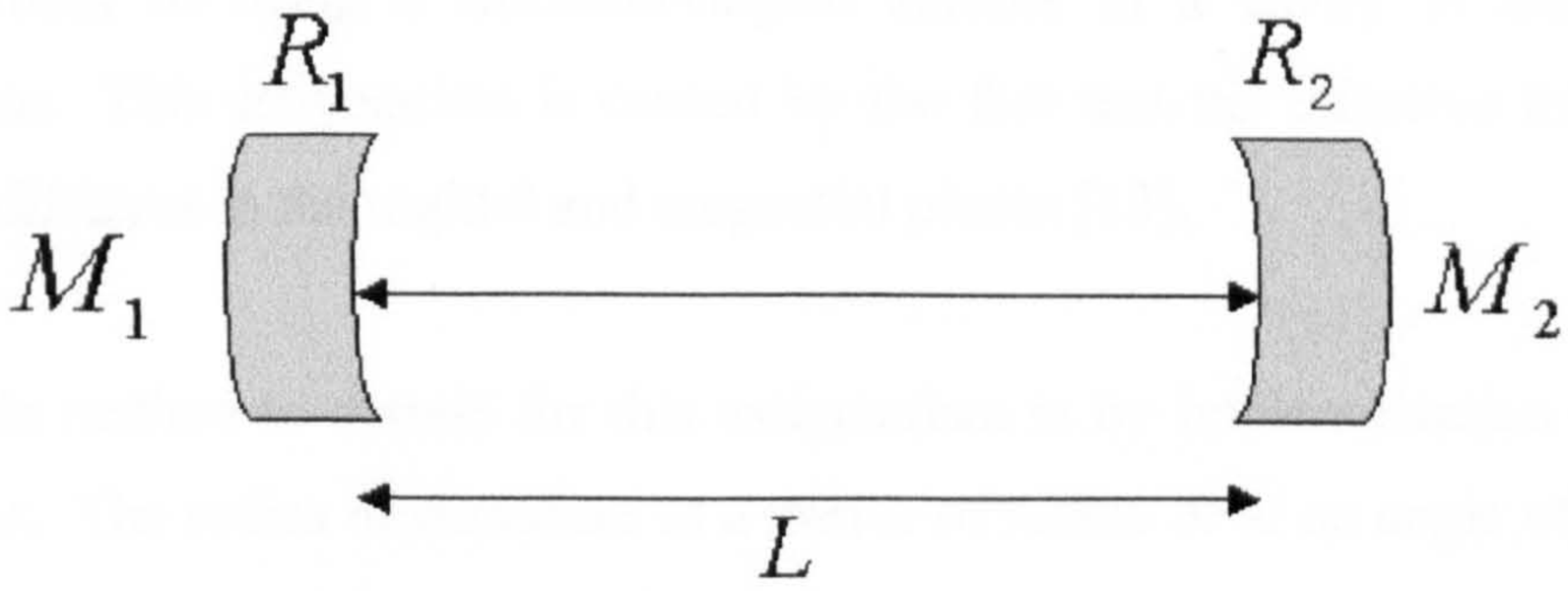

Figure 3. Schematic representation of open resonator. This consists of two mirrors of radii of curvature R_1 and R_2, separated by a distance L.

Using this method, the propagation of a ray along a distance L in air may be described using the ray transfer matrix system to yield [13]

$$0 < \left(1 - \frac{L}{R_1}\right)\left(1 - \frac{L}{R_2}\right) < 1 . \qquad (2.1)$$

This method can also be used to account for the inclusion of intracavity elements such as lenses, gain media and Brewster surfaces. Several software programs to evaluate optical systems exist that employ the ray transfer matrix approach, but that employed here is a simple and adaptable in-house MathCAD program.

2.4.1. Brewster surfaces and astigmatic compensation

Brewster-angled gain crystals are often used in solid state lasers to minimise loss that occurs due to the partial reflection of beams at the crystal surface and is of particular use in mode-locked lasers, where such reflections may cause etalon effects and disrupt mode-locking.

One drawback of using a Brewster-angled surface in a cavity is the resulting astigmatism. This astigmatism is caused by the fact that the effective thickness of the rod is different in the sagittal and tangential planes [13].

One simple method to correct for this astigmatism is by implementation of an off-axis mirror. The radius of curvature of a mirror of radius R at an angle of incidence θ is given by

$$R\sin(\theta)\tan(\theta) = \frac{2t\left[\left(n^2-1\right)\left(n^2+1\right)^{\frac{1}{2}}\right]}{n^4}, \tag{2.2}$$

where R is the radius of curvature of the mirror, n is the refractive index of the gain medium and t is the gain medium thickness. This relationship may then be used to calculate the mirror offset angle to compensate for astigmatism that results in a circular output beam from the cavity.

2.5. Laser gain materials

Solid-state lasers are devices that do not have a gas or liquid gain medium. Two types of solid-state laser exist: semiconductor diode lasers and those based on optically active ions introduced into a crystal host, known as a doped insulator laser. Although very high output powers are observed in single element semiconductor diode lasers, these devices are inflexible and have inferior beam properties to those based on the crystalline material. The doped insulator laser may be engineered to provide wider wavelength tunability and spectral purity, delivered in a single TEM_{00} mode. Such properties are of significance for a number of applications, including pumping nonlinear optical materials, therefore the doped insulator laser forms the focus of this research.

Doping of crystalline hosts with optically active rare-earth ions results in an increasing choice of gain medium which results in discontinuous laser operation over a range of 0.7-2.9μm [7]. The most-used solid-state gain media are based on neodymium dopants and as such will form the basis of this discussion.

2.5.1. Neodymium based lasers.

Neodymium (Nd) based lasers make very attractive sources for various applications, from low-power continuous-wave sources for surgery [14] to high-energy pulsed systems for micro-machining [15] and ultrashort-pulsed high-power lasers for pumping nonlinear materials [16]. As a dopant, trivalent neodymium may be introduced to an ever-increasing range of host materials. The dopant concentration is generally limited to around 1% (with glass as the exception) due to cross-relaxation at higher dopant levels, which subsequently reduces the capacity of energy storage [17]. The most prominent of these host materials is $Y_3Al_5O_{15}$ (YAG), which is an attractive choice for a host medium. When doped with neodymium, it is mechanically stable, has a gain bandwidth capable of supporting ultrashort pulses [18] and absorbs at a wavelength readily associated with commercially available GaAs/AlGaAs pump diodes [5].

Depending on the application, however, it may be advantageous to employ other host materials. For a high-power source, crystals based on a glass host medium, such as Nd^{3+}:glass, are not suitable due to a low melting point [7]. However, for generation of ultrashort pulses, Nd^{3+}:glass can deliver pulses as short as 60fs [19], when used in conjunction with a suitable mode-locking mechanism. This is due to the disordered nature of the material, which gives rise to a broader spectrum and consequently shorter pulses.

Occasionally, a trade-off between these two properties may be needed. $Nd^{3+}:YVO_4$, for example, compromises pulse duration, but permits high average powers. $Nd^{3+}:YVO_4$ is one such material and forms the basis of the work in this thesis.

2.5.2. Spectroscopic properties of Nd^{3+}:YVO_4

Nd^{3+}:YVO_4 is a four-level laser system, with the energy level positions as shown in figure 4. Neodymium ions in the ground state absorb photons and are raised in energy to one of the pump bands. The states in these bands have lifetimes on the order of 10^{-8} seconds, and the atoms drop to the upper lasing level by radiationless transitions that take place on a picosecond scale. The upper laser level, $^4F_3/_2$, has a fluorescent lifetime of about 90 μs. Given suitable excitation, a population inversion develops and in a resonant cavity, oscillation occurs, with the population being driven to the lower laser level. This level is very close to the ground state, and excited atoms rapidly return to the ground state by another radiationless transition.

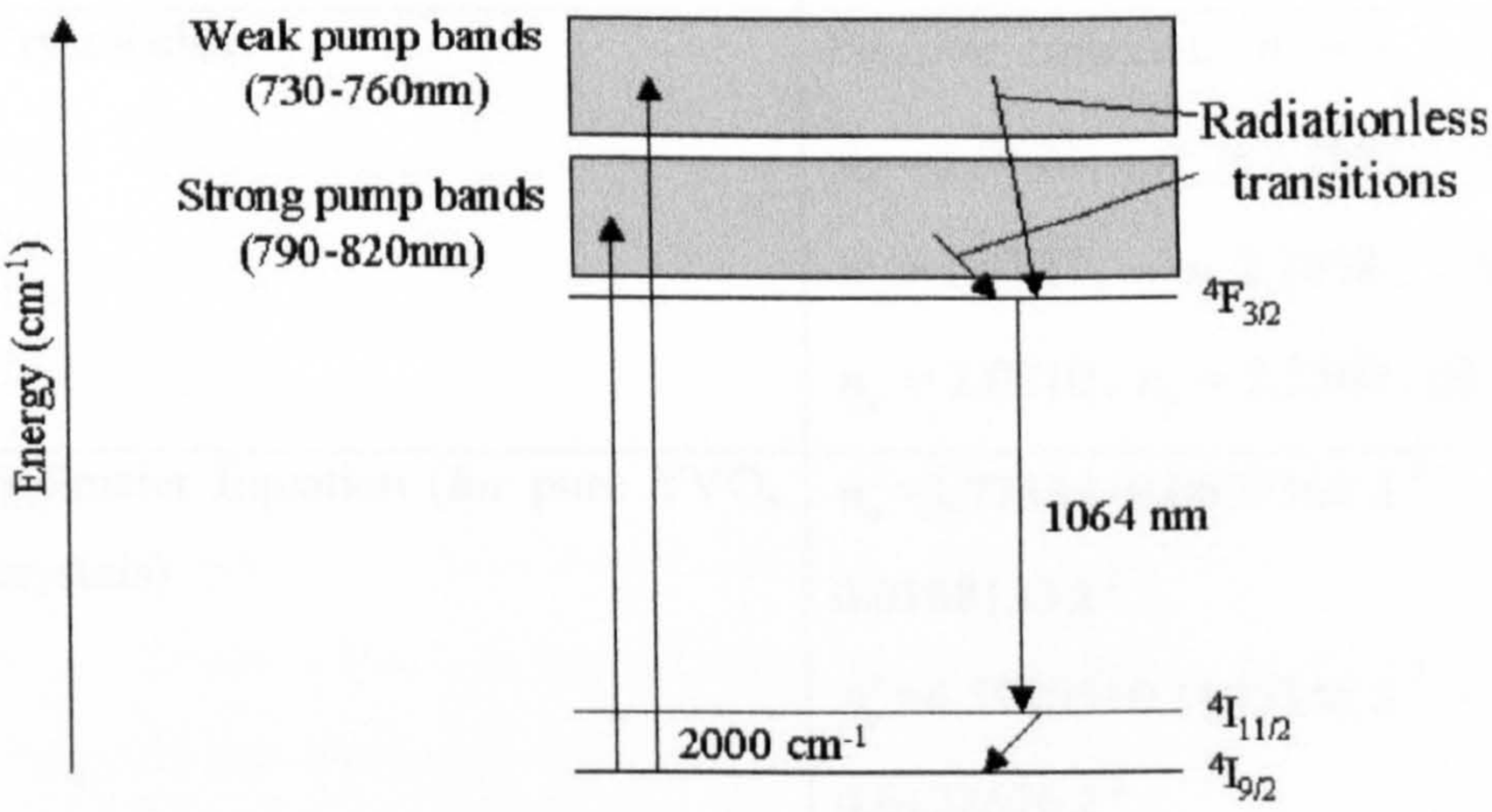

Figure. 4. Energy level diagram of Nd^{3+}:YVO_4.

The energy associated with radiationless transitions as well as the thermal and other optical cavity energy absorbed by the rod all add to the internal energy of the laser rod. If the gain medium temperature is too high, the lower laser level is thermally populated by atoms from the ground state, and the rate of transition from the lower laser level to the ground state is greatly reduced. This destroys the population inversion and quenches lasing. Thus, cooling to maintain a proper temperature is important in Nd^{3+}:YVO_4 lasers.

Compared with Nd^{3+}:YAG and Nd^{3+}:YLF for diode laser pumping, Nd^{3+}:YVO_4 lasers possess the advantages of lower dependency on pump wavelength and temperature control of a diode laser, wide absorption band, higher slope efficiency, lower lasing threshold, linearly polarised emission, shorter upper-state lifetime, larger cross-section and single-mode output [20].

These properties indicate that Nd^{3+}:YVO_4 is a good gain medium for a mode-locked laser and that the material can support pulses as short as 1ps. One advantage of this material is the polarised nature of the output, which is advantageous in pumping nonlinear optical materials. It is therefore this gain medium that is chosen as the basis for the work in this thesis. The principal optical properties are shown in table 2.

Emission wavelengths	914nm, 1064 nm (high gain), 1342 nm
Crystal class	Positive uniaxial, $n_o = n_a = n_b$, $n_e = n_c$ $n_o = 1.9573$, $n_e = 2.1652$, @ 1064nm $n_o = 1.9721$, $n_e 2.1858$, @ 808nm $n_o = 2.0210$, $n_e = 2.2560$, @ 532nm
Sellmeier Equation (for pure YVO_4 crystals)	n_o^2=3.77834+0.069736/(λ^2 - 0.04724) - 0.0108133 λ^2 n_e^2=4.59905+0.110534/(λ^2 - 0.04813) - 0.0122676 λ^2
Thermal Optical Coefficient	$\frac{\partial n_a}{\partial T}$ =8.5x10^{-6}/K, $\frac{\partial n_c}{\partial T}$ =3.0x10^{-6}/K
Stimulated Emission Cross-Section	25.0x10^{-19} cm^2, @1064 nm
Fluorescent Lifetime	90 μs @ 808 nm
Absorption Coefficient	31.4 cm^{-1} @ 808 nm
Absorption Length	0.32 mm @ 808 nm
Intrinsic Loss	Less than 0.1% cm^{-1} @1064 nm
Gain Bandwidth	0.96 nm (257 GHz) @ 1064 nm

Table 2. Electronic properties of Nd^{3+}:YVO_4 (1.1% Nd^{3+}) [21].

2.6. Generation of ultra-short pulses

Under normal operation, a laser resonator will support a large number of axial modes. This number will depend on the resonator design, gain excitation and gain medium properties. These modes are generally of random phase. However, an element may be introduced into the cavity that will force these modes to oscillate in phase. The result is the generation of pulses of radiation, less than 10^{-9}s in duration. This procedure is known as mode-locking [22].

The time varying electric field at any point in a laser resonator may be expressed as

$$E(t) = \sum_{n=-\infty}^{\infty} E_n \exp\left[i(\omega_0 + n\Delta\omega)t + \phi_n(t)\right], \tag{2.3}$$

where n is the nth axial mode, ω_0 is the central oscillation frequency, $\Delta\omega$ is the axial mode spacing and $\phi_n(t)$ and E_n are the phase and amplitude of the nth mode, respectively.

In a continuous wave laser the phase $\phi_n(t)$ varies randomly with time, however if the phase difference between the nth and $n-1$th modes is zero, the modes will then coherently superimpose. This leads to a well-defined output in both the time and frequency domains. Under this condition where N modes circulate and, for simplicity, $E_n = 1$,

$$E(t) = \sum_{n=-\frac{N}{2}}^{\frac{N}{2}} \exp[i(\omega_0 + n\Delta\omega)t] = \exp\left[i(\omega_0 t)\right] \frac{\sin\left(\frac{N\Delta\omega t}{2}\right)}{\sin\left(\frac{\Delta\omega t}{2}\right)}. \tag{2.4}$$

The corresponding expression for intensity $I(t)$ is

$$I(t) = E(t).E^*(t) = \frac{\sin^2\left(\frac{N\Delta\omega t}{2}\right)}{\sin^2\left(\frac{\Delta\omega t}{2}\right)}. \qquad (2.5)$$

As the modes superimpose, the intensity scales as N^2, therefore it is important to use a material with a broad gain bandwidth. This results in an enhancement in the peak power that is related to the pulse duration by

$$P_{peak} = \frac{P_{average}}{\delta\tau.\Delta\upsilon}, \qquad (2.6)$$

where $\delta\tau$ is the pulse duration and $\Delta\upsilon$ is the repetition rate of the laser. It is this peak power which makes mode-locked sources an attractive alternative to continuous wave lasers for frequency conversion experiments, which will be discussed in later chapters.

The pulse duration $\delta\tau$ and pulse bandwidth $\delta\omega$ are related by

$$\delta\tau\delta\omega = k, \qquad (2.7)$$

where k depends on the pulse shape. This is known as the time-bandwidth product. For a Gaussian pulse shape, $k = 0.414$, but for a sech^2 profile, $k = 0.315$. A table of time-bandwidth products for different pulse shapes may be found in reference 23.

2.6.1. Historical overview of mode-locking

The first demonstrations of mode-locked lasers were using ruby [24] and helium-neon [25] gain media. Both systems delivered pulses in the picosecond regime.

Since this time, however, the development of novel gain media capable of delivering ultrashort pulses and new mode-locking techniques has enabled the generation of low-maintenance high-power all-solid-state devices over a range of wavelengths and pulse durations.

An important advance in the area of mode-locking was the realisation of the saturable absorber as a modulation device and led to the first sub-picosecond devices when used in conjunction with a continuous wave dye laser [26]. However, dye lasers are notoriously difficult to handle and thus an alternative was sought in the form of a mode-locked solid-state laser.

Few solid-state materials at this time were of sufficient gain bandwidth to support ultrashort pulse generation. This problem was overcome with the emergence of materials such as Ti:sapphire and Nd^{3+}:YAG. However, mode-locking of these lasers was not a trivial problem.

The saturable absorber used in the dye laser was a slow saturable absorber. This slow saturable absorption mechanism is described by New in reference 27. The leading edge of the pulse is absorbed by the saturable absorber whilst the trailing edge is shaped by gain saturation. This means that only a single edge of the pulse is absorbed and therefore device recovery time is negligible. However, the comparatively low gain of the solid-state lasers means that a fast saturable absorber, capable of shaping both sides of the pulse is required.

One such means is described by Mollenauer [28]. The laser resonator was coupled using a beamsplitter mirror to an external resonator containing an optical fibre. Using an interference effect between pulses at the beamsplitter and correcting for the phase by controlling the length of the external resonator, a fast saturable effect was observed. This technique is known as additive pulse mode-locking (APM) and will be discussed in greater detail in Chapter Three.

Another significant development in the generation of ultrashort pulses was the discovery of Kerr-lens mode-locking (KLM) by Sibbett *et al.* [29]. Using a self-focussing effect inside the gain medium, pulses shorter than 5fs have been observed in Ti:sapphire [30].

Both the APM and KLM lasers have disadvantages. Although self-starting, such lasers are extremely sensitive to vibration and change in resonator length. The APM system, for example, requires complex electronics to ensure locking of the external resonator length to within a half-wavelength. These problems were largely overcome by the use of semiconductor materials as fast saturable absorbers.

The first laser to use such materials was a Ti:sapphire system. By employing an external cavity with a nonlinear quantum-well mirror, pulses of 2ps duration were realised without stabilisation or dispersion compensation, allowing a 2mm tolerance in cavity length and pulses over a 50nm wavelength range [31]. This method is known as coupled-cavity resonant passive mode-locking (RPM).

Progress in semiconductor growth led to monolithic semiconductor devices that comprised of both the reflecting mirror and quantum well structure that acted as fast saturable absorbers. This eliminated the need for an external cavity since these devices could be placed into the laser resonator due to the highly reflective nature. This family of devices is known generically as the semiconductor saturable absorbing mirror, or SESAM. These devices will be discussed in Chapter Four.

2.7. Conclusions

A background to diode-pumping of solid-state gain media has been presented. A comparison between the types of pumping and semiconductor diode lasers has been given, in context with a discussion on pumping methods. A synopsis of laser gain media with emphasis on Nd^{3+}:YVO_4 has been presented, due to the suitability of this material as the basis for a high-powered mode-locked laser. A review of the

motivation for mode-locking and associated techniques has also been presented. This will be explored further in the following two chapters.

2.8. References

[1] T.H. Maiman, "Optical and microwave-optical experiments in ruby", Physical Review Letters, Vol. 4, No. 11, 1960 (pp564-566).

[2] R. Newman, "Excitation of the Nd^{3+} fluorescence in $CaWO_4$ by recombination radiation in GaAs", Journal of Applied Physics, Vol. 34, 1963 (pp437-438).

[3] http://www.spectra-physics.com/products/spsl_products/multi-bar.html, "Spectra-Physics Products and Services" – see Appendix One.

[4] A.A. Kaminskii, "Laser crystals - their physics and properties (2^{nd} Edition)", Springer-Verlag, (ISBN 0-387-52026-0) 1990.

[5] C.J. Flood, D.R. Walker and H.M. van Driel, "CW diode pumping and FM mode locking of a Nd:KGW laser", Applied Physics B, Vol. 60, 1995 (pp309-312).

[6] Y. Kalisky, L. Kravchik and C. Labbe, "Repetitive modulation and passive Q-switching of diode-pumped Nd-KGW laser", Optics Communications, Vol. 189, 2001 (pp113-125).

[7] http://www.mt-berlin.com/charts/chart_03.htm, "Laser Elements from Moltech" – see Appendix Two.

[8] U. Brauch, A. Giesen and M. Karszewski *et al.*, "Multiwatt diode-pumped Yb:YAG thin disk laser continuously tunable between 1018 and 1053 nm", Optics Letters, Vol. 20, No. 7, 1995 (pp713-715).

[9] Anonymous, "Nichia claims room-temperature blue-purple diode laser", Photonics Spectra, Vol. 30, No. 1, 1996 (p27).

[10] D. Hofstetter, J. Faist and M. Beck *et al.*, "Demonstration of high-performance 10.16μm quantum cascade distributed feedback laser fabricated without epitaxial regrowth", Applied Physics Letters: Vol. 75, No. 5, 1999 (pp665-667).

[11] http://www.splasers.com/products/spsl_products/bars.html, "Spectra-Physics Products and Services, Semiconductor Laser Bars" – see Appendix One.

[12] W.F. Krupke, "Ytterbium solid-state lasers – The first decade", IEEE Journal of Selected Topics in Quantum Optics, Vol. 6, No. 6, 2000 (pp1287-1296).

[13] D.R. Hall, P.E. Jackson, "The Physics and Technology of Laser Resonators", Adam Hilger Press, 1989.

[14] Dornier Nd:YAG (Company literature, 2001).

[15] L. Tunna, A. Kearns and W. O'Neill *et al.*, "Micromachining of copper using Nd :YAG laser radiation at 1064, 532, and 355nm wavelengths", Optics and Laser Technology, Vol. 33, No. 3, 2001 (pp135-143).

[16] B. Ruffing, A. Nebel and Wallenstein R, "High-power picosecond LiB_3O_5 optical parametric oscillators tunable in the blue spectral range", Applied Physics B – Lasers, Vol. 72, No. 2, 2001 (pp137-149).

[17] J. Wilson and J.F.B. Hawkes, "Lasers, principles and applications", (ISBN 0135236975) 1998.

[18] J. Goodberlet, J. Jacobson and J.G. Fujimoto *et al.*, "Self-starting additive-pulse mode-locked diode-pumped Nd:YAG laser", Optics Letters, Vol. 15, No. 9, 1990 (pp504-506).

[19] J. Aus der Au, D. Kopf and F. Morier-Genoud *et al.*, "60-fs pulses from a diode-pumped Nd:glass laser", Optics Letters, Vol. 22, No. 5, 1997 (pp307-309).

[20] A. Agnesi, C. Pennachio and G.C. Reali *et al.*, "High-power diode-pumped picosecond $Nd^{3+}:YVO_4$ laser", Optics Letters, Vol. 22, No. 21, 1997 (pp1645-1647).

[21] http://www.casix.com/products/crystalls_laser_1.htm, Casix Inc. – see Appendix Three.

[22] A.E. Siegman, "Lasers", Oxford University Press, (ISBN 0935702113) 1986.

[23] K.L. Sala, G.A. Kenney-Wallace and G.E. Hall, "Cw autocorrelation measurements of picosecond laser pulses", IEEE Journal of Quantum Electronics, Vol. QE-16, No. 9, 1980 (pp990-996).

[24] K. Gurs, "Beats and modulation in optical ruby lasers", Quantum Electronics III, P.Grivet and N. Bloembergen, Eds. New York: Columbia University Press, 1964 (pp1113-1119).

[25] H. Statz and C.L. Tang, "Zeeman effect and nonlinear interactions between oscillating lasr modes", Quantum Electronics III, P. Grivet and N. Bloembergen, Eds. New York: Columbia University Press, 1964 (pp469-498).

[26] C.V. Shank and E.P. Ippen, "Sub-picosecond kilowatt pulses from a mode-locked cw dye laser", Applied Physics Letters, Vol. 24, 1974 (pp373-375).

[27] G.H.C. New, "Pulse evolution in mode-locked quasicontinuous lasers", IEEE Journal of Quantum Electronics, Vol. QE-10, 1974 (pp115-124).

[28] L.F. Mollenauer and R.H. Stolen, "The soliton laser", Optics Letters, Vol. 9, 1984 (pp13-15).

[29] D.E. Spence, P.N. Kean and W. Sibbett, "60-fsec pulse generation from a self-mode-locked Ti:sapphire laser", Optics Letters, Vol. 16, 1991 (pp42-44).

[30] D.H. Sutter, L. Gallmann and N. Matuschek *et al.*, "Sub-6-fs pulses from a SESAM-assisted Kerr-lens modelocked Ti:sapphire laser: at the frontiers of ultrashort pulse generation", Applied Physics B., Vol. 70, 2000 (ppS5-S12).

[31] U. Keller, W.H. Knox and H. Roskos, "Coupled-cavity resonant passive mode-locked Ti:sapphire laser", Optics Letters, Vol. 15, 1990 (pp1377-1379).

Chapter Three

Diode-pumped Additive Pulse Mode-locked $Nd^{3+}:YVO_4$ laser

3.1. Introduction

As discussed in § 2.6, the mode-locked diode-pumped solid-state laser is an intense, compact and efficient source of ultrashort pulses. These systems are ideal for nonlinear optical frequency conversion experiments due to the high peak power that arises from the pulsed nature of the source. The following two chapters concern alternative approaches to the experimental realisation of a high power mode-locked laser source.

Mode-locking techniques fall into two principal categories: active and passive. Active mode-locking techniques depend upon modulation by a driving force, such as an acousto-optic modulator placed within the resonator that periodically changes the gain or loss within the laser cavity with reference to the round-trip time of the cavity. This modulation frequency is fixed and therefore such lasers are largely inflexible and intolerant to cavity length detuning. Passive mode-locking techniques, such as saturable absorption, use a passive intracavity element that requires no external influence, but responds in a nonlinear manner to the intracavity field. This gives rise to a reliable and flexible mode-locking technique. Additive pulse mode-locking (APM) is one-such type of passive mode-locking, and is described here for the case of a $Nd^{3+}:YVO_4$ laser.

An overview of APM is presented, in context of previous results using this technique. The diode-pumped laser resonator features are given, followed by the

characteristics of the external resonator. The results of this system are presented, along with a discussion on the suitability of the source for nonlinear optical frequency conversion experiments.

3.2. Historical review of additive pulse mode-locking.

The primary reason for using the passive APM method is due to the commercial availability of the necessary components. This eliminates the requirement for specially engineered mode-locking elements. Furthermore, APM has been successfully demonstrated in other neodymium-based materials, generating pulses close to that prescribed by the gain bandwidth of the material.

Mollenauer and Stolen first realised mode-locking using a nonlinear element in an external resonator in 1984. Their configuration consisted of a synchronously-pumped mode-locked colour-centre resonator operating at $\lambda = 1.5\mu m$, coupled using a semi-transparent mirror to an external cavity which contained a length of single-mode polarisation preserving fibre. They observed a pulse compression effect, reducing the pulse duration from 2ps to 210fs. This pulse shortening was thought to be the result of group velocity dispersion. As broad noise pulses propagated through the fibre, they experienced negative group velocity dispersion, forcing the laser to produce narrower pulses. In the case of Mollenauer and Stolen, the process continued until the pulses in the fibre retained their shape on double propagation through the fibre. This was reported in the eponymous soliton laser publication [1].

This concept was reviewed by Blow and Wood in 1988 [2]. They proposed that negative group velocity dispersion was not a necessary condition for APM to occur, but that shorter mode-locked pulses could be achieved by coupling a laser to an external resonator containing any element which responds nonlinearly to an incident optical field. This theory was the basis for the first APM laser by Goodberlet *et al.* in 1989. They demonstrated an additive pulse mode-locked picosecond/femtosecond Ti:sapphire laser [3]. This technique has since been extended to other materials,

including colour centre lasers [4], thulium-doped fibre ring lasers [5] and Nd^{3+}:YAG [6] and Nd^{3+}:YLF lasers [7].

3.3. Basic theory of additive pulse mode-locking

A full treatment of the mechanisms underlying pulse-shortening in additive pulse mode-locking is provided by Ippen *et al.* [8].

The basic design of an additive pulse mode-locked laser is shown in figure 1. An external resonator is coupled via a beam-splitting mirror of reflectivity r to the laser resonator. The lengths of the external resonator and the laser cavity are matched such that the peak of two pulses may overlap at the beam splitter. It is this beating effect which gives rise to pulse shortening.

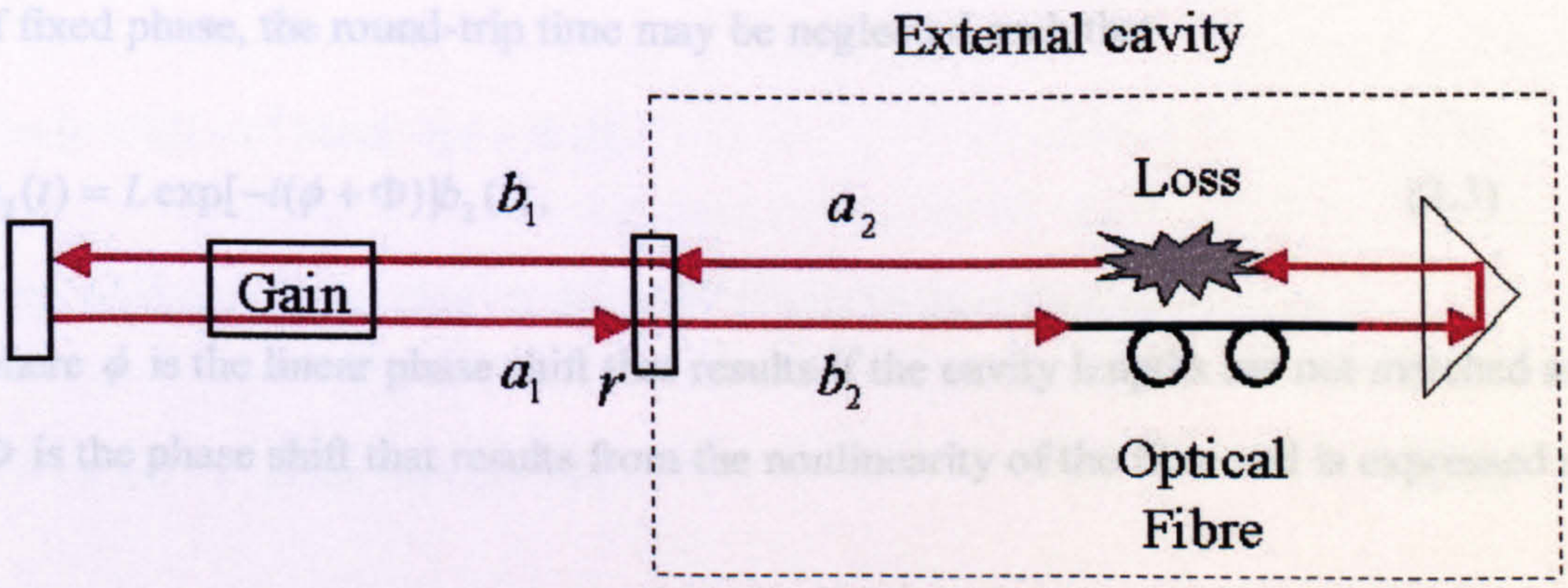

Figure 1. Schematic diagram of APM laser. The laser resonator output coupler, with reflectivity r, is the point of interference between the reflected and the transmitted fields. The external resonator contains a nonlinear element, in the form of an optical fibre. The inherent loss of the system is also considered. The monitor beam is used to determine the optimum external cavity length.

The expressions for the reflected and transmitted fields at the beam-splitting mirror are given by

$$b_1 = ra_1 + \sqrt{1-r^2}a_2 \tag{3.1}$$

and

$$b_2 = \sqrt{1-r^2}a_1 - ra_2, \tag{3.2}$$

where a_1, a_2, b_1 and b_2 are the field amplitudes and r is the beamsplitter reflectance, as shown in figure 1. The field b_2 propagates through the optical fibre (twice, in practice) and, after being subjected to a loss L, propagates as a_2.

The auxiliary cavity contains a nonlinear element, such as an optical fibre, which has an intrinsic loss, determined by an attenuation factor L. With the external resonator of fixed phase, the round-trip time may be neglected such that

$$a_2(t) = L\exp[-i(\phi + \Phi)]b_2(t), \tag{3.3}$$

where ϕ is the linear phase shift that results if the cavity lengths are not matched and Φ is the phase shift that results from the nonlinearity of the fibre and is expressed as

$$\Phi = \kappa[|a_2(t)|^2 - |a_2(0)|^2], \tag{3.4}$$

where κ is dependent on the length and nonlinearity of the nonlinear element.

By expressing $b_2(t)$ as a function of $a_2(t)$ and inserting the result into (3.1) and (3.2) where ϕ is constant,

$$b_1 = \frac{1}{\sqrt{1-r^2}}\left\{1+\frac{r}{L}\exp[i(\phi+\Phi)]\right\}a_2 \tag{3.5}$$

and

$$a_1 = \frac{1}{\sqrt{1-r^2}}\left\{r+\frac{1}{L}\exp[i(\phi+\Phi)]\right\}a_2 . \tag{3.6}$$

The reflection coefficient of the external resonator, Γ, is

$$\Gamma = \frac{b_1}{a_1} = \frac{1+\frac{r}{L}\exp[i(\phi+\Phi)]}{r+\frac{1}{L}\exp[i(\phi+\Phi)]}. \tag{3.7}$$

Under the assumption that the loss of the nonlinear element $L<<1$, the reflection coefficient Γ may be expressed as

$$\Gamma = \{r + L\{1-r^2)\exp[-i(\phi+\Phi)]\}. \tag{3.8}$$

If the nonlinear phase shift Φ is small, Γ can be described by

$$\Gamma = r + L(1-r^2)\exp(-i\phi).(1-i\Phi). \tag{3.9}$$

In order to treat every physical value of $|\Gamma|$, $\phi = \pm\frac{\pi}{2}$. At $\phi = -\frac{\pi}{2}$, the reflection coefficient is described by

$$|\Gamma| \cong r + L(1-r^2)\Phi. \tag{3.10}$$

This simple relationship indicates that the reflection coefficient is maximum at the pulse centre, which results in a significant decrease in the pulse duration. It is

therefore possible to use this effect to achieve continuous wave mode-locking of a laser source.

3.4. Design of diode-pumped APM $Nd^{3+}:YVO_4$ laser

The laser resonator was a diode-based side-pumped $Nd^{3+}:YVO_4$ system as shown schematically in figure 2. A 1cm long 17W diode bar (OPC-A020-809-CS/L) collimated in the fast-axis by a fibre microlens was used to pump a 12-mm long Brewster-Brewster 1.1 atm. % $Nd^{3+}:YVO_4$ parallelepiped crystal in the sagittal plane, supplied by Casix. The diode bar was mounted on an oxygen-free copper base with Teflon insulation at the base. The copper region was water-cooled to 15°C, which corresponded to a diode laser output wavelength of λ=808nm. This matches the peak absorption wavelength of $Nd^{3+}:YVO_4$. A side-pumped geometry was chosen to maximise the coupling efficiency of the pump spot into the cavity mode as discussed in Chapter Two, as well as enabling a simple means of power scaling by the addition of further pump diodes. The crystal was anti-reflection coated on both side faces by the crystal supplier to increase coupling of the pump radiation into the crystal. The crystal was held in a spring-loaded oxygen-free copper mount to allow expansion of the crystal due to thermal loading, whilst permitting a close contact. This mount was water-cooled to 15°C, which was enhanced by use of indium foil on the contact areas.

The pump radiation was focussed into the gain using an f=+80mm uncoated spherical lens. The lens was mounted on two translation stages to permit small adjustments to the vertical and horizontal positioning, with respect to the pump laser and crystal. The power after this lens was measured to be 14W.

The pump region within the crystal was a 250μm-thick layer, chosen to minimise undesirable thermal lensing effects and to ensure TEM_{00} laser output. This was measured using a CCD and imaging optics. A highly reflecting mirror of 75mm radius of curvature was placed behind the crystal to reflect some of the radiation not

absorbed on the first pass back into the gain medium. The radiation absorbed by the crystal was estimated to be 10W.

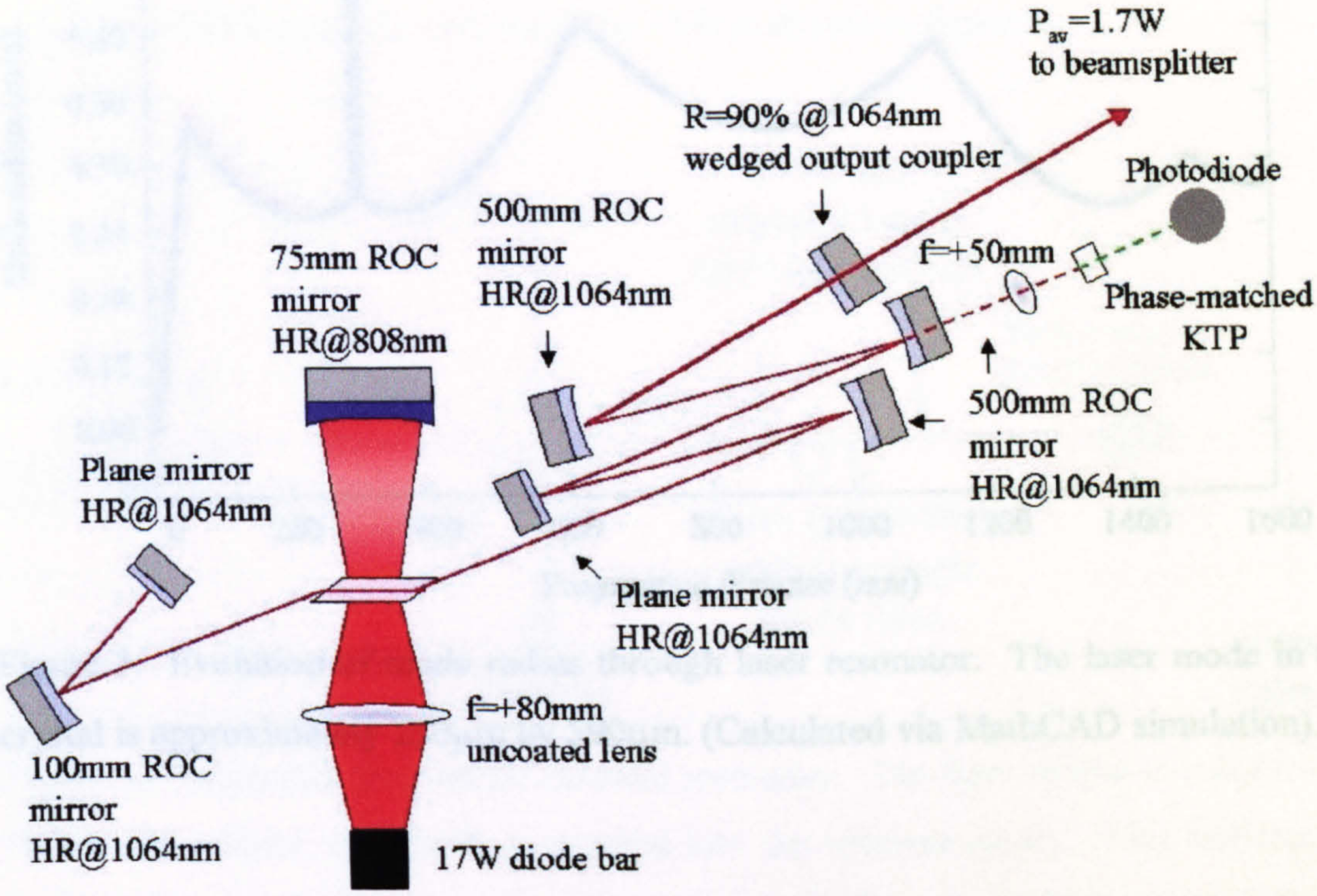

Figure 2. Schematic representation of laser resonator. A single 17W diode laser bar side-pumped the Nd^{3+}:YVO_4 crystal. Using a 10% transmitting wedged output coupler, 1.7W of average power was generated at $\lambda = 1064\,\text{nm}$. A phase-matched KTP crystal is used to generate second harmonic radiation, which is a monitor for the external resonator length.

The resonator was designed to overlap the pump volume to the cavity mode. Astigmatic-compensation was achieved using the expression in § 2.4.1 to provide a circular output beam. In accordance with the definition of peak power in § 2.7, a long cavity length is desirable to increase the peak power. Therefore, the resonator constructed had a length of over 1.5m, corresponding to a repetition rate of 90.7MHz. The evolution of the mode through the cavity is shown in figure 3, calculated via a MathCAD simulation.

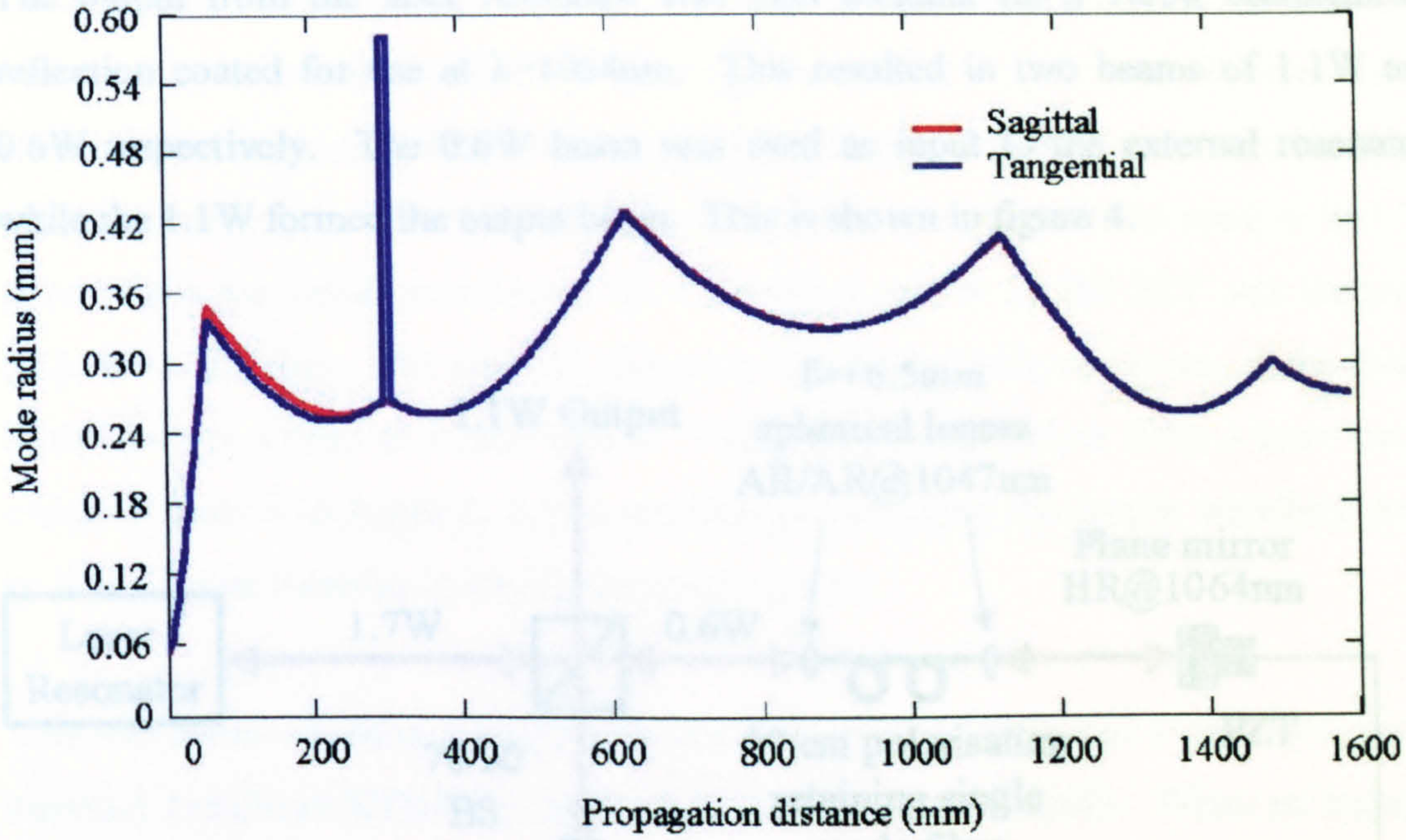

Figure 3. Evolution of mode radius through laser resonator. The laser mode in the crystal is approximately 250μm by 590μm. (Calculated via MathCAD simulation).

With the exception of the output coupler, the cavity mirrors were all wedged and highly reflection coated for the oscillating wavelength of λ=1064nm. A wedged output coupler of 10% transmission at the oscillating wavelength was used in this configuration. Mirrors without a wedge were found to introduce etalon effects that were detrimental to mode-locking performance.

With 14W pump power, continuous wave output of 1.7W was measured with a threshold of 600mW of pump power. Each of the 500mm radius of curvature mirrors (supplied by Casix) contributed to a loss of approximately 0.2% and therefore reduced the overall efficiency of the laser.

Using a CCD array, the near and far-field of the laser beam was determined to be almost diffraction limited, with M^2~1.1. With the cavity as specified, TEM_{00} operation was achieved at a repetition frequency of 90.7MHz. The output from the laser oscillator was observed to be horizontally polarised, due to the birefringent nature of Nd^{3+}:YVO_4 and the inclusion of a Brewster-cut gain medium.

The output from the laser resonator was then incident on a 70/30 beamsplitter, reflection coated for use at λ=1064nm. This resulted in two beams of 1.1W and 0.6W respectively. The 0.6W beam was used as input to the external resonator, while the 1.1W formed the output beam. This is shown in figure 4.

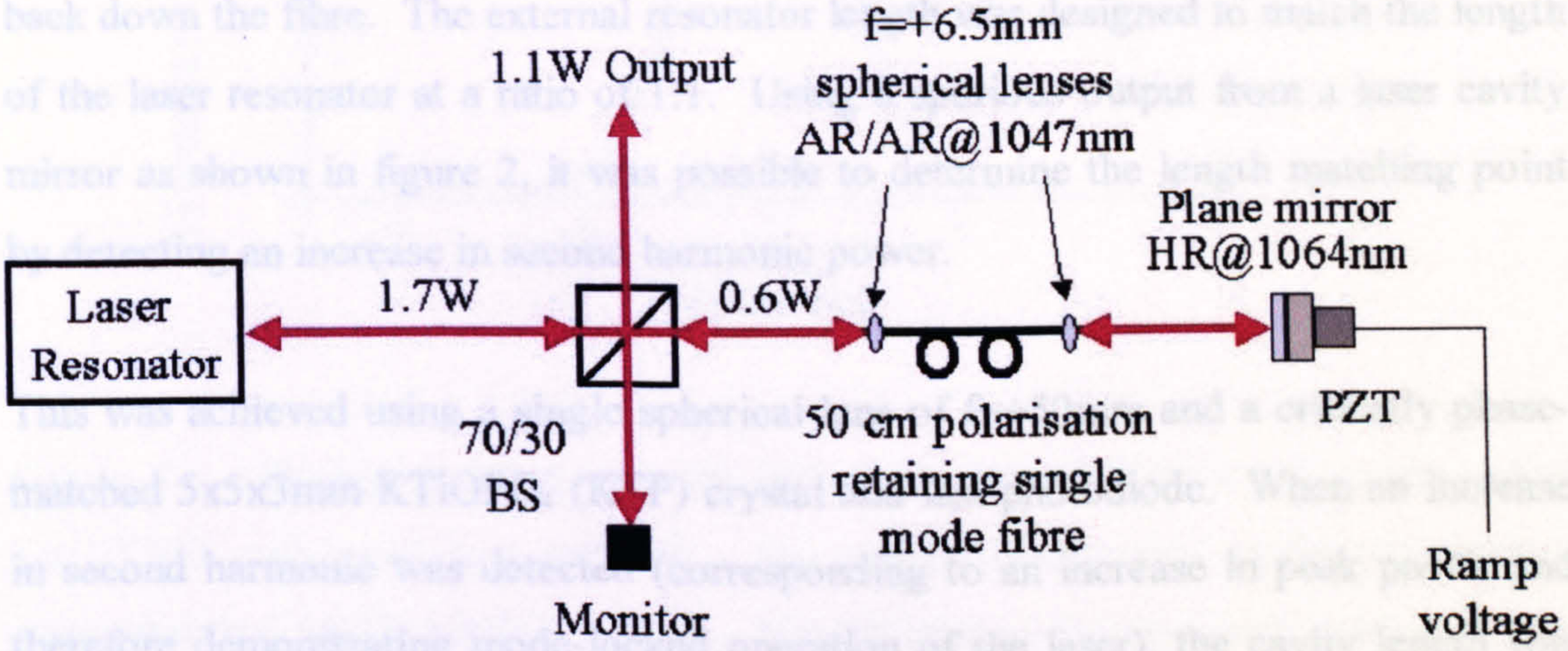

Figure 4. Schematic diagram of external resonator. The laser output is subject to a 70/30 beamsplitter, and 0.6W is coupled into the external cavity. This radiation is launched into a polarisation-preserving single-mode fibre at an efficiency of 60% and the output is focussed onto a plane highly reflecting mirror at normal incidence. This mirror is attached to a piezoelectric transducer (PZT) with an applied ramp voltage which permits fine-tuning of the cavity length.

The 0.6W beam was focussed into a standard 50-cm long single-mode polarisation-preserving fibre. This focussing was achieved using a f=+6.5 mm spherical lens (Thorlabs C170TM-B), anti-reflection coated for use at $\lambda = 1047$nm. The fibre ends were wedged to prevent feedback to the laser resonator. The output from the fibre was collimated using an identical f=+6.5 mm spherical lens. Both lenses were located in 3-dimensional translation stages to optimise the launch efficiency and collimation of the fibre output.

The output power measured after the fibre was 365mW, corresponding to a throughput efficiency of 60%. The collimated output radiation was then incident on

a plane mirror that was highly-reflecting at λ=1064nm placed at normal incidence which retro-reflected the radiation along the fibre. This was located on a piezoelectric transducer (PZT) with an applied voltage, which allowed fine-tuning of the resonator length. The monitor adjacent to the beamsplitter was used to find the point where the radiation reflected from the plane mirror on the PZT was launched back down the fibre. The external resonator length was designed to match the length of the laser resonator at a ratio of 1:1. Using a spurious output from a laser cavity mirror as shown in figure 2, it was possible to determine the length matching point by detecting an increase in second harmonic power.

This was achieved using a single spherical lens of f=+50mm and a critically phase-matched 5x5x3mm $KTiOPO_4$ (KTP) crystal and fast photodiode. When an increase in second harmonic was detected (corresponding to an increase in peak power and therefore demonstrating mode-locked operation of the laser), the cavity length was locked via stabilising electronics.

3.5. Results

Self-starting APM was observed with the cavity length stabilised at a ratio of 1:1 with the laser resonator. Pulse durations of 2.7ps were routinely measured at an average power of 1.1W via second-harmonic autocorrelation using a 5mm long MgO_2:$LiNbO_3$ crystal, heated to 50°C for phase-matched operation. A typical pulse duration measurement is shown in figure 5. Pulses of this duration correspond to a measured peak power of 4.5kW at a repetition rate of 90.7MHz. The measured pulse duration is comparable to that demonstrated in Nd^{3+}:YVO_4 by Krainer *et al.* [10], but the repetition rate of their semiconductor saturable absorber mirror mode-locked laser is 77GHz, which is unsuitable for nonlinear optical frequency conversion experiments. In addition, the output power of their high-repetition rate laser was measured as 65mW, which is considerably less than the average power of the APM laser.

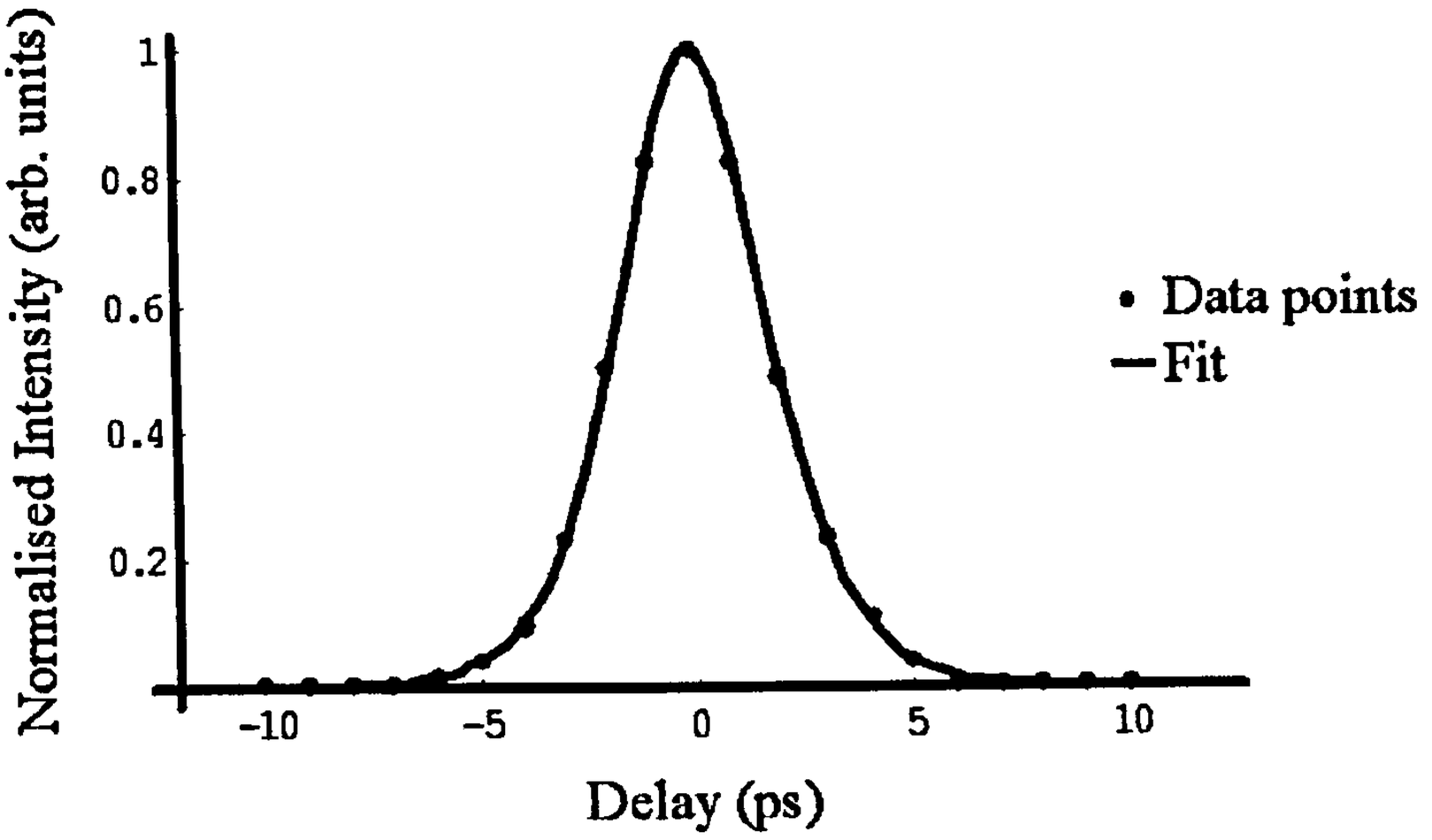

Figure 5. Background-free second harmonic autocorrelation of mode-locked Nd^{3+}:YVO_4 pulse and best $sech^2$ fit. The autocorrelation was performed using a phase-matched MgO_2:$LiNbO_3$ crystal. The FWHM of the measured pulse is 4.1ps, corresponding to a pulse width of 2.7ps.

At comparable output powers, Agnesi *et al.* demonstrated longer pulses of 7.9ps duration using the same gain medium but employing a nonlinear mirror mode-locking method [11].

A typical pulse train is shown in figure 6. The ripples observed at the base of the pulse train are a feature of the photodiode detector. The pulses are separated by approximately 2ns, which corresponds to the 90.7MHz repetition rate of the laser.

The pulse spectrum was also measured, as shown in figure 7. The spectral bandwidth was measured using a home-made scanning Fabry-Perot interformeter, and yielded a spectral width of 162GHz, resulting in a time-bandwidth product $\Delta\tau\Delta\upsilon = 0.44$.

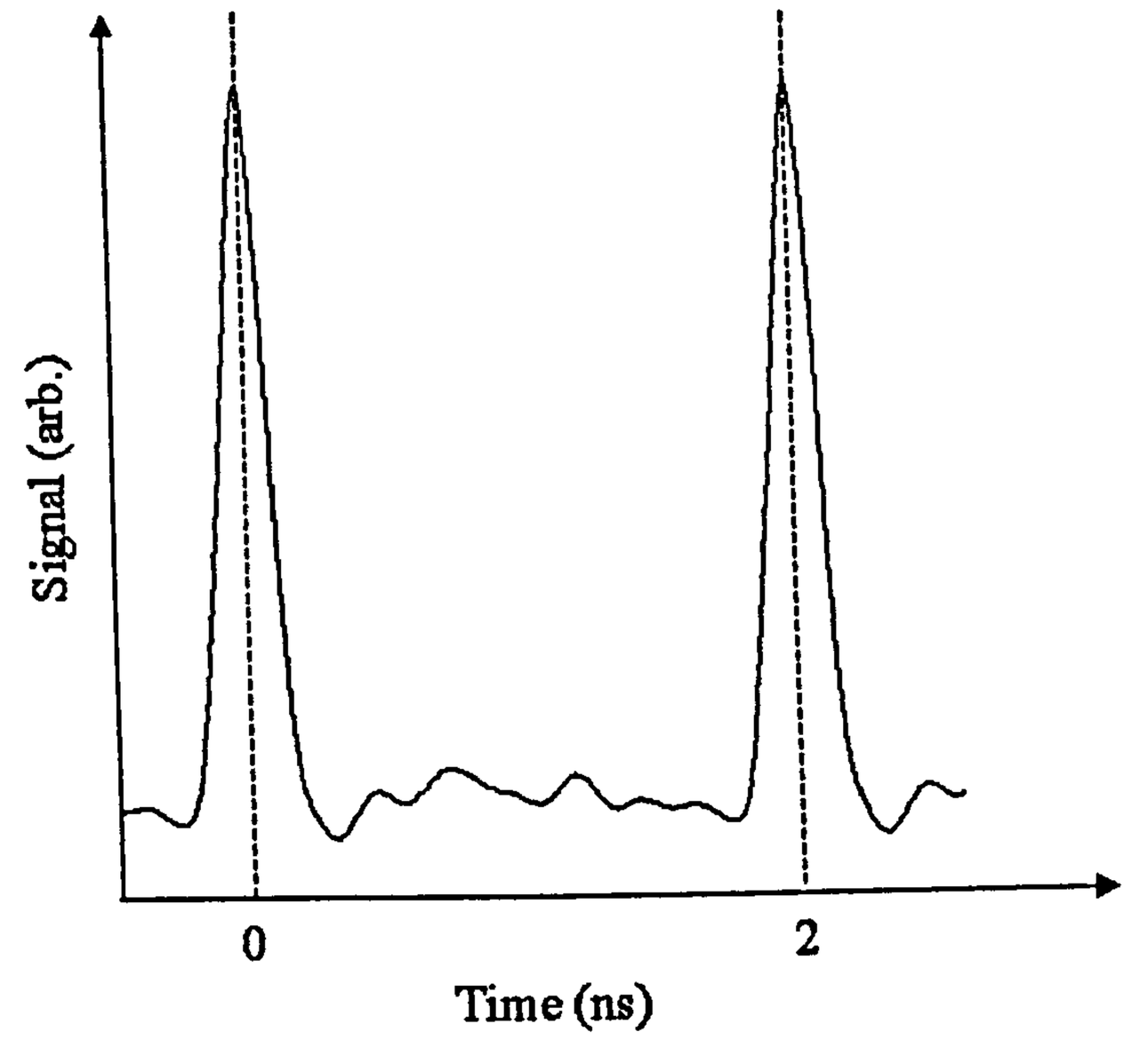

Figure 6. Pulse train from APM laser. The pulse separation is approximately 2ns. The ripples at the base of the pulse train arise from the detector and are not a feature of the pulse.

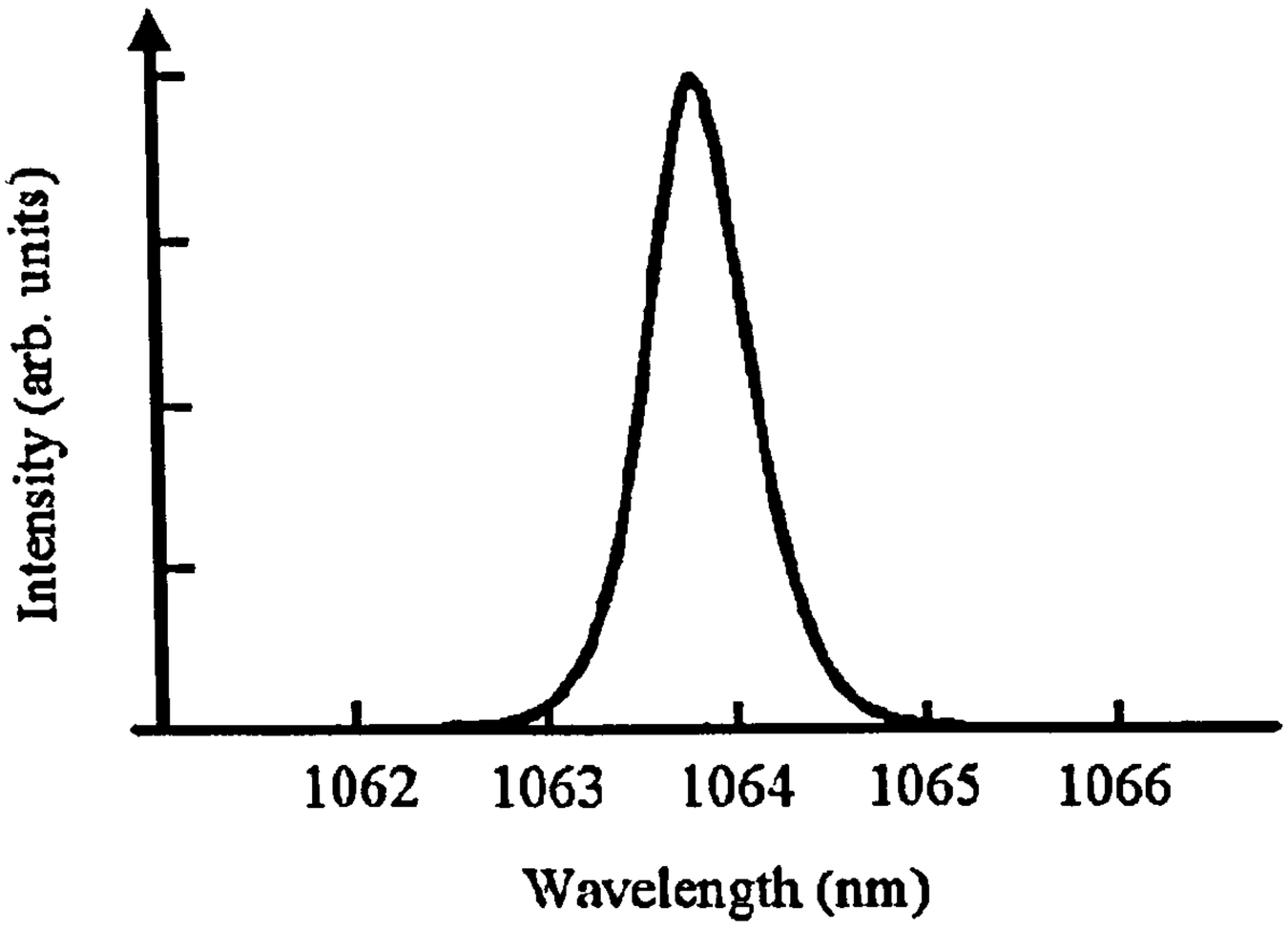

Figure 7. Spectrum of the output from APM laser. The FWHM, measured using a Fabry-Perot interferometer (2GHz resolution), is 0.57nm (162 ± 23 GHz). It is noted that the peak of the spectrum is not at the emitting wavelength of the laser. This is due to a calibration error of the spectrometer and is not a feature of the laser.

Based on the theoretical model and experiments of Braun and Kärtner [11, 12] a factor of three reduction in the pulse duration is possible if the crystal were placed at the end of the resonator, which would take the measured pulse duration to 1ps. This corresponds to the shortest accessible pulse duration, given the 0.96nm gain bandwidth of $Nd^{3+}:YVO_4$.

An increase in the generated output power is observed by using a coated lens to focus the pump radiation into the $Nd^{3+}:YVO_4$ crystal, as well as replacing the 500mm radius of curvature cavity mirrors with those of higher reflectivity. By doing so in a comparative system, output powers of greater than 4W were routinely achieved. Further improvements of the focussing optics for the optical fibre would also increase launch efficiency and reduce the mode-locking threshold.

No Q-switching or relaxation oscillations were observed when the cavity length was electronically locked. This is attributed to the properties of the $Nd^{3+}:YVO_4$ crystal which are favourable for mode-locked operation.

The external resonator length had to be stabilised to within a half-wavelength of the laser resonator in order for stable mode-locking to occur, due to the interferometric nature of the APM mechanism. When the cavity length was locked, mode-locking was observed to be stable over several hours of operation. The electronically locked laser was also extremely sensitive to vibration. Such disturbance resulted in the cavity length changing and therefore the laser ceased to mode-lock. For this reason, the system was not deemed sufficiently stable as a platform for nonlinear frequency conversion.

Additionally, investigation into using alternative lengths of optical fibre in the external resonator and thereby inducing a different magnitude of nonlinearity would affect the pulse duration.

3.6. Conclusions

In conclusion, a self-starting additive pulse mode-locked diode-pumped Nd^{3+}:YVO_4 laser has been demonstrated. A linearly polarised average power of 1.1W with a repetition frequency of 90.7 MHz, delivered in pulses of 2.7ps duration was measured. This leads to a generated peak power of 4.5kW. Possible areas of improvement to the system were recognised and discussed.

Although 4.5kW of peak power is certainly adequate for nonlinear optical frequency conversion experiments, the sensitivity to vibration did not lead to a robust platform. Consequently, an alternative mode-locking technique was investigated in the form of using a saturable Bragg reflector mode-locking device. This is discussed in the following chapter.

3.7. References

[1] L.F. Mollenauer and R.H. Stolen, "The soliton laser", Optics Letters, Vol. 9, 1984 (pp13-15).

[2] K.J. Blow and D. Wood, "Mode-locked lasers with nonlinear external cavities", Journal of the Optical Society of America B., Vol. 5, No. 3, 1988 (pp629-632).

[3] J. Goodberlet, J. Wang and J.G. Fujimoto *et al.*, "Femtosecond passively mode-locked Ti:Al_2O_3 laser with a nonlinear external cavity", Optics Letters, Vol. 14, No. 20, 1989 (pp1125-1127).

[4] P.N. Kean, X. Zhu and D.W. Crust *et al.*, "Enhanced mode-locking of color-centre lasers", Optics Letters, Vol. 14, No. 1, 1989 (pp39-41).

[5] L.E. Nelson, E.P. Ippen and H.A. Haus, "Broadly tunable sub-500fs pulses from an additive-pulse mode-locked thulium doped fiber ring laser", Applied Physics Letters, Vol. 67, No. 1, 1995 (pp19-21).

[6] J. Goodberlet, J.M. Jacobson and J.G. Fujimoto *et al.*, "Self-starting additive-pulse mode-locked diode-pumped Nd:YAG laser", Optics Letters, Vol. 15, No. 9, 1990 (pp504-506).

[7] G.P.A. Malcolm, P.F. Curley and A.I. Ferguson *et al.*, "Additive-pulse mode-locking of a diode-pumped Nd:YLF laser", Optics Letters, Vol. 15, No. 22, 1990 (pp1303-1305).

[8] E.P. Ippen, H.A. Haus and L.Y. Liue, "Additive pulse mode-locking", Journal of the Optical Society of America B, Vol. 6, No. 9, 1989 (pp1736-1745).

[9] T.W. Hänsch and B. Couillaud, "Laser frequency stabilization by polarization spectroscopy of a reflecting reference cavity", Optics Communications, Vol. 35, No. 3, 1980 (pp441-444).

[10] L. Krainer, R. Paschotta and M. Moser *et al.*, "77 GHz soliton modelocked Nd : YVO_4 laser", Electronics Letters, Vol. 36, No. 22, 2000 (pp1846-1848).

[11] A. Agnesi, C. Pennacchio and G.C. Reali et al., "High-power diode-pumped picosecond Nd^{3+}:YVO_4 laser", Optics Letters, Vol. 22, No. 21, 1997 (pp1645-1647).

[12] B. Braun, K.J. Weingarten and F.X. Kärtner *et al.*, "Continuous-wave mode-locked solid-state lasers with enhanced spatial hole burning. Part I: Experiments", Applied Physics B, Vol. 61, 1995 (pp429-437).

[13] F.X. Kärtner, B. Braun and U. Keller, "Continuous-wave mode-locked solid-state lasers with enhanced spatial hole burning. Part II: Theory", Applied Physics B, Vol. 61, 1995 (pp569-579).

Chapter Four

Saturable Bragg Reflector Mode-locked Diode-pumped $Nd^{3+}:YVO_4$ laser

4.1. Introduction

Although a coherent source of ultrashort pulses was demonstrated in the previous chapter, the mode-locked output was extremely sensitive to mechanical and vibrational perturbation. This is clearly undesirable for nonlinear optical frequency conversion experiments, since the conversion efficiency is dependent on the peak intensity of the pump source.

This chapter adopts a fast saturable absorber in the form of a saturable Bragg reflector (SBR) as the passive mode-locking element. These engineered solid-state passive devices are flexible, reliable, have fast recovery times, and can cope with very high intracavity electric fields.

This chapter is concerned with the mode-locking of lasers using semiconductor saturable absorbing mirrors, with emphasis on the saturable Bragg reflector. Experimental results of a SBR mode-locked diode-pumped $Nd^{3+}:YVO_4$ laser are presented and compared to those obtained in Chapter Three.

4.2. Saturable absorbers

Saturable absorbers fall into two categories: fast and slow, depending on the gain medium used. Slow saturable absorbers are employed for high gain materials, such as dye lasers, where the pulse shaping is a result of both the saturable absorber and the gain dynamics.

However, for low-gain solid-state materials, the pulse shaping results solely from the effect of the saturable absorber. Therefore, a device with a fast recovery time is desired, namely a fast saturable absorber. A full description of fast saturable absorption is provided in reference 1.

A fast saturable absorber performs modelocking by initially capitalising on intracavity noise. Where a broad noise pulse is incident onto a saturable absorber, the leading edge and the trailing edge of the pulse are absorbed, with the mid-section transmitted. Therefore the saturable absorber effectively behaves as an intensity-dependent switch. Since both edges of the pulse must be absorbed, a fast recovery time is essential [2].

Specially engineered organic dyes were originally used as a fast saturable absorber [3], but recently semiconductor devices in the form of the semiconductor saturable absorbing mirror (SESAM) have been developed which outperform these dyes.

4.3. Saturable Bragg reflectors

Semiconductor materials have good characteristics for use as saturable absorbers. They have very high nonlinearities and, depending on design, the response time can vary from milliseconds to femtoseconds. They are also very low-maintenance structures compared to the traditional liquid saturable absorbers. These simple

devices eliminate the need for external resonators, resulting in a very stable mode-locking technique.

4.3.1. Historical review of semiconductor saturable absorbing mirror mode-locking

The first SESAM device was the anti-resonant Fabry-Perot saturable absorber (A-FPSA) [4] and has been used to generate ultrashort pulses as short as 60fs in Nd:glass [5], as well as demonstrating stable mode-locking in other materials as diverse as Yb:YAG [6], Cr:LiSAF [7] and Ti:sapphire [8].

The operation of SESAM mode-locked lasers is not confined to the A-FPSA. Further improvements in semiconductor growth led to the development of the saturable Bragg reflector, or SBR [9]. This single-mirror fast saturable absorber relies upon a quantum well as the modulation device. This eliminates problems associated with cavity resonance to deliver stable ultrashort laser pulses. This structure was first implemented in a continuous wave Cr^{2+}:LiSAF laser which achieved 90fs pulses [10]. The simplicity of this structure has enabled mode-locking of materials such as Cr^{4+}:YAG [11], Ti:sapphire [12] and erbium/ytterbium fibre lasers [13].

Both the A-FPSA and SBR are good fast saturable absorbers, but the disadvantage of the A-FPSA structure arises through manufacture. The A-FPSA device requires post-processing, which is a source of considerable non-saturable losses. No such processing of the SBR is required, therefore more efficient saturable absorption is performed by this structure.

4.3.2. Basic operation of saturable Bragg reflector

If the energy of the incident photon is greater than that of the energy bandgap of the material, an electron will be excited from the valence band to the conduction band, forming free carriers. However, if the excitation energy is just below the conduction band an electron-hole pair (exciton) will be formed. The production of excitons will lower the absorption of the material on a fast scale (<ps). However, due to the presence of high-energy phonons present in the lattice, the excitons will be short-lived. The optical phonons interact with the exciton, which has a low binding energy and will subsequently split into its electron and hole components. The electron will recover via a radiative or non-radiative process on a comparatively longer nanosecond scale, thus allowing the process to restart. This bi-temporal device response is shown in figure 1. In order to let the device recover, however, the round-trip time of the cavity must be sufficiently long (~ns). The fast component has been found to perform the saturable absorption in gain materials that can support femtosecond pulse durations whereas picosecond materials follow the slow response. By engineering the slow component, it is believed that the device may be optimised, leading to shorter pulses. This is currently under investigation [15].

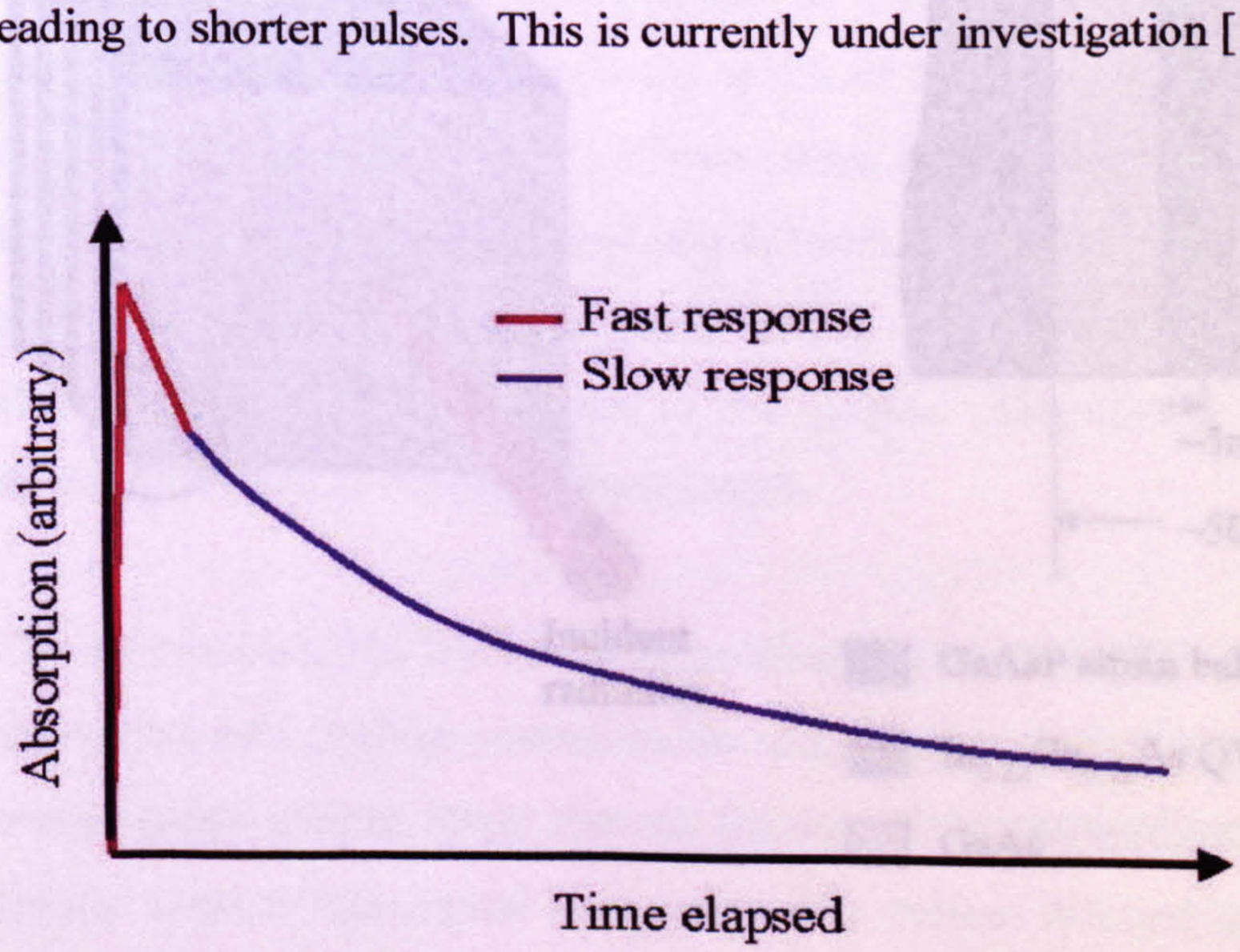

Figure 1. Response times of SBR structure (relative scale). The absorption occurs over a very short period, but the recovery of the device is slow in comparison.

4.3.3. Design of saturable Bragg reflector

The SBR structure consists of a Bragg mirror to provide a high reflectivity of the incident radiation and in the outermost layer, a quantum well structure is grown which performs the saturable absorption as described previously.

For these experiments, the SBR device was grown for optimal performance at $\lambda = 1047\text{nm}$ at normal incidence, since the wafers were originally grown for another application. Tight focusing of the incident radiation is imperative to increase the field strength at the device sufficiently to invoke nonlinear interaction.

The Bragg mirror consists of 30-period pairs of alternating GaAs/$Al_{0.8}Ga_{0.2}As$, chosen to provide high reflectance (>99%) over a broad (70nm) bandwidth. The saturable absorber consists of a single InGaAs quantum well, as shown in figure 2.

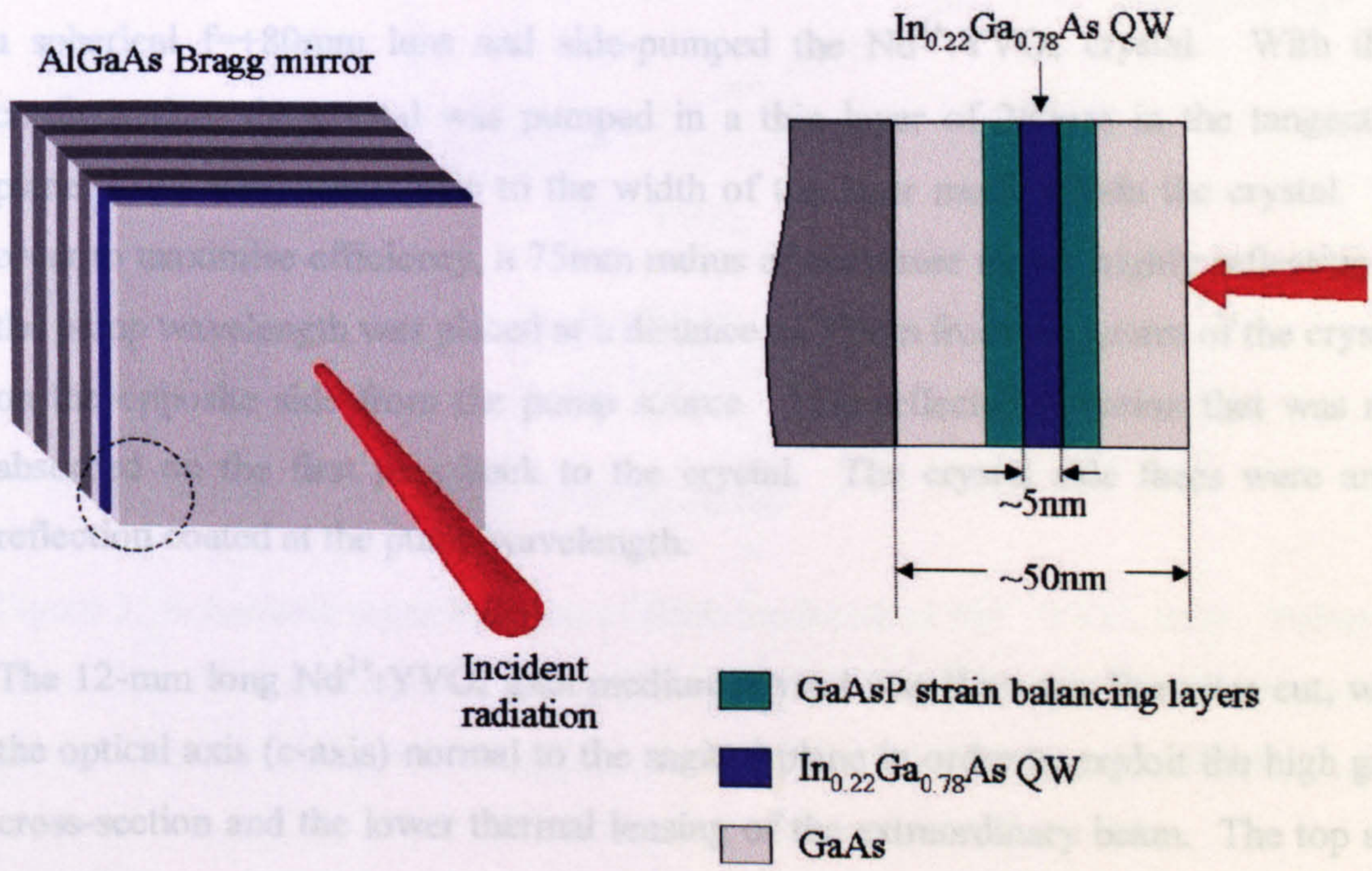

Figure 2. Schematic 3D representation of saturable Bragg reflector structure. A single-quantum well structure is shown.

A single quantum well is implemented to give rise to a larger modulation, thus increasing the overall saturable absorption of the device while keeping other losses minimal. The well-width and indium concentration were chosen specifically for incident radiation at λ=1047nm [16]. Further information on the design of these structures may be found in references 17 and 18.

4.4. Diode-pumped saturable Bragg reflector mode-locked Nd^{3+}:YVO_4 laser

Figure 3 shows a schematic diagram of the mode-locked Nd^{3+}:YVO_4 pump scheme and resonator. The pump geometry is similar to that adopted in Chapter Three, but using a coated lens to focus the pump radiation into the crystal. The pump source was a 17W fast-axis collimated diode-laser bar (OPC-A020-809-CS/L), temperature controlled for operation at λ=808nm. The output from the array was focussed using a spherical f=+80mm lens and side-pumped the Nd^{3+}:YVO_4 crystal. With this configuration, the crystal was pumped in a thin layer of 250μm in the tangential plane. This was comparable to the width of the laser mode within the crystal. In order to maximise efficiency, a 75mm radius of curvature mirror highly reflecting at the pump wavelength was placed at a distance of 75mm from the centre of the crystal on the opposite side from the pump source. This reflected radiation that was not absorbed on the first pass back to the crystal. The crystal side faces were anti-reflection coated at the pump wavelength.

The 12-mm long Nd^{3+}:YVO_4 gain medium crystal was Brewster-Brewster cut, with the optical axis (c-axis) normal to the sagittal plane in order to exploit the high gain cross-section and the lower thermal lensing of the extraordinary beam. The top and bottom faces of the crystal were covered in indium foil and held in a spring-loaded water-cooled oxygen-free copper mount. Cooling in the tangential plane generated a lower temperature gradient across the crystal. The Brewster end surfaces of the crystal were finished to laser quality. In order to suppress parasitic reflections,

ultraviolet cured optical glue (Norland NOA61) was placed on the crystal surfaces as shown in figure 4 [18]. This ensured a single circular beam output and reduced overall loss of the system.

In order to allow recovery of the SBR and access high peak powers, a resonator longer than 0.5m was chosen. To eliminate astigmatic effects, the resonator was designed with angular tolerance in mind, as described in Chapter 2.4.1. This corresponded to a 4 mirror (inclusive of SBR mirror) cavity. This permitted focussing of the laser mode into the gain medium to match the mode volume of the pump radiation.

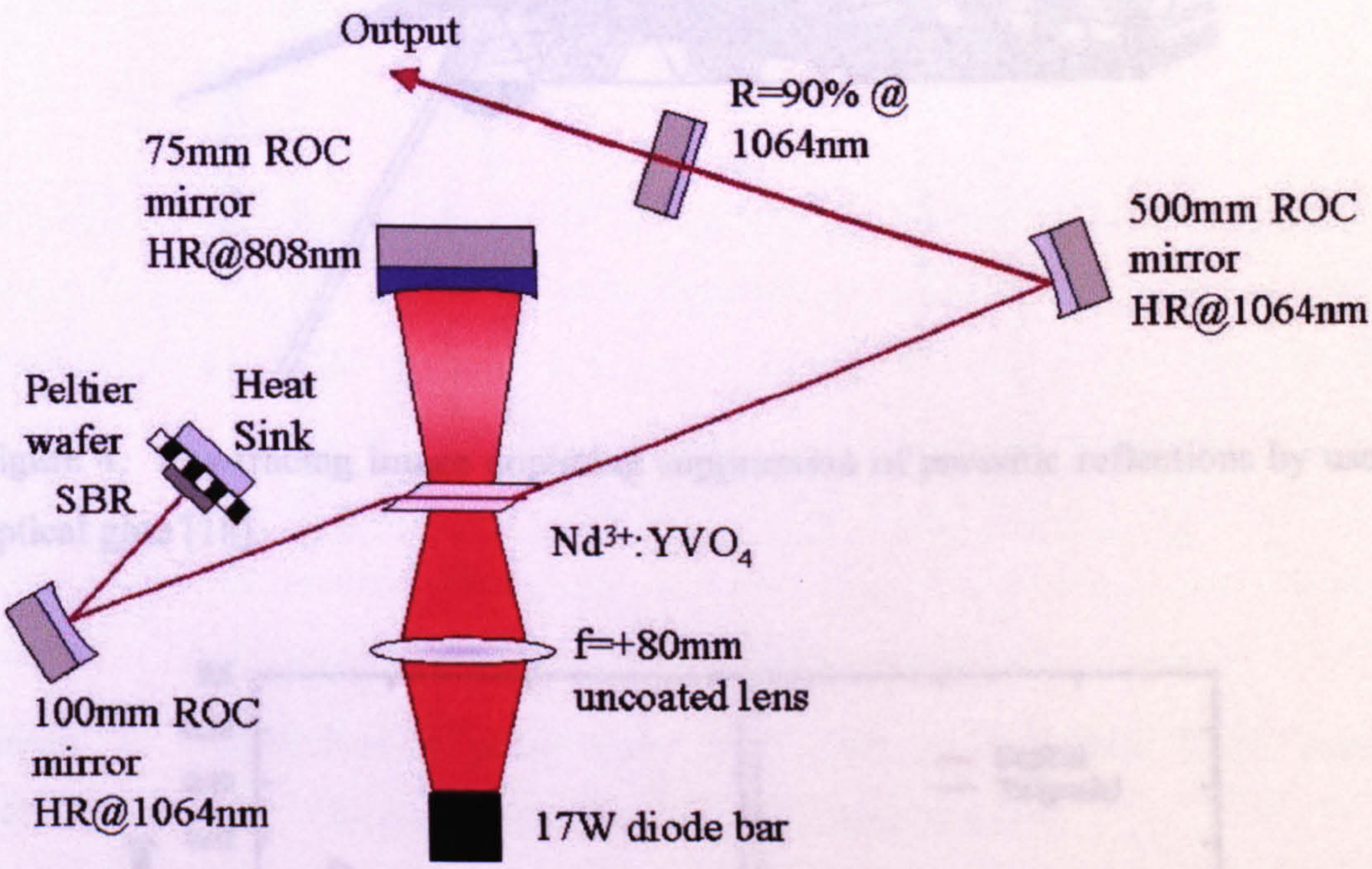

Figure 3. Schematic representation of SBR-modelocked $Nd^{3+}:YVO_4$ laser. Pulses of $\Delta\tau = 33$ps were measured at a repetition rate of 235MHz with 4.4W of average power. The oscillating wavelength is $\lambda = 1064$nm, and the output is a TEM_{00} beam.

To minimise feedback, the rear surface of the SBR was scratched and attached to a Peltier device to permit heating to tune the absorption of the quantum well to the oscillating wavelength of the laser. All cavity mirrors wedged with a minimum of 1°

and were specifically highly reflecting (>99.7%) at the oscillating wavelength of $\lambda = 1064\,\text{nm}$, with the exception of the output coupler. The output coupler was a plane mirror of 90% reflectivity at the oscillating wavelength and a 10° wedge on the rear surface to eradicate etalon effects. The evolution of the mode diameter is described by figure 5. The mode radius on the SBR was calculated to be around 50μm. This tight focussing was required to increase the intensity of the laser to decrease the mode-locking threshold. However, focussing too tightly was found to damage the SBR structure, with an estimated damage threshold for the structure discussed here on the order of $I = 3\text{x}10^6\ \text{Wcm}^{-2}$.

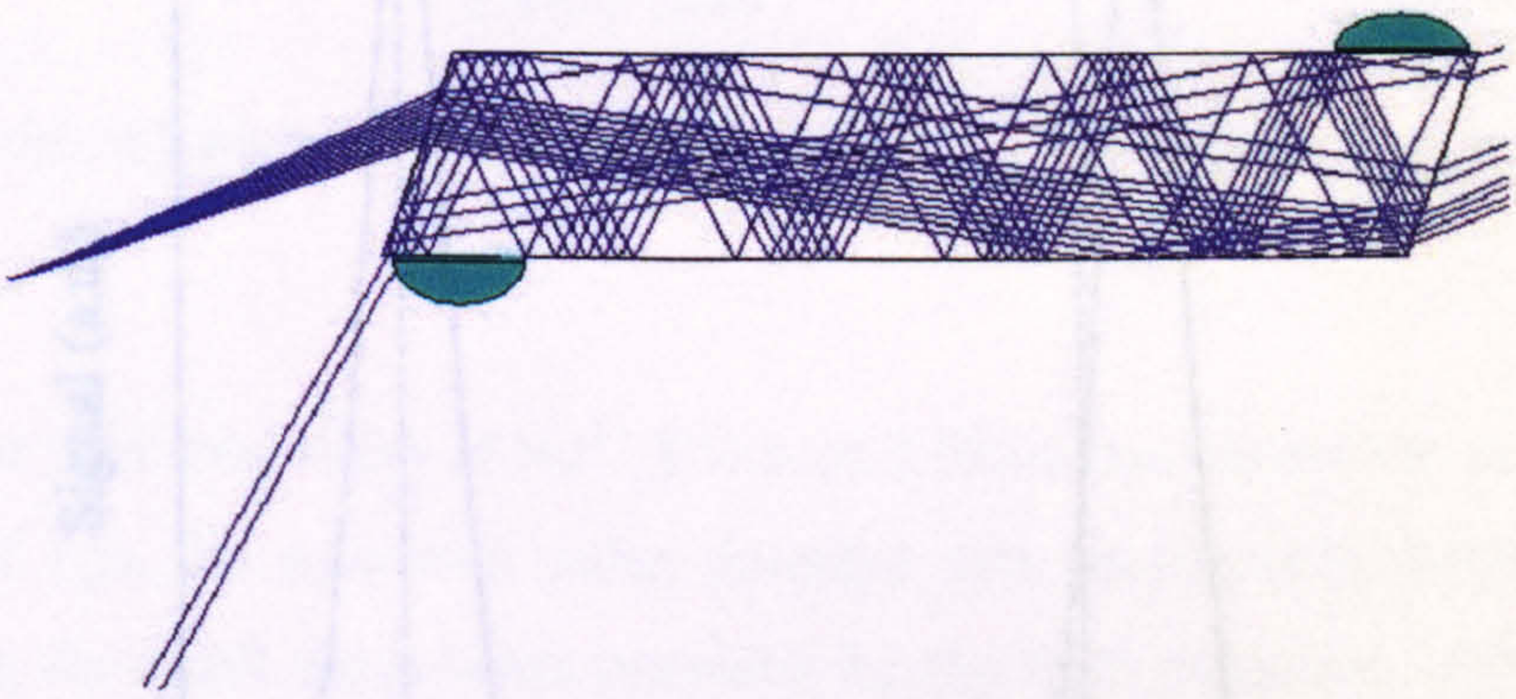

Figure 4. Ray-tracing image depicting suppression of parasitic reflections by use of optical glue [18].

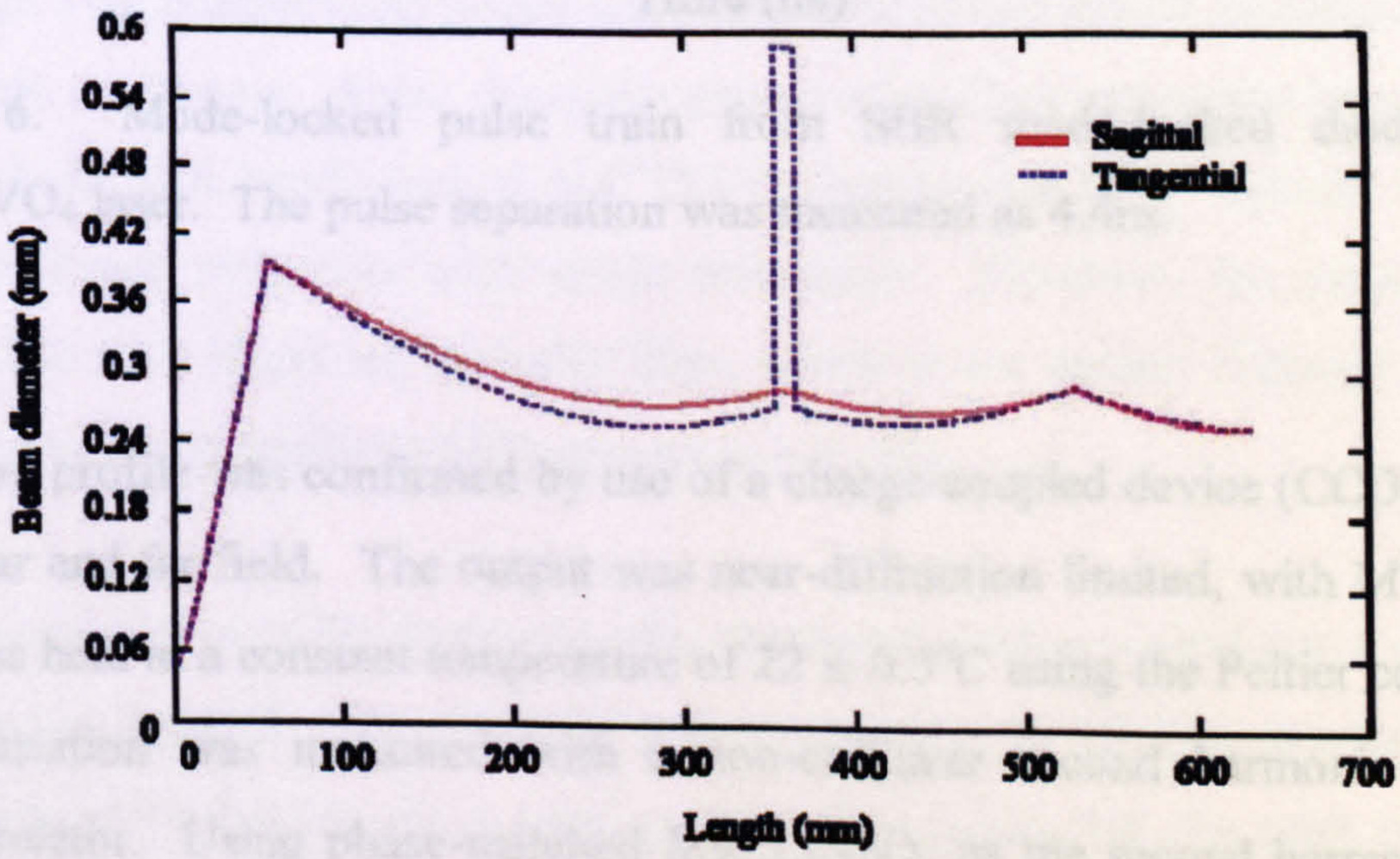

Figure 5. Evolution of mode diameter on propagation through resonator calculated via MathCAD v6.0 program.

4.5. Results

With 17W of pump power as described, an average power of 4.4W of radiation at $\lambda = 1064\,\text{nm}$ was measured in a TEM_{00} beam with a measured oscillation threshold of 600mW. The repetition rate of the laser was 235MHz, which is a pulse separation of 4.4ns, as shown in figure 6.

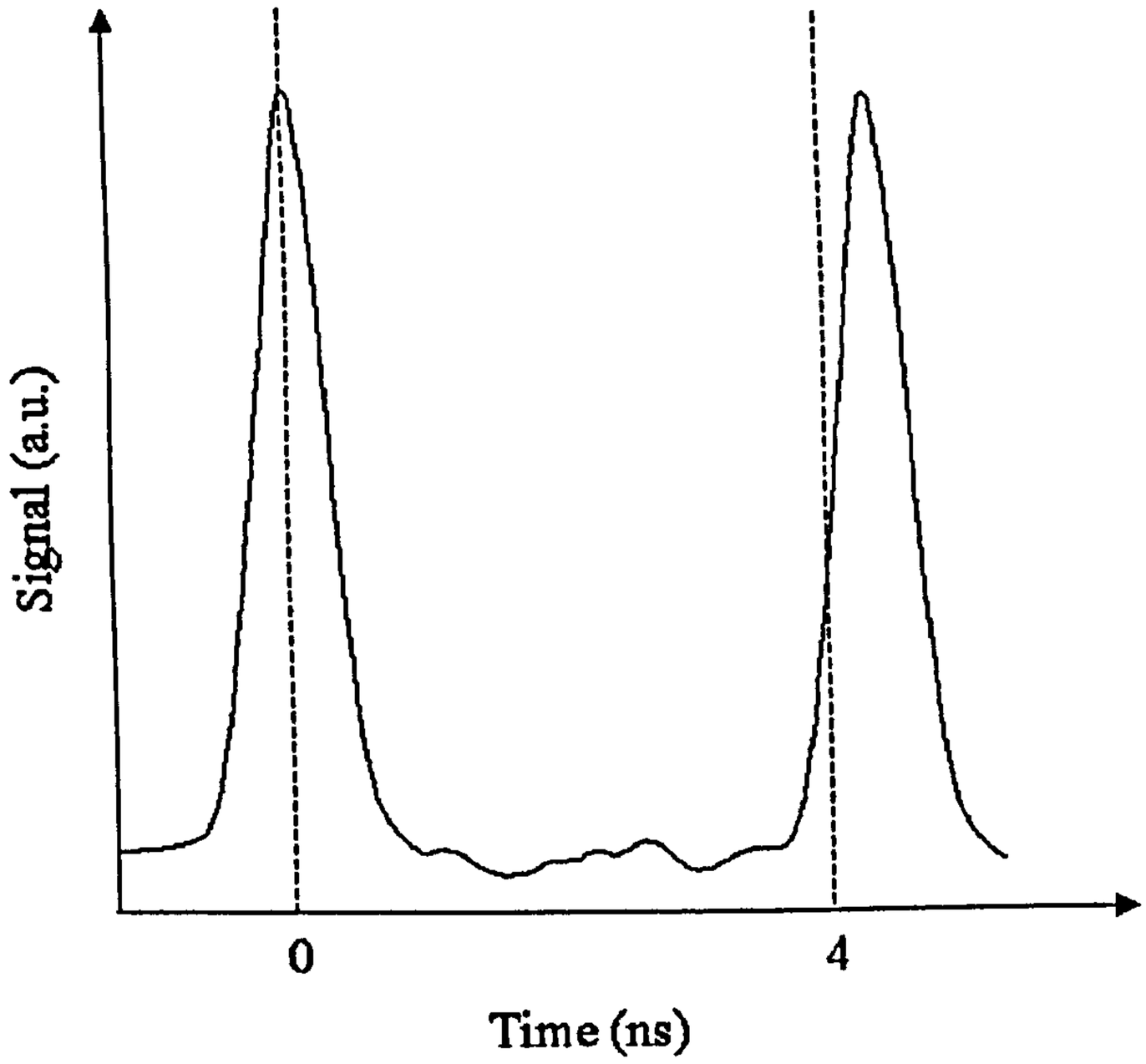

Figure 6. Mode-locked pulse train from SBR mode-locked diode pumped Nd^{3+}:YVO_4 laser. The pulse separation was measured as 4.4ns.

The beam profile was confirmed by use of a charge-coupled device (CCD) camera in both near and far field. The output was near-diffraction limited, with M^2~1.1. The SBR was held at a constant temperature of 22 ± 0.5°C using the Peltier control. The pulse duration was measured with a non-collinear second harmonic generation autocorrelator. Using phase-matched Mg_2:$LiNbO_3$ as the second harmonic crystal, the pulse duration was measured to be 33ps, under the assumption of a $sech^2$ pulse-shape. This corresponds to a peak power of 567W.

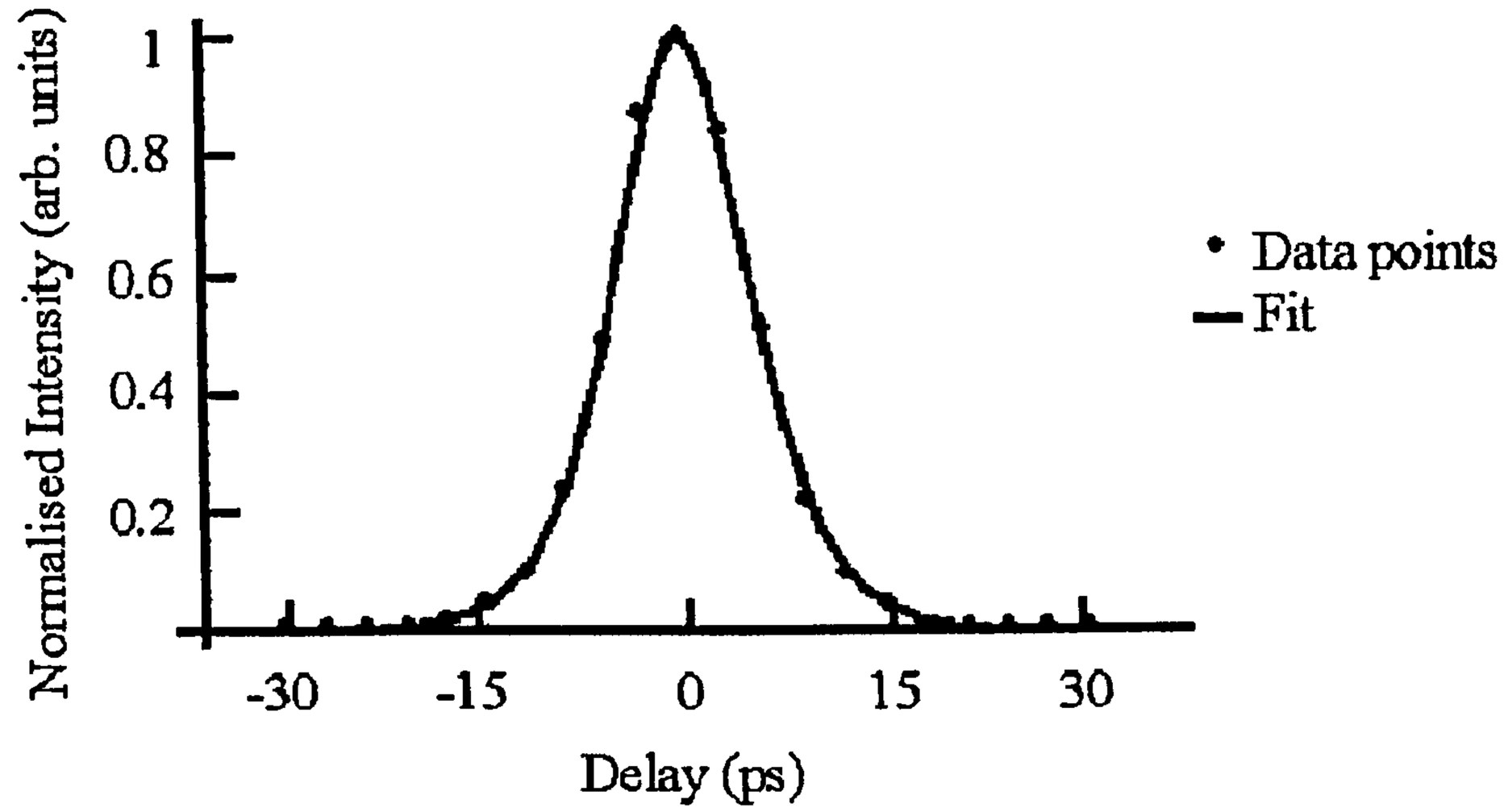

Figure 7. Pulse duration of SBR mode-locked Nd^{3+}:YVO_4 laser.

Although the gain bandwidth of Nd^{3+}:YVO_4 of 0.96nm corresponds to possible pulse durations of 1ps, the measured pulse duration was significantly longer. This is attributed to the small modulation provided by the SBR structure. Also, the SBR structure was originally grown for operation at $\lambda = 1047$nm and therefore is non-optimal. Although these longer pulses do not have the advantage of the higher peak powers, they are entirely suitable for pumping of nonlinear materials and have the advantage over femtosecond pulses with regards to cavity length tolerances in optical parametric oscillators. Pulse durations shorter than those presented here have been measured in SBR mode-locked Nd^{3+}:YVO_4 lasers, but these sources incorporate saturable Bragg reflectors with strain relaxation. However, the pulse durations observed in such lasers are typically 20ps, which is not greatly different from those obtained using conventional SBR structures [19, 20].

The spectral output of the laser was also measured, with a typical pulse spectrum as illustrated in figure 8. The spectrum was measured to be 16GHz, approximately 1.6 times bandwidth limited for a $sech^2$ pulse. It is noted that the peak of the pulse spectrum does not correspond to the wavelength of the emitted radiation, due to a calibration error in the spectrometer.

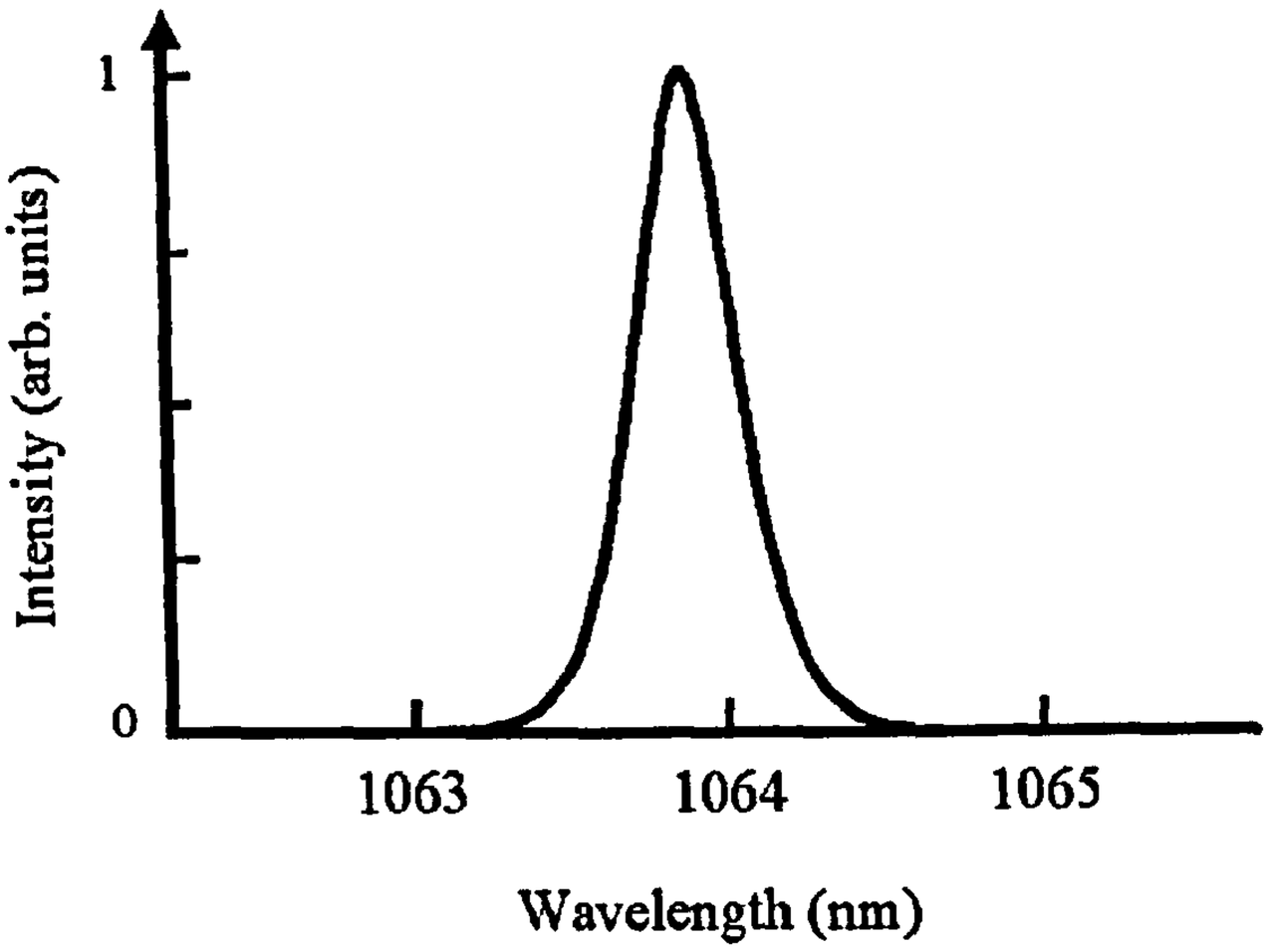

Figure 8. Pulse spectrum of SBR laser output. The peak of the spectrum is not at the wavelength of emission due to a calibration error. A spectral bandwidth of 16GHz was measured.

Stable mode-locking was observed for average powers greater than 2W. At lower powers, the output was subject to relaxation oscillations and Q-switched modelocking.

Laser	Average power (W)	Repetition frequency (MHz)	Pulse duration (ps)	Peak power (W)
APM laser	1.1	90.7	2.7	4500
SBR laser	4.4	235	33	567

Table 1. Comparison of APM and SBR laser characteristics.

The principal properties of the APM laser and SBR mode-locked laser are displayed in table 1. The characteristic high peak power delivered by the APM laser is ideal for frequency conversion experiments. However, as discussed in Chapter Three, the APM laser is extremely sensitive to vibration, unlike the SBR laser. Additionally,

the SBR mode-locked laser does not require complex cavity locking electronics. Since a reliable platform is required, the SBR mode-locked laser was chosen as the basis for further experiments.

4.6. Conclusions

In conclusion, a robust and reliable laser delivering 33ps pulses at a repetition rate of 235MHz with an average power of 4.4W was demonstrated. This corresponds to a peak power of 567W. Although this is significantly less than the peak power obtained from the additive pulse mode-locked laser described in Chapter Three, the SBR mode-locked laser was considerably more tolerant to vibration, resulting in a turnkey system. Therefore, it is the SBR mode-locked laser that forms the basis for the nonlinear experiments that follow.

4.7. References

[1] H.A. Haus, "Theory of mode-locking with a fast saturable absorber", Journal of Applied Physics, Vol. 46, No. 7, 1975 (pp3049-3058).

[2] A.E. Siegman, "Lasers", Oxford University Press, (ISBN 0935702113) 1986.

[3] V.P. Mikhailov, Q.Z Wang and M. Chu *et al.*, "Ultrahigh repetition rate picosecond pulses from a passively mode-locked neodymium glass-laser by solid-state saturable dye films", Applied Optics, Vol. 32, No. 21, 1993 (pp3944-3947).

[4] U. Keller, D.A.B. Miller and G.D. Boyd *et al.*, "Solid-state low-loss intracavity saturable absorber for Nd:YLF lasers – An antiresonant semiconductor Fabry-Perot saturable absorber", Optics Letters, Vol. 17, 1992 (pp505-507).

[5] J. Aus der Au, D. Kopf and F. Morier-Genoud *et al.*, "60-fs pulses from a diode-pumped Nd:glass laser", Optics Letters, Vol. 22, No. 5, 1997 (pp307-309).

[6] J. Aus der Au, S.F. Schaer and R. Paschotta *et al.*, "High-power diode-pumped passively mode-locked Yb:YAG lasers", Optics Letters, Vol. 24, No. 18, 1999 (pp1281-1283).

[7] D. Kopf, K.J. Weingarten and R. Brovelli *et al.*, "Diode-pumped 100fs passively mode-locked Cr:LiSAF laser with an anti-resonant Fabry-Perot saturable absorber", Optics Letters, Vol. 19, 1994 (pp2143-2145).

[8] L.R. Brovelli, I.D. Jung and D. Kopf *et al.*, "Self-starting soliton modelocked Ti-sapphire laser using a thin semiconductor saturable absorber", Electronics Letters, Vol. 31, 1995 (pp287-289).

[9] S. Tsuda, W.H. Knox and E.A. de Souza *et al.*, "Low-loss intracavity Al/AlGaAs saturable Bragg reflector for femtosecond mode locking in solid state lasers", Optics Letters, Vol. 20, 1995 (pp1406-1408).

[10] S. Tsuda, W.H. Knox and S.T. Cundiff, "High efficiency diode pumping of a saturable Bragg reflector-mode-locked Cr:LiSAF femtosecond laser", Applied Physics Letters, Vol. 69, 1996 (pp1538-1540).

[11] B.C. Collings, J.B. Stark and S. Tsuda *et al.*, "Saturable Bragg reflector self-starting passive mode-locking of a Cr^{4+}:YAG laser pumped with a diode-pumped Nd:YVO_4 laser", Optics Letters, Vol. 21, 1996 (pp1171-1173).

[12] T.A. Liu, K.F. Huang and C.L. Pan *et al.*, "High average power mode locked Ti:sapphire laser with intracavity continuous wave amplifier and strained saturable Bragg reflector", Japanese Journal of Applied Physics. Vol. 2, No. 38 (10A), 1999 (L1109-L1111).

[13] B.C. Collings, K. Bergman and S.T. Cundiff *et al.*, "Short cavity erbium/ytterbium fiber lasers mode-locked with a saturable Bragg reflector", IEEE Journal of Selected Topics in Quantum Electronics, Vol. 3, No. 4, 1997 (pp1065-1075).

[14] U. Keller, D.A.B. Miller, and G.D. Boyd *et al.*, "Solid-state low-loss intracavity saturable absorber for Nd:YLF lasers – an Antiresonant semiconductor Fabry-Perot saturable absorber", Optics Letters, Vol. 17, No. 7, 1992 (pp.505-507).

[15] S. Tsuda, W.H. Knox, and S.T. Cundiff *et al.*, "Mode-locking ultrafast solid-state lasers with saturable Bragg reflectors", IEEE Journal of Selected Topics in Quantum Electronics, Vol. 2, No. 3, 1996 (pp454-464).

[16] M.D. Dawson, Institute of Photonics, University of Strathclyde (private communication).

[17] P.K. Bhattacharya, U. Das and F.Y. Juang *et al.*, "Material properties and optical guiding in InGaAs-GaAs strained layer superlattices – A review", Solid-State Electronics, Vol. 29, No. 2, 1986, (pp261-267).

[18] E. Bente, Institute of Photonics, University of Strathclyde (private communication).

[19] Y.F. Chen, S.W. Tsai and Y.P. Lan *et al.*, "Diode-end-pumped passively mode-locked high-power Nd:YVO_4 laser with a relaxed saturable Bragg reflector", Optics Letters, Vol. 26, No. 4, 2001 (pp199-201).

[20] T. Graf, A.I. Ferguson and E. Bente *et al.*, "Multi-Watt Nd:YVO_4 laser, mode locked by a semiconductor saturable absorber mirror and side-pumped by a diode-laser bar", Optics Communications, Vol. 159, No. 1-3, 1999 (pp84-87).

Chapter Five

Nonlinear Optical Frequency Conversion

5.1. Introduction

The advent of the laser in the 1960's opened up areas of research which were previously inaccessible with incoherent sources of radiation. One such field is that of nonlinear optics. Since the first experiment by P.A. Franken *et al.* in 1961 [1], this branch of optics has given rise to unique sources for a variety of applications. Using second and third order properties which are exploited by using the large electric fields generated by a laser, effects such as the Kerr effect, Raman scattering and nonlinear optical frequency conversion have become standard. The latter of these effects is of particular consequence in the development of laser sources that operate at unique wavelengths.

Currently, the majority of laser gain materials emit in the infrared region of the electromagnetic spectrum. However, sources that operate in other ranges are sought after for applications such as data storage [2], micromachining [3] and remote sensing [4]. To realise such sources, a common approach is to convert the frequency of existing lasers using nonlinear optical materials via parametric interactions. By doing so, coherent sources spanning from deep-UV to far-infrared have been created [5, 6].

This chapter presents a review of nonlinear optics and the basic theory of important effects. A brief discussion of materials and properties is provided, followed by a synopsis of design considerations for efficient optical frequency conversion.

5.2. Fundamental aspects of nonlinear optics

A small electric field applied to a material induces a polarisation of the electrons with respect to the nuclei. This may be expressed as

$$\mathbf{P} = \varepsilon\chi^{(1)}\mathbf{E}, \tag{5.1}$$

where ε is the permittivity of the medium, $\chi^{(1)}$ is the linear polarisation susceptibility of the medium and $\mathbf{P}$ and $\mathbf{E}$ are the polarisation and electric field vectors, respectively. However, when a large electric field is applied to a material, the material no longer responds linearly. This means that the second and third order effects are no longer negligible and therefore (5.1) above must be written in terms of a power series to account for this effect. This leads to the expression

$$\mathbf{P} = \varepsilon\left(\chi^{(1)} + \chi^{(2)}\mathbf{E} + \chi^{(3)}\mathbf{E}^2 + \ldots\right)\mathbf{E}, \tag{5.2}$$

where $\chi^{(2)}$ and $\chi^{(3)}$ are the second- and third-order nonlinear susceptibilities of the medium. The first-order term, $\chi^{(1)}$, describes the normal linear optical response of a material and accounts for properties such as the refractive index, dispersion and absorption. The second-order nonlinear susceptibility accounts for processes such as second harmonic generation, sum- and difference-frequency mixing and the Pockels effect. These processes are described in table 1.

Frequency of incident fields	Frequency of resulting field	Process
ω_1	$\omega_2 = 2\omega_1$	Second harmonic generation
ω_1, ω_2	$\omega_3 = \omega_1 + \omega_2$	Sum-frequency generation
ω_1, ω_2	$\omega_3 = \omega_1 - \omega_2$	Difference-frequency generation
$\omega_1, 0$	$\omega = \omega_1$	Pockels effect

Table 1. Second-order nonlinear processes.

It is noted, however, that in materials lacking a centre of inversion that $\chi^{(2)}$ is zero and therefore only asymmetric materials are suitable for the above processes. The third-order nonlinear susceptibility gives rise to the Kerr effect, three-frequency mixing and the Raman effect.

By using Maxwell's equations, it is possible to analyse the generation of these new frequencies. In an insulating, non-magnetic medium, Maxwell's equation for an electromagnetic wave can be expressed as

$$\frac{\partial^2 \mathbf{E}}{\partial t^2} = \mu\varepsilon \frac{\partial^2 \mathbf{E}}{\partial t^2} + \mu \frac{\partial^2}{\partial t^2}\left(\chi^{(2)}\mathbf{E}^2\right), \tag{5.3}$$

where μ is the magnetic permeability of the material. To interpret the significance of this relation, three plane waves of frequency ω_1, ω_2 and ω_3 are assumed present in the material. It is then possible to treat these as coupled waves and thus describe the interaction between the three frequencies. These wave equations may be written as

$$\frac{\partial \mathrm{E}_1}{\partial z} = -\frac{i\omega_1}{2}\sqrt{\frac{\mu}{\varepsilon_1}} d_{\text{eff}} \mathrm{E}_3 \mathrm{E}_2^* \exp[-i(k_3 - k_2 - k_1)z], \tag{5.4}$$

$$\frac{\partial \mathrm{E}_2}{\partial z} = -\frac{i\omega_2}{2}\sqrt{\frac{\mu}{\varepsilon_2}} d_{\text{eff}} \mathrm{E}_3 \mathrm{E}_1^* \exp[-i(k_3 - k_2 - k_1)z], \tag{5.5}$$

$$\frac{\partial \mathrm{E}_3}{\partial z} = -\frac{i\omega_3}{2}\sqrt{\frac{\mu}{\varepsilon_3}} d_{\text{eff}} \mathrm{E}_1 \mathrm{E}_2 \exp[-i(k_1 + k_2 - k_3)z], \tag{5.6}$$

where k_1, k_2 and k_3 describe the wave-vectors of the relative frequencies and d_{eff} is the effective nonlinear coefficient which is a measure of the strength of the coupling between the fields. Equations (5.4) to (5.6) describe the rate of change with distance of the wave amplitude at one frequency as a function of the wave amplitudes at the other two frequencies.

The term in round brackets in (5.4) and (5.5), $\Delta k = k_3 - k_2 - k_1$, is known as the wave-vector mismatch. By analysis of the frequencies of interest and the material in which they interact, it is possible to increase the efficiency of the frequency conversion via a phase-matching process.

5.3. Review of phase-matching

Phase-matching is the physical process of reducing Δk to zero, such that

$$\Delta k = \frac{2\pi}{\lambda}\Delta n = \frac{\omega}{c}(n_{\omega_3} - n_{\omega_2} - n_{\omega_1}) = 0, \qquad (5.7)$$

where n_{ω_3}, n_{ω_2} and n_{ω_1} are the refractive indices of the nonlinear material experienced by the three interacting frequencies. The standard method to achieve phase-matching is to exploit crystal birefringence Δn, and may described for the simple case of second harmonic generation, where $\omega_1 = \omega_2 = \omega$ and $\omega_3 = 2\omega$. The exact nature of phase-matching is, however, dependent on the properties of the nonlinear optical crystal.

5.3.1. Uniaxial and biaxial crystals

Nonlinear crystals fall into two principal categories: uniaxial and biaxial. Uniaxial crystals have an axis of symmetry about one axis, known as the optic axis. The plane containing the optic axis and the wave-vector k of the input radiation to the crystal is called the principal plane. If an input beam is polarised perpendicularly to the principal plane, the radiation is termed an ordinary ray. Such a beam will experience a refractive index of n_o on propagation through the nonlinear crystal. If the input beam is polarised parallel to the principal plane, the beam then travels in the extraordinary direction and will experience a refractive index of n_e. The difference

between these refractive indices is known as the birefringence, Δn. The extraordinary refractive index is dependent on the input angle, such that

$$n_e(\theta) = n_o \sqrt{\frac{1+\tan^2(\theta)}{1+\left(\frac{n_o}{n_e}\right)^2 \tan^2(\theta)}}. \tag{5.8}$$

For anisotropic crystals, $n_o \neq n_e$. If $n_o > n_e$, the crystal is negative, if $n_o < n_e$, the crystal is positive. This is shown schematically in figures 1(a) and 1(b). Using this difference in refractive indices, it is possible to find a direction of propagation which meets the phase-matching criterion, as described by equation (5.7).

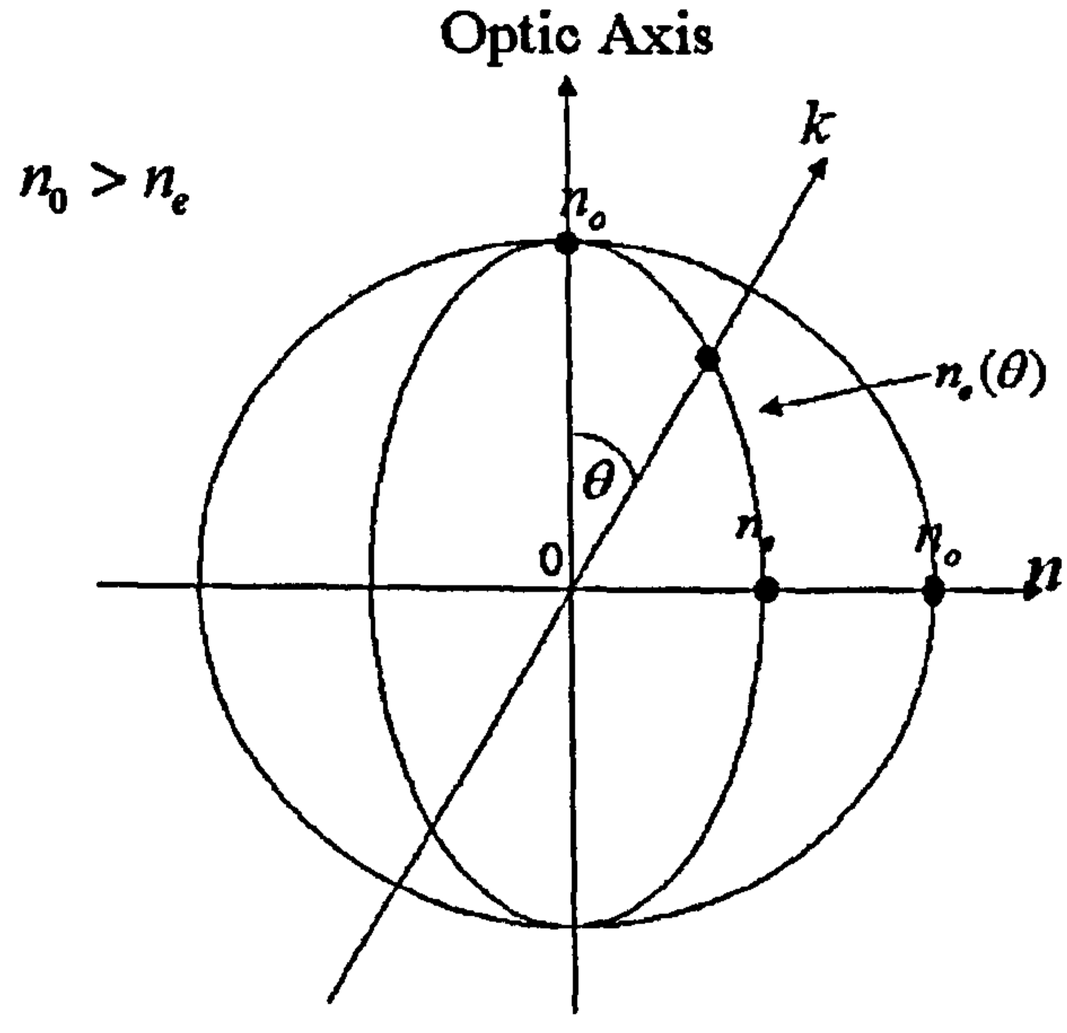

Figure 1a. Schematic representation of negative uniaxial crystal refractive indices.

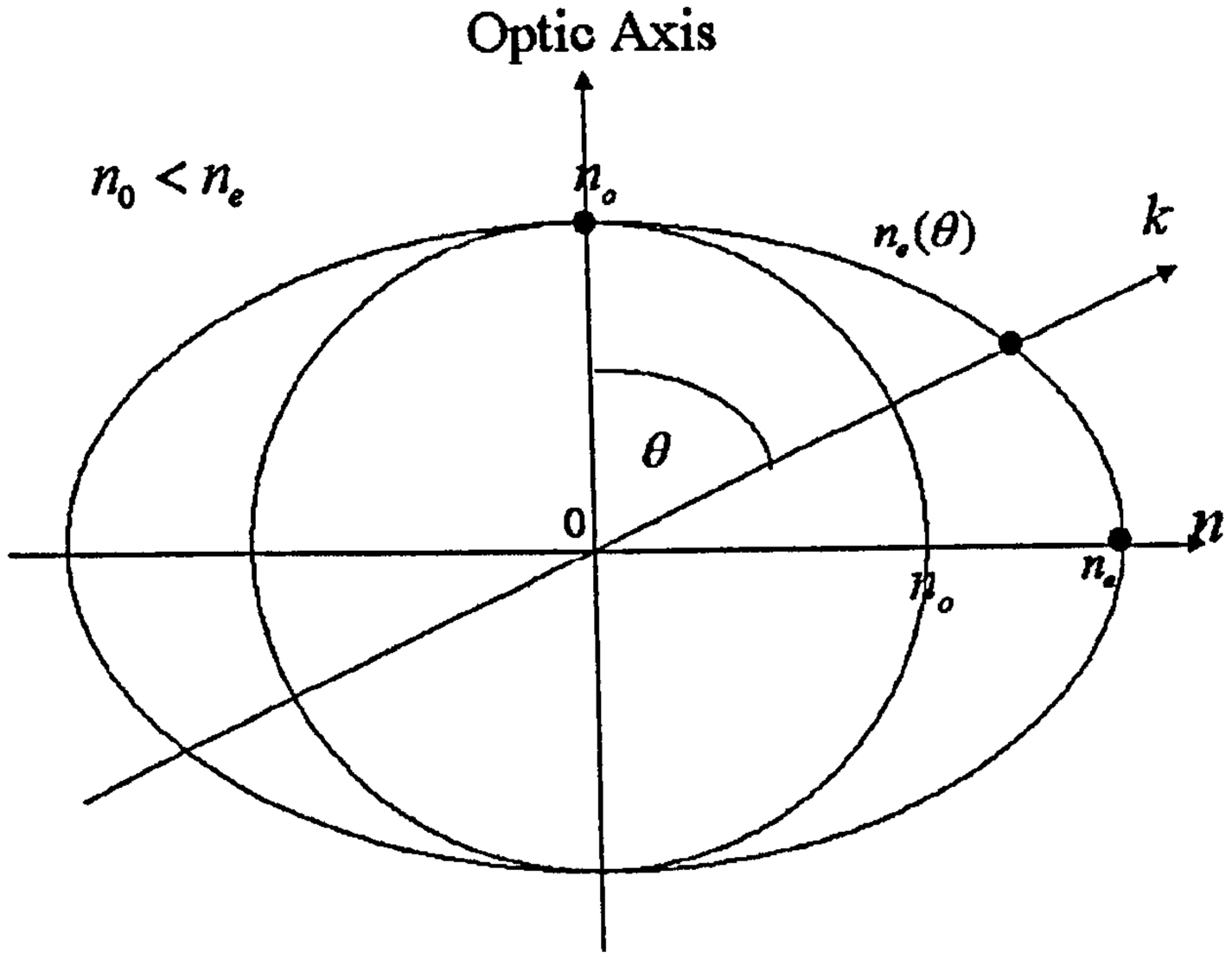

Figure 1b. Schematic illustration of positive uniaxial crystal refractive indices.

Assuming a three-wave process, such as sum-frequency generation, it is simple to analyse the underlying phase-matching types.

5.3.2. Type I and Type II phase-matching

A Type I phase-matching process arises from two input beams of the same polarisation mixing to form a third beam which is polarised perpendicularly to the input beam.

In negative crystals, this is called ooe phase-matching, referencing the direction of propagation of the beams, and may be described by

$$k_{o,input1} + k_{o,input2} = k_{e,output}. \tag{5.9}$$

In positive crystals, the process is known as eeo phase-matching, such is the polarisation of the beams. Similarly to equation (5.9) above, the condition may be expressed as

$$k_{e,input1} + k_{e,input2} = k_{o,output}\,. \tag{5.10}$$

A Type II phase-matching process occurs when the input beams are of orthogonal polarisation. Four permutations are permitted in total, as described in table 2.

Type of Crystal	Phase-matching process	Phase-matching condition
Negative	oee	$k_{o,\,input1} + k_{e,\,input2}(\theta) = k_{e,\,output}(\theta)$
Negative	eoe	$k_{e,\,input1}(\theta) + k_{o,\,input2} = k_{e,\,output}(\theta)$
Positive	oeo	$k_{o,\,input1} + k_{e,\,input2}(\theta) = k_{o,\,output}$
Positive	eoo	$k_{e,\,input1}(\theta) + k_{o,\,input2} = k_{o,\,output}$

Table 2. Type II phase-matching permutations for negative and positive uniaxial crystals.

Conversely, biaxial crystals have three optic axes and the refractive index is different for propagation along the x,y and z directions. This leads to more complex phase-matching conditions and are therefore omitted, but a full description of phase-matching in biaxial crystals is presented in reference [7].

5.4. Effective nonlinear coefficient

Nonlinear optical susceptibilities, as described in § 5.1, depend on the electronic structure of the medium and differ for uniaxial and biaxial crystals. For materials lacking a centre of inversion, the $\chi^{(2)}$ parameters are described by tensors. In a

Cartesian reference frame, where Z is the optic axis, the linear dielectric polarisation tensor ε_0 may be described by

$$\varepsilon_{0XX} = \varepsilon_{0YY} = n_o^2 \tag{5.11}$$

and

$$\varepsilon_{0ZZ} = n_e^2 . \tag{5.12}$$

It is common to use the tensor d_{ijk} instead of χ_{ijk}, where

$$\chi_{ijk} = 2d_{ijk} \tag{5.13}$$

Since the crystal is three-dimensional, χ and d must also take a three dimensional representation. To simplify the case, a plane-wave approximation is used and in the form of d_{il}, where l is expressed in relation to the orientation of the crystal as shown in table 3.

Orientation	XX	YY	ZZ	YZ=ZY	XZ=ZX	XY=YX
l =	1	2	3	4	5	6

Table 3. Simplification of tensors by adopting planar approximation.

It is therefore straightforward to express (5.2) in terms of d_{il} (with respect to the components)

$$P_i = \varepsilon E_k + 2d_{il}E_l^2 + \ldots, \tag{5.14}$$

where E_l^2 is the six-dimensional vector of the field products. For the case of sum-frequency mixing, the fields may be described by matrix form thus:

$$\left[\begin{pmatrix} P_X \\ P_Y \\ P_Z \end{pmatrix}\right] = \begin{bmatrix} d_{11} & d_{12} & d_{13} & d_{14} & d_{15} & d_{16} \\ d_{21} & d_{22} & d_{23} & d_{24} & d_{25} & d_{26} \\ d_{31} & d_{32} & d_{33} & d_{34} & d_{35} & d_{36} \end{bmatrix} \begin{bmatrix} E_X^2 \\ E_Y^2 \\ E_Z^2 \\ 2E_Y E_Z \\ 2E_X E_Z \\ 2E_X E_Y \end{bmatrix}. \tag{5.15}$$

It is apparent that the number of components of the nonlinearity tensor d is 18. In materials with a centre of inversion, each of these components is zero. This is not the case in materials without a centre of inversion, where the components are largely non-zero. Kleinman proposed in 1962 that the number of these components may be reduced in many cases from 18 to 10 [7]. This arises from the symmetry conditions

$$d_{12} = d_{26},\ d_{13} = d_{35},\ d_{14} = d_{36} = d_{25},\ d_{15} = d_{31},\ d_{16} = d_{21},\ d_{24} = d_{32}. \tag{5.16}$$

These components are related to the useful parameter d_{eff}, known as the effective nonlinear coefficient, which is the effective coupling strength of the interacting fields and is given by the expression

$$d_{eff} = \mathrm{p}_1 d \mathrm{p}_3 \mathrm{p}_2 = \mathrm{p}_2 d \mathrm{p}_3 \mathrm{p}_1 = \mathrm{p}_3 d \mathrm{p}_1 \mathrm{p}_2, \tag{5.17}$$

where p is the unit polarisation vector given in polar co-ordinates θ and ϕ,

$$\begin{aligned} \mathrm{p}_{oX} &= -\sin\phi,\ \mathrm{p}_{eX} = \cos\theta\cos\phi \\ \mathrm{p}_{oY} &= \cos\phi, \mathrm{p}_{eY} = \cos\theta\sin\phi \\ \mathrm{p}_{oZ} &= 0, \mathrm{p}_{eZ} = -\sin\theta. \end{aligned} \tag{5.18}$$

Depending on the interaction type, the values of the p vector and thus d_{eff} may be calculated for a uniaxial crystal of known point group. Similar calculations for biaxial crystals are given in reference 8. For both uniaxial and biaxial crystals, it is apparent that an increase in d_{eff} leads to a higher $\chi^{(2)}$ coefficient and therefore a material with a large d_{eff} is sought for efficient nonlinear optical frequency conversion.

5.5. Nonlinear crystal properties

In nonlinear frequency conversion, certain conditions (including phase-matching) should be met in order to maximise the conversion efficiency from the fundamental to the new wavelength(s). These include manipulation of the pump radiation and choice of nonlinear crystal.

So far, the model presented has assumed a plane wave. However, in a real experiment the pump laser will be divergent, may be pulsed and will be subject to dispersion on propagating through a nonlinear medium. Therefore, any crystal used for frequency conversion must be engineered to account for such properties. This includes calculation of parameters such as the angular, spectral and temperature bandwidths. These limiting factors depend on the type of phase-matching and orientation of pump radiation and therefore will be discussed in later chapters for individual cases.

Frequently, the direction of the wave-vector and the wave-energy do not coincide. This results in a walk-off $\rho(\theta)$ between the fundamental and the converted frequencies, which manifests itself in a reduction in conversion efficiency and is expressed as

$$\rho(\theta) = \tan^{-1}\left[\left(\frac{n_o}{n_e}\right)^2 \tan(\theta)\right]. \tag{5.19}$$

This walk-off effect can be reduced by using a non-critically phase-matched (NCPM) crystal. This crystal has zero walk-off, which arises from a phase-matching angle of $\theta = 90°$. Critical phase-matching (CPM) relies upon angular rotation of the crystal to reach the phase-matching point. CPM induces more loss than the non-critical method due to reflections from the crystal surfaces and angular walk-off. In practice, it is convenient to choose a material that phase-matches at room temperature or above, to avoid condensation.

Focussing of the pump radiation is also important, as described by the theoretical study by Boyd and Kleinman [9]. For a continuous wave laser, a focussing parameter can be calculated to account for optimum focussing of the pump radiation in a crystal of prescribed length to achieve optimum conversion efficiency. The study was performed in the case of second harmonic generation for which the focussing parameter was established to be $\xi = 2.84$, where

$$\xi = \frac{l}{b}, \tag{5.20}$$

where l is the length of the nonlinear crystal and b is the confocal parameter.

For a NCPM crystal, the ideal spot size of the pump radiation w_0 for a laser operating at a wavelength of λ_ω in a material of refractive index n_ω can then be calculated by substitution into (5.20) above.

$$w_0 = \frac{l\lambda_\omega}{2.84(2\pi n_\omega)}. \tag{5.21}$$

In the case of a pulsed laser, the length of the crystal is chosen as a result of the pump pulse duration, τ_ω. The fundamental and the converted frequency will travel with different group velocities due to the wavelength dependence of refractive index (as dictated by the Sellmeier equation [8]). As an approximation, the length of the

crystal is the distance over which the fundamental and frequency converted pulse travel before splitting and may be expressed as

$$l = \frac{c\tau_{\omega}}{\Delta n}, \tag{5.22}$$

where Δn is the birefringence of the material. In practice, however, a crystal length must be chosen that is commercially available.

Any crystalline material applied for frequency conversion experiments must also possess a wide transparency across the wavelength regions of interest to minimise loss. Furthermore, it should also have a high damage threshold and should ideally be non-hygroscopic at room temperature, for ease of handling.

5.6. Conclusions

A brief review of the basic principles underlying nonlinear optics has been presented. This has included a synopsis of the origins of nonlinear optics and means of increasing the optical conversion efficiency by means of phase-matching, focussing and crystal design. This will be expanded upon in the following chapters for specific cases.

5.7. References

[1] P.A. Franken, A.E. Hill and C.W. Peters *et al.*, "Generation of optical harmonics", Physical Review Letters, Vol. 7, 1961 (pp118-119).

[2] H.K. Shin, I. Kim and E.J. Kim *et al.*, "Vertical-cavity surface emitting lasers for optical data storage", Japanese Journal of Applied Physics, Vol. 1, No. 35 (1B), 1996 (pp506-507).

[3] D.A. Belforte, "Micromachining: the growth engine for industrial lasers", Laser Focus World, Vol. 36, No. 7, 2001 (p181).

[4] L. Gianfrani, P. de Natale and G. de Natale, "Remote sensing of volcanic gases with a DFB-laser-based fiber spectrometer", Applied Physics B, Vol. 70, No. 3, 2000 (pp467-470).

[5] N. Umemura and K.Kato, "Phase-matched UV generation at 0.1774μm in $KB_5O_5.4H^{(2)}O$", Applied Optics, Vol. 35, No. 27, 1996 (pp5332-5335).

[6] T.Q. Qiu, T. Tillert and M. Maier, "Tunable, kilowatt, picosecond far-infrared pulse generation in $LiNbO_3$", Optics Communications, Vol. 119, No. 1-2, 1995 (pp149-153).

[7] D.A. Kleinman, "Nonlinear dielectric polarization in optical media", Physical Review, Vol. 126, 1962 (pp1977-1979).

[8] V.G. Dmitriev, G.G. Gurzadyan and D.N. Nikogosyan, "Handbook of Nonlinear Optical Crystals (2nd Edition)", Springer-Verlag, (ISBN 0-387-52026-0) 1990.

[9] G.D. Boyd and D.A. Kleinman, "Parametric interaction of focussed Gaussian light beams", Journal of Applied Physics, Vol. 39, 1968 (pp3597-3639).

Chapter Six

Singly Resonant Third Harmonic Generation

6.1. Introduction

Many applications exist for high efficiency third harmonic generation of mode-locked solid state lasers to the ultraviolet region of the spectrum including materials processing [1], spectroscopy [2], and pumping of optical parametric oscillators in the visible region of the spectrum [3]. As outlined in Chapter One, however, the aim of this project is to develop a source which relies upon nonlinear frequency conversion to generate ultrashort-pulsed visible radiation that is tunable between $\lambda = 600\text{nm}$ and $\lambda = 700\text{nm}$. One approach to achieving such a source is to pump an optical parametric oscillator with a laser that operates in the ultraviolet region of the electromagnetic spectrum. In order to achieve optical parametric oscillation, the ultraviolet laser source must exhibit sufficiently high peak power and good beam qualities.

However, neither of these issues are trivial since there are currently few solid-state materials that emit in the ultraviolet region of the spectrum. To this end, ultra-short pulsed third harmonic generation is most commonly achieved by sum frequency mixing of second harmonic and fundamental radiation in two-crystal single pass geometry, pumped by a mode-locked source [4]. This cascaded nonlinear process is conventionally rather inefficient particularly for sources of modest average power.

This chapter is concerned with the design and development of an efficient mode-locked ultraviolet laser source. This is achieved by adapting an existing model for resonant second harmonic generation. A model for resonant third harmonic

generation and numerical simulation based using the saturable Bragg reflector laser described in Chapter Four as a pump source are reported. An experimental demonstration is also presented based on this laser source. A discussion follows, with comparison to results predicted by the simulation.

6.2. Historical review of resonant enhancement cavities

Ashkin *et al.* [5] first established the model for resonant second harmonic generation of a single-frequency continuous wave (cw) source. By resonating the fundamental radiation and placing a phase-matched nonlinear crystal within an impedance matched cavity, conversion efficiencies are greatly increased. This arises from the fact that the nonlinear crystal experiences the enhanced intracavity field rather than that delivered by the laser.

In 1990, Persaud *et al.* [6] modified the cw model to consider second harmonic generation via mode-locked pulses circulating within a similar cavity. By using a mode-locked laser as the input to the resonant enhancement cavity conversion efficiencies from fundamental to second harmonic exceeding 50% were achieved. It is this model that has been adapted further to account for a second intracavity crystal to generate the third harmonic of a mode-locked laser via sum-frequency mixing.

6.3. Theory of resonant second harmonic generation

The model by Persaud *et al.* [6] describes a mode-locked pulse train mode-matched to an external resonator that contains a single phase-matched BBO crystal, as shown in figure 1. The radiation is coupled into the cavity through a mirror of power reflectivity r_{in} and power transmission t_{in}, which is assumed to be free of loss such that the condition $r_{in} + t_{in} = 1$ holds true. The remainder of the cavity mirrors are highly reflecting at the fundamental wavelength and fully transmitting at the second

harmonic wavelength. The external resonator round-trip time is synchronously matched to that of the laser source.

For low conversion efficiencies (<40%), the generated second harmonic may be described as a transmission loss in the fundamental power due to the principle of energy conservation, such that

$$t_{2\omega} = (1 - \eta_{2\omega}), \tag{6.1}$$

where the second harmonic conversion efficiency $\gamma_{2\omega}$ is related to fundamental intracavity power P_{ω} by

$$\eta_{2\omega} = \gamma_{2\omega} P_{\omega}. \tag{6.2}$$

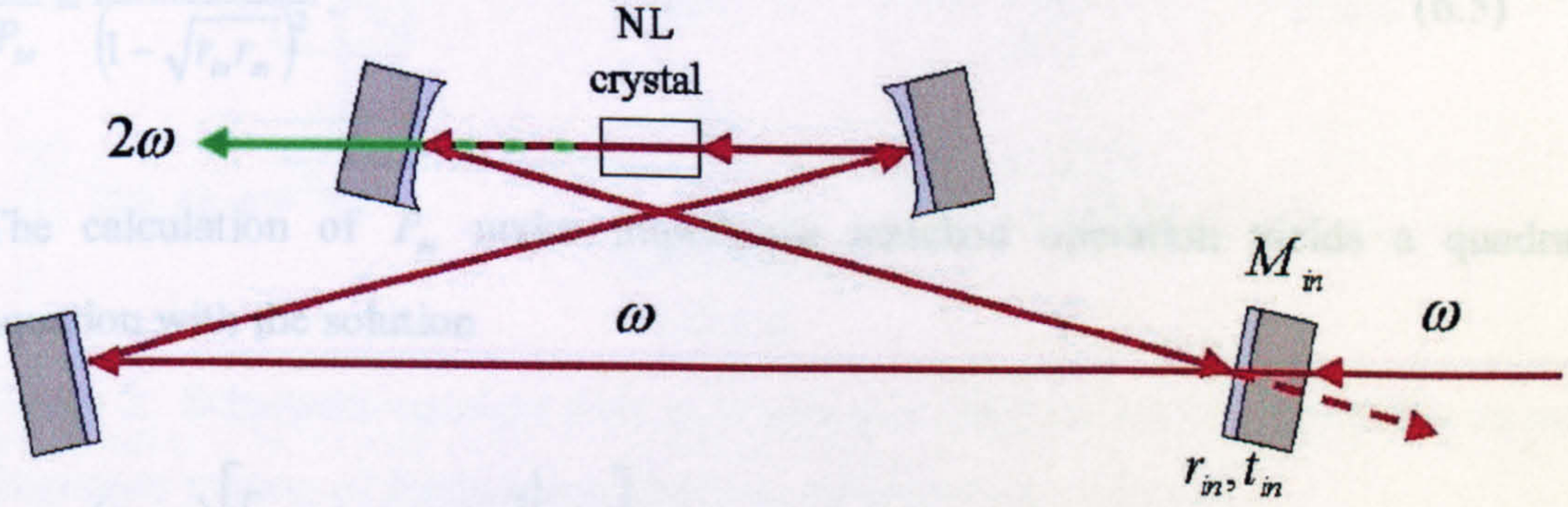

Figure 1. Schematic diagram of single-crystal ring cavity for second harmonic generation. The cavity mirrors (excepting input coupler) are highly reflecting at the resonating fundamental wavelength and fully transmitting at the second harmonic wavelength.

The crystal transmission t and the reflectivity of the cavity mirrors r can be combined with the depletion in fundamental radiation to produce an effective reflectivity for the cavity, given by

$$r_m = t_{2\omega} tr \,. \tag{6.3}$$

The power reflected from the cavity on resonance may be shown to be

$$P_r = P_{in} \frac{\left(\sqrt{r_{in}} - \sqrt{r_m}\right)^2}{\left(1 - \sqrt{r_{in} r_m}\right)^2}, \tag{6.4}$$

where P_{in} is the incident fundamental power (W).

For maximum intracavity field, the external resonator should be impedance matched. This occurs where the reflected power, P_r, is zero. Under impedance matching, the enhancement factor of the cavity on resonance is then described by

$$\frac{P_\omega}{P_{in}} = \frac{r_{in}}{\left(1 - \sqrt{r_{in} r_m}\right)^2}. \tag{6.5}$$

The calculation of P_ω under impedance matched operation yields a quadratic equation with the solution

$$P_\omega = \frac{(1-rt)}{2rt\gamma_{2\omega}} \left[\left[1 + \frac{4rt\gamma_{2\omega} P_{in}}{(1-rt)^2} \right]^{\frac{1}{2}} - 1 \right]. \tag{6.6}$$

The generated second harmonic power then becomes

$$P_{2\omega} = \gamma_{2\omega} P_\omega^{\,2}. \tag{6.7}$$

It is this model that is adapted to account for a second phase-matched nonlinear crystal within the resonant enhancement cavity to perform sum-frequency mixing of the second harmonic and fundamental frequencies to reach the third harmonic wavelength.

6.4. Extension of model to account for resonant third harmonic generation.

For conventional non-resonant third harmonic generation, a cascaded process is usually adopted, as demonstrated in figure 2. The first nonlinear crystal is used to frequency double the pump radiation. This second harmonic radiation then undergoes a sum-frequency mixing with fundamental radiation in a second nonlinear crystal to generate the third harmonic wavelength. This process is largely inefficient, with conversion efficiencies from fundamental to third harmonic wavelengths of less than 5%. Since a resonant enhancement cavity has successfully demonstrated an increase in second harmonic conversion efficiency, the same procedure is modelled in the case of third harmonic generation.

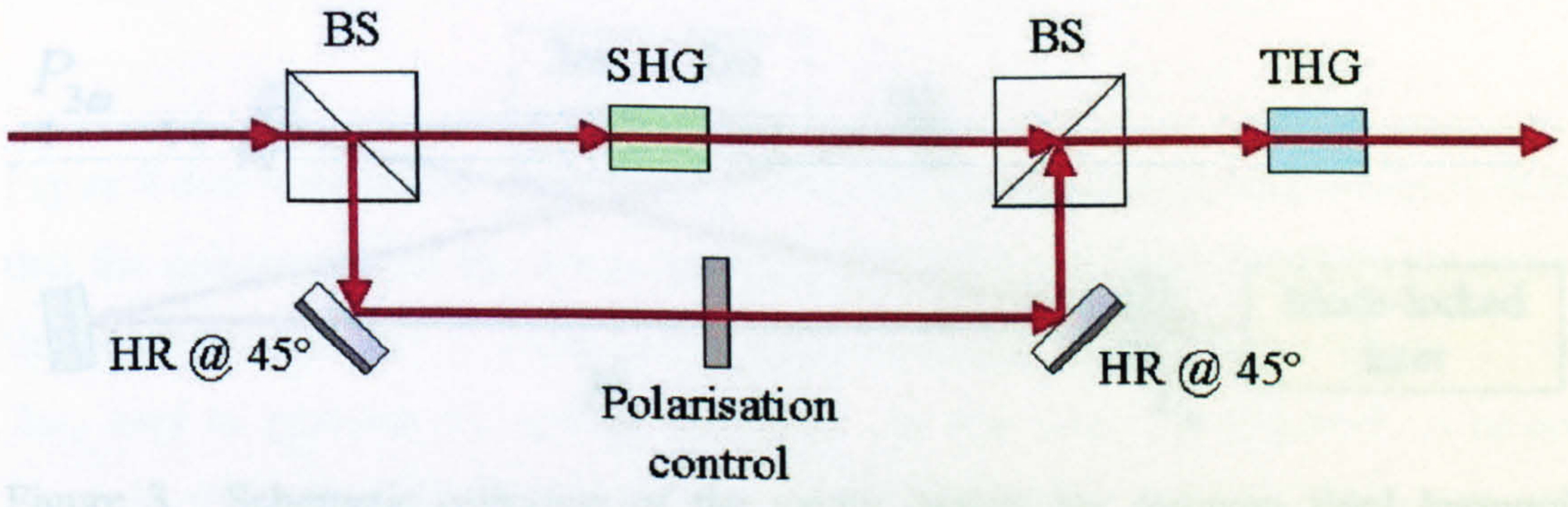

Figure 2. Schematic configuration of single-pass third harmonic generation via sum-frequency mixing of fundamental and second harmonic radiation.

6.5. Resonant third harmonic generation

A schematic diagram of the external cavity used to perform the resonant third harmonic generation is shown in figure 3. Enhancement will only be effective if the cavity round-trip time of the external resonator is matched to that of the mode-locked laser, such that each successive pulse will overlap at the input coupler. This leads to a build-up of intracavity power.

With the exception of the input coupler, the cavity mirrors are assumed to be of 100% reflectivity at the fundamental wavelength and fully transmitting at the third harmonic (3ω) wavelength. Negligible loss at the input mirror is assumed and an impedance-matched cavity is chosen for simplicity. Impedance matching in this case refers to no reflected radiation leaving the cavity via the input coupler, thus increasing the overall optical efficiency. In accordance with the experiment, a bow-tie cavity design is assumed with two nonlinear crystals placed between two curved mirrors to permit tight focusing of the fundamental radiation. The first crystal 2ω performs frequency doubling of the resonated fundamental power and crystal 3ω is that for the sum-frequency mixing process, which uses the generated second harmonic radiation and the depleted intracavity fundamental radiation. The relative positions of both crystals will be discussed later.

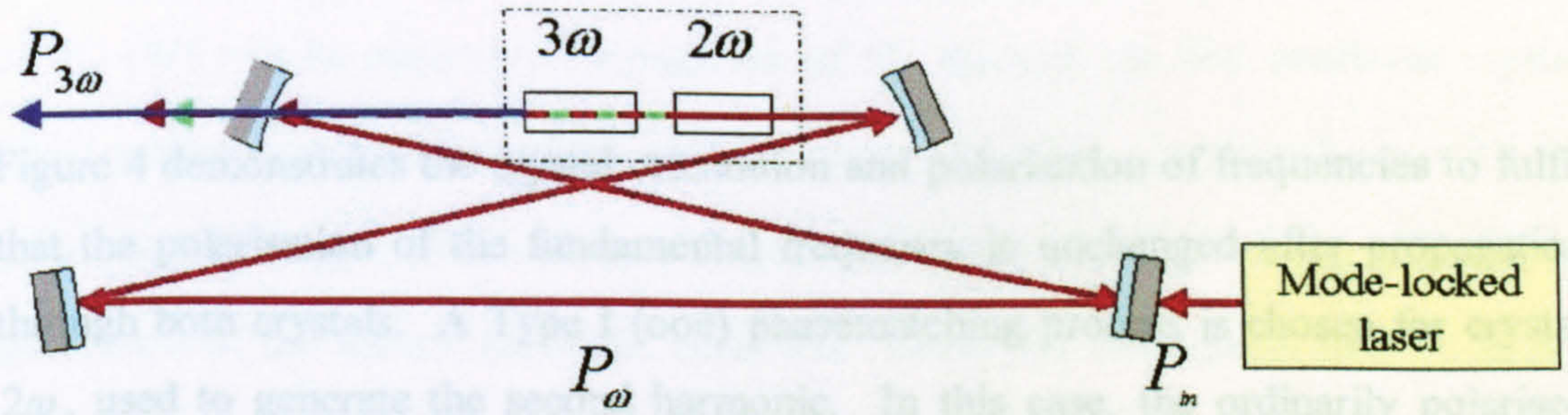

Figure 3. Schematic overview of the cavity design for resonant third harmonic generation. The output from the mode-locked laser is mode-matched to the resonant enhancement (mode-matching optics not shown).

6.5.1. Boundary conditions of the model

In order for the cavity to resonate the fundamental input, the polarisation of the input beam must not be changed on propagating through both nonlinear crystals. To fulfil this criterion, it is imperative to employ the correct phase-matching type. Type I phase-matching assumes input waves with the same polarisation state, leading to orthogonally polarised output (often described as ooe or eeo interactions). Type II phase-matching relies upon input waves with orthogonal polarisation states which

will generate either parallel or perpendicularly polarised emission, depending on the nature of the nonlinear crystal.

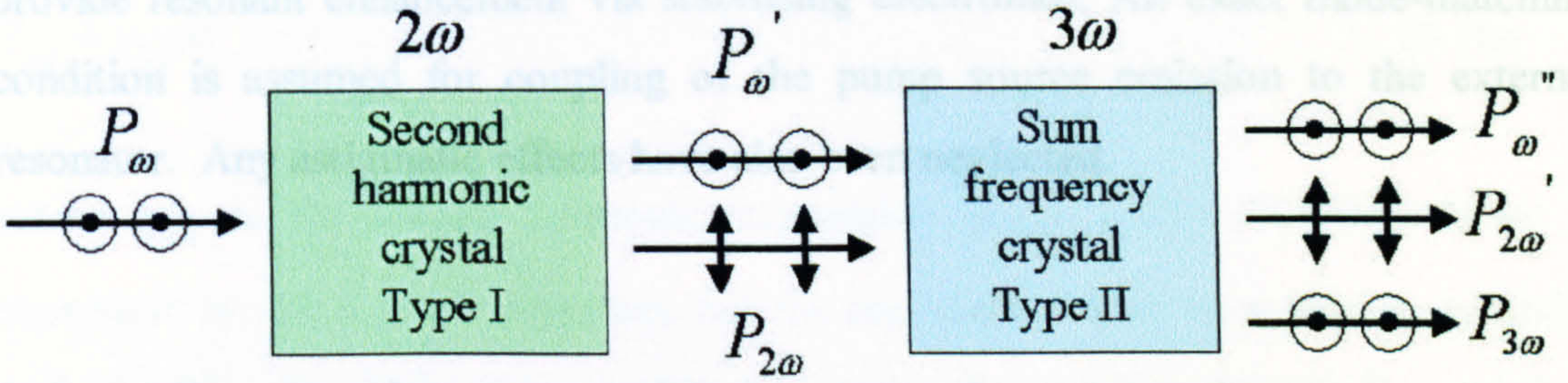

Figure 4. Polarisation and phase-matching type chosen for resonant third harmonic simulation (with reference to figure 3). The polarisation of the fundamental frequency is retained on propagation through both crystals to ensure a constructive resonant process.

Figure 4 demonstrates the crystal orientation and polarisation of frequencies to fulfil that the polarisation of the fundamental frequency is unchanged after propagation through both crystals. A Type I (ooe) phasematching process is chosen for crystal 2ω, used to generate the second harmonic. In this case, the ordinarily polarised input is frequency doubled and the second harmonic radiation emerges with extraordinary polarisation. In the second crystal, 3ω, a Type II (oeo) phasematching process is chosen to perform sum-frequency mixing. The orthogonally polarised fundamental and second harmonic states mix within the crystal to generate third harmonic radiation of ordinary polarisation. The fundamental radiation polarisation remains unchanged on traversing both crystals, therefore permitting a resonant process.

Several parameters have been established to simplify the generic model. A low-single-pass conversion efficiency process is assumed in the following simulation and sum-frequency process is considered to be specific to the generation of third harmonic radiation. Furthermore, the model does not account for the effect of pulse re-shaping by frequency conversion. A plane-wave approximation is assumed, with

perfect phase-matching and zero temporal and spatial walk-off of a TEM_{00} profile. The free-spectral range of the external cavity is matched to that of the repetition rate of the mode-locked laser. In addition, the optical phase is controlled such as to provide resonant enhancement via stabilising electronics. An exact mode-matching condition is assumed for coupling of the pump source emission to the external resonator. Any astigmatic effects have also been neglected.

6.6. Theory of resonant third harmonic generation

An average power P_{in} (W) delivered by the pump laser at the fundamental frequency is implemented as the input to the external cavity. On entering the enhancement cavity and reaching steady-state operation, an intracavity fundamental average power of P_{ω} (W) will be observed. Propagation of P_{ω} through the first nonlinear crystal (2ω) generates second harmonic average power $P_{2\omega}$ (W). In accordance with the principle of energy conservation, it therefore follows that P_{ω} will be reduced on generation of the second harmonic radiation. Under the assumption that P_{ω} is not subject to scatter, walk-off, absorption or other detrimental effects, the depleted intracavity average power P_{ω}' (W) may be expressed as

$$P_{\omega}' = P_{\omega} - P_{2\omega}. \tag{6.8}$$

Likewise, P_{ω}' is subject to further depletion to "twice-depleted" average power P_{ω}'' after propagation through the second nonlinear crystal. This second crystal performs the sum-frequency mixing process (3ω), producing third harmonic average power $P_{3\omega}$ (W). The second harmonic average power also reduces from $P_{2\omega}$ to $P_{2\omega}'$ (W).

The twice-depleted fundamental average power may be expressed by

$$P_{\omega}'' = P_{\omega} - P_{2\omega}' - P_{3\omega}. \tag{6.9}$$

As described by equation (6.7), the second harmonic average power $P_{2\omega}$ may be expressed as a function of intracavity fundamental power P_{ω} such that

$$P_{2\omega} = \gamma_{2\omega} P_{\omega}^2, \tag{6.10}$$

where $\gamma_{2\omega}$ is the second harmonic conversion factor (W^{-1}) [7]. This factor is dependent on the crystal properties, but for continuous wave operation, is typically 10^{-5}-10^{-3} W^{-1}. Similarly, it is possible to express $P_{3\omega}$ as a function of P_{ω}' and $P_{2\omega}$, since these powers mix in the second crystal to generate a third harmonic output power

$$P_{3\omega} = \gamma_{3\omega} P_{2\omega} P_{\omega}', \tag{6.11}$$

where $\gamma_{3\omega}$ is the third harmonic conversion factor (W^{-1}). By substitution of equations (6.8) and (6.10) into (6.11), an expression for $P_{3\omega}$ in terms of the intracavity fundamental average power P_{ω} is determined to be

$$P_{3\omega} = \gamma_{3\omega}\gamma_{2\omega} P_{\omega}^2 \left(P_{\omega} - \gamma_{2\omega} P_{\omega}^2\right). \tag{6.12}$$

Frequency conversion can be considered as a transmission loss in the fundamental power. For low conversion efficiencies, these transmission losses in the second and third harmonic may be described by

$$t_{2\omega} = 1 - \eta_{2\omega} \tag{6.13}$$

and

$$t_{3\omega} = 1 - \eta_{3\omega} \tag{6.14}$$

respectively, where $\eta_{2\omega}$ is the conversion efficiency of intracavity power to second harmonic power and $\eta_{3\omega}$ is the is the conversion efficiency of intracavity power to third harmonic power. Substitution of equations (6.10) and (6.12) into (6.13) and (6.14) respectively generates expressions for $t_{2\omega}$ and $t_{3\omega}$ in terms of the intracavity power P_ω as

$$t_{2\omega} = 1 - \frac{P_{2\omega}}{P_\omega} = 1 - \gamma_{2\omega} P_\omega \tag{6.15}$$

and

$$t_{3\omega} = 1 - \frac{P_{3\omega}}{P_\omega} = 1 - \gamma_{2\omega}\gamma_{3\omega} P_\omega \left(P_\omega - \gamma_{2\omega} P_\omega^2\right). \tag{6.16}$$

An effective reflectivity for a single round trip of the cavity, r_{eff}, taking into account the harmonic conversion transmission of both crystals and the cavity mirror transmission and reflectivity (exclusive of the input coupler mirror reflectivity), t and r respectively, may be defined as

$$r_{eff} = trt_{2\omega}t_{3\omega}. \tag{6.17}$$

Following the model of Ashkin *et al.* [5], the power reflected from the enhancement cavity on resonance P_r is given by

$$P_r = \frac{\left(\sqrt{r_{in}} - \sqrt{r_{eff}}\right)^2}{\left(1 - \sqrt{r_{in}}\sqrt{r_{eff}}\right)^2} P_{in}, \tag{6.18}$$

where r_{in} is the input coupler reflectivity at fundamental wavelength. The input coupler reflectivity is critical in achieving an impedance matched resonator. In this impedance matched case, the reflected power P_r reduces to zero when $r_{in} = r_{eff}$.

Under the assumption of a perfect input coupler such that $r_{in}+t_{in}=1$, where t_{in} is the input coupler mirror transmission, the intracavity fundamental power for an impedance matched resonator is described by

$$P_{\omega}=\frac{P_{in}}{1-r_{eff}}. \tag{6.19}$$

Substitution of equation (6.17) into (6.19) generates a fifth order polynomial, in terms of P_{ω},

$$tr\gamma_{3\omega}\gamma_{2\omega}^{3}P_{\omega}^{5}-2tr\gamma_{3\omega}\gamma_{2\omega}^{2}P_{\omega}^{4}+tr\gamma_{3\omega}\gamma_{2\omega}P_{\omega}^{3}+tr\gamma_{2\omega}P_{\omega}^{2}+(1-tr)P_{\omega}-P_{in}=0. \tag{6.20}$$

A real solution for P_{ω} may be found from equation (6.20) and is used in conjunction with equations (6.10) and (6.12) to obtain analytical solutions for $P_{2\omega}$ and $P_{3\omega}$. This was achieved using Mathematica v3.0, although the solutions generated by this method are not explicitly produced by the software and therefore are omitted for simplicity. The intracavity enhancement factor is defined as the ratio of intracavity power, given as the solution to (6.20), to fundamental average input power.

The model for evaluating the optimum impedance matching conditions is based on equations (6.15), (6.16) and (6.17). In terms of fundamental input power, r_{eff} is defined as

$$r_{eff}=tr-tr\gamma_{2\omega}\gamma_{3\omega}P_{\omega}^{2}+tr\gamma_{2\omega}\gamma_{3\omega}P_{\omega}^{3}-tr\gamma_{2\omega}P_{\omega}+tr\gamma_{3\omega}\gamma_{2\omega}^{2}P_{\omega}^{3}-tr\gamma_{3\omega}\gamma_{2\omega}^{3}P_{\omega}^{4}. \tag{6.21}$$

In conjunction with equation (6.12), an iterative method is used to find the optimal value of the input mirror reflectivity with input of parameters based on the SBR mode-locked laser described in Chapter Four.

The model as described so far applies to a continuous wave case. To describe the case of a mode-locked source, the values of $\gamma_{2\omega}$ and $\gamma_{3\omega}$ must be adjusted accordingly to account for the peak power. Average power is defined as the energy per pulse divided by the time between pulses. Peak power P_p, under assumption of a Gaussian pulse form, however, is given by [5]

$$P_p = 2\sqrt{\frac{\ln 2}{\pi}}\frac{P_{av}T}{\tau_p}, \tag{6.22}$$

where P_{av} is the average power (W), T is the total cavity round trip time (s) and τ_p is the pulse duration (s). Equation (6.15) may be adapted to describe various pulse-shapes such as hyperbolic secant and Lorentzian pulses, but the Gaussian case serves well as an approximation for other similar pulse-forms [8]. Modification of equation (6.15) allows evaluation for the mode-locked case, where the mode-locked second and third harmonic conversion factors $\gamma'_{2\omega}$ and $\gamma'_{3\omega}$ are described as

$$\gamma'_{2\omega} = 2\gamma_{2\omega}\sqrt{\frac{\ln 2}{\pi}}\frac{T}{\tau_p} \tag{6.23}$$

and

$$\gamma'_{3\omega} = 2\gamma_{3\omega}\sqrt{\frac{\ln 2}{\pi}}\frac{T}{\tau_p}. \tag{6.24}$$

These may be approximated to

$$\gamma'_{2\omega} = \gamma_{2\omega}\frac{T}{\tau_p} \tag{6.25}$$

and

$$\gamma'_{3\omega} = \gamma_{3\omega} \frac{T}{\tau_p}, \tag{6.26}$$

respectively.

6.7. Numerical simulation of resonant third harmonic generation

For continuous wave systems, an order-of-magnitude estimate of conversion factors leads to $\gamma_{2\omega} = \gamma_{3\omega} = 10^{-3} - 10^{-5}\, W^{-1}$. Under the assumption of a mode-locked source with input pulses of picosecond duration with 4.4 ns cavity round trip time, approximate values may be assigned as $\gamma'_{2\omega} = \gamma'_{3\omega} = 2\text{x}10^{-2}\,\text{W}^{-1}$, as described by equations (6.25) and (6.26). The mode-locked case has been considered with approximate cavity parameters, as shown in Appendix Four. Given an assumed loss on each crystal surface of 1%, a transmission value of $t = 0.96$ has been assigned. Estimating a loss of <1% for each mirror (exclusive of input coupler), a reflectivity loss of $r = 0.98$ is chosen. These parameters hold in the following analysis unless stated otherwise.

By applying these numerical parameters to equation (6.20), analysis of the intracavity power P_ω with respect to input power P_{in} and cavity mirror reflectivity r may be obtained. This is shown in figure 5. By analogy with the existing model for second harmonic generation, the intracavity power is dependent on the cavity mirror reflectivity. As cavity mirror transmission increases, the intracavity power decreases. A further dependency on input power is noted. As input fundamental power increases, the intracavity power will increase.

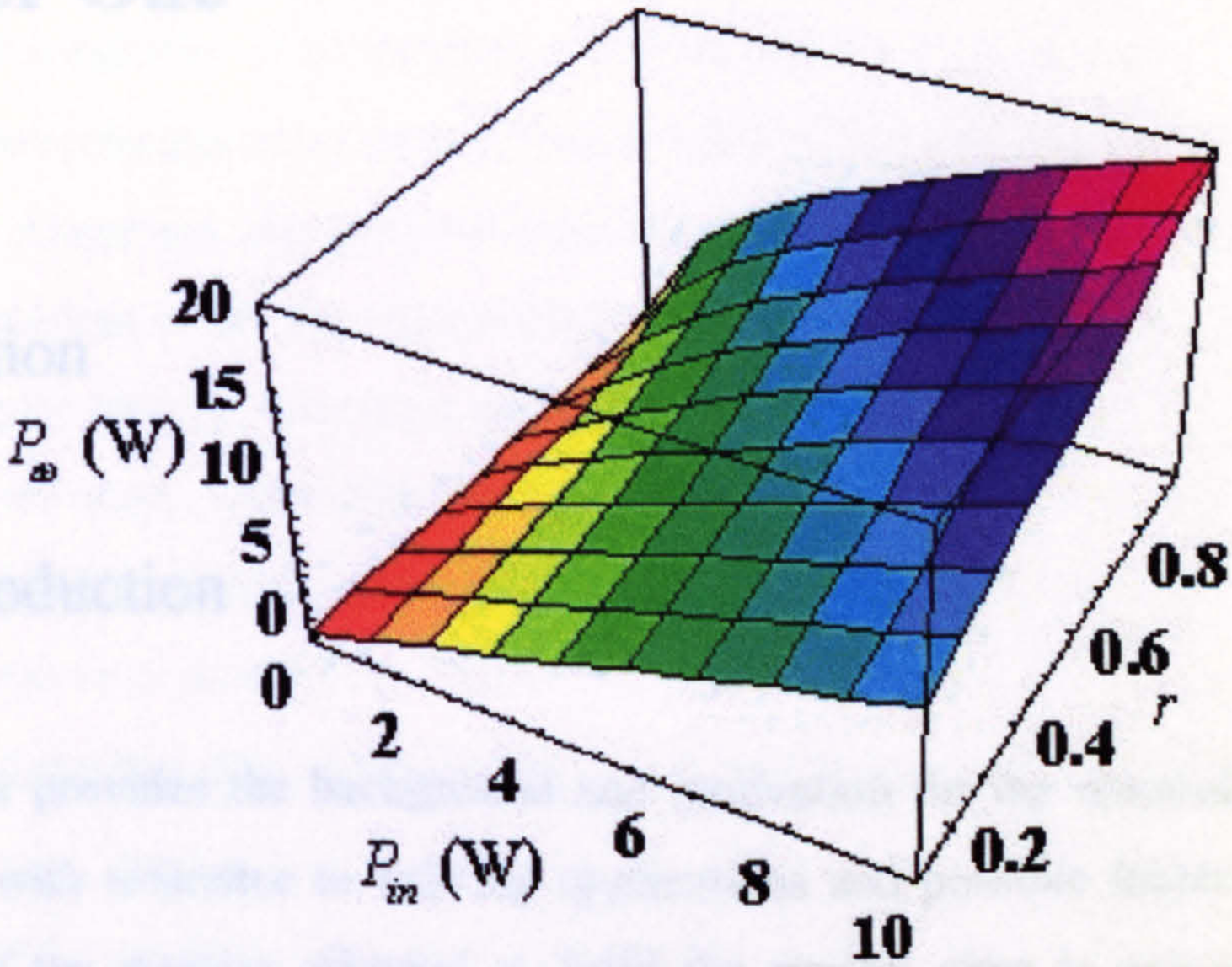

Figure 5. Theoretical prediction of fundamental intracavity power P_ω (W), where the input power varies from 0 to 10W and the introduced total cavity mirror reflectivity r varies from 20% to 99%. The second and third harmonic conversion efficiencies are fixed as $\gamma'_{2\omega} = \gamma'_{3\omega} = 2\text{x}10^{-2}$ W^{-1}.

The intracavity average power P_ω does not scale linearly with input power. At lower (<2W) input powers, the intracavity enhancement factor is greater than that of high input powers. It is possible to conclude from this feature that this resonant method is of particular benefit when generating third harmonic radiation of moderate average power mode-locked sources. Based on these findings, it is imperative that loss is minimised. Experimentally, this may be realised by employing specifically anti-reflection coated crystals and using high-reflectivity mirrors over both the wavelength and angular position as required.

Generated third harmonic average power $P_{3\omega}$ with respect to intracavity fundamental is shown in figure 6. Once again, the generated radiation is expressed as a function of cavity mirror reflectivity r. For low cavity mirror reflectivity, the resulting third

harmonic average power is comparable to that generated in a single-pass geometry and therefore may be neglected in this analysis. Typical conversion efficiencies from fundamental to third harmonic wavelength output for low loss ($r \geq 96\%$) of 30% are theoretically observed for modest input powers.

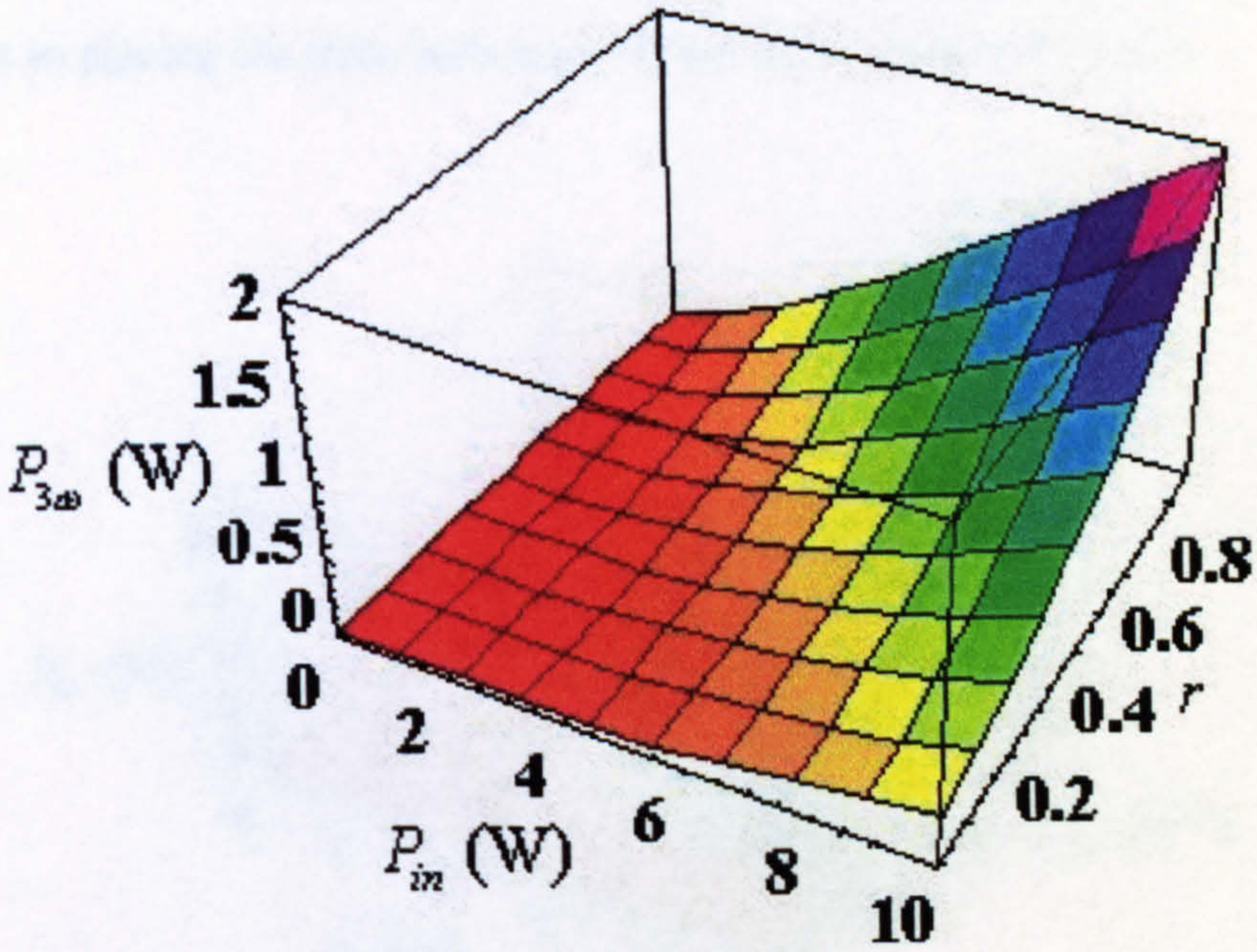

Figure 6. Theoretical prediction of generated third harmonic power $P_{3\omega}$ (W) where the input power varies from 0 to 10W and the total cavity mirror reflectivity is scaled from 20% to 99%. $\gamma'_{2\omega} = \gamma'_{3\omega} = 2\text{x}10^{-2}\ \text{W}^{-1}$.

Previous calculations have been carried out for fixed values of $\gamma'_{2\omega}$ and $\gamma'_{3\omega}$. Depending on the crystal properties and location within the resonator, however, these values may be adjusted. To this end, the effect of these parameters on the resulting third harmonic average power has been investigated. By establishing the second harmonic conversion factor as $\gamma'_{2\omega} = 2\text{x}10^{-2}\ \text{W}^{-1}$, it is possible to evaluate the dependency of $\gamma'_{3\omega}$ on $P_{3\omega}$. The values of $r = 0.98$ and $t = 0.96$ remain unchanged.

The third harmonic conversion factor is scaled from $2x10^{-2}$ to 10^{-1} W^{-1} as shown in figure 7. It is evident that increasing $\gamma'_{3\omega}$ leads to a subsequent increase in the third harmonic average power, across the range of input powers. This indicates that even under high input average power conditions, the process will be inefficient without implementation of a nonlinear material with a high $\gamma'_{3\omega}$ factor. Experimentally, this corresponds to placing the third harmonic crystal at an intracavity focus.

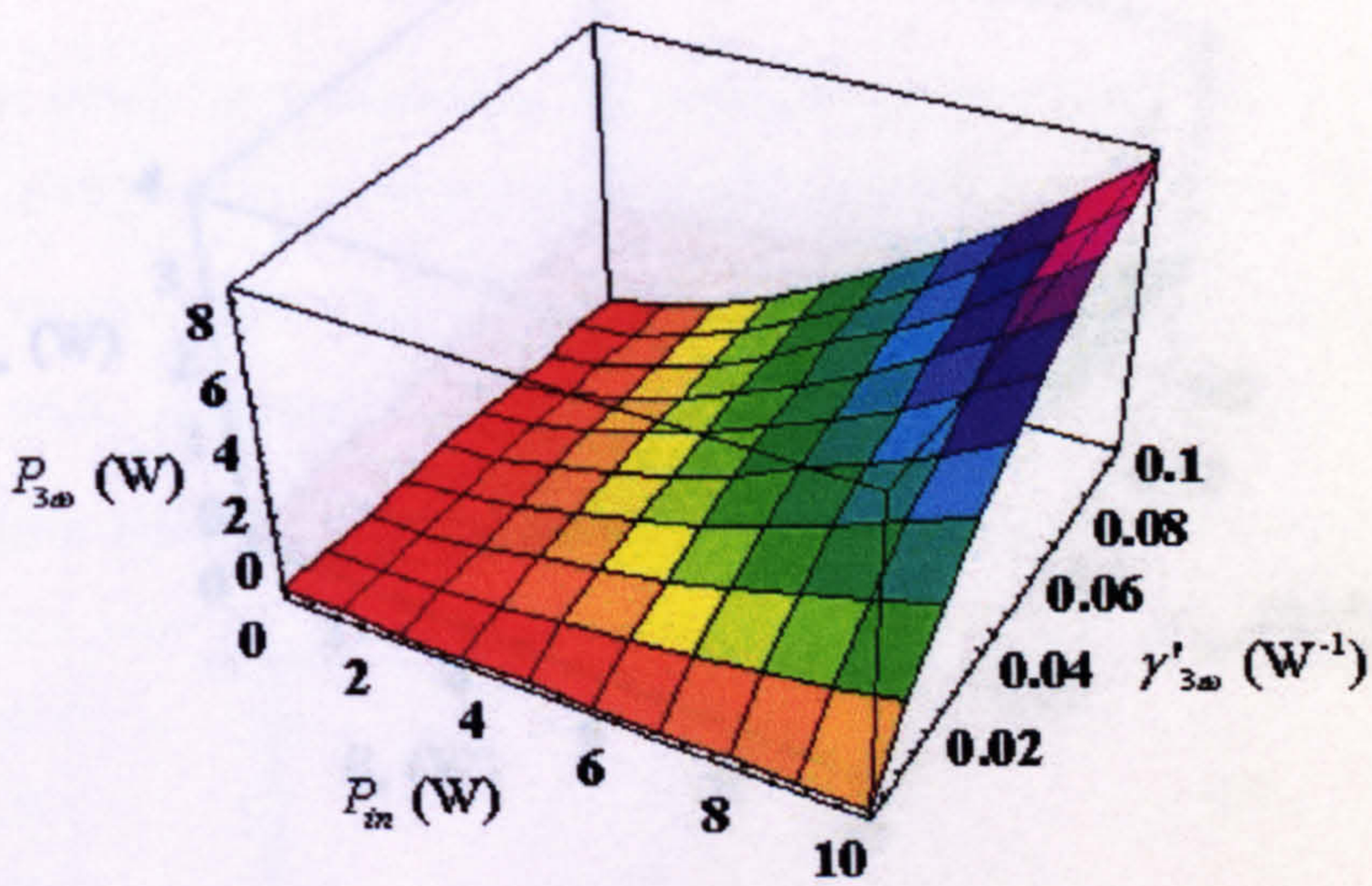

Figure 7. Theoretical prediction of third harmonic power, $P_{3\omega}$ (W), where input power scales from 0 to 10W and the third harmonic conversion efficiency $\gamma'_{3\omega}$ scales from $2x10^{-2}$ to 10^{-1} W^{-1}. As previously, $r = 0.98, t = 0.96$. Second harmonic conversion is fixed as $\gamma'_{2\omega} = 2x10^{-2}$ W^{-1}.

Similarly, the effect of the second harmonic conversion factor $\gamma'_{2\omega}$ on the generated third harmonic average power has been investigated. This is shown in figure 8. The third harmonic conversion factor $\gamma'_{3\omega}$ is fixed as $2x10^{-2}$ W^{-1} and $\gamma'_{2\omega}$ is varied from $2x10^{-2}$ to 10^{-1} W^{-1}. It is apparent that an efficient third harmonic process does not require a high value of $\gamma'_{2\omega}$. Thus the crystal performing the second harmonic

generation may be placed away from an intracavity focus whilst still maintaining a high overall conversion efficiency. This holds true for the singly resonant enhancement cavity. However, should the cavity also be resonant at the second harmonic wavelength, the model no longer holds true since operation is now in the high conversion (>40%) efficiency regime.

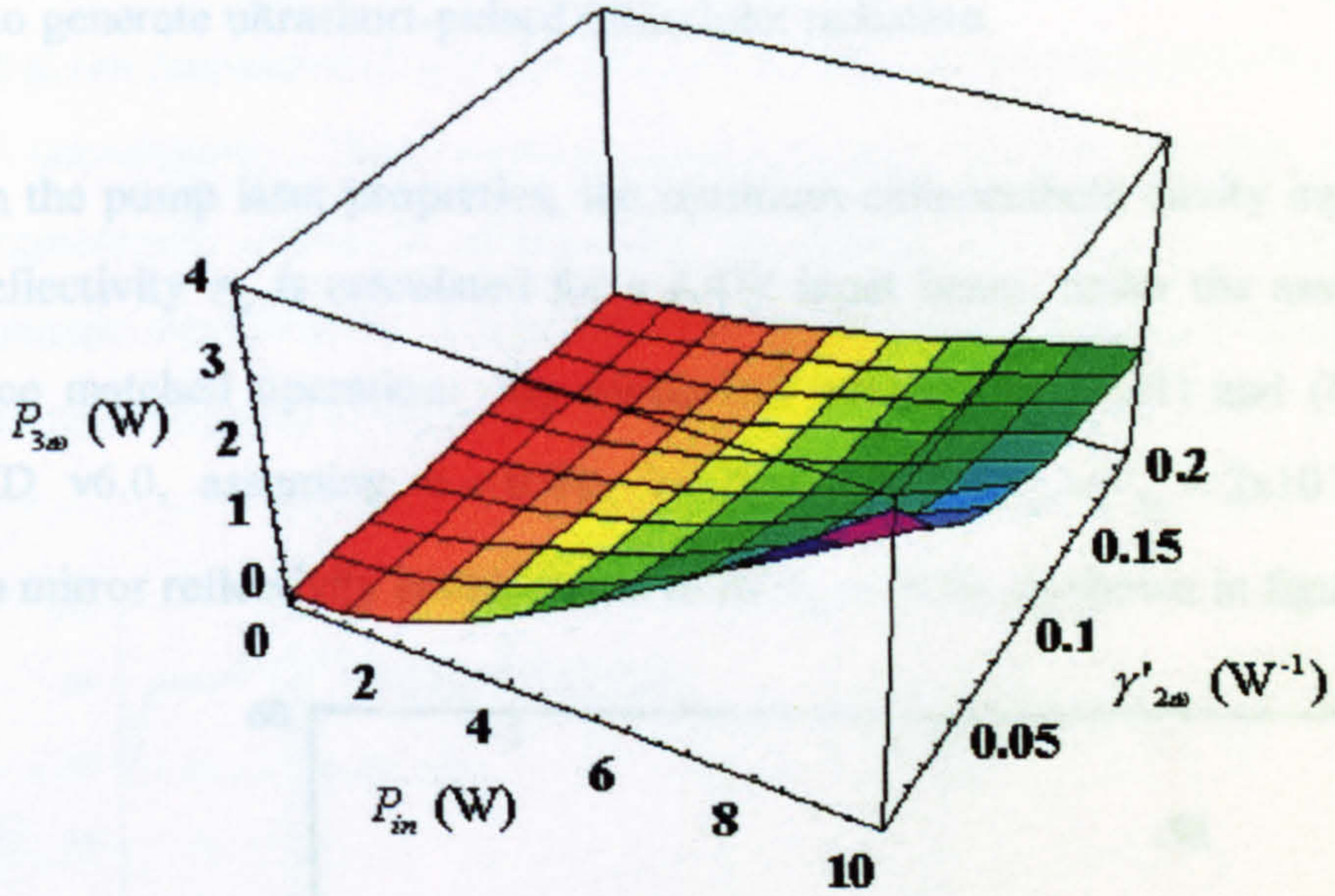

Figure 8. Theoretical prediction of third harmonic power, $P_{3\omega}$ (W), where input power scales from 0 to 10 Watts and the second harmonic conversion efficiency $\gamma'_{2\omega}$ scales from $2\text{x}10^{-2}$ to 0.1W^{-1}. As previously, $r = 0.98, t = 0.96$. Third harmonic conversion is fixed as $\gamma'_{3\omega} = 2\text{x}10^{-2}$ W^{-1}.

A full graphical analysis of the dependency of $\gamma'_{2\omega}$ and $\gamma'_{3\omega}$ is presented in Appendix Four, along with the Mathematica v3.0 code used to generate the plots.

6.8. Experimental realisation of resonant third harmonic generation

Based on the conclusions of the model outlined previously, the corresponding experiment may be performed. To this end, the saturable Bragg reflector mode-locked laser described in Chapter Four is employed as input to the external resonator in order to generate ultrashort-pulsed ultraviolet radiation.

Based on the pump laser properties, the optimum enhancement cavity input coupler mirror reflectivity r_{in} is calculated for a 4.4W input beam, under the assumption of impedance matched operation. By numerical iteration of (6.21) and (6.23) using MathCAD v6.0, assuming $r = 0.98$, $t = 0.96$ and $\gamma'_{2\omega} = \gamma'_{3\omega} = 2\text{x}10^{-2}$ W^{-1}, the optimum mirror reflectivity is calculated to be $r_{in} = 91\%$, as shown in figure 9.

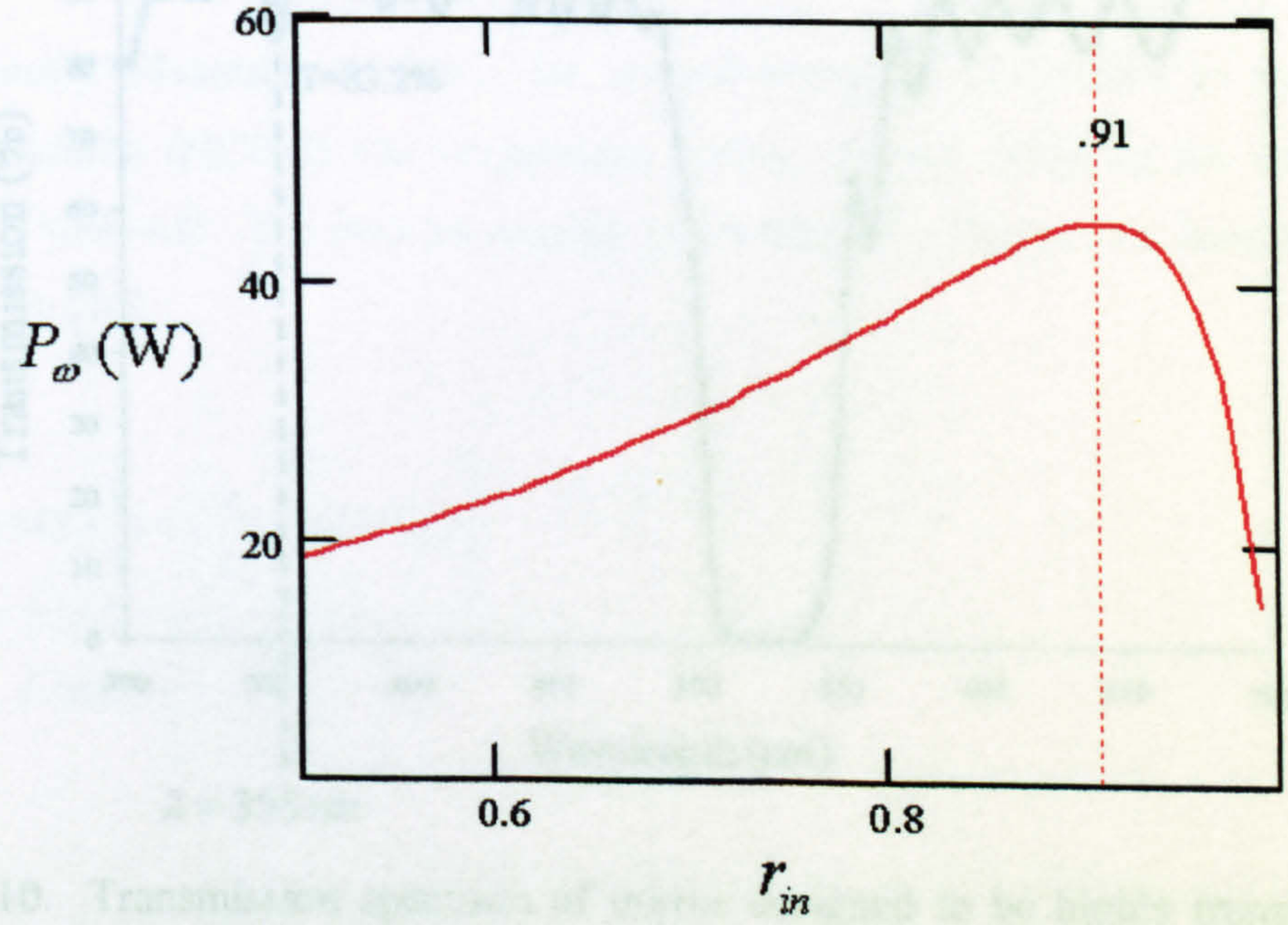

Figure 9. Theoretical prediction of optimum input mirror reflectivity. For 4.4W average fundamental input power, the intracavity power (and therefore enhancement) is a maximum where the input coupler is 91% reflecting at the pump wavelength.

This curve illustrates that choice of a higher reflectivity input coupler mirror results in a lesser degree of impedance matching compared to one of lower reflectivity than optimal. Therefore, an $r_{in} = 90\%$ mirror has been implemented as the input coupler.

The external cavity was formed by two plane mirrors and two zero-lens curved mirrors in a bow-tie configuration, as demonstrated in figure 3. The curved mirrors both had a radius of curvature of 150mm with both mirrors coated highly-reflecting (>98.5%) at the fundamental wavelength and highly transmitting (~83%) at the third harmonic wavelength. These mirrors were specially designed for this experiment, since commercially available mirrors are, by design, also highly reflecting at the third harmonic wavelength. A transmission spectrum of the output coupler for the third harmonic radiation is shown in figure 10.

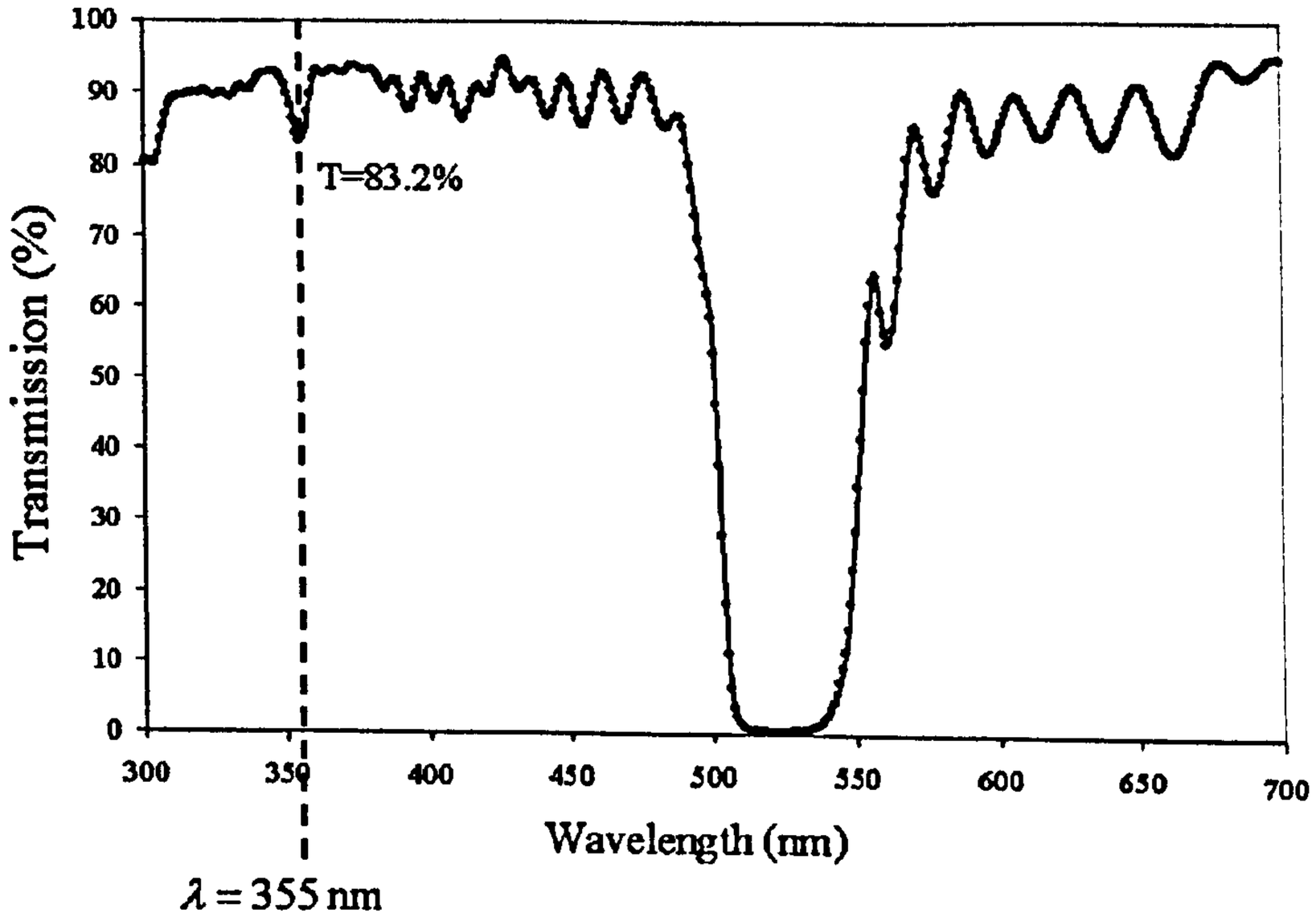

Figure 10. Transmission spectrum of mirror designed to be highly transmitting at λ=355nm (as sourced from LaserOptik, GmbH). It is noted that at the third harmonic wavelength, the mirror has approximately 17% reflectance (~98.5% at $\lambda = 1064\,\text{nm}$). The spectrum was measured using an in-house spectrometer.

The first plane mirror serves as the input coupler and as described previously, has reflectivity $r_{in} = 90\%$ at the fundamental wavelength. The second plane mirror was located on a piezoelectric transducer (not pictured in figure 3) and was highly-refection coated at the fundamental wavelength of $\lambda = 1064\text{nm}$ for near-normal incidence. An applied voltage to the piezoelectric crystal allowed locking of the cavity length via servo-electronics using the Hänsch-Couillaud technique. A full description of this locking method is described in reference 9. After transmission through both the nonlinear materials, the second of the curved mirrors was used as an output coupler for the third harmonic radiation.

The nonlinear crystals were chosen on merit of both nonlinearity and retaining the polarisation of the pump pulse on one round trip. For the first frequency conversion from fundamental to second harmonic (2ω), LiB_3O_5 (LBO) was used in a Type I interaction. The properties of LBO are shown in table 1.

The primary advantage of LBO for second-harmonic generation is non-critical phase-matching (NCPM) via temperature tuning, thereby reducing the detrimental effects of walk-off. The internal angular bandwidth of a Type I ooe interaction $\Delta\theta$ is given by [10]

$$\Delta\theta = \frac{0.443\lambda_1\left[1+\left(\frac{n_o}{n_e}\right)^2\tan^2(\theta)\right]}{L\tan(\theta)\left[1-\left(\frac{n_o}{n_e}\right)^2\right]n_e} \qquad (6.27)$$

where λ_1 is the pump wavelength, n_o and n_e are the ordinary and extraordinary refractive indices and L is the length of the crystal. For second harmonic generation of $\lambda = 1064\,\text{nm}$, $\Delta\theta.L$ is calculated to be 247.88 mrad.cm.

Crystal	LiB_3O_5 (LBO)
Crystal type [11]	Negative biaxial
Point Group	mm2
d tensor components	$d_{16} = d_{21} = -0.67$ $d_{34} = d_{23} = 0.85$ $d_{22} = 0.04$
Transparency range [12]	160-2600nm
Effective nonlinear coefficient, d_{322} [13]	1.16 pm/V
Sellmeier Equations at 20°C, $\lambda(\mu m)$ [14]	$n_x^2 = 1.4426279 + 1.0109932/(\lambda^2 - 0.0112101) - 1.2363218.\lambda^2 + 91\lambda^4$ $n_y^2 = 1.5014015 + 1.0388217/(\lambda^2 - 0.0121571) - 1.7567133.\lambda^2 + 91\lambda^4$ $n_z^2 = 1.4489240 + 1.1365228/(\lambda^2 - 0.0116767) - 1.5830069.\lambda^2 + 91\lambda^4$
Relevant refractive indices [15]	$n_x(1.064\mu m) = 1.564659,$ $n_y(1.064\mu m) = 1.5903993$ $n_z(1.064\mu m) = 1.6054126$ $n_x(0.532\mu m) = 1.5784358,$ $n_y(0.532\mu m) = 1.6066633$ $n_z(0.532\mu m) = 1.6215472$ $n_x(0.355\mu m) = 1.5970652,$ $n_y(0.355\mu m) = 1.6274817$ $n_z(0.355\mu m) = 1.6429572$

Table 1. Optical properties of LBO

Similarly, the temperature bandwidth ΔT of the same interaction may be calculated using [10]

$$\Delta T = \frac{0.443\lambda_1}{L}\left|\frac{\partial n_o}{\partial T} - \frac{\partial n_e}{\partial T}\right|^{-1}. \tag{6.28}$$

For second harmonic generation of $\lambda = 1064$ nm in LBO, the temperature bandwidth $\Delta T.L$ is calculated to be 5.36 K.cm. The spectral acceptance bandwidth of LBO for second harmonic generation may also be calculated using [10]

$$\Delta \upsilon = \frac{0.443}{\lambda_1 L}\left|\frac{\partial n_o}{\partial \lambda_1} - \frac{\partial n_e}{\partial \lambda_2}\right|^{-1}, \tag{6.29}$$

and yields the result $\Delta \upsilon.L = 76.23$ cm^{-1}.cm

These acceptance parameters are suitable for the application described. For third harmonic generation via sum-frequency mixing of fundamental and second harmonic wavelengths, similar equations to that described in (6.27)-(6.29) are employed. However, the expressions used for Type II interactions are more complex than those for Type I, therefore the numerical results specific to sum-frequency mixing of $\lambda_1 = 1064$nm and $\lambda_2 = 532$nm to generate radiation at $\lambda = 355$nm in LBO are presented in Table 2 [10].

Parameter	Numerical value
$\Delta\theta.L$	3.53 mrad.cm
$\Delta T.L$	3.46 K.cm
$\Delta \upsilon.L$	11.85 cm^{-1}.cm

Table 2. Acceptance parameters of LBO crystal for Type II sum-frequency mixing.

Additionally, as shown in the calculations in Appendix Five, this pump pulse duration of $\tau_p = 33$ps requires long (>12mm) interaction lengths with the crystal for maximum harmonic generation. LBO is one-such crystal that is commercially available in 15mm long sections and therefore a plane-plane cut 3x3x15mm crystal was chosen, which is of suitable dimensions for the pump pulse duration. The crystal was temperature controlled using an oxygen-free copper mount to maximise non-critical phase-matching at T=148.2°C [15]. Calculations of this phase-matching temperature are shown in Appendix Five.

In previous experiments where LBO crystals were used to frequency double $\lambda = 1064\text{nm}$, a few crystals fractured. This is attributed to the expansion of LBO with increasing temperature and thus the material was subjected to pressure from the crystal mount. To eliminate this problem, thin (<1mm) pieces of Teflon were placed on the four 3mm x 15mm faces of the LBO crystal and the crystal mounting area increased marginally to account for this increase in effective crystal size. The Teflon served as a cushion between the copper mount and the crystal. By applying this Teflon buffer, no damage to the LBO occurred.

To reduce reflections and therefore minimise loss, both faces of the NCPM LBO crystal were anti-reflection coated at both the fundamental and second harmonic wavelengths.

The second crystal performing the third harmonic (3ω) generation was a 10mm-long Type II LBO angle-tuned crystal, placed at the cavity focus. Calculations of the phase-matching angle and the required crystal length are given in Appendix Five. The crystal faces were anti-reflection coated at the fundamental, second harmonic and third harmonic wavelengths. Since the crystal is critically phase-matched, there is no requirement for temperature controlling and thus the Teflon cushioning, as described for the previous LBO crystal, is not required. The mode waist of the resonating fundamental within the 3ω crystal had a measured radius of 70μm which corresponds to confocal focussing. The separation between the crystals was set at 6mm, the maximum allowed by cavity design and mechanical parameters.

With this configuration, third harmonic efficiency in the region of 30% is possible based on the predictions illustrated in figure 6. This corresponds to approximately 1.3W of average power at $\lambda = 355\text{nm}$ in pulses of picosecond duration with 4.4W average input power.

6.9. Experimental results and discussion

With the resonator electronically locked to generate maximum third harmonic power, cavity output was observed to be consistently stable. Experimentally, 320mW of mode-locked radiation at $\lambda = 355$nm was observed in the configuration outlined above. The generated power, however, was calculated to be 500mW. With a single pass geometry, only 15mW of ultraviolet radiation was achieved. Given the wavelength of operation, it was not viable to measure the pulse duration of the third harmonic emission, but a conservative estimate of the pulse duration is 20ps. This assumed pulse duration leads to a peak power $P_p = 68$W. Although several all-solid-state ultraviolet sources have demonstrated higher output power than those achieved using a resonant enhancement cavity, these lasers are based on significantly higher near-infrared pump powers [16].

The difference between the predictions of the model and the experimental results may be a consequence of cavity losses. The sum-frequency crystal employs critical phase-matching and is therefore placed at an angle. This reduces the overall conversion as a small percentage of both fundamental and second harmonic radiation will be reflected by the crystal faces. Additionally, the output mirror for $\lambda = 355$nm transmits approximately 1% of the fundamental radiation, thus contributing to considerable loss. In addition, the effects of group velocity dispersion have not been taken into account when choosing the nonlinear materials and this may contribute to a reduction in efficiency. It is also noted that the calculated values for $\gamma'_{2\omega}$ and $\gamma'_{3\omega}$ are based on a beam waist within both crystals. The nonlinear crystal performing the second harmonic generation is not placed at an intracavity focus and therefore further adaptation of the model would be necessary to optimise this factor. Furthermore, focussing of the fundamental radiation is not optimised for this resonant process and thus decreases the conversion efficiency factor. Assuming that $\gamma'_{2\omega}$ reduces by a factor of 2 for non-optimal focussing, and the cavity mirror reflectivity decreases to 92%, typical output powers of 800mW are predicted.

With an output power of 320mW measured at $\lambda = 355\text{nm}$, this radiation was used as the pump source for an optical parametric oscillator based on critically phase-matched β-BaB_2O_4 (BBO). However, the pump power was insufficient to reach the oscillation threshold. Calculations predict that the minimum pump power needed to reach threshold would be approximately 0.5W. With further improvements to the resonant frequency tripling method of generating ultraviolet radiation, such as investigation into the effect of group velocity mismatch and the use of different nonlinear materials, it is conceivable that this system would be adequate for pumping of this optical parametric oscillator.

6.10. Conclusion

In conclusion, singly resonant third harmonic generation for both continuous wave and mode-locked cases has been modelled. For input pulses of approximately 33ps duration at 4.4 ns intervals, the model predicts >30% conversion from fundamental to third harmonic which is particularly attractive for fundamental sources of modest average power. Experimentally, 0.5W of mode-locked ultraviolet radiation at $\lambda = 355\,\text{nm}$ was generated. However, the useful output of 320mW was below the oscillation threshold for a β-BBO optical parametric oscillator.

6.11. References

[1] P. Balling and R. Lausten, "On-the-fly depth profiling during ablation with ultrafast laser pulses: a tool for accurate micromachining and laser surgery", Applied Physics Letters, Vol. 79, No. 6, 2001 (pp884-886).

[2] P.J. Campagnola, H.A. Clark and W.A. Mohler *et al.*, "Second-harmonic imaging microscopy of living cells", Journal of Biomedical Optics, Vol. 6, No. 3, 2001 (pp277-286).

[3] S.Wu, G.A. Blake and Z.Y. Sun *et al.*, "Simple, high performance type II beta-BaB_2O_4 optical parametric oscillator", Applied Optics, Vol. 36, No. 24, 1997 (pp5898-5901).

[4] T.J. Zhang, Y. Kato and H. Daido, "Efficient third-harmonic generation of a picosecond laser pulse with time delay", IEEE Journal of Quantum Electronics, Vol. 32, No. 1 1996 (pp127-136).

[5] A. Ashkin, G.D. Boyd and J.M. Dziedzic, "Resonant optical second harmonic generation and mixing", IEEE Journal of Quantum Electronics, Vol. QE-2, 1966 (pp109-123).

[6] M.A. Persaud, J.M. Tolchard and A.I. Ferguson, "Efficient generation of picosecond pulses at 243 nm", IEEE Journal of Quantum Electronics QE-26, 1990 (pp1253-1258).

[7] R.H. Kingston, "Parametric amplification and oscillation at optical frequencies", Proceedings of the IRE, Vol. 50, No. 4, 1962 (p472).

[8] K.L. Sala, G.A. Kenney-Wallace and G.E. Hall, "Cw autocorrelation measurements of picosecond laser pulses", IEEE Journal of Quantum Electronics, Vol. QE-16, No. 9, 1980 (pp990-996).

[9] T.W. Hänsch and B. Couillaud, "Laser frequency stabilization by polarization spectroscopy of a reflecting reference cavity", Optics Communications, Vol. 35, No. 3, 1980 (pp441-444).

[10] V.G. Dmitriev, G.G. Gurzadyan and D.N. Nikogosyan, "Handbook of Nonlinear Optical Crystals (2nd Edition)", Springer-Verlag, (ISBN 0-387-52026-0) 1990.

[11] V.G. Dmitriev and D.N. Nikogosyan, "Effective nonlinearity coefficients for 3-wave interactions in biaxial crystals of mm2 point group symmetry", Optics Communications, Vol. 35, No. 1-3, 1993 (pp173-182).

[12] S.J. Lin, B.C. Wu and F.L. Wie *et al.*, "Phase matching retracing behaviour for 2nd harmonic-generation in LiB_3O_5 crystal", Journal of Applied Physics, Vol. 73, No. 3, 1993 (pp1029-1034).

[13] S.P. Velsko, M. Webb and L. Davis *et al.*, "Phase-matched harmonic-generation in lithium triborate (LBO)", IEEE Journal of Quantum Electronics, Vol. 27, No.9, 1991 (pp2182-2192).

[14] S.J. Lin, B.C. Wu and F.L. Wie *et al.*, "Phase-matching retracing behaviour – new features in LiB_3O_5", Applied Physics Letters, Vol. 59, No. 13, 1991 (pp1541-1543).

[15] G. Ghosh, "Temperature dispersion of refractive indices in β-BaB_2O_4 and LiB_3O_5 crystals for nonlinear optical devices", Journal of Applied Physics 78, 1995 (pp6752-6760) – see Appendix Five.

[16] J.C. Garcia, A.K. Newman and J.M. Liu *et al.*, "Cw mode-locked deep UV pulses at an average power of 1.8W", Journal of Optics A, Vol. 2, 2000 (ppL41-L43).

Chapter Seven

Synchronously Pumped Periodically Poled Lithium Niobate Optical Parametric Oscillator

7.1. Introduction

As described in the preceding two chapters, the use of nonlinear materials in conjunction with mode-locked lasers has enabled the generation of pulsed radiation at wavelengths not easily achieved by conventional sources. This has been of particular consequence in the development of widely tunable coherent sources by the use of optical parametric oscillators (OPOs), which have applications in spectroscopy [1] and remote sensing [2].

The all-solid-state nature of these devices are an attractive alternative to gas or dye lasers, and offer greater mechanical stability, as well as exhibiting significantly broader tuning ranges at high average powers.

This chapter contains a review of optical parametric oscillators and the basic principles of operation. This is followed by a description of quasi-phase-matching, with emphasis on periodically poled lithium niobate (PPLN). An optical parametric oscillator based on this material is synchronously pumped by the SBR mode-locked laser described in Chapter Four and experimental results are presented.

7.1.1. Historical review of synchronously pumped optical parametric oscillators (OPOs)

The first demonstration of a tunable optical parametric oscillator was presented by Giordmaine and Miller in 1965, based on a $LiNbO_3$ crystal pumped by a frequency doubled and pulsed Nd^{3+}:$CaWO_4$ laser source [3]. This was followed shortly thereafter by a demonstration of an optical parametric oscillator based on KDP [4]. In 1968, the first continuous wave optical parametric oscillator was demonstrated by Smith *et al.*, using $Ba_2NaNb_5O_{15}$ [5]. The development of the first continuous wave visible optical parametric oscillator in 1968 by Byer *et al.* was also of great significance, due to the low threshold observed [6]. However, the key to obtaining high conversion efficiencies is in the peak power of the system and therefore ultrashort-pulsed lasers are frequently employed to synchronously pump optical parametric oscillators.

The first synchronously pumped optical parametric oscillator was a $KTiOPO_4$ (KTP) system, developed in 1972 by Burneika *et al.* [7]. This method of matching the optical path length of the laser to that of the optical parametric oscillator increased the conversion efficiency significantly. This has since been adopted as the conventional means for ultrashort pulsed optical parametric oscillators, as first demonstrated by Laubereau *et al.* in 1974 [8].

The conception of two new materials, BaB_2O_4 (BBO) and LiB_3O_5 (LBO) [9, 10] revolutionised optical parametric oscillators, allowing the construction of optical parametric oscillators pumped by ultraviolet radiation that have been shown to generate radiation that is tunable from $\lambda = 300$nm to 4800nm [11, 12]. Improvements in pump lasers have also enabled operation at multi-watt average power levels [13, 14].

7.2. Optical Parametric Oscillation

The generic optical parametric oscillator consists of a nonlinear crystal placed within an optical resonator, as shown in figure 1.

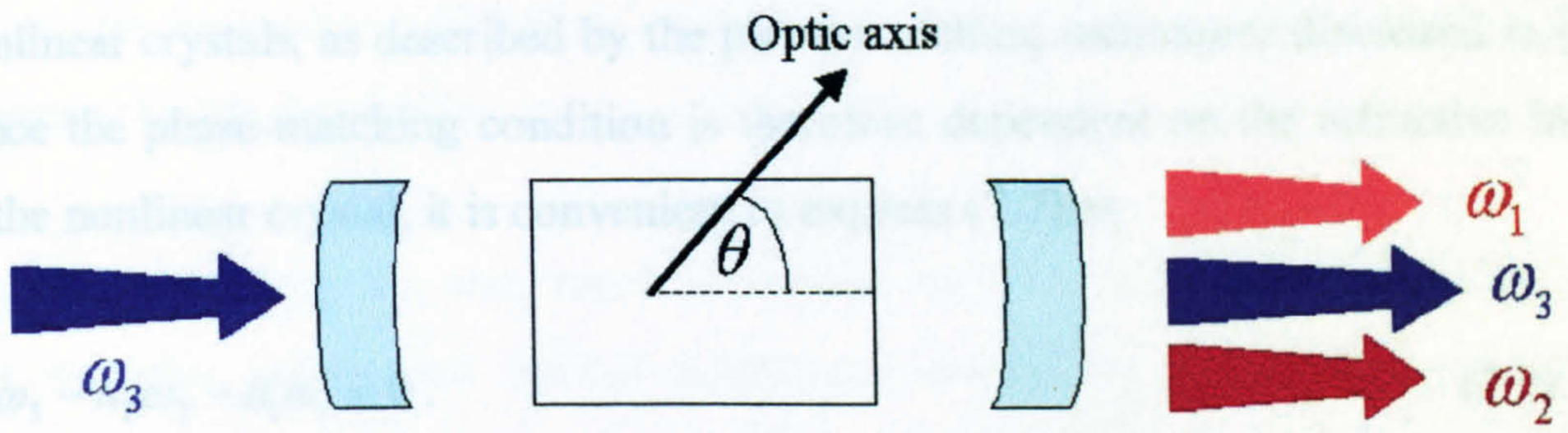

Figure 1. Schematic representation of optical parametric oscillator pumped at a frequency ω_3, where θ is the internal angle of the crystal.

An intense optical field of frequency ω_3, known as the pump frequency, is applied to the nonlinear crystal. The birefringent nature of the crystal gives rise to the creation of two new optical fields, namely the signal and idler frequencies, such that

$$\omega_3 = \omega_1 + \omega_2, \tag{7.1}$$

where ω_1 is the signal frequency and ω_2 is the idler frequency ($\omega_1 > \omega_2$). As a consequence of the principle of energy conservation, the total photon energy is conserved during the process.

The signal and idler frequencies generated through application of the pump frequency is dependent on the properties of the nonlinear medium. In theory, however, there exist an infinite number of signal and idler frequencies that can satisfy equation (7.1). However, phase-matching (as discussed in Chapter Five) once again limits the frequencies that may be generated in practice. For an optical parametric oscillator, the phase-matching condition is

$$\Delta k = k_3 - k_2 - k_1 . \tag{7.2}$$

This holds true for conventionally phase-matched materials. In practice, this is achieved by using the anisotropic nature of the crystal to compensate for dispersion. This is largely accomplished by either angular or temperature controlling of the nonlinear crystals, as described by the phase-matching techniques discussed in § 5.5. Since the phase-matching condition is therefore dependent on the refractive indices in the nonlinear crystal, it is convenient to express (7.2) as

$$n_3\omega_3 - n_2\omega_2 - n_1\omega_1 = 0 . \tag{7.3}$$

The resulting fields from the parametric process arise from noise. These fields grow over a gain interaction length L, and the effective gain coefficient Γ for either signal or idler beams is given by

$$\Gamma^2 = \frac{2\omega_2\omega_1 \left| d_{eff} \right|^2}{\varepsilon_0 n_3 n_2 n_1 c^3} \frac{P_p}{A_{eff}}, \tag{7.4}$$

where d_{eff} is the effective nonlinear coefficient, as described in § 5.4, P_p is the peak power of the pump radiation and A_{eff} is the effective area of the pump mode in the nonlinear crystal. The oscillation threshold condition is

$$(1-\alpha)\cosh(\Gamma L) = 1, \tag{7.5}$$

where α is the round-trip amplitude loss for the resonated field. Since the gain exhibited is typically very low, even with high peak powers, an oscillator is typically required to enhance the generated fields.

By use of the optical cavity surrounding the nonlinear crystal, it is possible to resonate one or more of these fields. The simplest OPO is the singly resonant type. This means that only one of the pump, signal or idler frequencies is resonated in the

cavity. When two of the above frequencies is resonated, the device is doubly resonant and with three fields resonant, the system is triply resonant. Doubly and triply resonant devices are attractive because they offer low thresholds of operation. However, such systems also exhibit spectral and amplitude instability. These effects are particularly evident in the case of the ultrashort pulsed OPOs, especially when the source is tunable. Therefore, a singly resonant OPO is demonstrated here, at expense of high thresholds.

The resonator design is very much dependent on the nature of the pump radiation. For example, picosecond optical parametric oscillators operate by synchronous pumping. This problem was first addressed by Piskarsis *et al.* in synchronously pumping a $Ba_2NaNb_5O_{15}$ crystal with output from a mode-locked Nd^{3+}:YAG laser [15]. The need for synchronism between the OPO and the laser resonator arises because the short time which the nonlinear crystal is irradiated by the pump laser is insufficient to sustain oscillation of the signal and idler frequencies. This means that the optical path length of the optical parametric oscillator must be matched to that of the picosecond pump laser in order for the fields to resonate.

Another basic requirement of the resonator is also to ensure good overlap between the pump and resonated mode. This is achieved by using curved mirrors in the resonator to focus the resonated field within the nonlinear material. The approach taken by Boyd and Kleinman in § 5.5 holds for harmonic generation, but the calculation has been extended by Guha *et al.* [16, 17] to consider the effect of focussing on the efficiency of a singly resonant optical parametric oscillator given arbitrary beam waists.

The coupled wave equations (5.4), (5.5) and (5.6) described in Chapter Five can be used to analyse parametric amplification and gain in a nonlinear material. The solution is non-trivial and therefore is not presented. For a small gain, however, Harris developed an analogous expression to (7.4) for the parametric amplification of the signal and idler frequencies [18]

$$G(\omega_1,\omega_2)=\frac{\omega_1\omega_2\mu(\chi^{(2)})^2\ell^2}{2n_1n_2n_3c}I_0(\omega_3)\left[\frac{\sin^2\left(\frac{\Delta k\ell}{2}\right)}{\left(\frac{\Delta k\ell}{2}\right)^2}\right], \tag{7.6}$$

where $G(\omega_1,\omega_2)$ is the single-pass gain after propagation through a material of length ℓ, under irradiance with a fundamental intensity I_0. Given the sinc^2 nature of equation (7.6), it is apparent that the single-pass gain is at a maximum for $\Delta k\ell = 0$, and is zero for $\Delta k\ell = 2\pi$.

The crystals used in optical parametric oscillators are anisotropic media, and therefore follow the characteristics outlined in Chapter Five.

7.3. Quasi-phase-matching (QPM)

One current trend in nonlinear crystalline materials is towards quasi-phase-matching (QPM) in periodically poled materials. This simple method conceived simultaneously by Bloembergen [19] and Franken [20] permits use of the highest d component via phase-matching in any direction, and permits phase-matching in isotropic media or that which has inadequate birefringence for conventional phase-matching.

QPM provides an alternative to birefringent phase-matching, which places a severe requirement of a zero phase mismatch ($\Delta k=0$). In QPM, $\Delta k\neq 0$ is permitted, but after one coherence length, the mismatch is reset to zero. This is performed by reversing the sign of the nonlinear coefficient, which has the effect of adding π to the relative phase shift of the interacting waves. This is illustrated in figure 2. The rate of growth of the converted frequency is also shown in figure 2 for both conventional phase-matching and QPM.

In a QPM OPO, the phase-matching condition is

$$\Delta k_{QPM} = k_p - k_s - k_i - 2\pi/\Lambda, \tag{7.7}$$

where $2\pi/\Lambda$ is the phase mismatch.

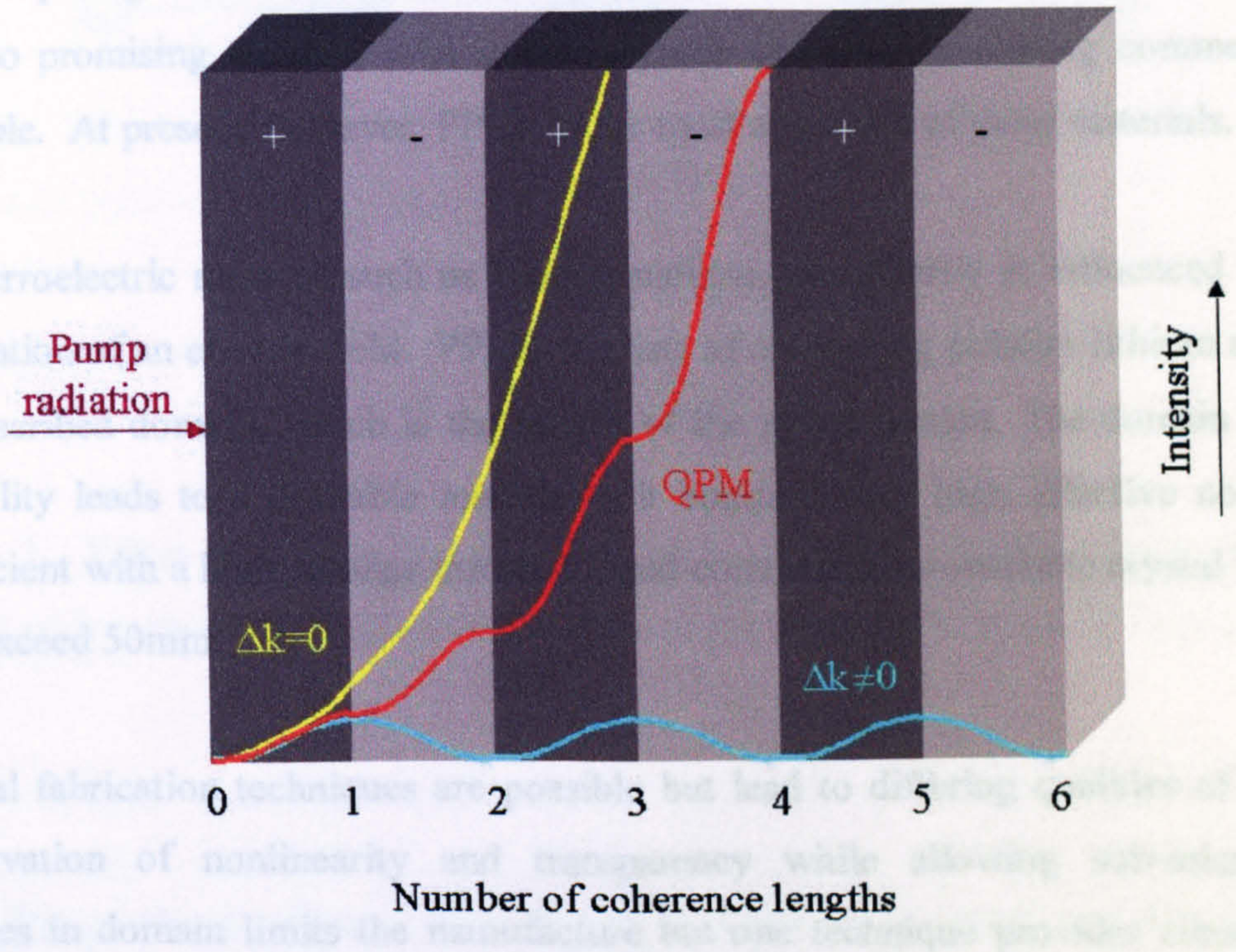

Figure 2. The effect of reversal of the nonlinear coefficient in a periodically poled structure. It is also noted that it is possible to design a single crystal with a number of different domain period lengths, or an aperiodic structure.

Λ is referred to as the period, which is twice the coherence length of the material. This is determined at the point of manufacture. As a whole, however, the phase-matching property is temperature dependent, hence scanning the temperature over the transparency range will generate a range of signal and idler wavelengths with a fixed pump wavelength.

7.3.1. Fabrication of QPM devices

First developed by Fejer in the Byer group at Stanford [21, 22], periodic poling of a nonlinear crystal allows quasi-phase-matching to occur. Although developed for periodic poling of lithium niobate (PPLN), however PPRTA [23] and PPKTP [24] are also promising devices, with longer crystals (>30mm) becoming commercially available. At present, however, PPLN is the most advanced of these materials.

In a ferroelectric material such as lithium niobate, the polarity is influenced by the application of an electric field. PPLN consists of alternating polarity lithium niobate of prescribed domain, which is the length of the poled section. The domain period flexibility leads to a desirable material – it boasts a very high effective nonlinear coefficient with a high damage threshold, and commercially-available crystal lengths now exceed 50mm.

Several fabrication techniques are possible but lead to differing qualities of PPLN. Preservation of nonlinearity and transparency while allowing sub-micrometre changes in domain limits the manufacture but one technique provides consistently good results – application of electric field directly to the crystal regions with an insulator obstructing domain growth between the grating lines.

A qualitative description of ferroelectricity is shown in figure 3. In the case of lithium niobate ($LiNbO_3$), the lithium and niobium ions will shift relative to the oxygen layers subject to a critical electric field, thus changing the polarity of the crystal. For field exposure times below 50ms, the poling effects are temporary and the lithium ions return to their original position. Above 50ms, and the domain reversal is permanent [25]. The domain length can be controlled to sub-micrometre accuracy for infrared applications, where the domain period is >10μm. Shorter period structures do exist [26], but are currently scarce.

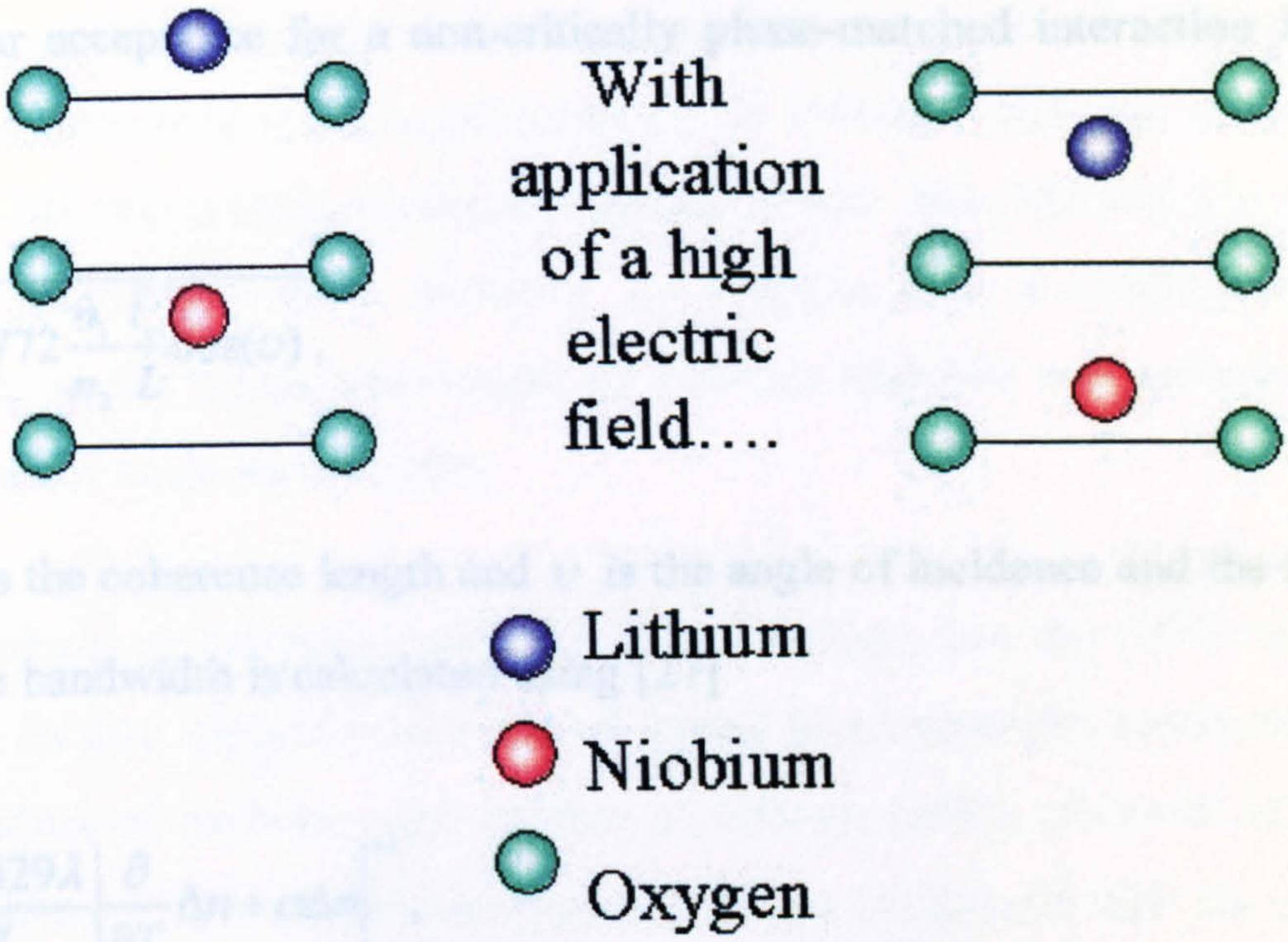

Figure 3. Effect of electric field on $LiNbO_3$. The lithium and niobium ions are shifted with respect to the position of the oxygen ions when exposed to an electric field.

7.4. Properties of periodically poled lithium niobate (PPLN)

The calculation of the acceptance parameters for PPLN differ for those of conventional bulk nonlinear media as described in Chapters Five and Six. For example, the spectral bandwidth of periodically poled materials is given by [27]

$$\delta\lambda = \frac{0.4429\lambda}{L}\left|\frac{n_2 - n_1}{\lambda} + \frac{\partial}{\partial\lambda}n_1 - \frac{1}{2}\frac{\partial}{\partial\lambda}n_2\right|^{-1}, \tag{7.8}$$

where the derivatives are evaluated at the respective wavelengths. For the case of PPLN, the refractive indices may be calculated using the Sellmeier equations and fit for bulk $LiNbO_3$.

The angular acceptance for a non-critically phase-matched interaction is given by [27]

$$\delta\upsilon = 2\sqrt{1.772\frac{n_1}{n_2}\frac{l_c}{L}\cos(\upsilon)}, \tag{7.9}$$

where l_c is the coherence length and υ is the angle of incidence and the temperature acceptance bandwidth is calculated using [27]

$$\Delta T = \frac{0.4429\lambda}{L}\left|\frac{\partial}{\partial T}\Delta n + \alpha\Delta n\right|^{-1}, \tag{7.10}$$

where α is the coefficient of linear thermal expansion (K^{-1}) and Δn is the crystal birefringence.

The acceptance parameters for QPM devices tend to be larger than those for conventionally phase-matched devices, since QPM permits the use of the same polarisation for the input and generated frequencies. This gives rise to flexible and useful systems. These acceptance parameters are calculated in Appendix Five along with the wavelength dependent refractive indices and oscillation threshold for an optical parametric oscillator based on 50mm long periodically poled lithium niobate.

7.5. PPLN OPO synchronously pumped by SBR mode-locked Nd^{3+}:YVO_4 laser

The laser used to synchronously pump with OPO is the SBR mode-locked Nd^{3+}:YVO_4 laser described in Chapter Four. The pump system delivered pulses of 33ps measured duration at a repetition rate of 235MHz in 4.4W average power at $\lambda = 1064\,\text{nm}$. This corresponds to a peak power of 567 W.

As is evident in figure 4, a bow-tie cavity geometry was utilised. M1 and M2 were zero-lens mirrors with a radius of curvature of 100mm. M3 was a plane wedged mirror and M4 was a wedged output coupling mirror. M1, M2 and M3 were coated as highly reflecting mirrors between $\lambda = 1460$nm and $\lambda = 1600$nm and highly transmitting at the pump wavelength of 1064nm and M4 was coated to be 98% reflecting at the same wavelengths.

Mode-matching of the pump radiation from the laser into the OPO resonator was performed by two anti-reflection coated lenses in a telescopic arrangement, one of 500mm radius of curvature and another of 100mm radius of curvature. The mode waist inside the PPLN crystal was typically 52μm, positioned near the centre of the crystal. Both were placed on translation stages to optimise the mode-size. In order to correct for deviations in polarisation, an anti-reflection coated half-wave plate was used to optimise the input polarisation to the OPO resonator.

Feedback from the OPO to the laser resonator led to fluctuations in the mode-locking stability. To minimise this problem, a Faraday isolator was employed. However, this element was not anti-reflection coated at the pump wavelength and so the power was reduced from 4.4W to 3.2W on propagation through the isolator. This corresponds to a peak power of 320W.

The 50-mm long PPLN crystal had eight different gratings with domain periods between 28.5 and 29.9 μm in 0.2μm steps. A theoretical calculation of the domain periods with incident pump radiation at $\lambda = 1064$nm is shown in figure 5. The PPLN crystal length was chosen due to the comparatively long pump pulses and commercial availability. Both faces of the crystal were anti-reflection coated at the pump wavelength of $\lambda = 1064$nm and the expected signal wavelengths of $\lambda = 1460$-1600nm.

The crystal was held in an insulated oxygen-free copper mount to allow temperature controlling up to 250°C, with an accuracy of 0.1°C.

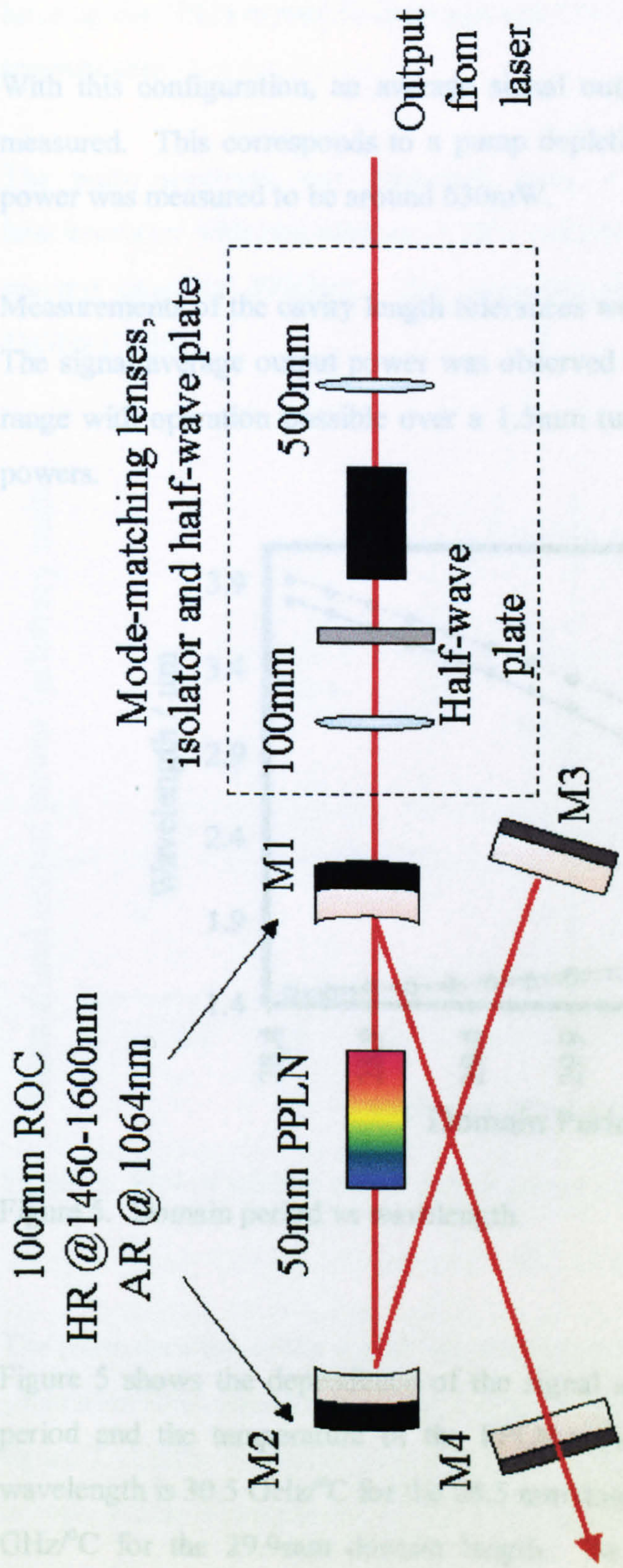

Figure 4. Schematic representation of synchronously pumped PPLN OPO.

7.6. Optical parametric oscillator results

With this configuration, an average signal output power of 0.99W was routinely measured. This corresponds to a pump depletion of 78%. The threshold average power was measured to be around 630mW.

Measurements of the cavity length tolerances were taken. This is shown in figure 6. The signal average output power was observed to be stable over a 0.5mm detuning range with operation possible over a 1.5mm tuning range, albeit at reduced output powers.

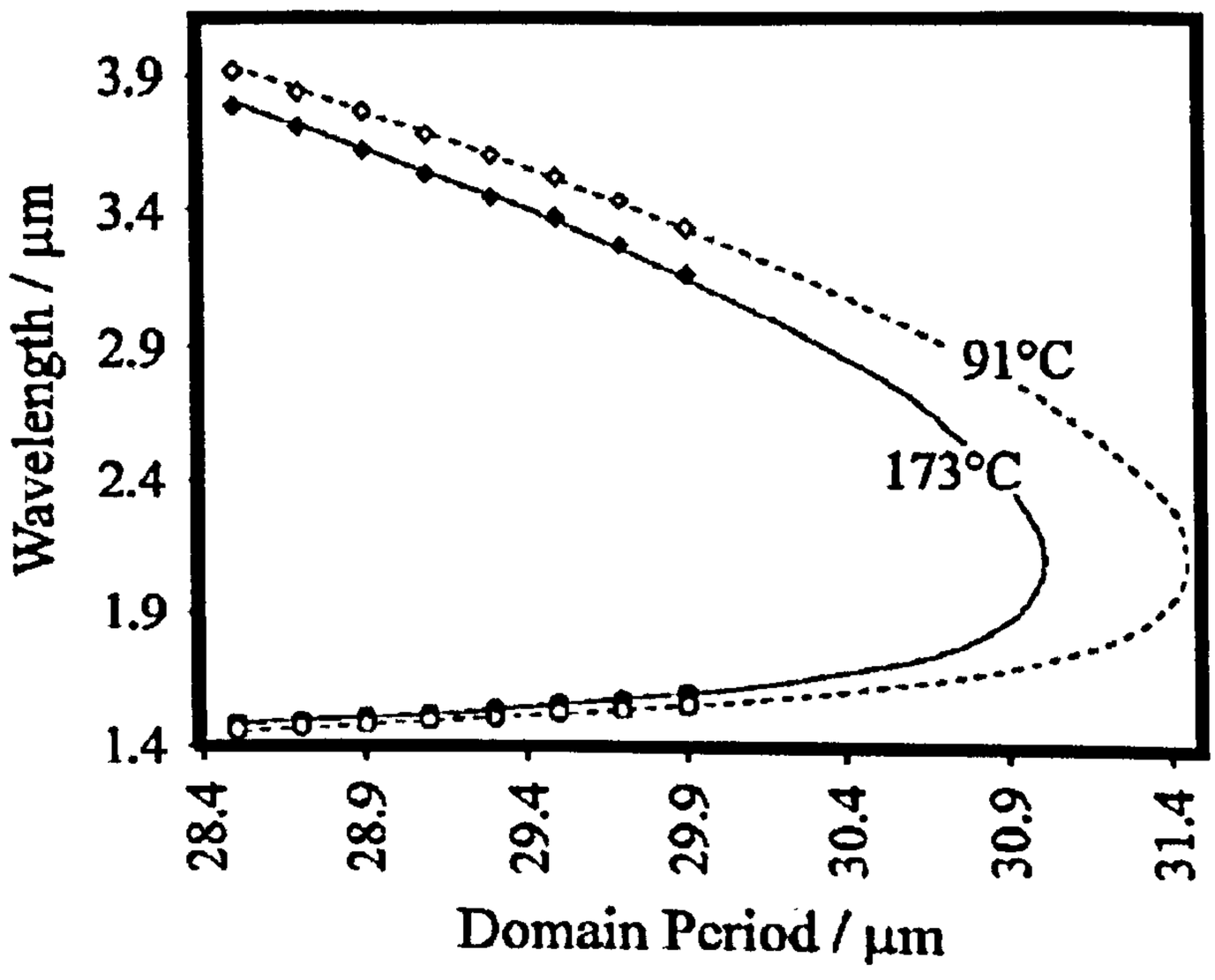

Figure 5. Domain period vs wavelength.

Figure 5 shows the dependence of the signal and idler wavelength on the domain period and the temperature of the PPLN crystal. The tuning rate of the signal wavelength is 30.5 GHz/°C for the 28.5 mm domain period length, increasing to 60.7 GHz/°C for the 29.9mm domain length. As shown in Figure 5., scanning the temperature of the crystal from 91°C to 173°C corresponded to a wavelength range of 1461nm to 1601nm. This wavelength range may be limited by the OPO mirror

reflectivity and could be improved by both using broader-band reflecting mirrors and housing the PPLN crystal in an oxygen-rich environment to permit heating to higher temperatures.

The pulse spectrum was measured using a home-made scanning Fabry-Perot interferometer with two mirrors of 98% reflectivity at $\lambda = 1460\text{-}1600$nm with a free spectral range of 300GHz. The measured spectral bandwidth was found to be 15GHz FWHM.

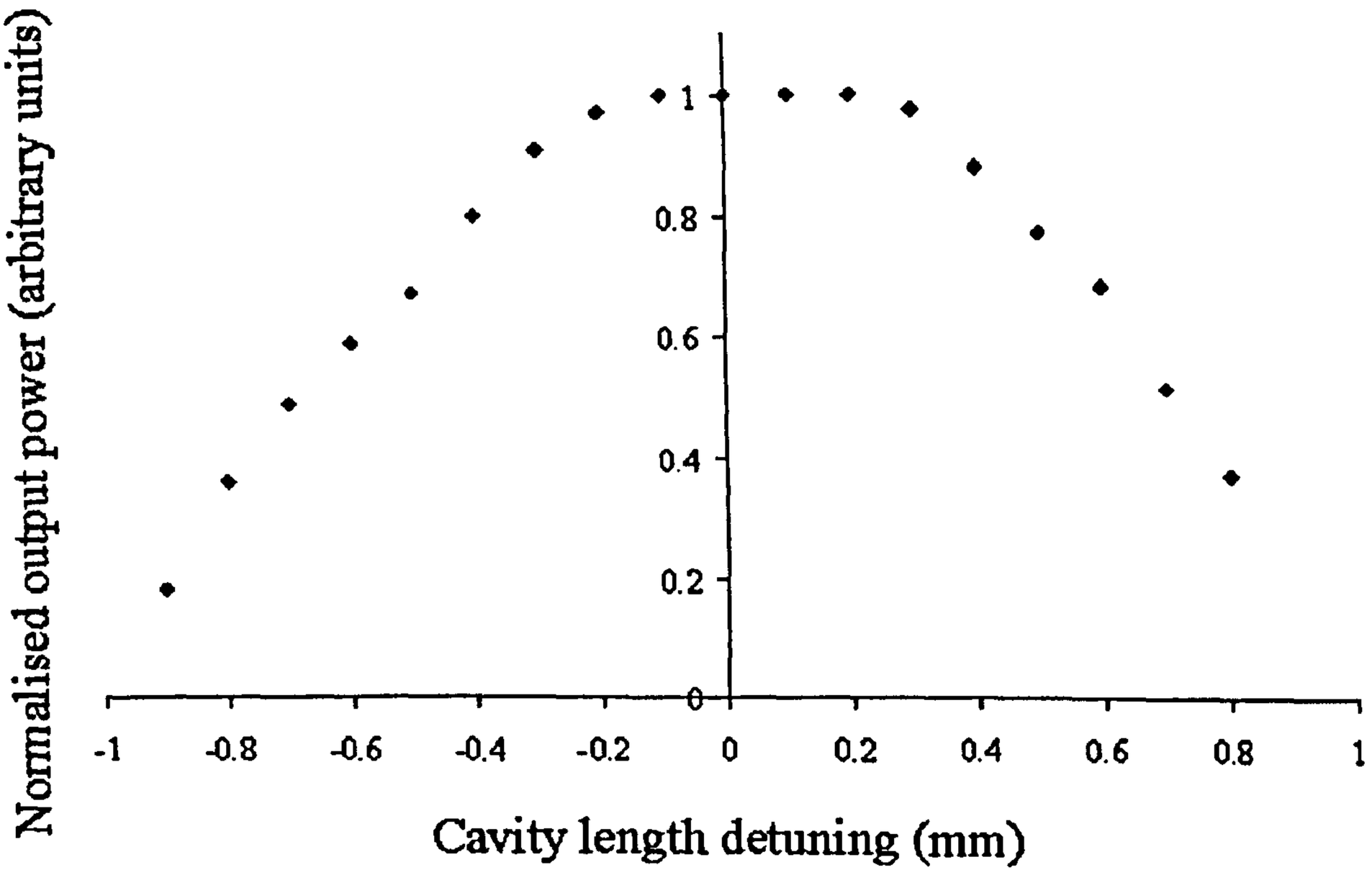

Figure 6. Plot of relative signal output power with cavity length detuning.

The pulse duration of the signal was measured using a noncollinear second-harmonic generation autocorrelator based on $LiIO_3$. A typical autocorrelation trace is shown in figure 7. Under the assumption of a $sech^2$ pulse-shape, the measured pulse duration is 34ps, which is comparable to that of the pump pulse duration.

Assuming mirrors with perfect 98% reflectance, the finesse of the scanning Fabry-Perot interferometer would be 155, leading to a resolution of approximately 2GHz.

In practice, however, these mirrors are not ideal and therefore the finesse is not so large as that predicted. This means that the bandwidth of the signal output is likely to be smaller than that measured.

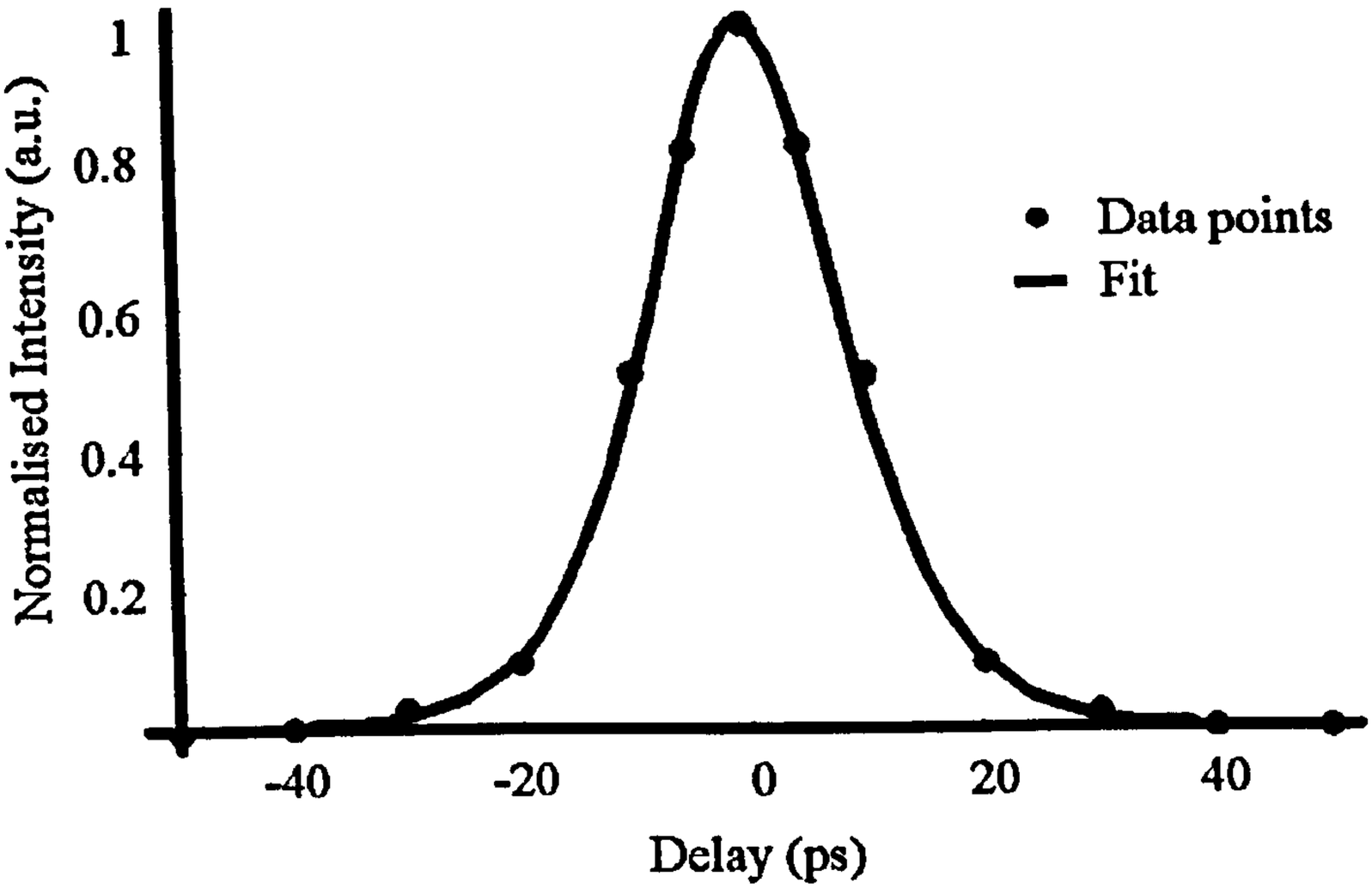

Figure 7. Second harmonic autocorrelation of signal pulse from synchronously pumped periodically poled lithium niobate optical parametric oscillator.

7.7. Tunable visible radiation for multi-photon microscopy

Multi-photon microscopy exploits nonlinear optical effects to image the cross-section of a sample. In two-photon microscopy, for example, the sample is treated with a fluorescent dye called a fluorophore. The sample is then irradiated by a source that has an emission wavelength around twice the peak absorption wavelength of the fluorophore.

When a high peak power, ultrashort-pulsed laser is applied to the sample, two-photon absorption can occur if the intensity of the laser beam is sufficiently high. Under this condition, two photons can be absorbed by the fluorophore simultaneously. The main advantage of two-photon imaging over the single-photon approach is that the

fluorophore will only be excited at a focal point, therefore very precise measurements can be made [28].

One wavelength region of interest is $\lambda = 600$ to 700nm. Conventional gain media do not emit at such wavelengths, therefore a nonlinear optical approach can be adopted. Given that the signal wavelength of the optical parametric oscillator was observed to be tunable over $\lambda = 1460$ to 1601nm when pumped with radiation at $\lambda = 1064$nm, a sum-frequency mixing operation on these wavelengths would generate emission that is tunable from $\lambda = 615$ to 640nm. This was investigated using a nonlinear $KTiOAsO_4$ (KTA) crystal. KTA was chosen due to the high effective nonlinear coefficient, with further evidence of the benefits of KTA for efficient sum-frequency mixing of similar wavelengths demonstrated by Ruffing *et al.* [29]. The optical properties of KTA are described in table 1.

KTA	$KTiOAsO_4$
Transparency range (nm)	350 - 5500
Point group	mm2
Density ($g.cm^3$)	3.45
Refractive indices (at 1064nm)	n_x=1.782, n_y=1.790, n_z=1.863
Refractive indices (at 632.8nm)	n_x=1.805, n_y=1.814, n_z=1.911
Nonlinear coefficient (pm/V)	3.3

Table 1. Optical properties of KTA [30]

The 10mm long KTA crystal was obtained from Cristal Laser with a $3x3mm^2$ aperture. The end faces were anti-reflection coated by the supplier at the pump wavelength $\lambda = 1064$nm, central signal wavelength $\lambda = 1530$nm and the central sum-frequency output wavelength of $\lambda = 629$nm. The crystal was intended for Type I critical phase-matching via angular rotation, therefore the crystal was cut as $\theta = 90^\circ$ and $\varphi = 32.6^\circ$.

The pump sources used as a basis for sum-frequency mixing were the SBR mode-locked laser described in Chapter Four, and the periodically poled lithium niobate optical parametric oscillator described in §7.5 and §7.6. Approximately 300mW of fundamental average power was redirected and used as input to the KTA crystal, with the remainder of the 4.1W of average power delivered by the laser pumping the PPLN OPO as described previously. This meant a reduction in signal wavelength average power to 800mW. The signal wavelength was directed towards the KTA crystal using aluminium-coated mirrors that resulted in a 200mW loss of power. Therefore, after beam-steering optics, only 600mW of signal wavelength radiation was available to the KTA crystal. Further loss was incurred in recombining the beams, since a mirror highly reflecting at the pump wavelength and 90% transmitting at the signal wavelength was used. A single lens anti-reflection coated at $\lambda = 1064$nm of focal length f=+50mm was used to focus both beams within the KTA crystal in a single pass. This is shown schematically in figure 8.

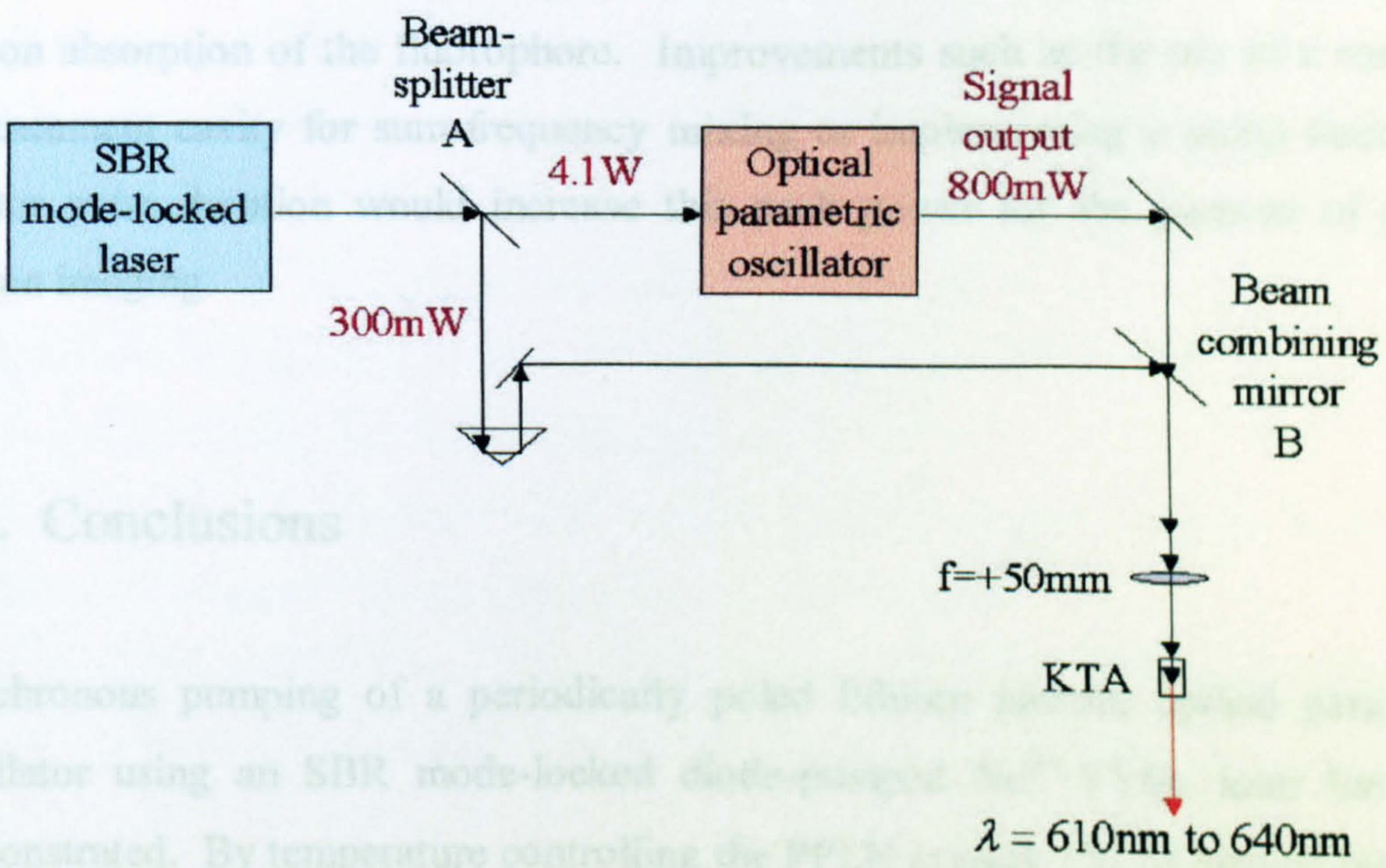

Figure 8. Illustration of sum-frequency mixing experiment configuration. The pump and signal pulses overlap at the beam combining mirror B. Not pictured is the mount for the KTA crystal, which incorporates an angular rotation stage.

The signal wavelength average power was measured after the lens to be 400mW, whereas the pump wavelength average power was measured as 220mW. The optical path lengths of the signal and pump wavelength radiation were matched to ensure overlap of the pulses in the KTA crystal. This involved a trombone arrangement for the pump radiation that used a rooftop prism on a translation stage. This length was adjusted to find the matching point of the optical path lengths.

7.8. Sum-frequency mixing results

Tunable visible radiation was generated using sum-frequency mixing between $\lambda = 615$nm and 640nm, at an average output power of 20mW in a TEM_{00} mode. Although the pulse duration was not measured, a conservative pulse duration estimate is 25ps. Given these properties, the peak power of the radiation is calculated to be 4.3W. Unfortunately, this peak power is insufficient to invoke two-photon absorption of the fluorophore. Improvements such as the use of a resonant enhancement cavity for sum-frequency mixing or implementing a pump laser with shorter pulse duration would increase this peak power for the purpose of multi-photon imaging.

7.9. Conclusions

Synchronous pumping of a periodically poled lithium niobate optical parametric oscillator using an SBR mode-locked diode-pumped $Nd^{3+}:YVO_4$ laser has been demonstrated. By temperature controlling the PPLN crystal, 1W of tunable radiation between 1461nm and 1601nm was achieved at a repetition rate of 235MHz. The pulse duration at the signal wavelength was measured to be 34ps, comparable to that of the pump laser. Using a scanning Fabry-Perot interferometer, a spectral bandwidth of 15GHz was measured. The OPO resonator was demonstrated to allow a detuning tolerance of 0.5mm.

Sum-frequency mixing of the pump and signal wavelengths was also demonstrated in nonlinear KTA. Tunable visible radiation was generated using sum-frequency mixing between wavelengths of $\lambda = 615$nm and 640nm, at an average output power of 20mW in a TEM_{00} mode. Although appropriate wavelength coverage for multi-photon imaging was achieved, the peak power of 4.3W was determined to be insufficient for two-photon processes.

7.10. References

[1] T. Petelski, R.S. Conroy and K. Bencheikh *et al.*, "All-solid-state, tunable, single-frequency source of yellow light for high-resolution spectroscopy", Optics Letters, Vol. 26, No. 13, 2001 (pp1013-1015).

[2] V.M. Gordienko, A.I. Kholodnykh and V.I. Pryalkin, "New potentialities of a broadband femtosecond optical parametric oscillator for remote sensing multicomponent aerosol and gaseous atmospheric pollutions", Quantum Electronics, Vol. 30, No. 9, 2000 (pp839-842).

[3] J.A. Giordmaine and R.C. Miller, "Tunable coherent parametric oscillation in LiNbO at optical frequencies", Physical Review Letters, Vol. 14,1965 (pp973-976).

[4] A.G. Akmanov, S.A. Akhmanov and R.V. Khokhlov *et al.*, "Parametric interactions in optics and tunable light oscillators", IEEE Journal of Quantum Electronics, Vol. QE-4, 1968 (pp828-831).

[5] R.G. Smith, J.E. Geusic and H.J. Levinson *et al.*, "Continuous optical parametric oscillator in $Ba_2NaNb_5O_{15}$", Applied Physics Letters, Vol. 13, 1968 (p308).

[6] R.L. Byer, M.K. Oshman and J.F. Young *et al.*, "Visible CW parametric oscillator", Applied Physics Letters, Vol. 13, 1968 (pp109-111).

[7] K. Burneika, M. Ignatavicius and V. Kabelka *et al.*, "Parametric light amplification and oscillation in KDP with mode-locked pump", IEEE Journal of Quantum Electronics, Vol. QE-8, 1972, (p574).

[8] A. Laubereau, L. Greiter and W. Kaiser, "Intense tunable picosecond pulses in the infrared", Applied Physics Letters Vol. 25, 1974, (p87).

[9] C.T. Chen, Y.C. Wu and A.D. Jiang *et al.*, "New nonlinear-optical crystal – LiB_3O_5", Journal of the Optical Society of America B, Vol. 6, No. 4, 1989 (pp616-621).

[10] J.G. Haub, M.J. Johnson and B.J. Orr *et al.*, "Spectroscopic and nonlinear-optical applications of a tunable beta-barium borate optical parametric oscillator", Journal of the Optical Society of America B, Vol. 10, No. 9, 1993 (pp1765-1777).

[11] N.V. Kondratyuk, A.A. Shagov and K.L. Demidchik *et al.*, "BBO-crystal optical parametric oscillator tunable over the 300-2340 nm range and pumped by the

4th harmonic of a Nd:YAG laser", Quantum Electronics, Vol. 30, No. 3, 2000 (pp253-254).

[12] P. Ditrapani, A. Andreoni and D, Podenas *et al.*, "Ultrashort pulses of high-power and spectral quality tunable between 1.6 and 4.6 μm", Optics Communications, Vol. 118, No. 3-4, 1995 (pp338-344).

[13] D.C. Hanna, M. V. O'Connor and M.A. Watson et al., "Synchronously pumped optical parametric oscillator with diffraction-grating tuning", Journal of Applied Physics D, Vol. 34, No. 16, 2001 (pp2440-2454).

[14] M.S. Webb, P.F. Moulton and J.J. Kasinski *et al.*, "High-average-power $KtiOAsO_4$ optical parametric oscillator", Optics Letters, Vol. 23, No. 15, 1998 (pp1161-1163).

[15] A. Piskarskas, V. Smilgyavichyus and A. Umbrasas, "Continuous parametric generation of picosecond light pulses", Soviet Journal of Quantum Electronics, Vol. 18, 1987 (pp155-156).

[16] S. Guha, F. Wu and J. Falk, "The effects of focusing on parametric oscillation", IEEE Journal of Quantum Electronics, Vol. QE-18, No. 5, 1982 (pp907-912).

[17] S. Guha, "Focusing dependence of the efficiency of a singly resonant optical parametric oscillator", Applied Physics B, Vol. 66, 1998 (pp663-675).

[18] S. E. Harris, M. K. Oshman and R. L. Byer, "Observation of tunable optical parametric fluorescence", Physical Review Letters, Vol. 18, 1967 (p732).

[19] J.A. Armstrong, N. Bloembergen and J. Ducuing *et al.*, "Interactions between light waves in a nonlinear dielectric", Physical Review, Vol. 127, 1962 (pp1918-1939).

[20] P.A. Franken and J.F. Ward, "Optical harmonics and nonlinear phenomena", Review of Modern Physics, Vol. 35, 1963 (pp23-39).

[21] E.J. Lim, M.M. Fejer and R.L. Byer *et al.*, "2nd-harmonic generation of green light in periodically poled planar lithium-niobate wave-guide", Electronics Letters, Vol. 25, No. 3, 1989 (pp174-175).

[22] L.E. Myers, G.D. Miller and R.C. Eckardt *et al.*, "Quasi-phase-matched 1.064-μm-pumped optical parametric oscillator in bulk periodically poled $LiNbO_3$", Optics Letters, Vol. 20, No. 1, 1995 (pp52-54).

[23] T.J. Edwards, G.A. Turnbull and M.H. Dunn *et al.*, "Continuous-wave singly resonant optical parametric oscillator based on periodically poled $RbTiOAsO_4$", Optics Letters, Vol. 23, No. 11, 1998 (pp837-839).

[24] Y.F. Chen, S.W. Tsai and S.C. Wang, "High-power diode-pumped nonlinear mirror mode-locked Nd:YVO_4 laser with periodically-poled KTP", Applied Physics B, Vol. 72, No. 4, 2001 (pp395-397).

[25] L.E. Myers, R.C. Eckhardt and M.M. Fejer *et al.*, "Quasi-phase-matched optical parametric oscillators in bulk periodically poled $LiNbO_3$", Journal of the Optical Society of America B, Vol. 12, No. 11, 1995 (pp2102-2116).

[26] Y.Wang, V. Petrov and Y.J. Ding YJ, *et al.*, "Ultrafast generation of blue light by efficient second-harmonic generation in periodically-poled bulk and waveguide potassium titanyl phosphate", Applied Physics Letters, Vol. 73, No.7 1998 (pp873-875).

[27] M.M. Fejer, G.A. Magel and D.H. Jundt *et al.*, "Quasi-phase-matched second harmonic generation: tuning and tolerances", IEEE Journal of Quantum Electronics, Vol. 28, No. 11, 1992 (pp2631-2654).

[28] D. Wokosin, Centre for Biophotonics, University of Strathclyde (private communication).

[29] B. Ruffing, A. Nebel and R. Wallenstein, "High-power picosecond LiB_3O_5 optical parametric oscillators tunable in the blue spectral range", Applied Physics B, Vol. 72, No. 2, 2001 (pp137-149).

[30] Moltech, Berlin (Company literature).

Chapter Eight

Conclusions

This thesis presents research on the development of diode-pumped near-infrared ultra-short pulsed lasers for application to nonlinear optical frequency conversion, with emphasis on the creation of a tunable visible source of high peak power radiation for multi-photon microscopy experiments.

The design considerations of the laser platform were considered, with investigation and comparison of two mode-locking techniques, namely additive pulse mode-locking and fast saturable absorption via a saturable Bragg reflector. Both methods were applied to a $Nd^{3+}:YVO_4$ gain medium and high average and peak powers were observed.

In Chapter Three, additive pulse mode-locking of a diode-pumped $Nd^{3+}:YVO_4$ laser operating at $\lambda = 1064\text{nm}$ was presented. Using this technique, pulses as short as 2.7ps were measured at an average power of 1.1W. Given the laser repetition frequency of 90.7MHz, the peak power was calculated to be 4.5kW.

In Chapter Four, a diode-pumped $Nd^{3+}:YVO_4$ laser emitting at $\lambda = 1064\text{nm}$ and mode-locked using a saturable Bragg reflector (SBR) was presented. Pulses of 33ps duration were measured at an average power of 235MHz. The laser peak power was calculated to be 567W. Since the gain medium is side-pumped, power scaling of this system would be simple and effective. Although the peak power of the SBR mode-locked laser is significantly lower than that of the laser described in Chapter Three, the saturable Bragg reflector mode-locked laser was considerably more robust and insensitive to mechanical perturbation. Improvements to the cavity mirrors and

locking electronics would lead to a more robust and reliable system. Without such changes, however, the SBR laser was chosen as the platform for nonlinear optical frequency conversion.

Following a brief review of the fundamental principles of nonlinear optical frequency conversion in Chapter Five, a numerical and theoretical treatment of resonant frequency tripling was presented in Chapter Six. Building upon an existing model for resonant second harmonic generation, a plane-wave treatment of singly resonant third harmonic generation was described. Using the SBR mode-locked laser described in Chapter Four as the pump source, conversion efficiencies from fundamental to third harmonic in excess of 30% were predicted. Experimentally, conversion efficiencies greater than 12% were observed with application of the SBR mode-locked laser. This corresponded to 500mW of radiation generated at $\lambda = 355\text{nm}$. The viability for this ultraviolet source as a pump to a BaB_2O_4 optical parametric oscillator was also briefly discussed. Further investigation of the system would include better coatings for cavity optics, exploration of the effect of group velocity mismatch on the generated third harmonic output power and the use of alternative nonlinear media and pump sources.

An optical parametric oscillator based on periodically poled lithium niobate (PPLN) was described in Chapter Seven. The device was also based on the SBR mode-locked laser described in Chapter Four. Using a 50mm long PPLN crystal, an average power of 1W was measured at the signal wavelength, which was tunable from $\lambda = 1460\text{nm}$ to 1601nm. This system was also used in conjunction with the SBR-modelocked laser in a sum-frequency mixing process to generate visible radiation which was tunable from $\lambda = 615\text{nm}$ to 640nm. The peak power of this emission was less than 5W, which was insufficient to perform the proposed multi-photon imaging process. The effect of using a pump laser with higher peak power to pump the optical parametric oscillator is currently underway, with a view to obtaining femtosecond-pulsed radiation at this wavelength region.

Appendix One.

Spectra-Physics laser diode bars (extract from http://www.spectra-physics.com/products/spsl_products/multi-bar.html)

Typical Laser Bars Specifications (Open Heatsink)

Output Power (W)	Wavelengths (nm)				
	808	830	915	975	1800
7	N	N	N	N	Y
20	Y	Y	Y	Y	Y
40	Y	N	Y	N	N

Typical Multi Bar Module Specifications

Output Power (W)	Configuration	Type	Wavelengths (nm)	
			808	940
40	Single Bar (1x1 Array)		Y	Y
50	Single Bar (1x1 Array)	ProLite™ M 50	Y	N
240	6x1 Vertical Array		Y	Y
300	6x1 Vertical Array	ProLite™ 300	Y	N
480	12x1 Vertical Array		Y	Y
600	12x1 Vertical Array	ProLite™ 600	Y	N

P_o[1] (W)	I_{th}[2] (A)	I_{op}[3] (A)	λ_o[4] (nm)	Part Number
20	≤12	≤35	808	BCS-808-20-01
			830	BCS-830-20-01
			915	BCS-915-20-01
			975	BCS-975-20-01
40	≤15	≤80	808	BCS-808-40-01
			915	BCS-915-40-01

(1).... P_o Typical output power in cw regime

(2).... I_{th} Typical current threshold

(3).... I_{op} Typical operating current

(4).... l_o center wavelength @ 25°C case temperature, +/- 5nm tolerance. Typical wavelength temperature coefficient : 0.2-0.3 nm/°C

Common Specifications

Spectral Width	<4nm
Typical Conversion Efficiency	<40%
Polarisation	TE
Beam Divergence (FWHM)	40° ⊥ x 12°// at max. power
Centre Wavelength Tolerance	±5nm standard
Operating Voltage	<2 Volts
Reverse Voltage	<3 Volts
Negative Current Transient	<25 µA
Monolithic Array Length	12.5 mm
Storage Temperature Range	-30oC to 80oC
Recommended Case Temperature	25°C

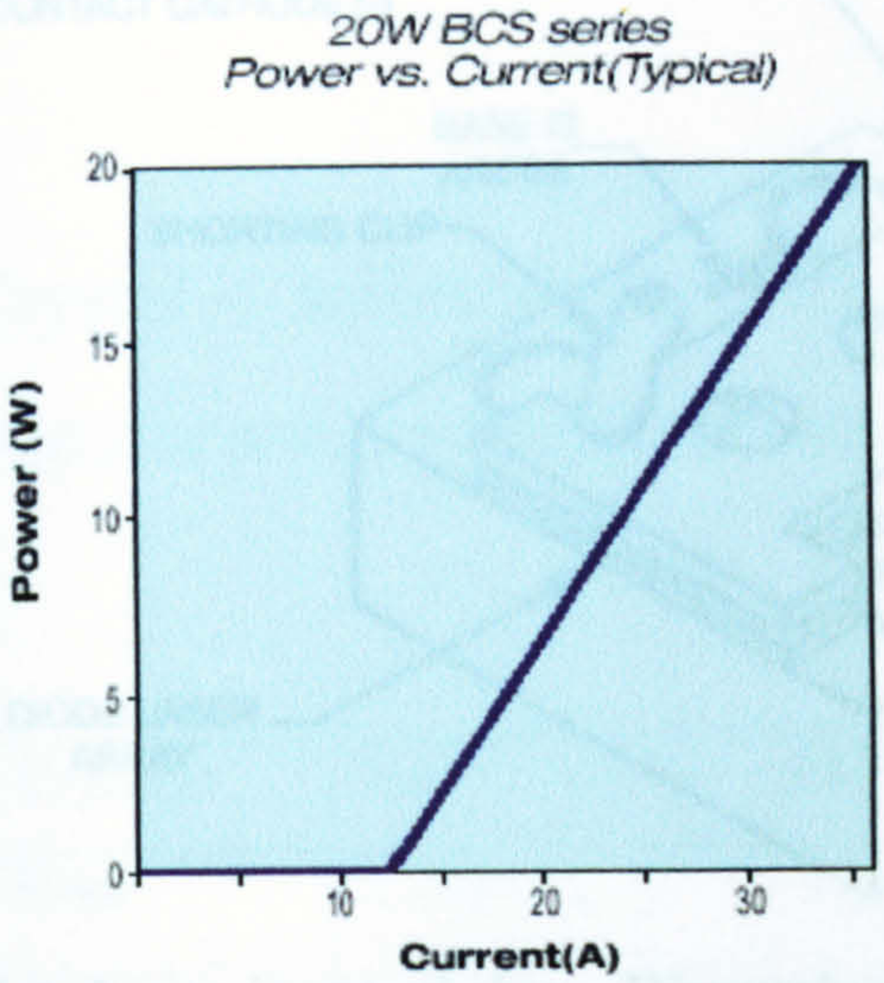
20W BCS series
Power vs. Current(Typical)
Power (W)
20
15
10
5
0
10
20
30
Current(A)

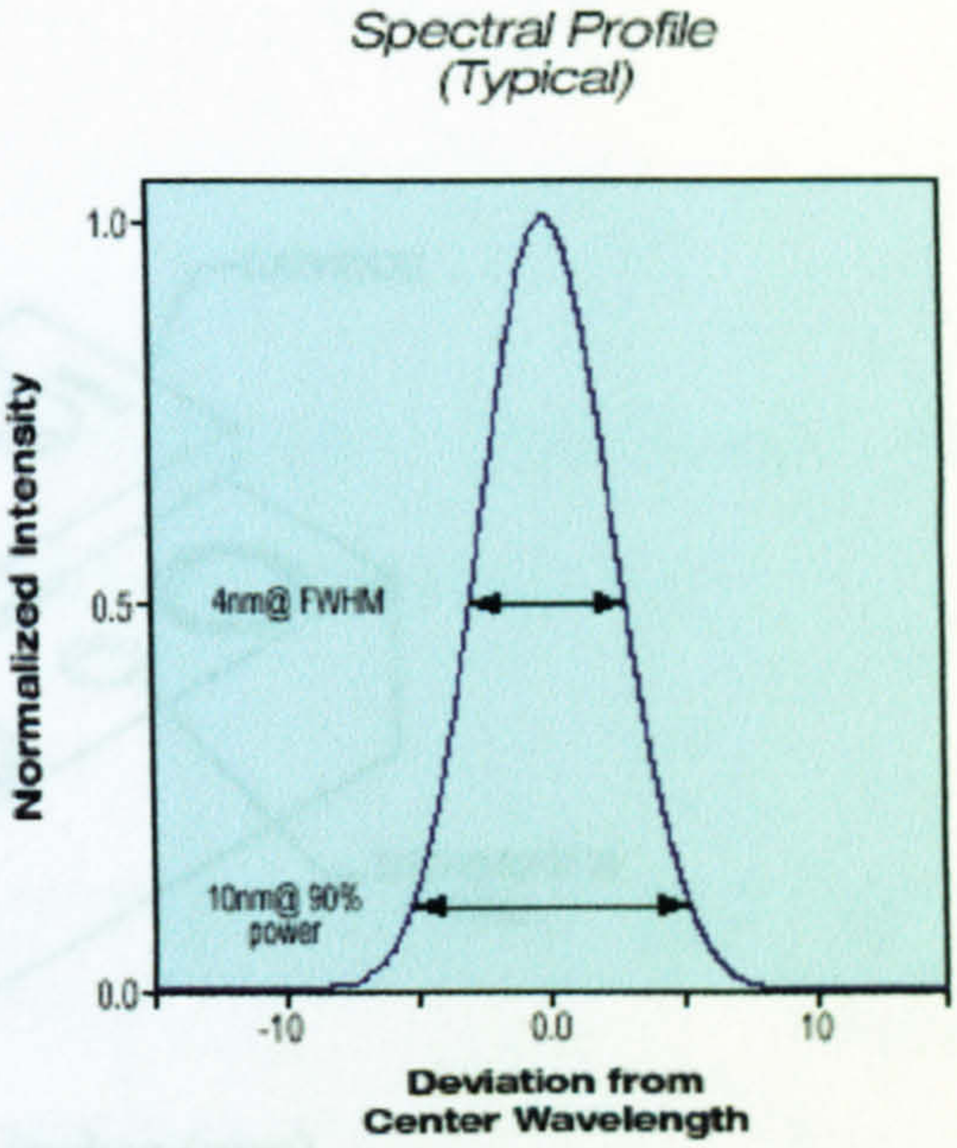
Spectral Profile
(Typical)
Normalized Intensity
1.0
0.5
0.0
4nm@ FWHM
10nm@ 90% power
-10
0.0
10
Deviation from
Center Wavelength

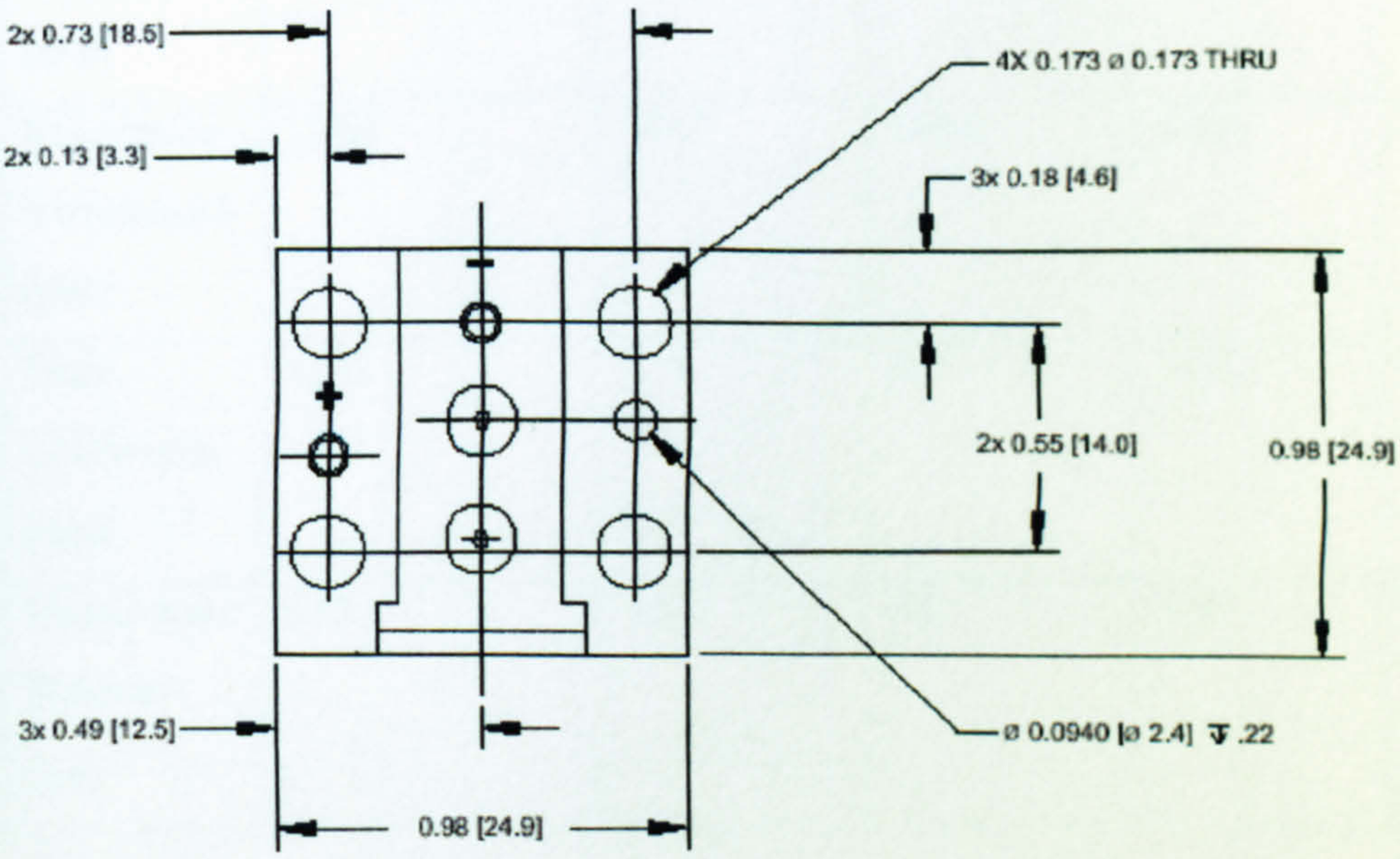
2x 0.73 [18.5]
2x 0.13 [3.3]
4X 0.173 ø 0.173 THRU
3x 0.18 [4.6]
2x 0.55 [14.0]
0.98 [24.9]
3x 0.49 [12.5]
ø 0.0940 [ø 2.4] ⏷ .22
0.98 [24.9]

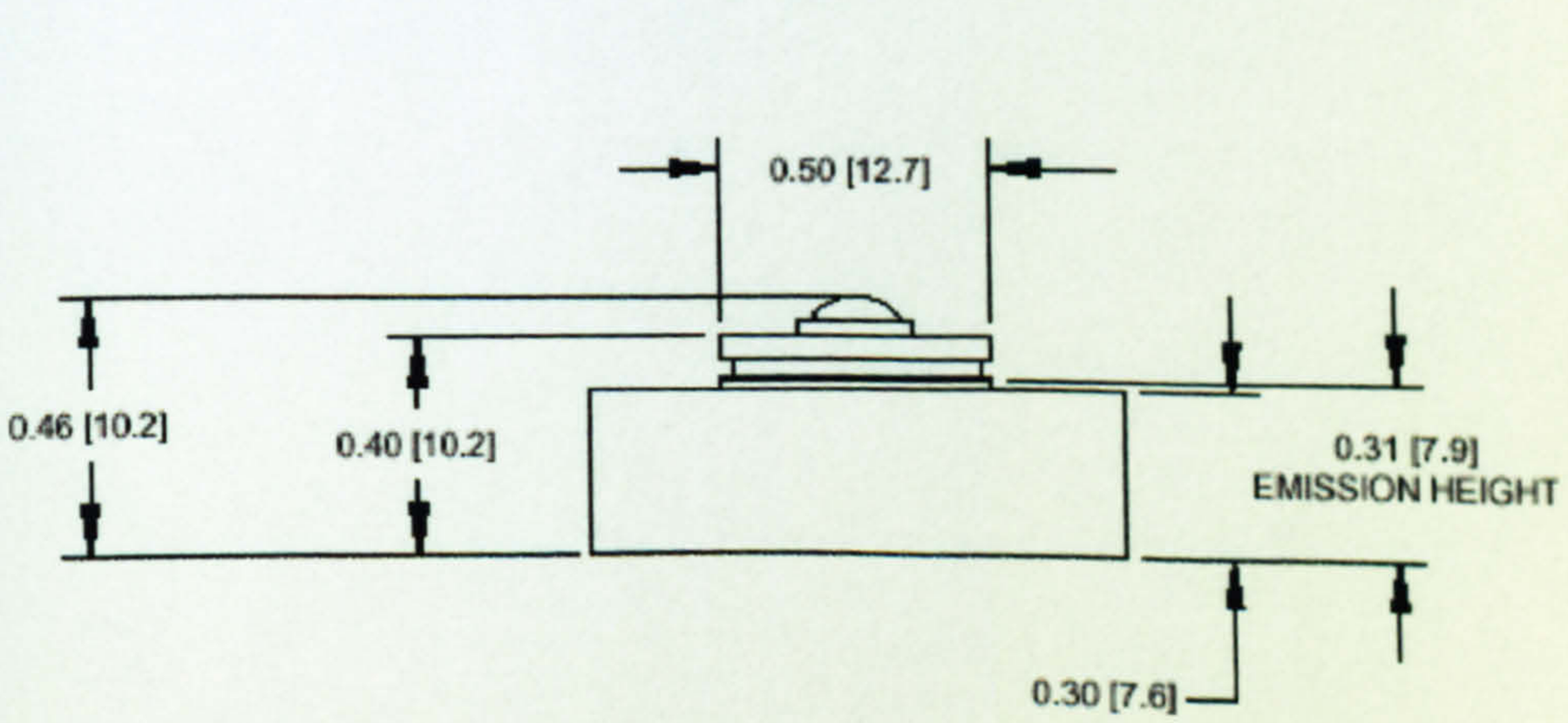
0.50 [12.7]
0.46 [10.2]
0.40 [10.2]
0.31 [7.9]
EMISSION HEIGHT
0.30 [7.6]

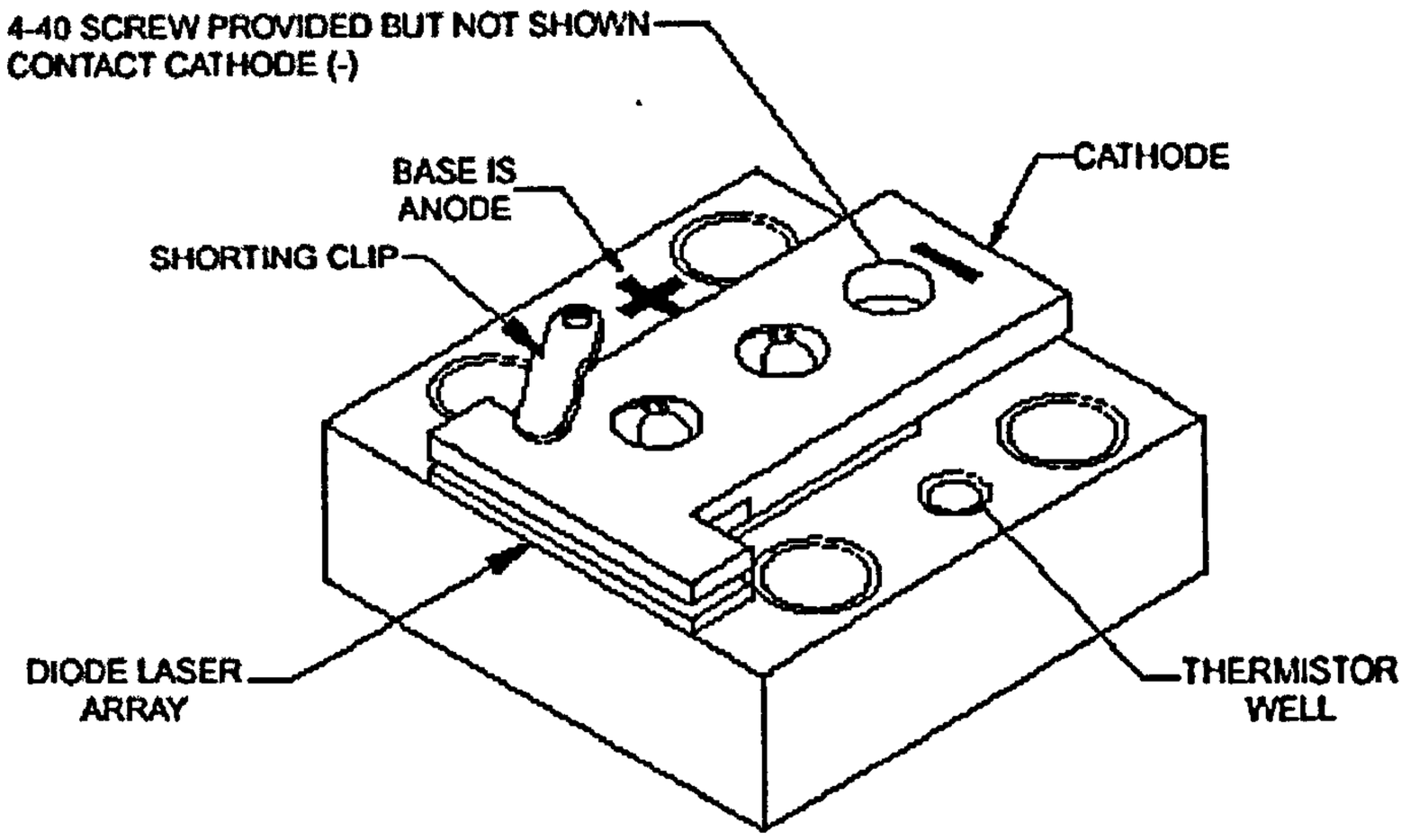

Not shown in actual size – Dimensions in inches (mm)

Appendix Two.

Crystal information from MolTech (Extracted from http://www.mt-berlin.com/charts/chart_03.htm.)

Crystal	Nd^{3+}:YAG	Nd^{3+}:YLF	Nd^{3+}:YVO_4	Nd^{3+}:glass	Yb^{3+}:YAG
Host formula	$Y_3Al_5O_{12}$	$YLiF_4$	YVO_4	NA	$Y_3Al_5O_{12}$
Pump wavelength (nm)	808	797	808	~800	940
Oscillation wavelength (nm)	1064	1047	1064	1064	1030
Gain bandwidth (nm)	0.45	1.4	1	>2.5	20
Upper state lifetime (μs)	250	480	98	300	950

Appendix Three.

Properties of $Nd^{3+}:YVO_4$ crystal (Extracted from http://www.casix.com/products/crystalls_laster_1.htm)

Main Features:

- ❖Low lasing threshold and high slope efficiency
- ❖Large stimulated emission cross-section at lasing wavelength
- ❖High absorption over a wide pumping wavelength bandwidth
- ❖Optically uniaxial and large birefringence emits polarised laser

Basic Properties

Atomic Density	~$1.37x10^{20}$ atoms/cm^2
Crystal Structure	Zircon Tetragonal, space group D_{4h}, a=b=7.12, c=6.29
Density	4.22 g/cm^2
Mohs Hardness	Glass-like, ~5
Thermal Expansion Coefficient	α_a=$4.43x10^{-6}$/K, α_c=$11.37x10^{-6}$/K
Thermal Conductivity Coefficient	C//: 5.23 W/m/K; C⊥: 5.10 W/m/K

Optical Properties

Emission wavelengths	914nm, 1064 nm, 1342 nm
Crystal class	positive uniaxial, $n_o = n_a = n_b$, $n_e = n_c$ $n_o = 1.9573$, $n_e = 2.1652$, @ 1064nm $n_o = 1.9721$, $n_e 2.1858$, @ 808nm $n_o = 2.0210$, $n_e = 2.2560$, @ 532nm
Sellmeier Equation (for pure YVO_4 crystals)	$n_o^2 = 3.77834 + 0.069736/(\lambda^2 - 0.04724) - 0.0108133.\lambda^2$ $n_e^2 = 4.59905 + 0.110534/(\lambda^2 - 0.04813) - 0.0122676.\lambda^2$
Thermal Optical Coefficient	$\frac{\partial n_a}{\partial T} = 8.5 \times 10^{-6}/K$, $\frac{\partial n_c}{\partial T} = 3.0 \times 10^{-6}/K$
Stimulated Emission Cross-Section	25.0×10^{-19} cm^2 , @1064 nm
Fluorescent Lifetime	90 µs @ 808 nm
Absorption Coefficient	31.4 cm^{-1} @ 808 nm
Absorption Length	0.32 mm @ 808 nm
Intrinsic Loss	Less 0.1% cm^{-1} , @1064 nm
Gain Bandwidth	0.96 nm (257 GHz) @ 1064 nm
Polarised Laser Emission	P polarisation, // to optic axis
Diode pumped Optical to Optical Efficiency	>60%

Absorption and fluorescence spectra of Nd^{3+}:YVO_4 crystal

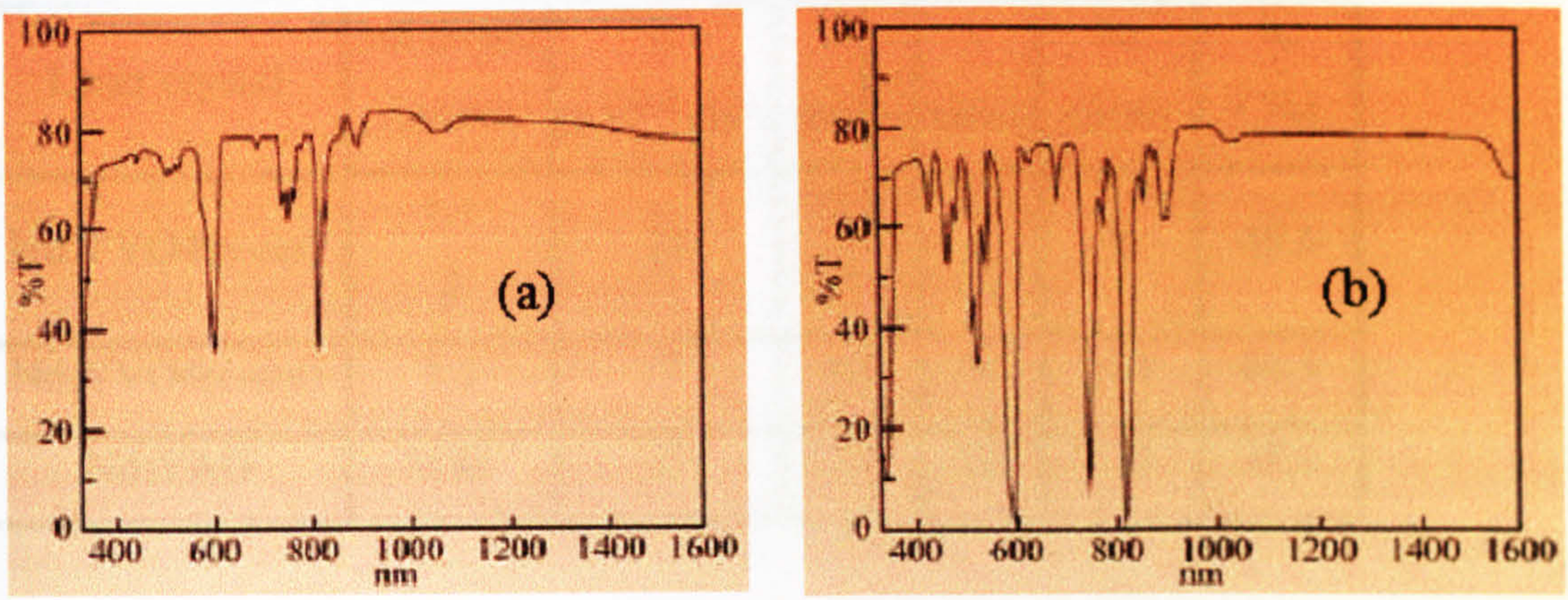

Absorption spectra for 1mm thick Nd^{3+}:YVO_4 crystal for (a) 0.5% dopant concentration and (b) 3% dopant concentration.

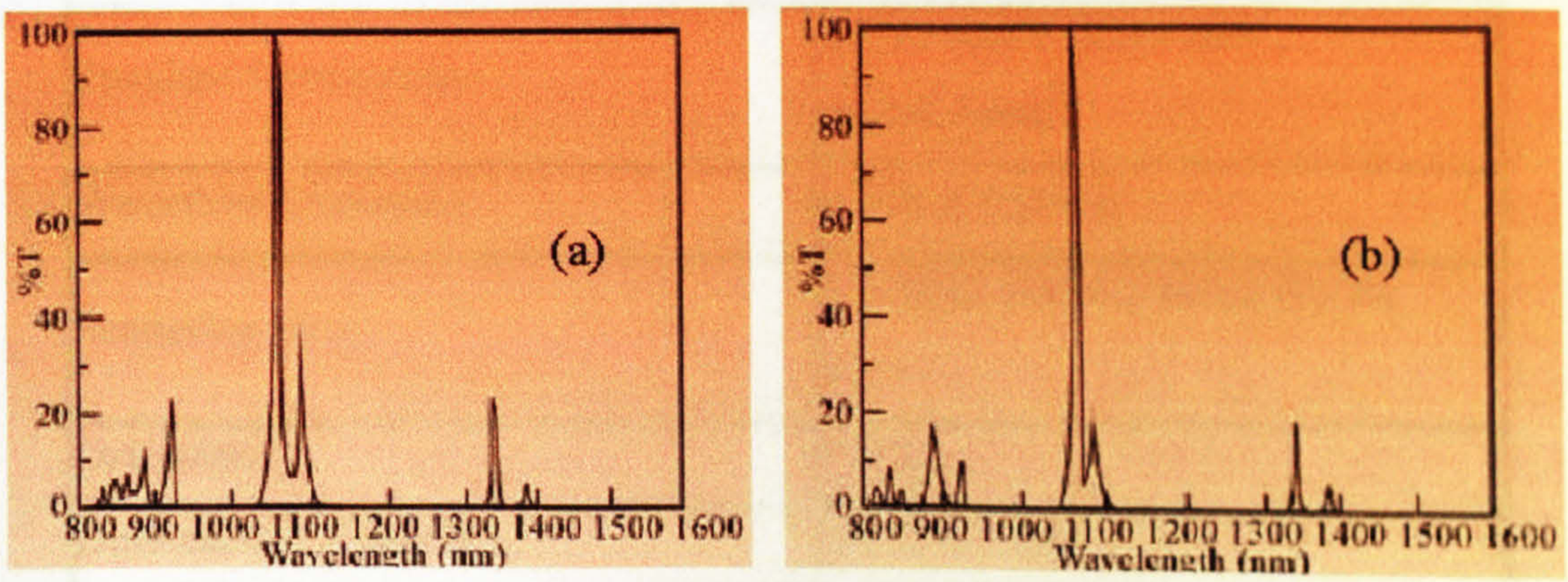

Normalised fluorescence spectra for Nd 1.1% at. % doped Nd^{3+}:YVO_4 crystal for (a) σ polarisation and (b) π polarisation

Laser properties of $Nd^{3+}:YVO_4$ crystals vs $Nd^{3+}:YAG$

Laser crystal	Nd doped (atm%)	σ ($x10^{-19}cm^2$)	a (cm^{-1})	t (ms)	P_{th} (mw)	h_s (%)
Nd:YVO4(a-cut)	1.1 2	25	31.2 72.4	90 50	78	48.6
Nd:YVO4(c-cut)	1.1	7	9.2	90	231	45.5
Nd:YAG	0.85	6	7.1	230	115	38.6

Standard Specs. of CASIX's $Nd^{3+}:YVO_4$ Crystals

Nd: Dopant Level	0.1 - 3.0 atm%
Standard Dimensions	3x3x3 mm^3, 3x3x1 mm^3, 3x3x0.5 mm^3
Wavefront Distortion	< λ/8 at 633 nm
Scattering Sites	invisible, probed with a He-Ne laser
Orientation	0.5 deg
Dimensional Tolerance	+0.1/-0.1 mm
End-faces Configuration	Plano/Plano
Surface quality	10/5 Scratch/Dig per MIL-O-13830B
Flatness	λ/10 at 633 nm
Clear Aperture	> Central 90%
Parallelism	< 10 arc sec.
Intrinsic Loss	< 0.1% cm^{-1}

Appendix Four.

(a) Mathematica v3.0 Programs and output for calculation of resonant third harmonic generation.

The program for calculation of the solution to the polynomial as described in Chapter Six is shown below, along with the commands to generate 3D plots. Comments describing function of program line are indicated by (* comment *) notation.

```
Clear[a,b,c,d,e,f,g,P,gsh,g,gsf,gprod]        (* Clear variables *)
gsf=0.02;      (* Sum-frequency conversion efficiency = γ3ω'(W^-1) *)
gsh=0.005;     (* Second harmonic conversion efficiency = γ2ω'(W^-1) *)
gprod=gsh gsf;
 a[r_,t_]:=t r gsf gsh^3;          (* Coefficients of polynomial *)
 b[r_,t_]:=-2 t r gsf gsh^2;       (*     "          "       *)
 c[r_,t_]:=t r gsf gsh;            (*     "          "       *)
 d[r_,t_]:=t r gsh;                (*     "          "       *)
 f[r_,t_]:=1-t r;                  (*     "          "       *)
p2[g_,r_,t_]:=P/.Solve[(a[r,t] P^5) + (b[r,t] P^4) + (c[r,t] P^3) + (d[r,t] P^2) + (f[r,t] P)
– g = = 0, P][[3]]
(* Solution 3 is real, g is fundamental average input power to resonator *)

(* First 3D plot is Input Fundamental Power (W) from 0.1W to 10W, varying
r=0.1 to 0.99, evaluating the fundamental intracavity power (W) *)

plottotal1:=Plot3D[p2[g,r,0.98],{g,0,10}, {r,0.1,0.99}, PlotPoints -> 10,
Mesh -> False, ColorFunction -> Hue, AxesLabel -> {"Pin (W)", " r", "Pω
(W)"},
```

```
TextStyle -> {Fontsize -> 15, FontFamily -> "Times", FontWeight -> "Bold"},
BoxRatios -> {2,2,1.25}, Axes -> True];
plottotal1

(*Second 3D plot is Input Fundamental Power (W) from 0.1W to 10W, varying
r=0.1 to 0.99, evaluating the Third Harmonic Power (W) generated *)

Psum[g_,r_,t_]:=(gsf gsh (p2[g,r,t])^3)-( gsf gsh^2 (p2[g,r,t])^4);
Plottotal2:=Plot3D[Psum[g,r,0.98],{g,0,10},{r,0.01,0.99}, PlotPoints -> 10,
Mesh -> False, ColorFunction -> Hue, AxesLabel -> {"Pin (W)", " r", "P_3ω
(W)"}, TextStyle -> {FontSize -> 15, FontFamily -> "Times", FontWeight ->
"Bold"}, BoxRatios -> {2,2,1.25}, Axes -> True];
Plottotal2

(* Third 3D plot is Input Fundamental Power (W) from 0.1W to 10W, varying
r=0.1 to 0.99, evaluating the Second Harmonic Power (W) generated *)

Psec[g_,r_,t_]:=(gsh(p2[g,r,t])^2);
Plottotal3:=Plot3D[Psec[g,r,0.98],{g,0.10},{r,0.01,0.99}, PlotPoints -> 10,
Mesh -> False, ColorFunction -> Hue, AxesLabel -> {"P_in (W)", " r", "P_2ω
(W)"), TextStyle -> {FontSize -> 15, FontFamily -> "Times", FontWeight ->
"Bold"}, BoxRatios -> {2,2,1.25}, Axes - > True];
Plottotal3
```

Code for generation of plots which indicate dependence of second and third harmonic conversion efficiency on average third harmonic power. Assumes input of first four lines from program above.

```
a[r_, t_, gsf_, gsh_] := t r gsf gsh^3;
b[r_, t_, gsf_, gsh_] := -2 t r gsf gsh^2;
c[r_, t_, gsf_, gsh_] := t r gsf gsh;
d[r_, t_, gsf_, gsh_] := t r gsh;
f[r_, t_, gsf_, gsh_] := 1 – tr;
p2[g_, r_, t_, gsf_, gsh_] := P /. Solve[( a [r, t, gsf, gsh] P ^5) + ( b [r, t, gsf, gsh] P^4)
+ ( c [r, t, gsf, gsh] P ^3) + ( d [r, t, gsf, gsh] P ^2) + ( f [r, t, gsf, gsh] P) – g == 0,
P][[3]]
(* Solution 3 is real *)

Psec[g_, r_, t_, gsf_, gsh_] := gsh (p2[g, r, t, gsf, gsh])^2;
Psum[g_, r_, t_, gsf_, gsh_] := (gsf gsh (p2[g, r, t, gsf, gsh]) ^3) – gsf gsh2 (p2[g, r,
t, gsf, gsh]^4);

(* First plot is dependency of sum frequency conversion efficiency (second
harmonic conversion efficiency fixed at 0.02 W-1) on fundamental intracavity
power with input power from 0 to 10W and r = 0.98, t = 0.96 *)

Plot3D[p2[g, 0.98, 0.96, gsf, 0.02], {g, 0, 10}, {gsf, 10-7, 0.5}, PlotPoints -> 10,
ColorFunction -> Hue, Mesh -> False, AxesLabel -> {"Pin (W)", "g 3w'", "Pw
(W)}, TextStyle ->{FontSize -> 15, FontFamily -> "Times", FontWeight ->
"Bold"}, BoxRatios -> {2,2,1.25}

(* Second plot is dependency of second harmonic conversion efficiency (third
harmonic conversion efficiency fixed at 0.02 W-1) on fundamental intracavity
power, with input power from 0 to 10W and r=0.98, t=0.96 *)
```

```
Plot3D[p2[g, 0.98, 0.96, 0.02, gsh], {g, 0, 10}, {gsh, 10-7, 0.5}, PlotPoints -> 10,
ColorFunction -> Hue, Mesh -> False, AxesLabel -> {"Pin (W)", "g 2w'", "Pw
(W)}, TextStyle ->{FontSize -> 15, FontFamily -> "Times", FontWeight ->
"Bold"}, BoxRatios -> {2,2,1.25}]

(*Third Plot is dependency of third harmonic conversion efficiency (second
harmonic conversion efficiency fixed at 0.02 W-1) on generated second
harmonic power, where r=0.98, t=0.96 and the fundamental input power ranges
from 0 to 10W. *)

Plot3D[Psec[g,0.98,0.96,gsf,0.02],{g,0,10},{gsf,10-7, 0.5}, PlotPoints -> 10,
ColorFunction -> Hue, Mesh -> False, AxesLabel -> {"Pin (W)", " g3w' (W-1)",
"P2w (W)"}, TextStyle ->{FontSize -> 15, FontFamily -> "Times", FontWeight -
> "Bold"}, BoxRatios -> {2,2,1.25} ]

(*Fourth Plot is dependency of second harmonic conversion efficiency (third
harmonic conversion efficiency fixed at 0.02 W-1) on generated second
harmonic power, where r=0.98, t=0.96 and the fundamental input power ranges
from 0 to 10W. Note that the third harmonic conversion frequency acts as a
loss.*)

Plot3D[Psec[g,0.98,0.96,0.02,gsh],{g,0,10},{gsh,10-7, 0.5}, PlotPoints -> 10,
ColorFunction -> Hue, Mesh -> False, AxesLabel -> {"Pin (W)", " g2w' (W-1)",
"P2w (W)"}, TextStyle ->{FontSize -> 15, FontFamily -> "Times", FontWeight -
> "Bold"}, BoxRatios -> {2,2,1.25} ]

(*Fifth Plot is dependency of third harmonic conversion efficiency (second
harmonic conversion efficiency fixed at 0.02 W-1) on generated third harmonic
power, where r=0.98, t=0.96 and the fundamental input power ranges from 0 to
10W. *)
```

```
Plot3D[Psum[g,0.98,0.96,gsf,0.02],{g,0,10},{gsf,10-7, 0.5}, PlotPoints -> 10,
ColorFunction -> Hue, Mesh -> False, AxesLabel -> {"Pin (W)", " g3w' (W-1)",
"P3w (W)"}, TextStyle ->{FontSize -> 15, FontFamily -> "Times", FontWeight -
> "Bold"}, BoxRatios -> {2,2,1.25} ]

(*Sixth plot is dependency of second harmonic conversion efficiency (third
harmonic conversion efficiency fixed at 0.02 W-1) on generated third harmonic
power, where r=0.98, t=0.96 and the fundamental input power ranges from 0 to
10W. *)

Plot3D[Psum[g,0.98,0.96,0.02,gsh],{g,0,10},{gsh,10-7, 0.5}, PlotPoints -> 10,
ColorFunction -> Hue, Mesh -> False, AxesLabel -> {"Pin (W)", " g2w' (W-1)",
"P3w (W)"}, TextStyle ->{FontSize -> 15, FontFamily -> "Times", FontWeight -
> "Bold"}, BoxRatios -> {2,2,1.25} ]
```

The plots overleaf are generated using the above code, with the assumptions outlined in Chapter Six. These plots are used to justify the arguments and discussions presented in the same chapter.

Appendix Four.

(b) Dependency of cavity mirror reflectivity r (exclusive of input coupling) on the fundamental intracavity power, P_{ω} (W) for various values of $\gamma'_{2\omega}$ and $\gamma'_{3\omega}$. The transmission, t is fixed as t=0.98.

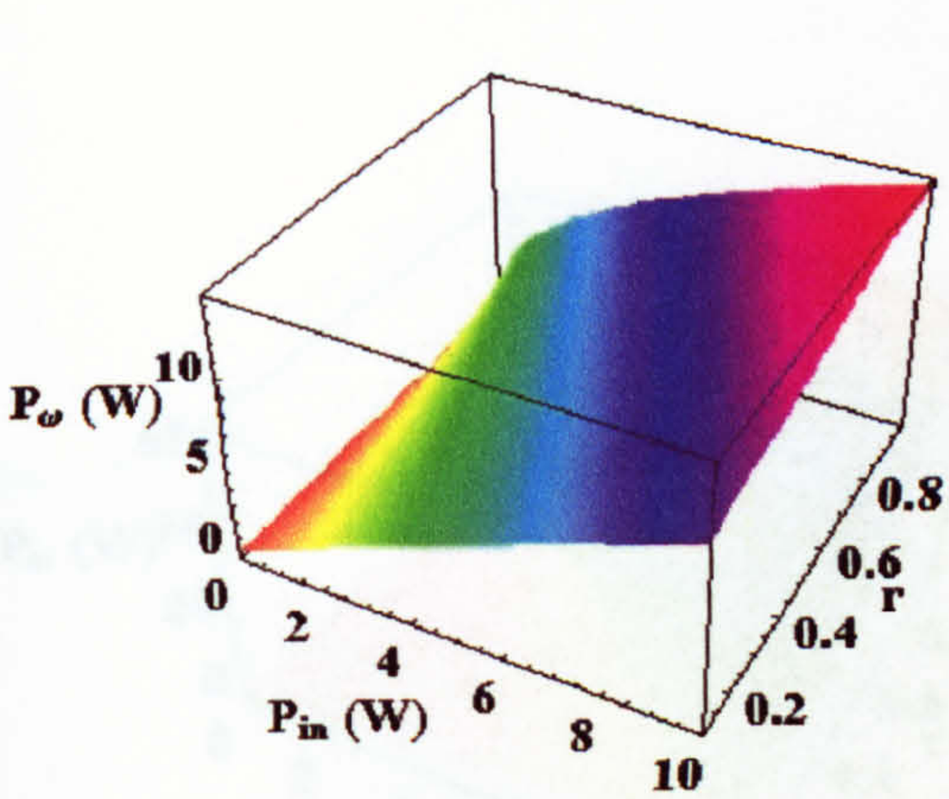

$\gamma'_{3\omega} = 0.2\ \mathrm{W}^{-1}, \gamma'_{2\omega} = 0.02\ \mathrm{W}^{-1}$

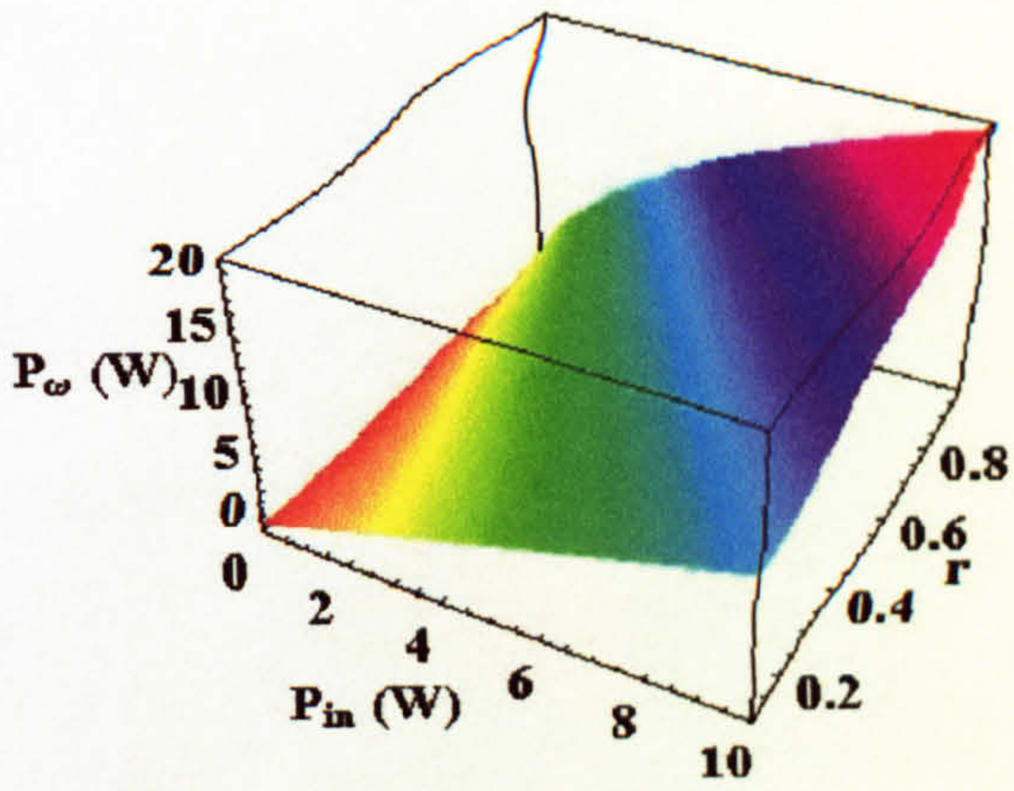

$\gamma'_{3\omega} = 0.02\ \mathrm{W}^{-1}, \gamma'_{2\omega} = 0.02\ \mathrm{W}^{-1}$

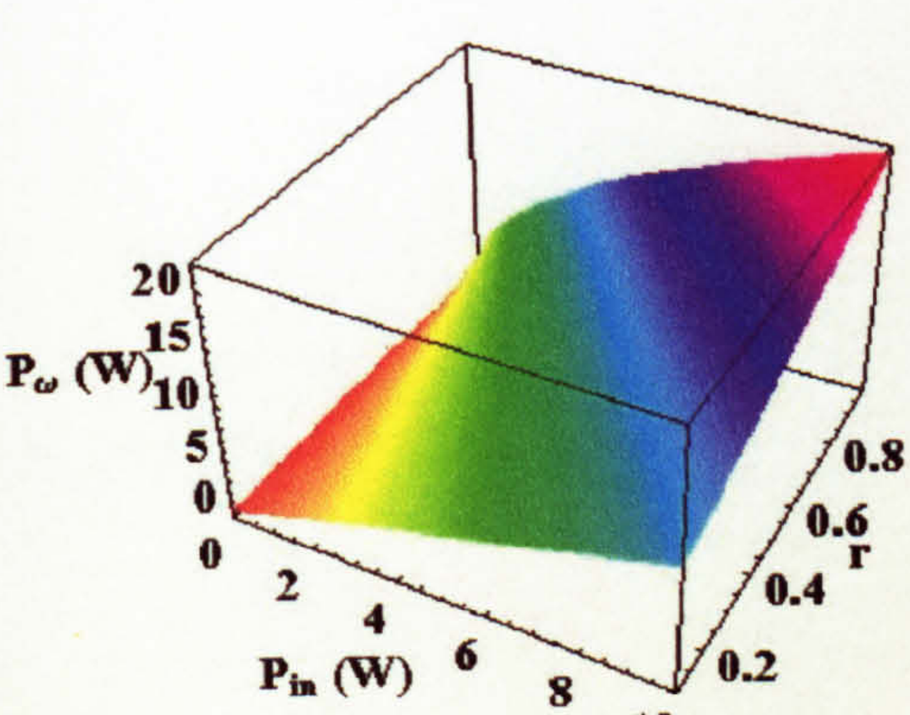

$\gamma'_{3\omega} = 0.002\ \mathrm{W}^{-1}, \gamma'_{2\omega} = 0.02\ \mathrm{W}^{-1}$

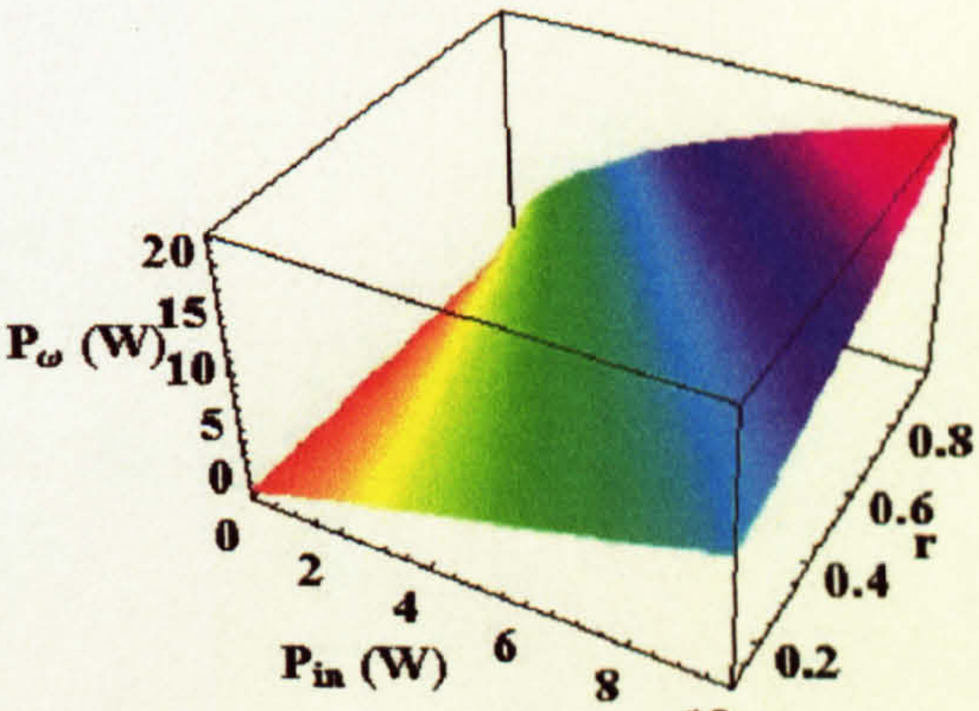

$\gamma'_{3\omega} = 0.0002\ \mathrm{W}^{-1}, \gamma'_{2\omega} = 0.02\ \mathrm{W}^{-1}$

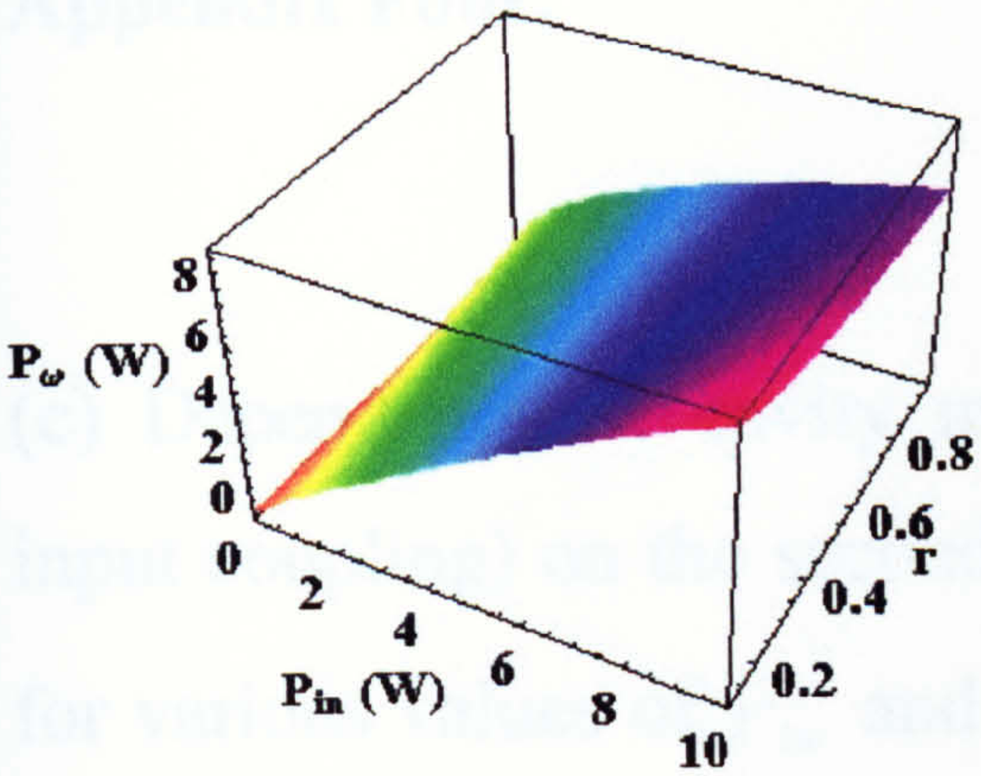

$\gamma'_{3\omega} = 0.02\ \mathrm{W}^{-1}, \gamma'_{2\omega} = 0.2\ \mathrm{W}^{-1}$

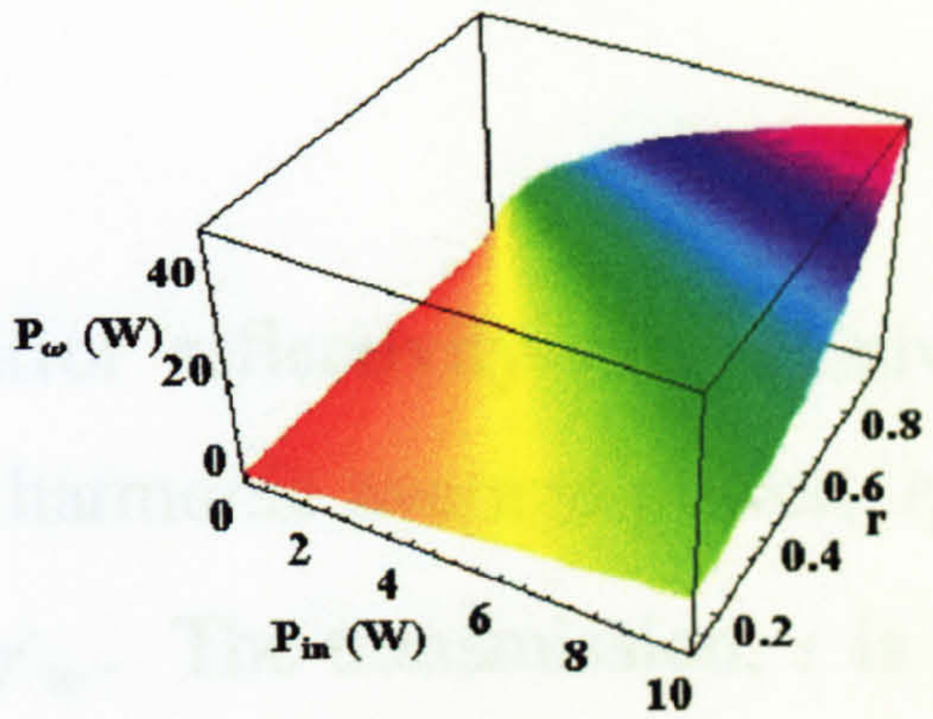

$\gamma'_{3\omega} = 0.02\ \mathrm{W}^{-1}, \gamma'_{2\omega} = 0.002\ \mathrm{W}^{-1}$

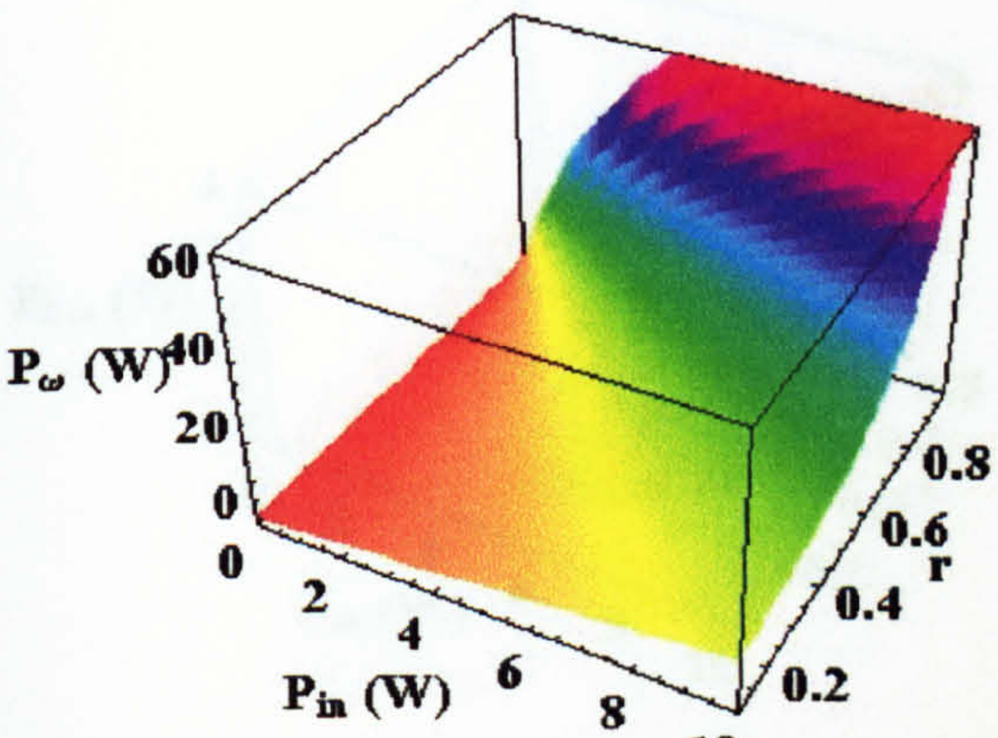

$\gamma'_{3\omega} = 0.02\ \mathrm{W}^{-1}, \gamma'_{2\omega} = 0.0002\ \mathrm{W}^{-1}$

Appendix Four.

(c) Dependency of cavity mirror reflectivity r (exclusive of input coupling) on the second harmonic average power, $P_{2\omega}$ (W) for various values of $\gamma'_{2\omega}$ and $\gamma'_{3\omega}$. The transmission, t is fixed as t=0.98.

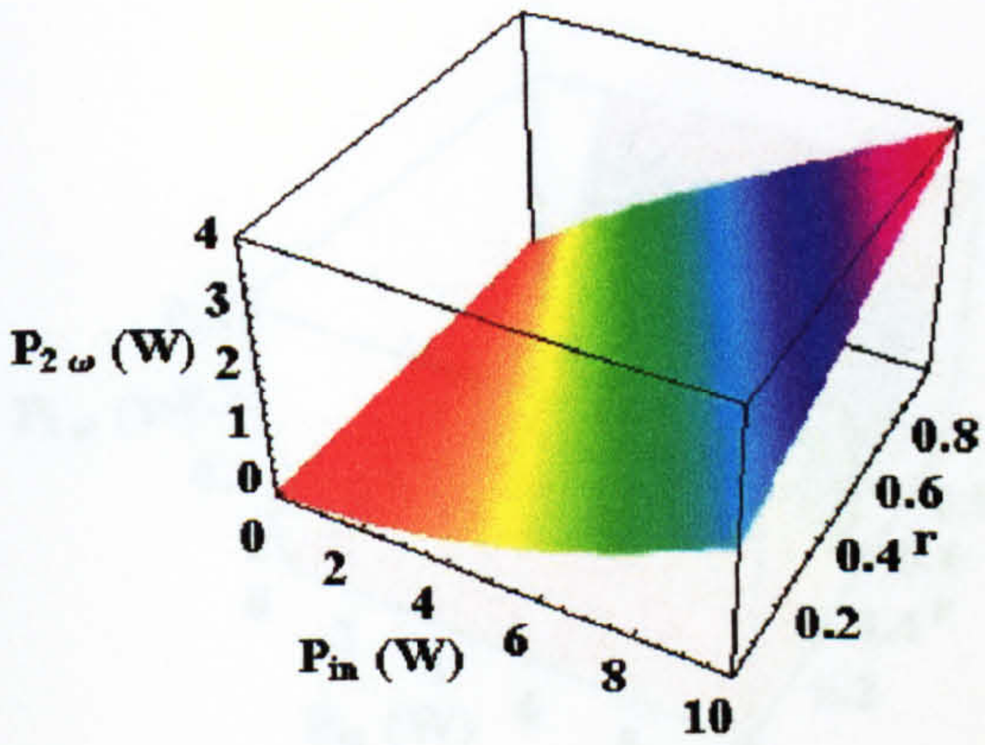

$\gamma'_{3\omega} = 0.2\ \mathrm{W}^{-1}, \gamma'_{2\omega} = 0.02\ \mathrm{W}^{-1}$

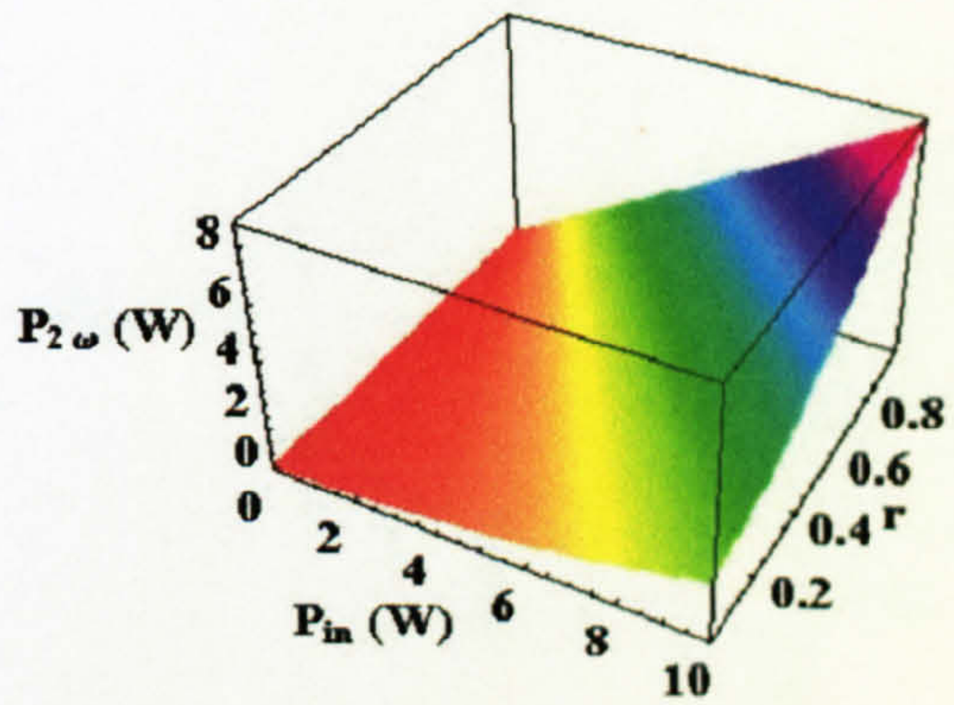

$\gamma'_{3\omega} = 0.02\ \mathrm{W}^{-1}, \gamma'_{2\omega} = 0.02\ \mathrm{W}^{-1}$

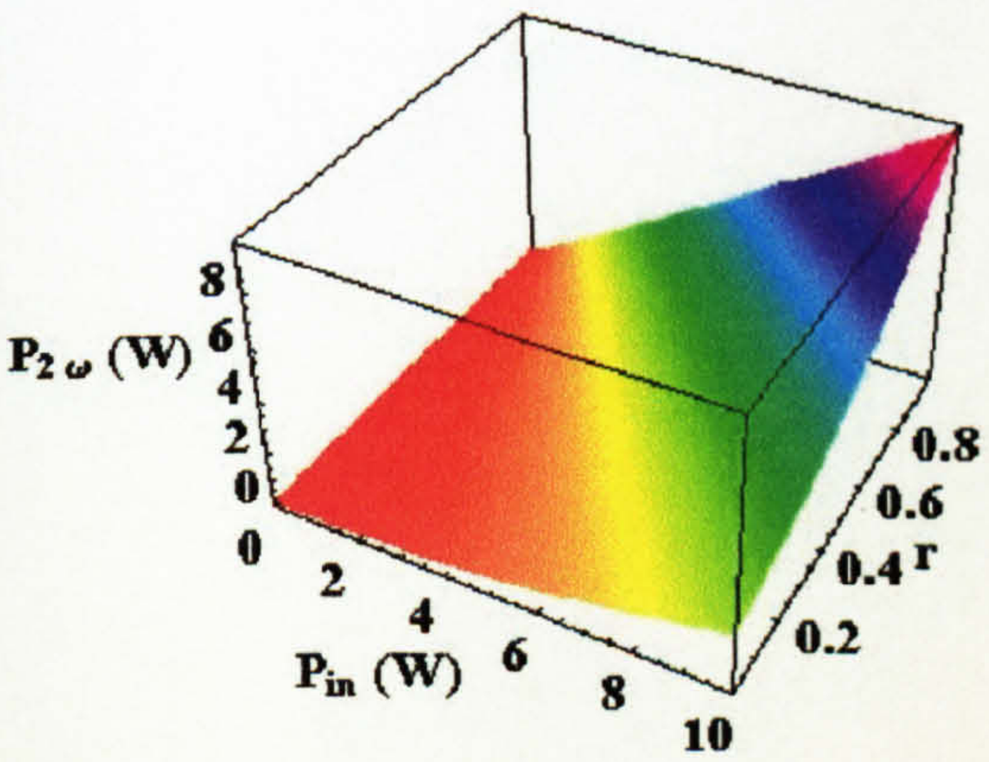

$\gamma'_{3\omega} = 0.002\ \mathrm{W}^{-1}, \gamma'_{2\omega} = 0.02\ \mathrm{W}^{-1}$

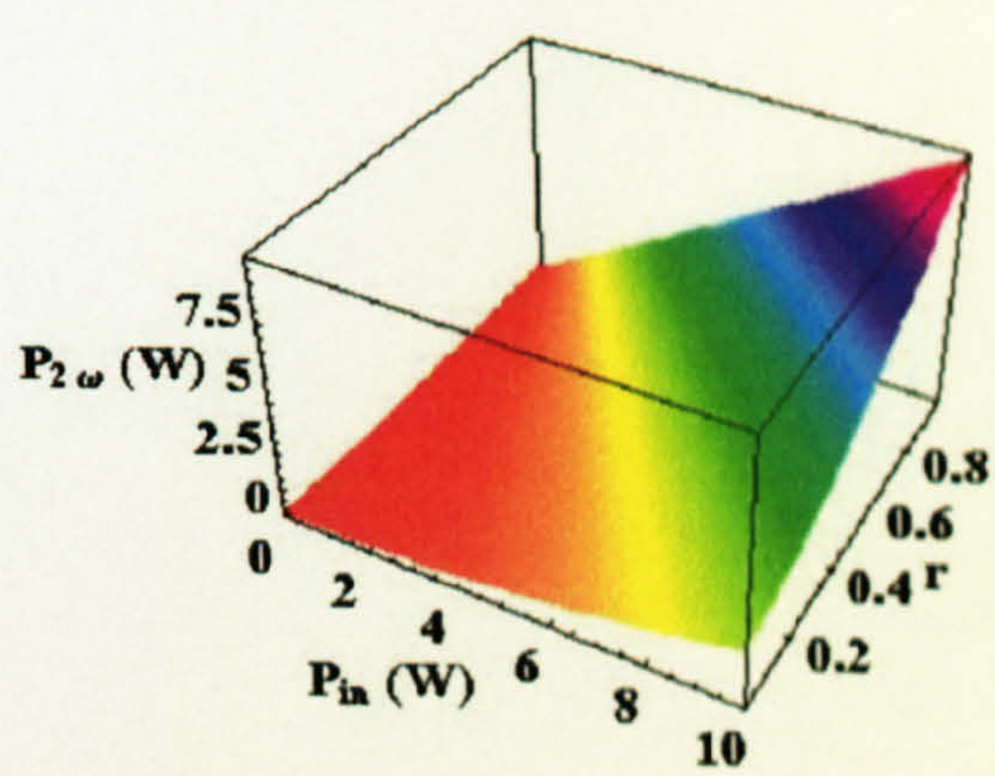

$\gamma'_{3\omega} = 0.0002\ \mathrm{W}^{-1}, \gamma'_{2\omega} = 0.02\ \mathrm{W}^{-1}$

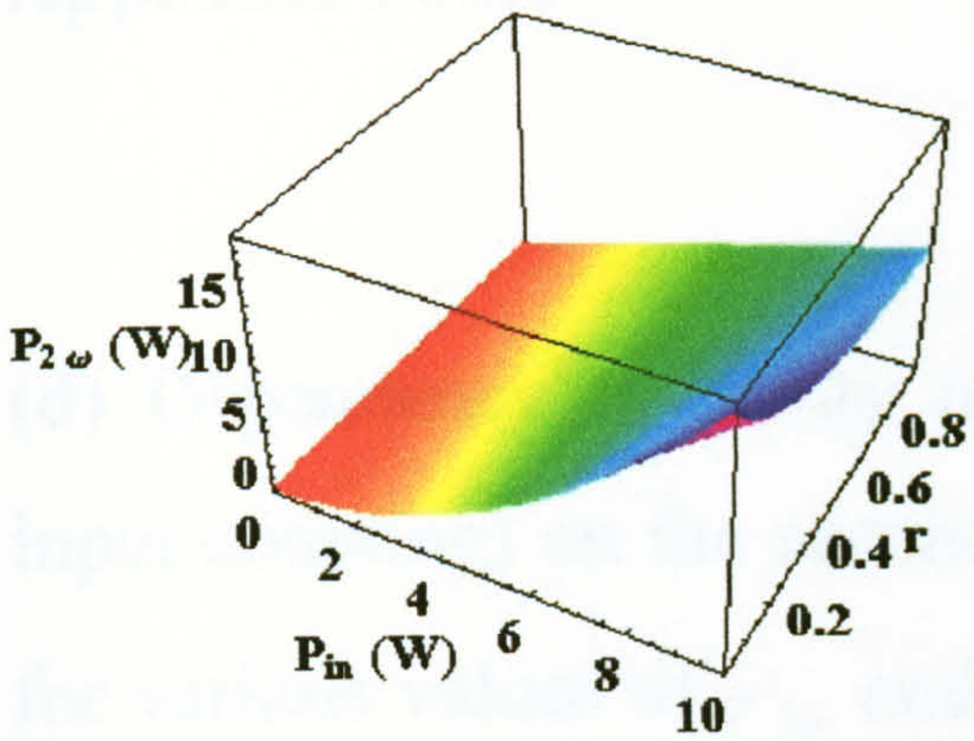

$\gamma'_{3\omega} = 0.02\text{W}^{-1}, \gamma'_{2\omega} = 0.2\ \text{W}^{-1}$

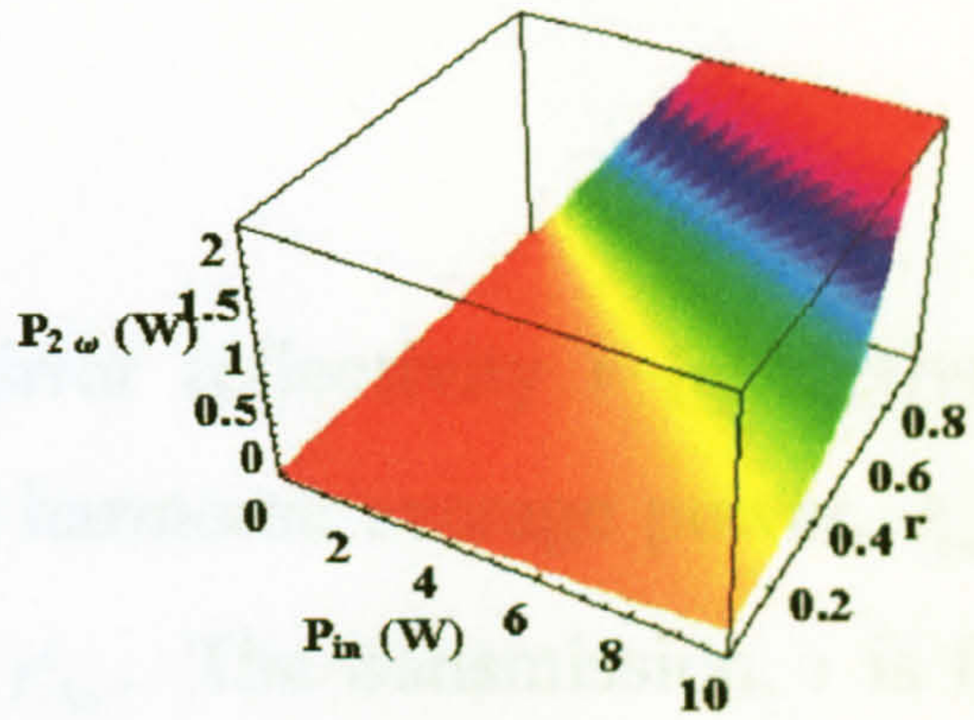

$\gamma'_{3\omega} = 0.02\text{W}^{-1}, \gamma'_{2\omega} = 0.002\ \text{W}^{-1}$

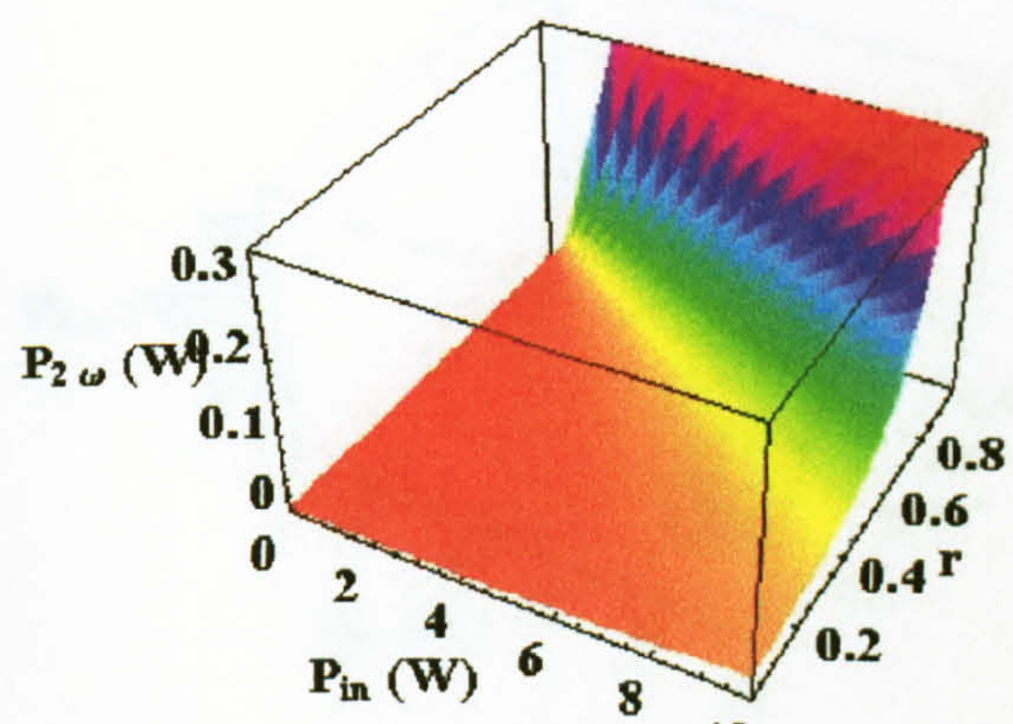

$\gamma'_{3\omega} = 0.02\text{W}^{-1}, \gamma'_{2\omega} = 0.0002\ \text{W}^{-1}$

Appendix Four.

(d) Dependency of cavity *mirror* reflectivity r (exclusive of input coupling) on the second harmonic average power, $P_{3\omega}$ (W) for various values of $\gamma'_{2\omega}$ and $\gamma'_{3\omega}$. The transmission, t is fixed as t=0.98.

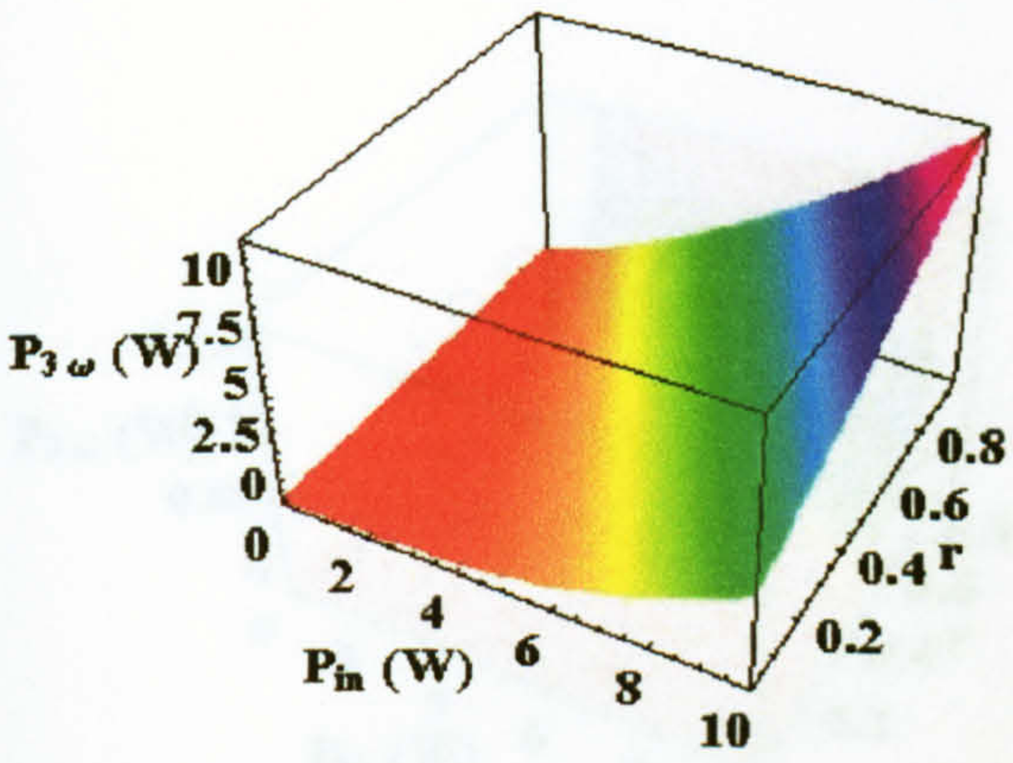

$\gamma'_{3\omega} = 0.2\text{W}^{-1}, \gamma'_{2\omega} = 0.02\ \text{W}^{-1}$

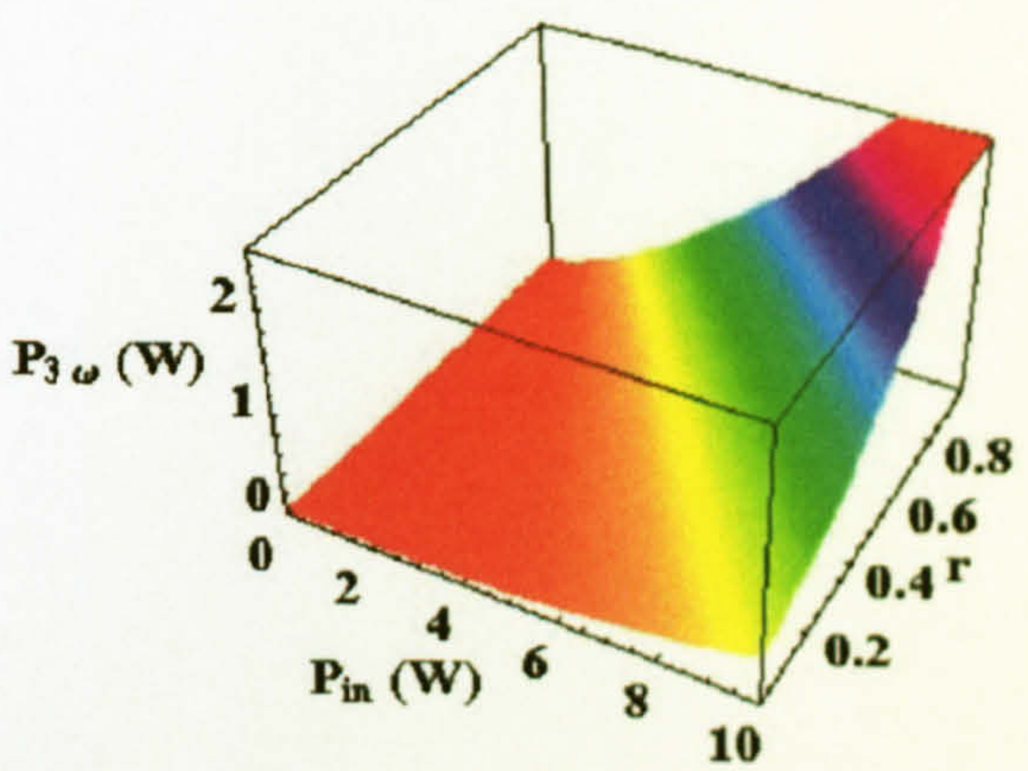

$\gamma'_{3\omega} = 0.02\text{W}^{-1}, \gamma'_{2\omega} = 0.02\ \text{W}^{-1}$

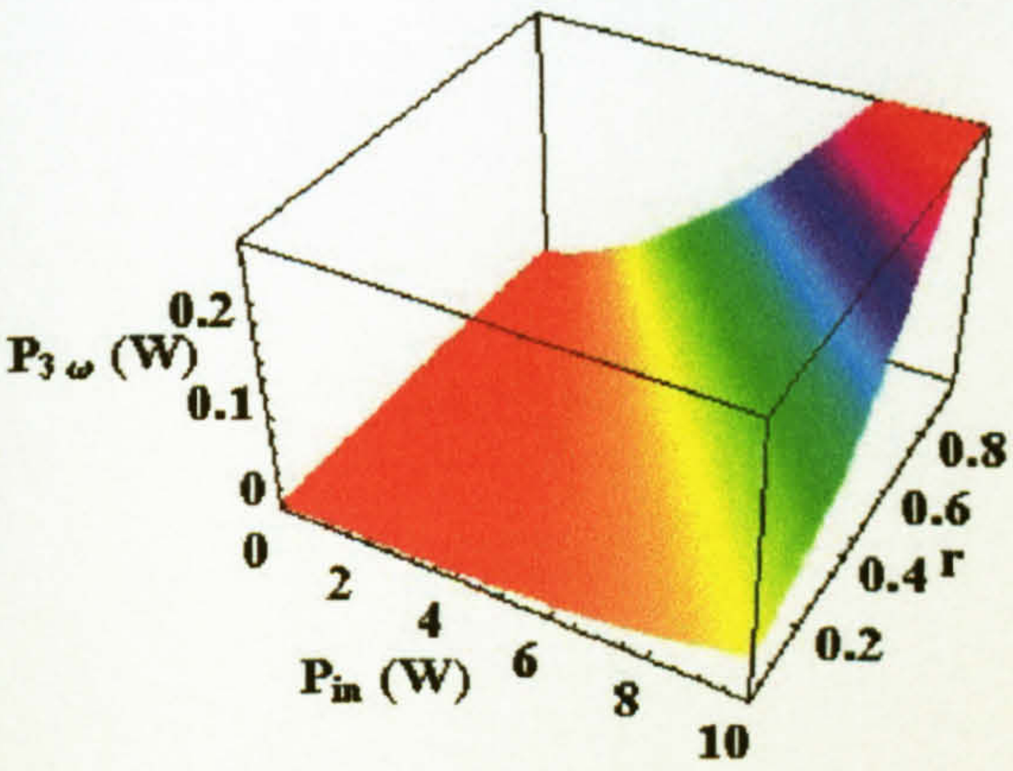

$\gamma'_{3\omega} = 0.002\text{W}^{-1}, \gamma'_{2\omega} = 0.02\ \text{W}^{-1}$

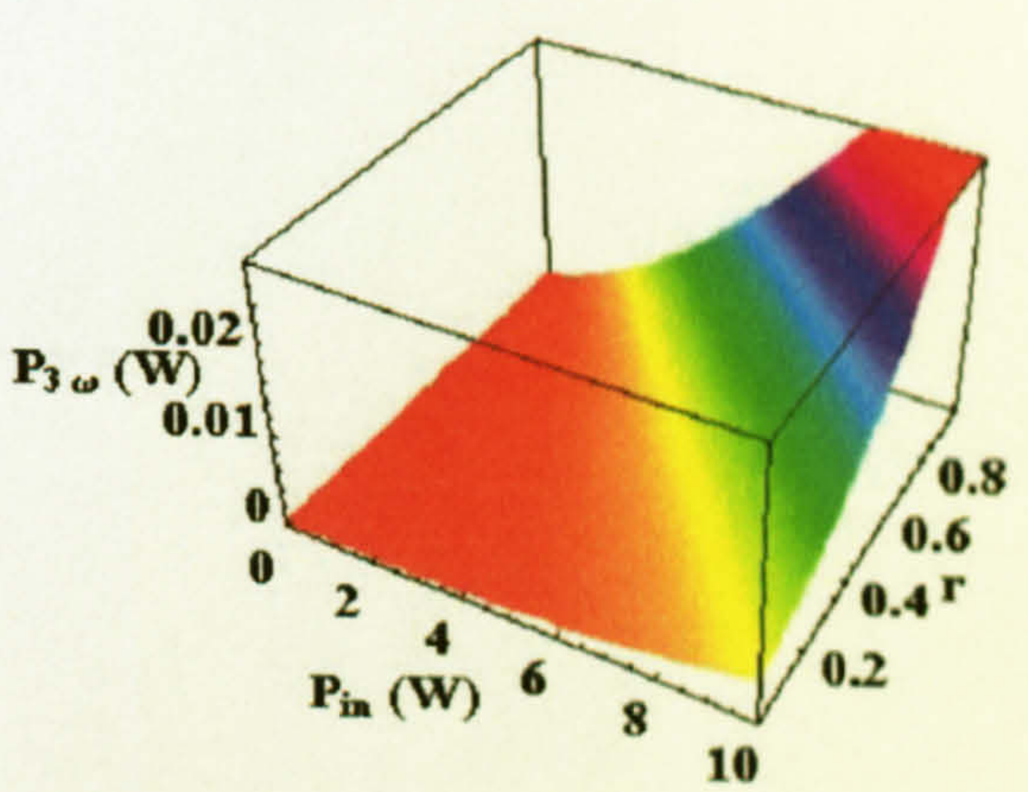

$\gamma'_{3\omega} = 0.0002\text{W}^{-1}, \gamma'_{2\omega} = 0.02\ \text{W}^{-1}$

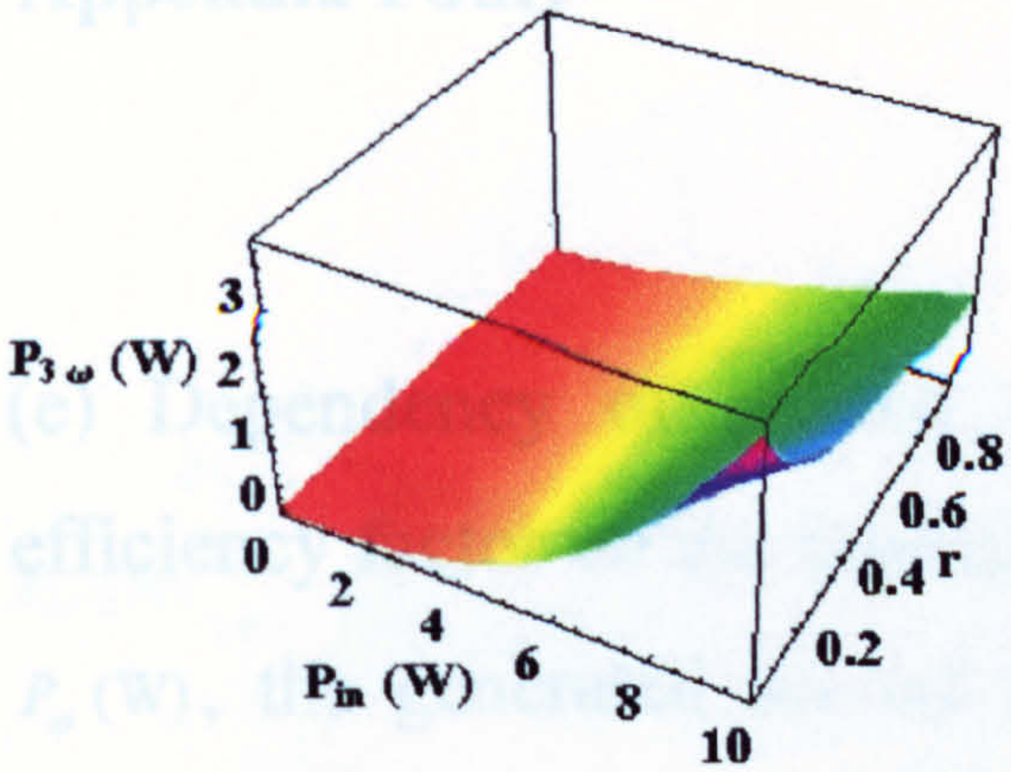

$\gamma'_{3\omega} = 0.02\text{W}^{-1}, \gamma'_{2\omega} = 0.2\ \text{W}^{-1}$

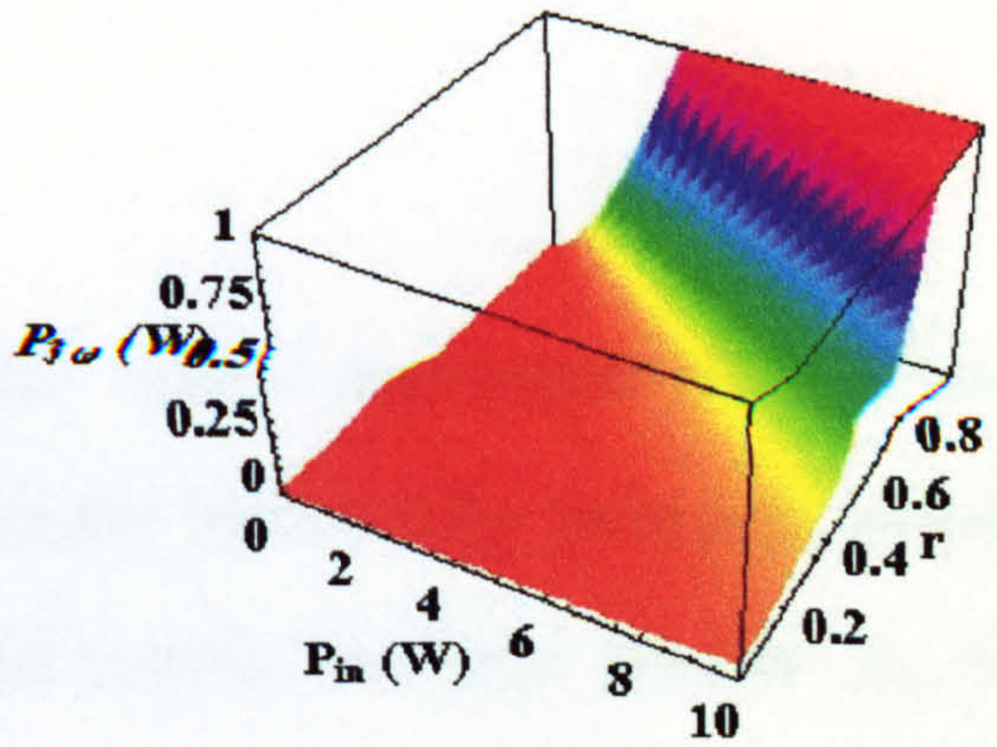

$\gamma'_{3\omega} = 0.02\text{W}^{-1}, \gamma'_{2\omega} = 0.002\ \text{W}^{-1}$

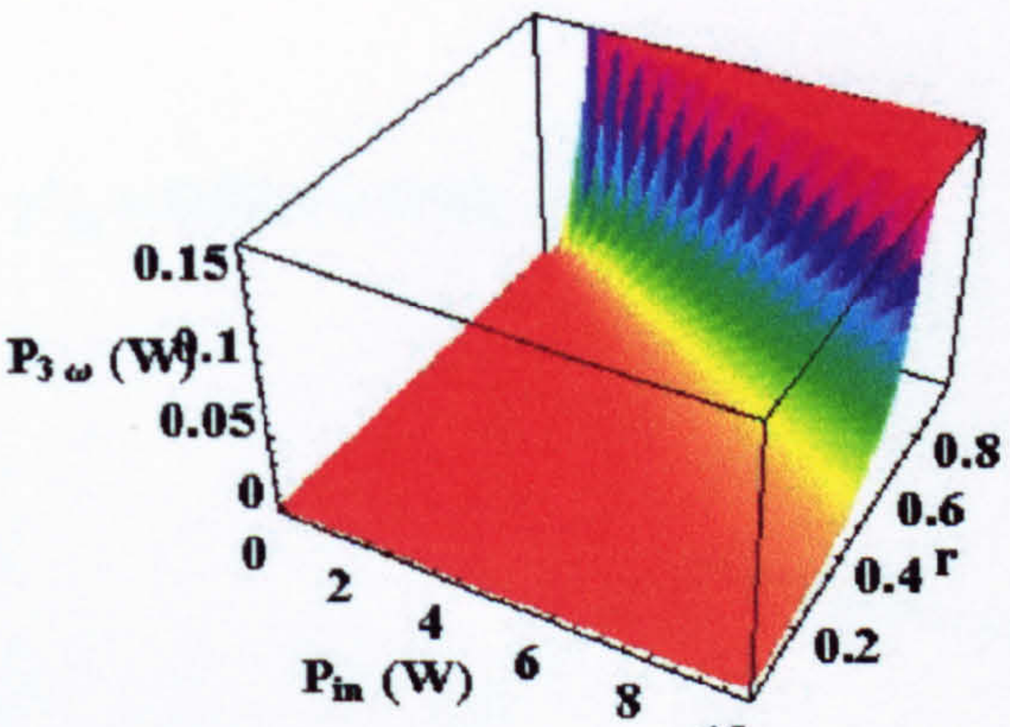

$\gamma'_{3\omega} = 0.02\text{W}^{-1}, \gamma'_{2\omega} = 0.0002\ \text{W}^{-1}$

Appendix Four.

(e) Dependency of second and third harmonic conversion efficiency factor on the fundamental intracavity average power, P_{ω} (W), the generated second harmonic average power $P_{2\omega}$ (W) and the generated third harmonic average power $P_{3\omega}$ (W) for fixed r and t.

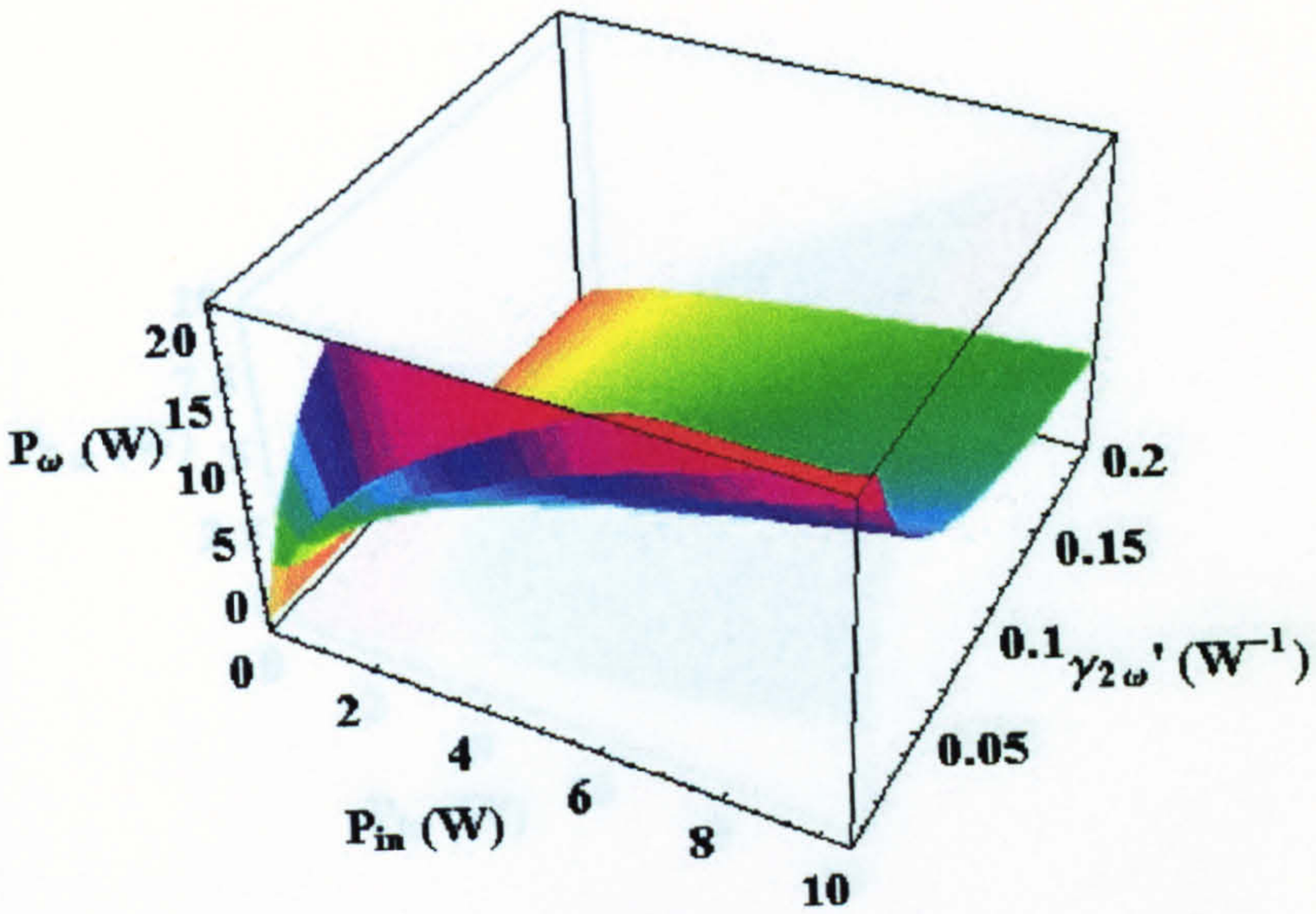

$\gamma'_{3\omega} = 0.02, r = 0.96,\ t = 0.98$

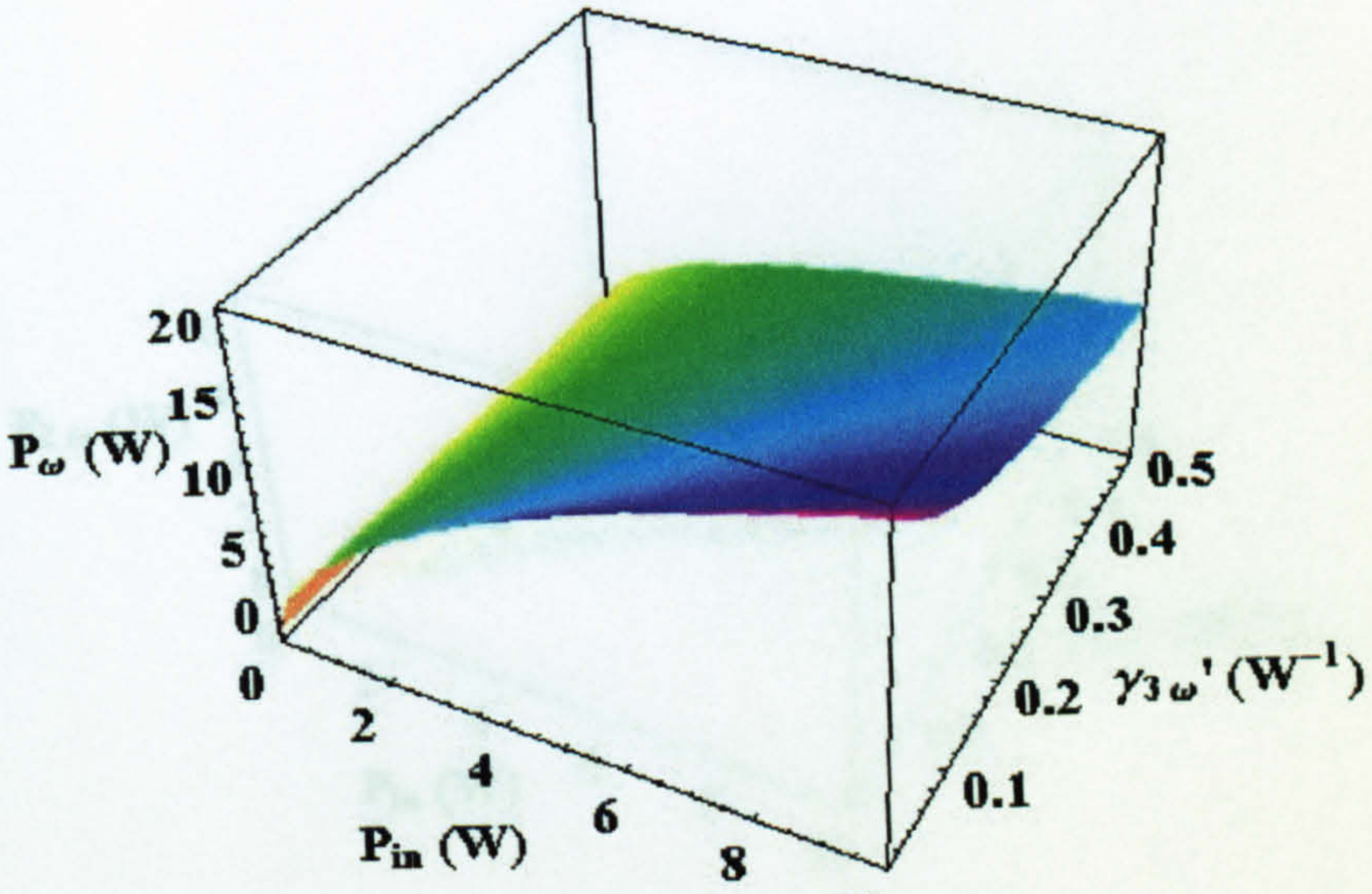

$\gamma'_{2\omega} = 0.02, r = 0.96,\ t = 0.98$

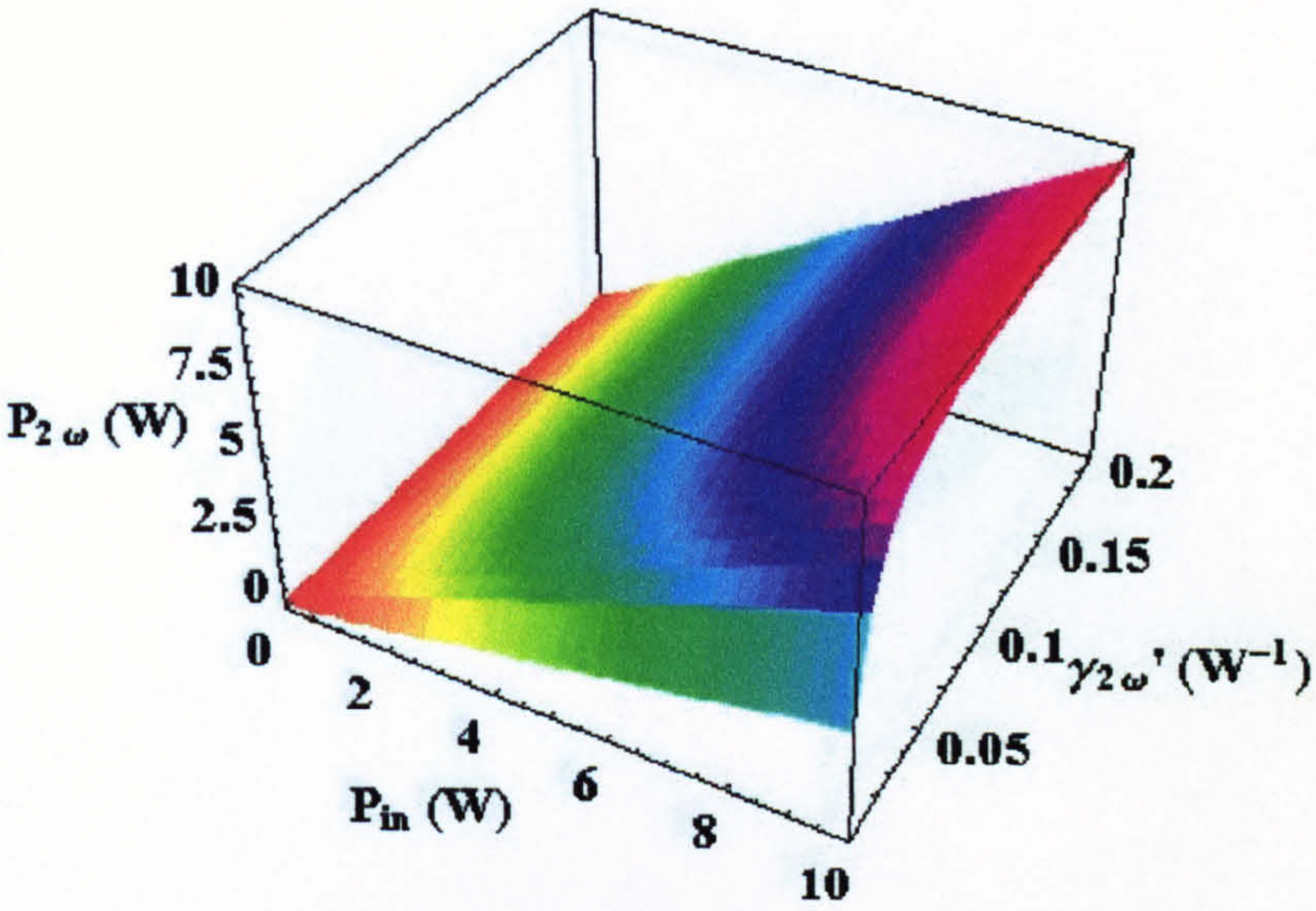

$\gamma'_{3\omega} = 0.02, r = 0.96,\ t = 0.98$

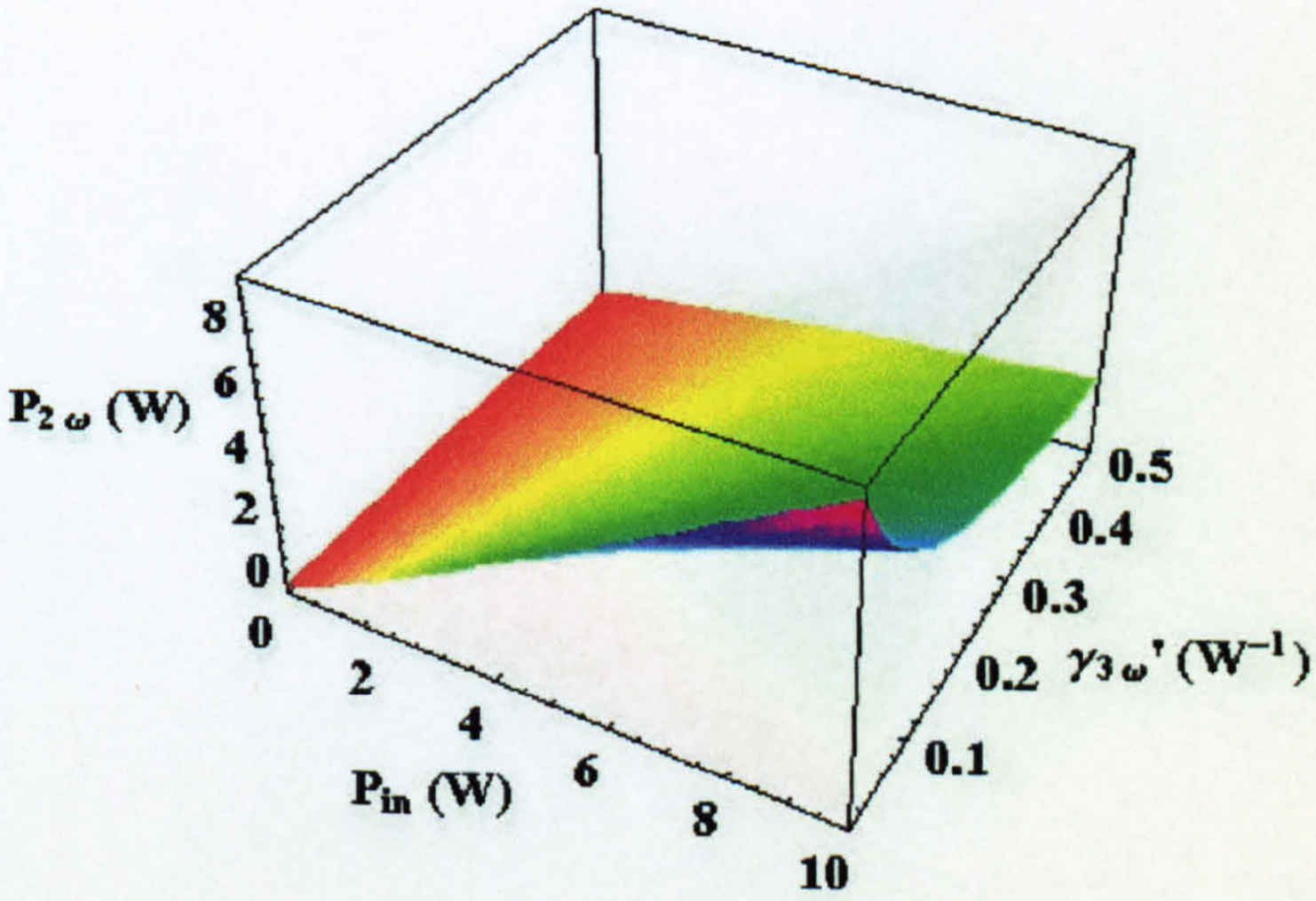

$\gamma'_{2\omega} = 0.02, r = 0.96,\ t = 0.98$

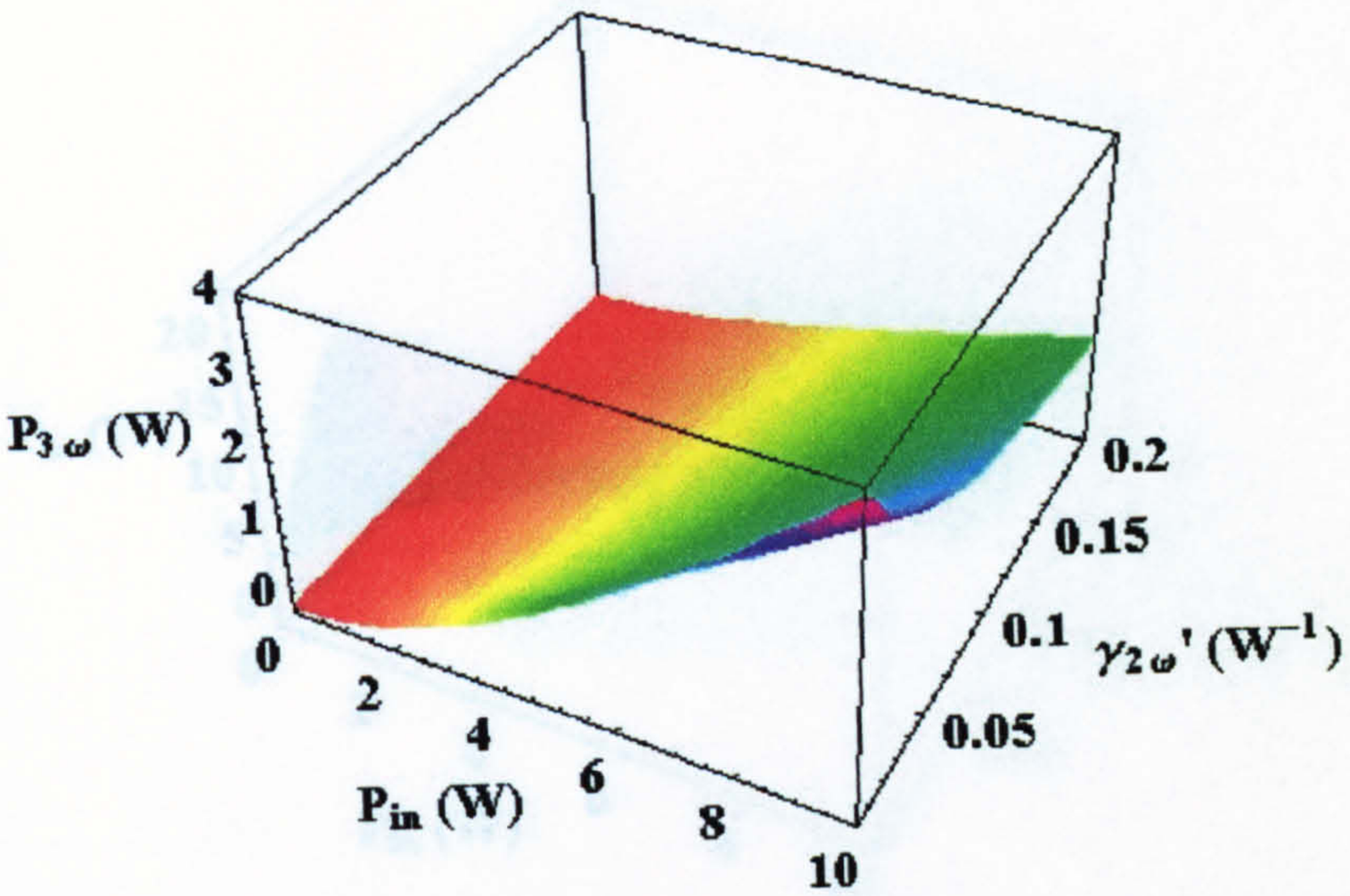

$\gamma'_{3\omega} = 0.02, r = 0.96,\ t = 0.98$

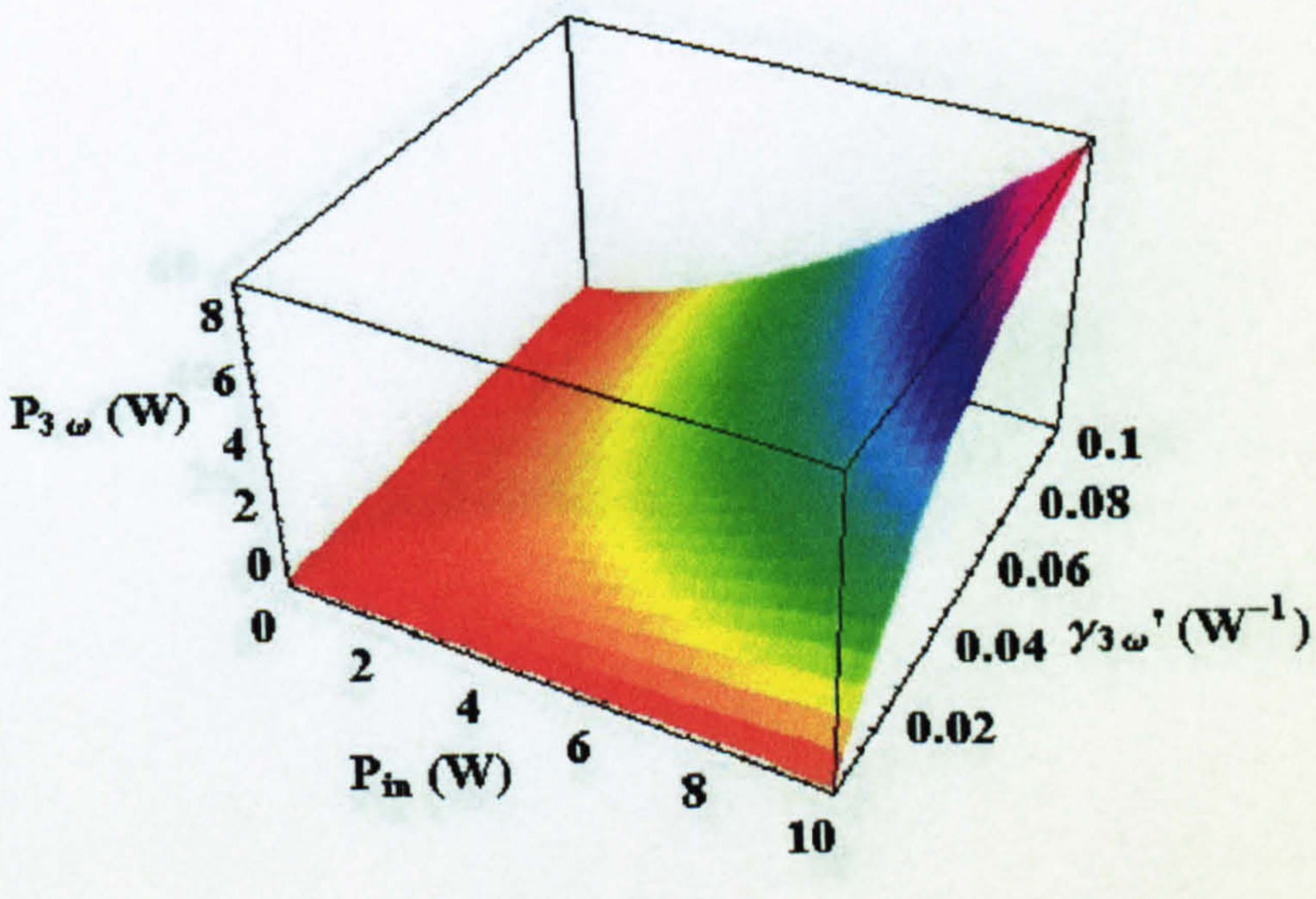

$\gamma'_{2\omega} = 0.02, r = 0.96,\ t = 0.98$

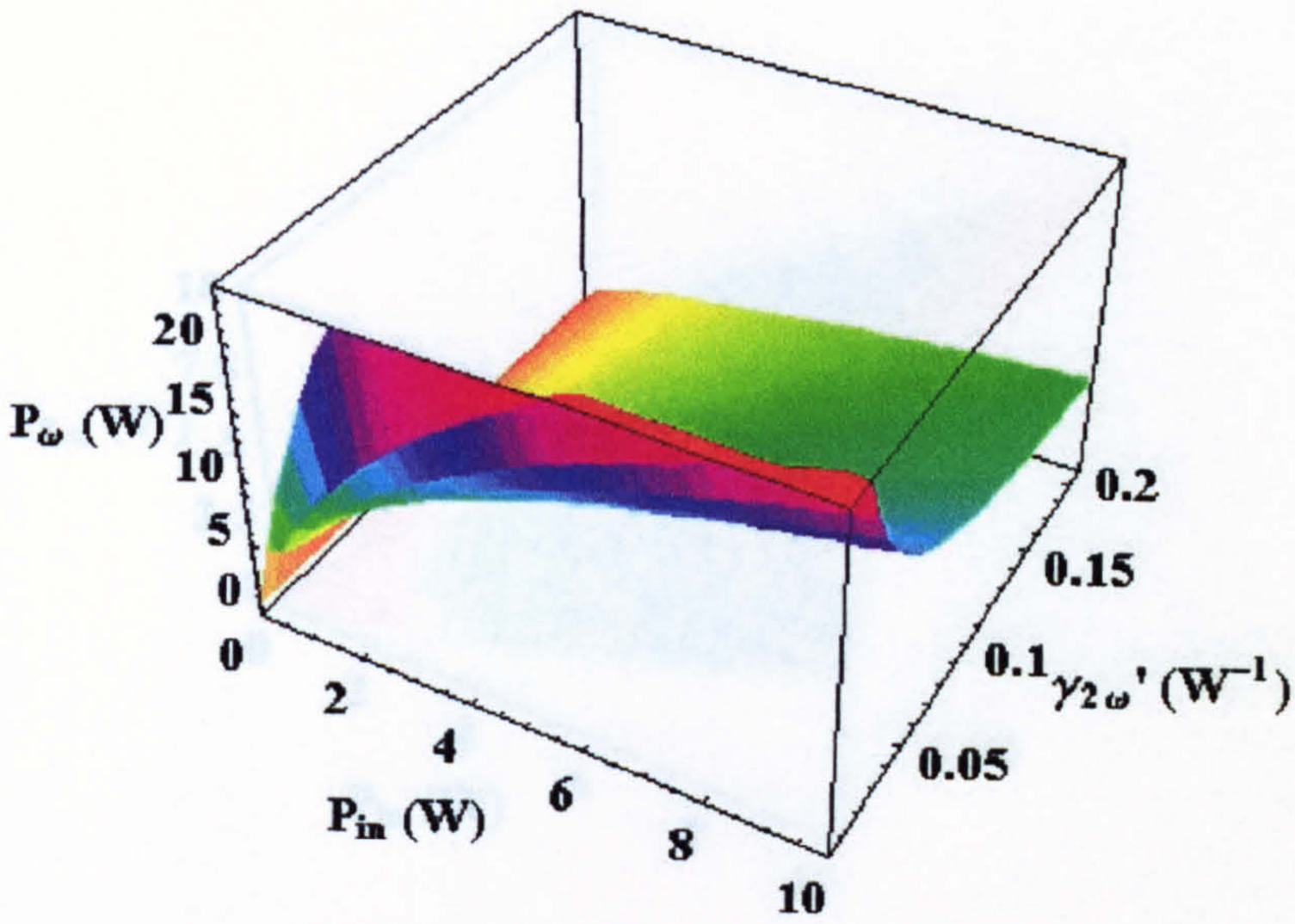

$\gamma'_{3\omega} = 0.002, r = 0.96,\ t = 0.98$

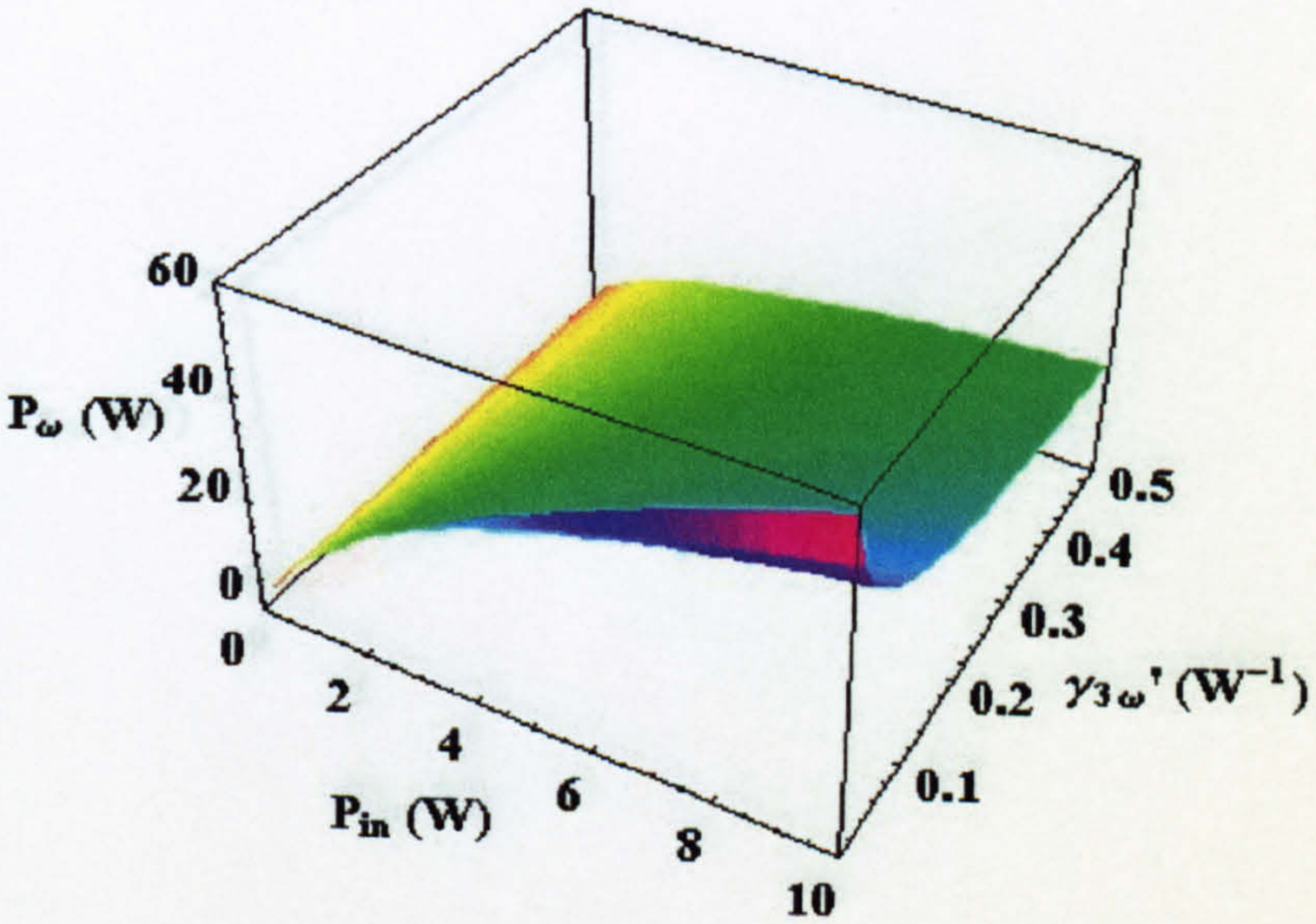

$\gamma'_{3\omega} = 0.002, r = 0.96,\ t = 0.98$

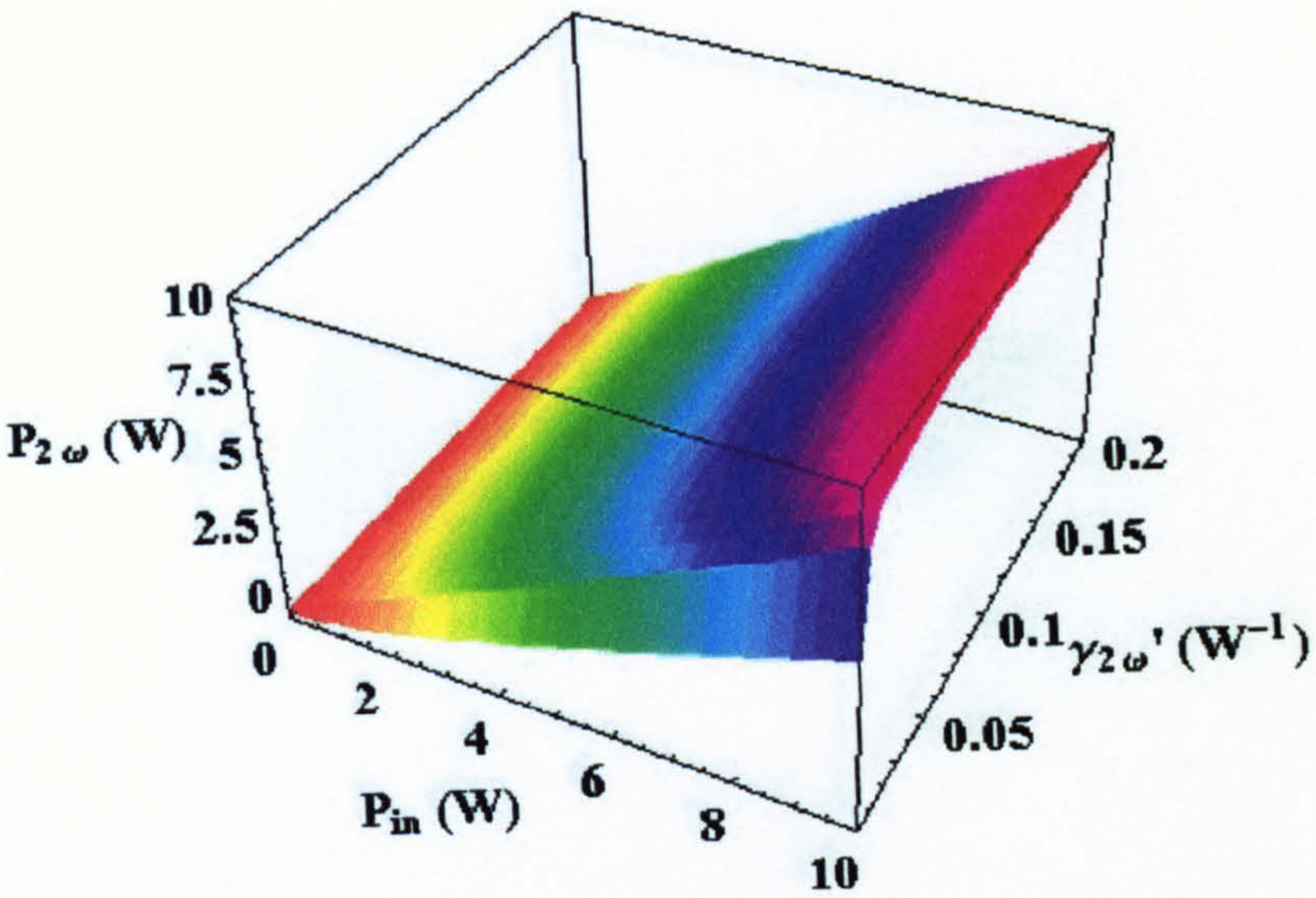

$\gamma'_{3\omega} = 0.002, r = 0.96,\ t = 0.98$

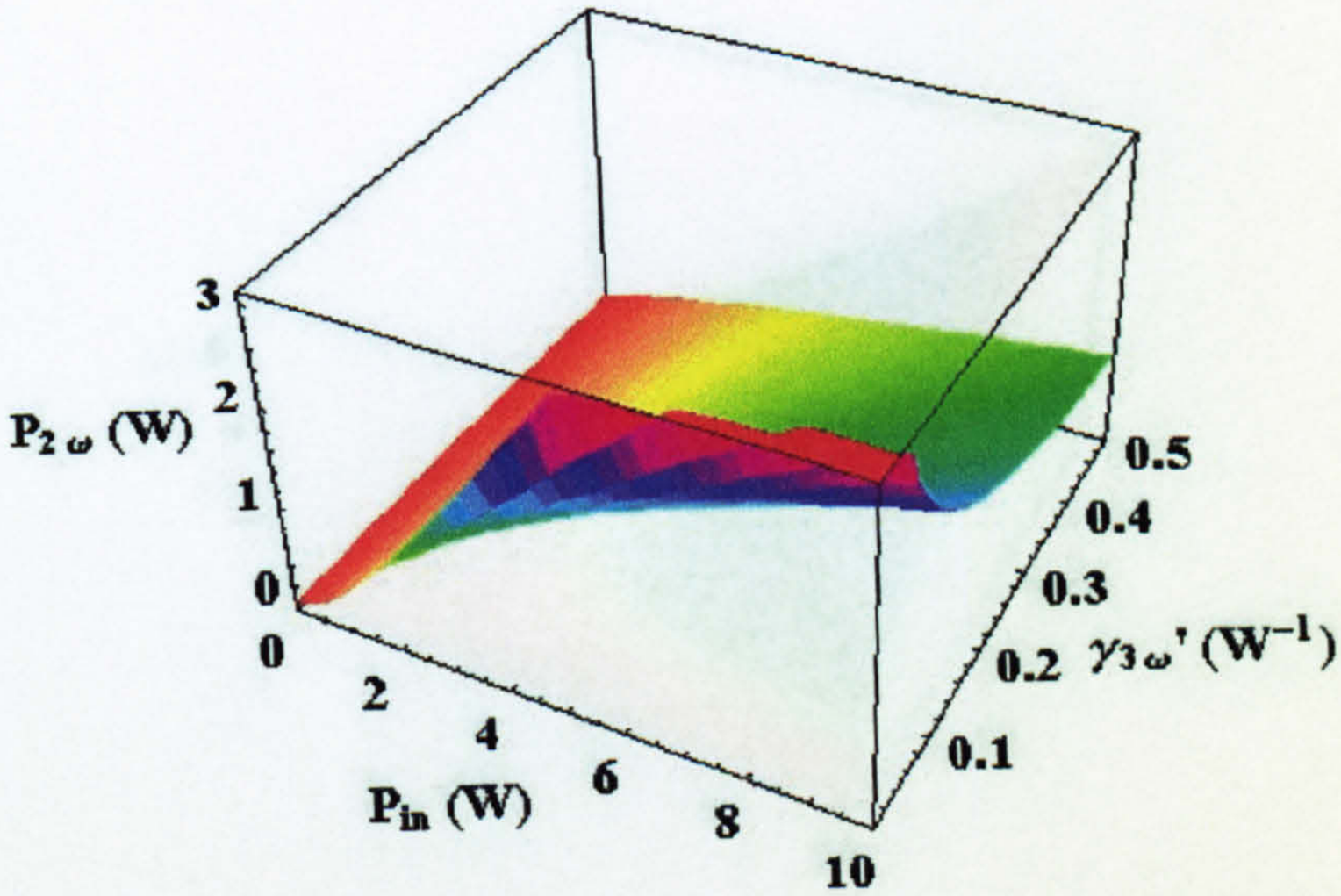

$\gamma'_{2\omega} = 0.002, r = 0.96,\ t = 0.98$

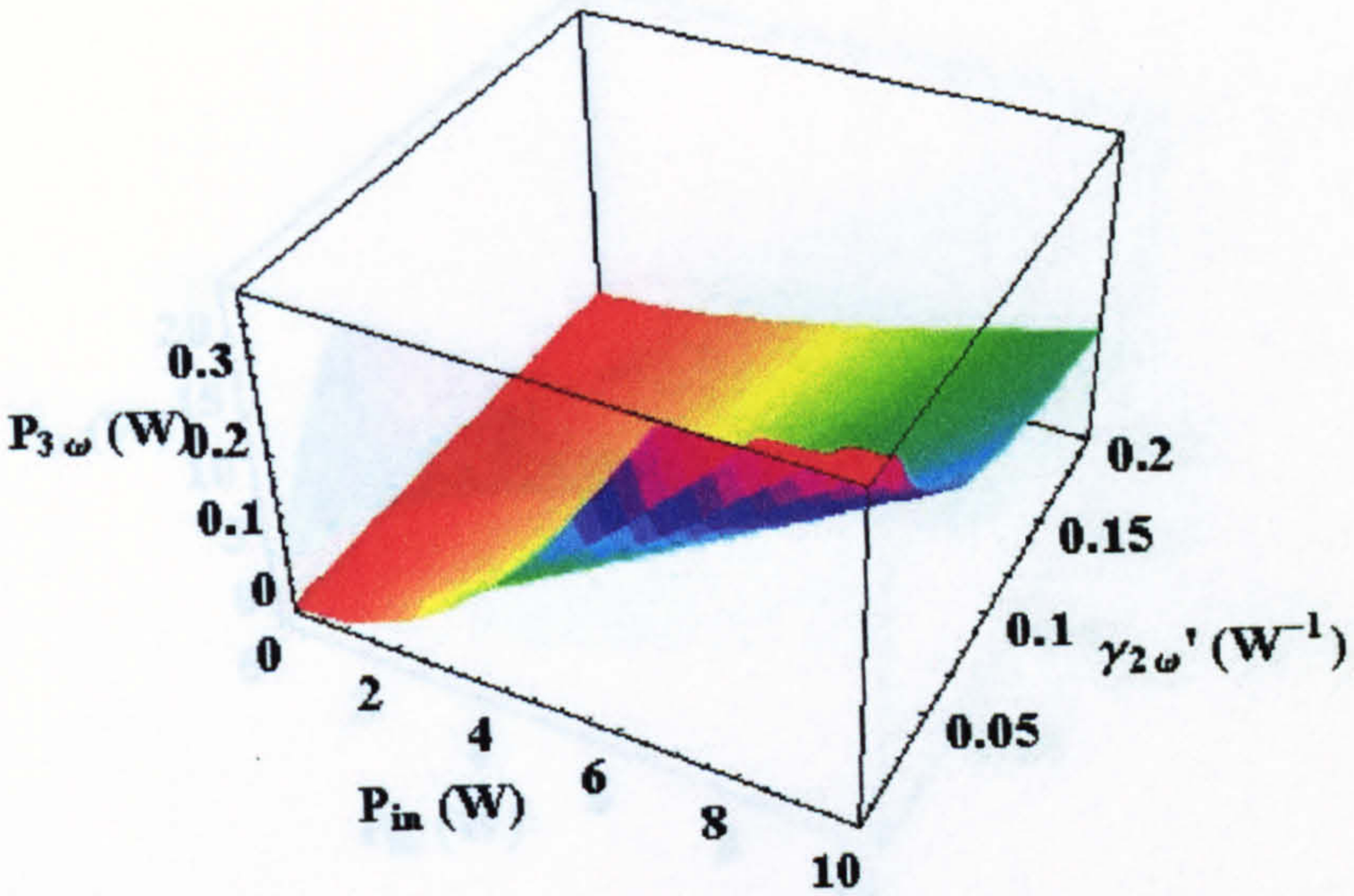

$\gamma'_{3\omega} = 0.002, r = 0.96,\ t = 0.98$

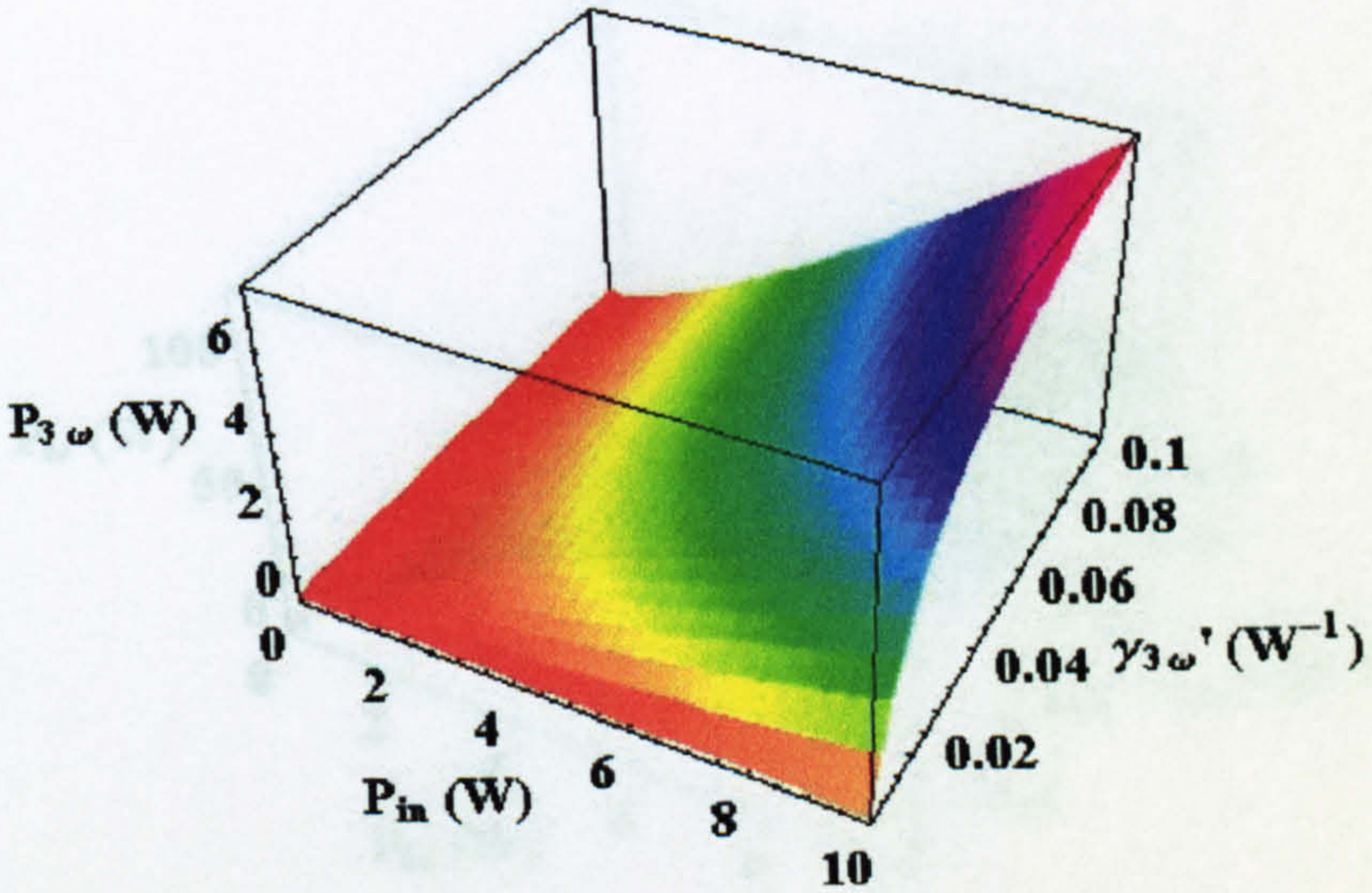

$\gamma'_{2\omega} = 0.002, r = 0.96,\ t = 0.98$

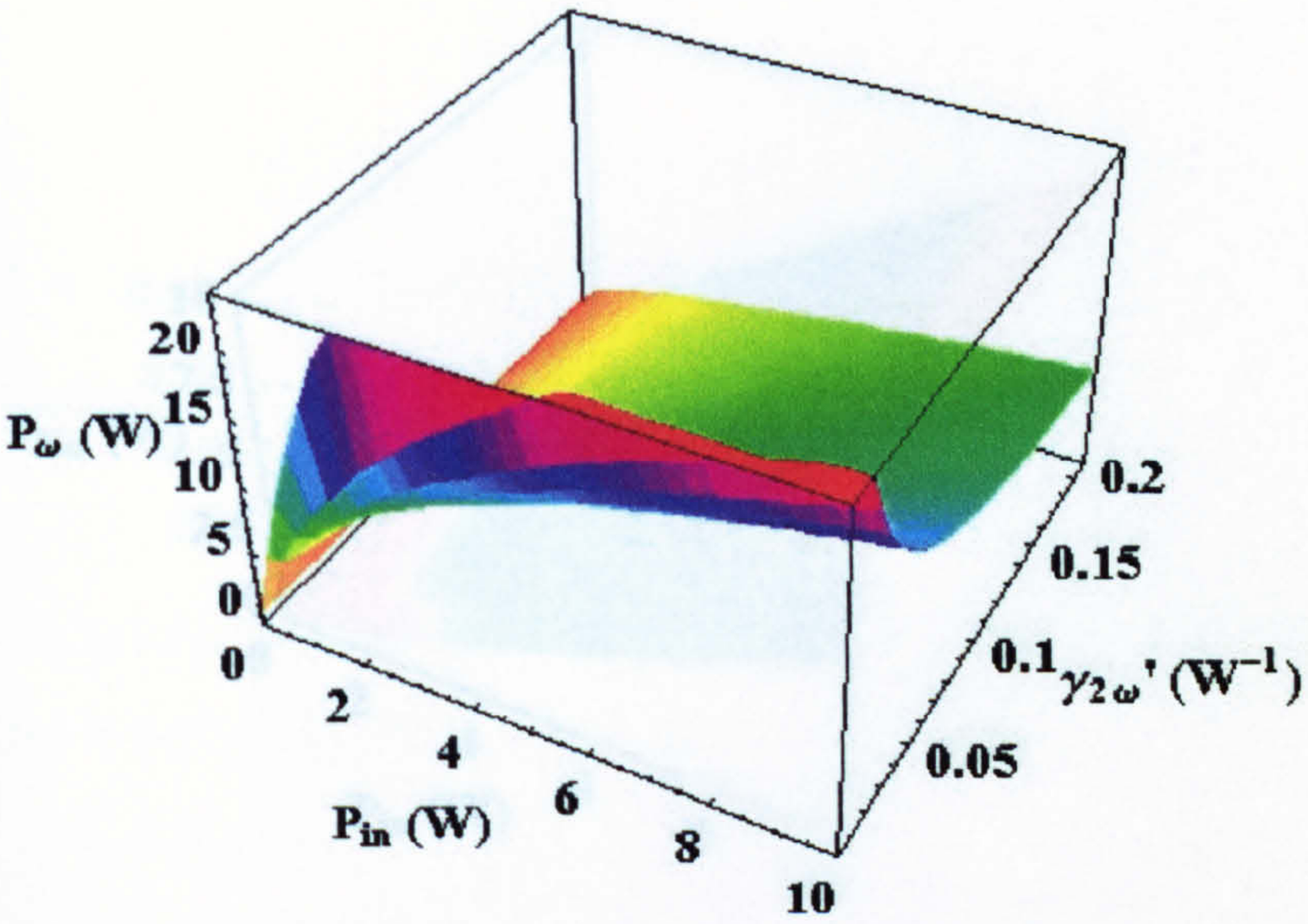

$\gamma'_{3\omega} = 0.0002, r = 0.96,\ t = 0.98$

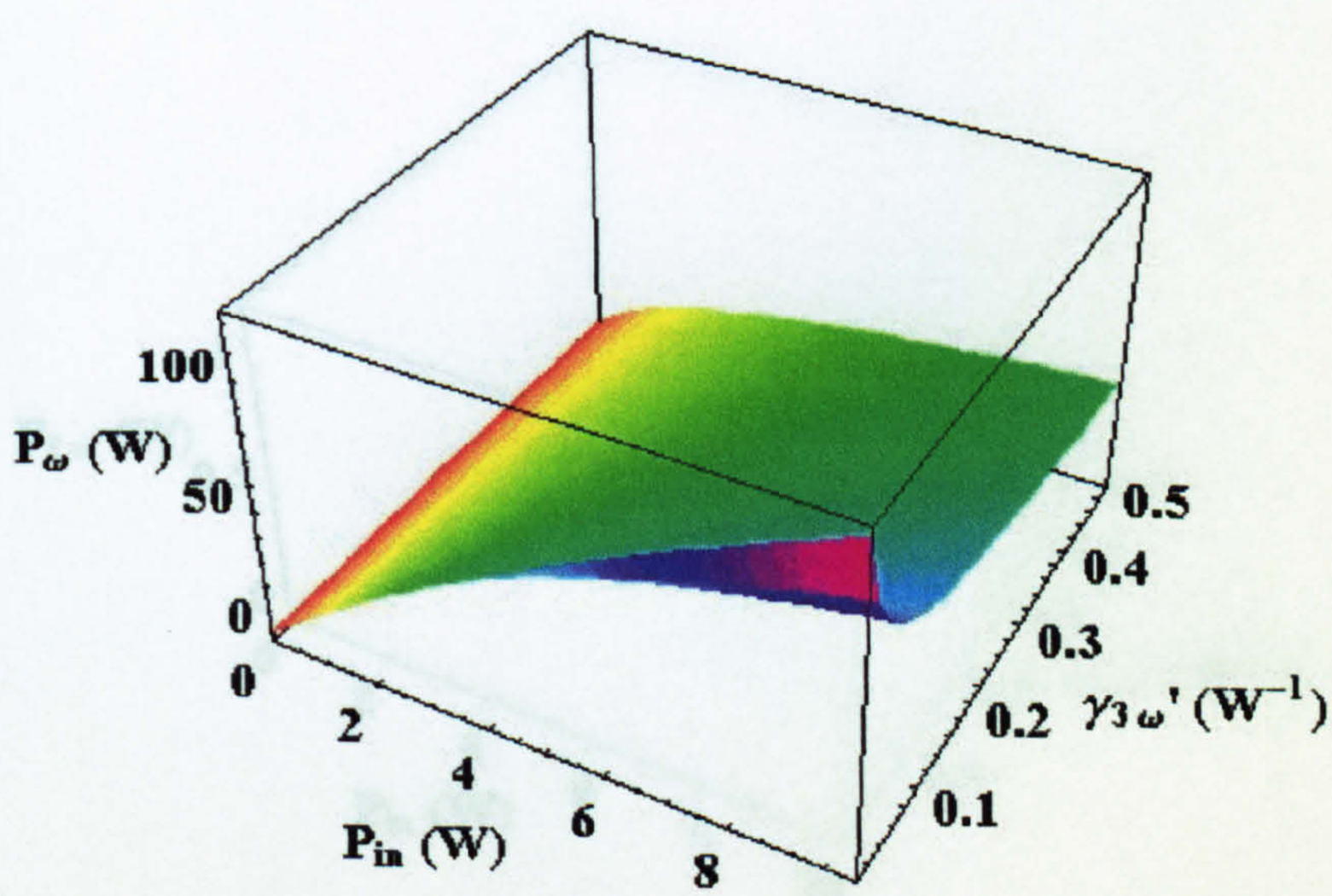

$\gamma'_{2\omega} = 0.0002, r = 0.96,\ t = 0.98$

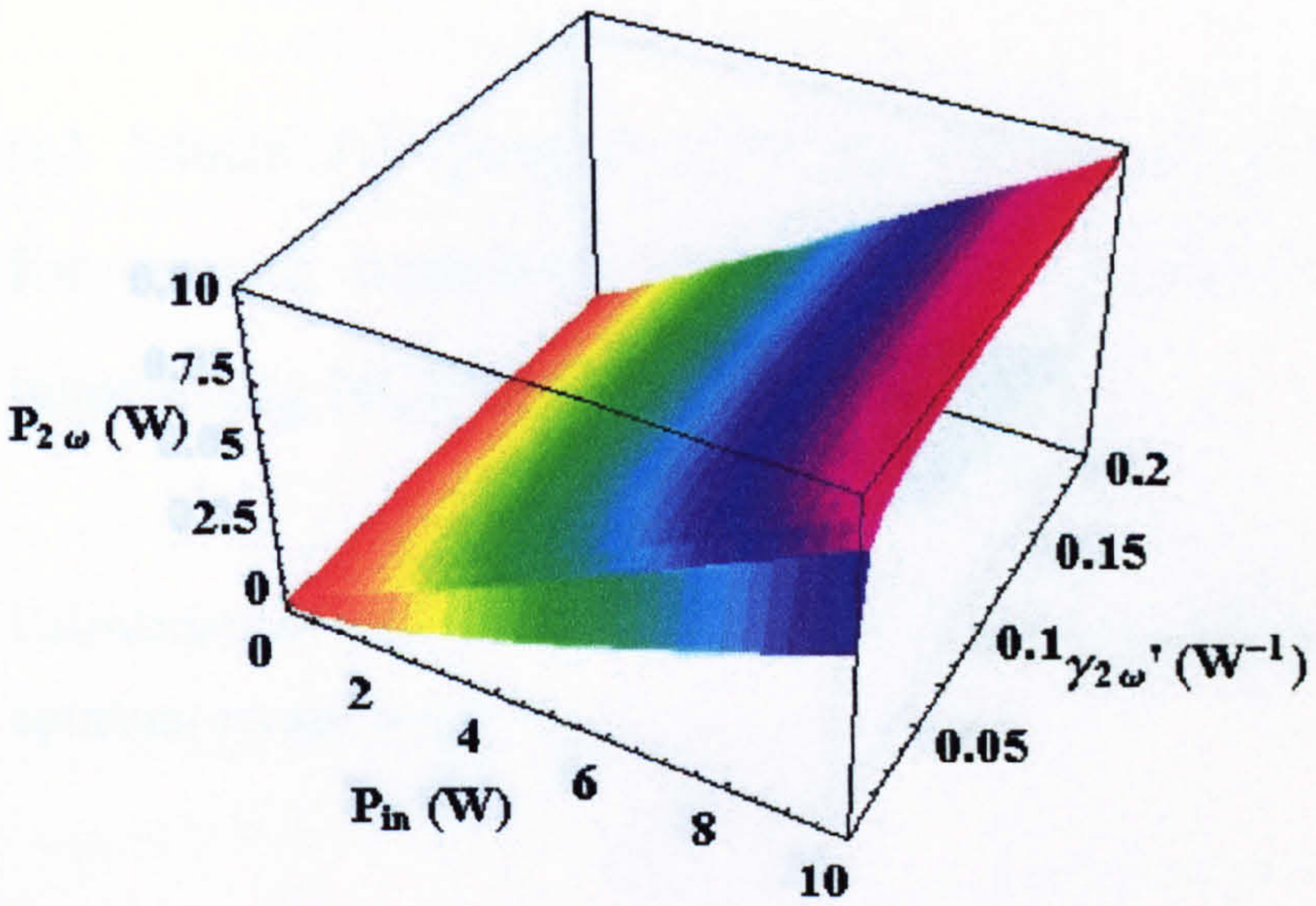

$\gamma'_{3\omega} = 0.0002, r = 0.96,\ t = 0.98$

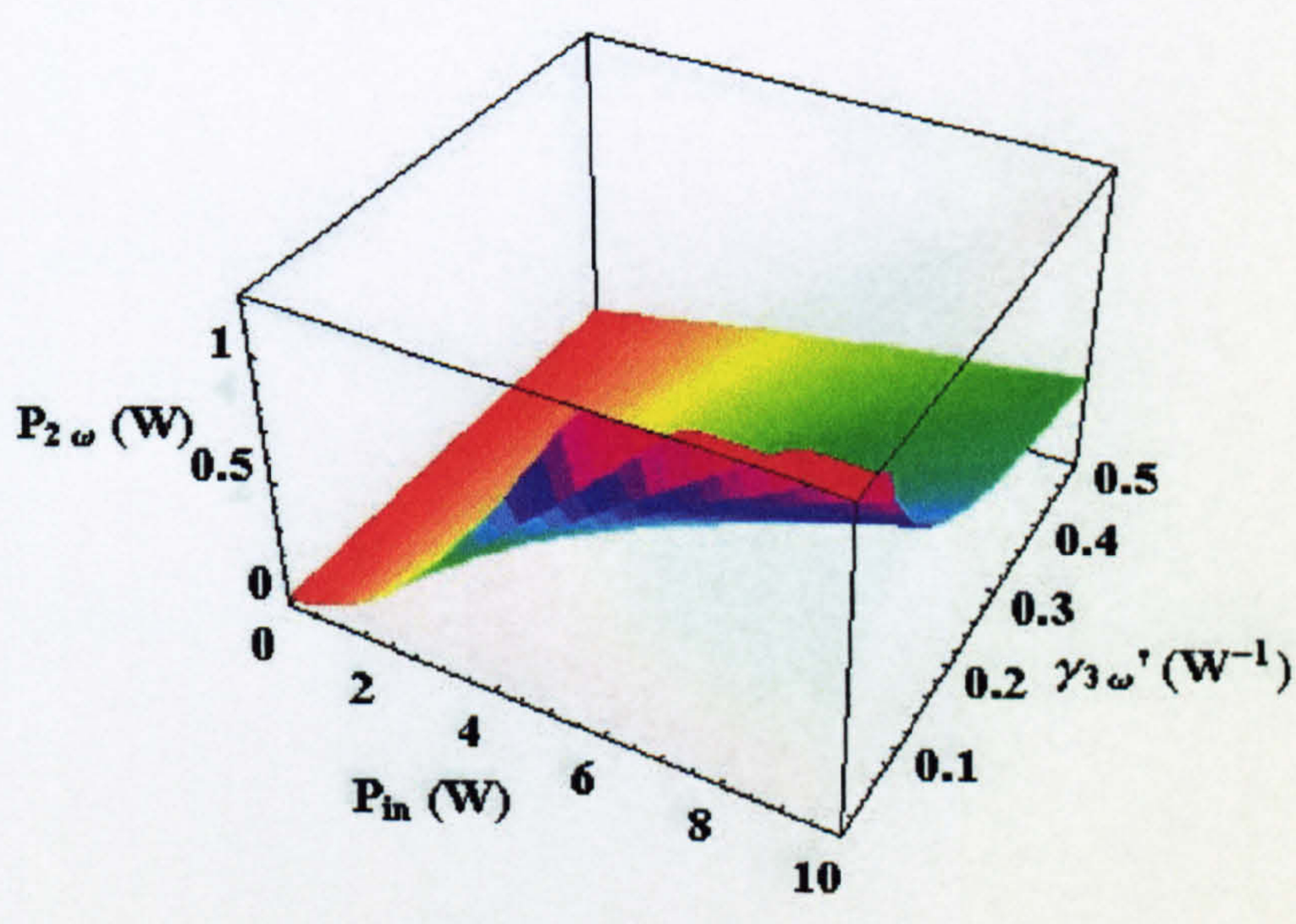

$\gamma'_{2\omega} = 0.0002, r = 0.96,\ t = 0.98$

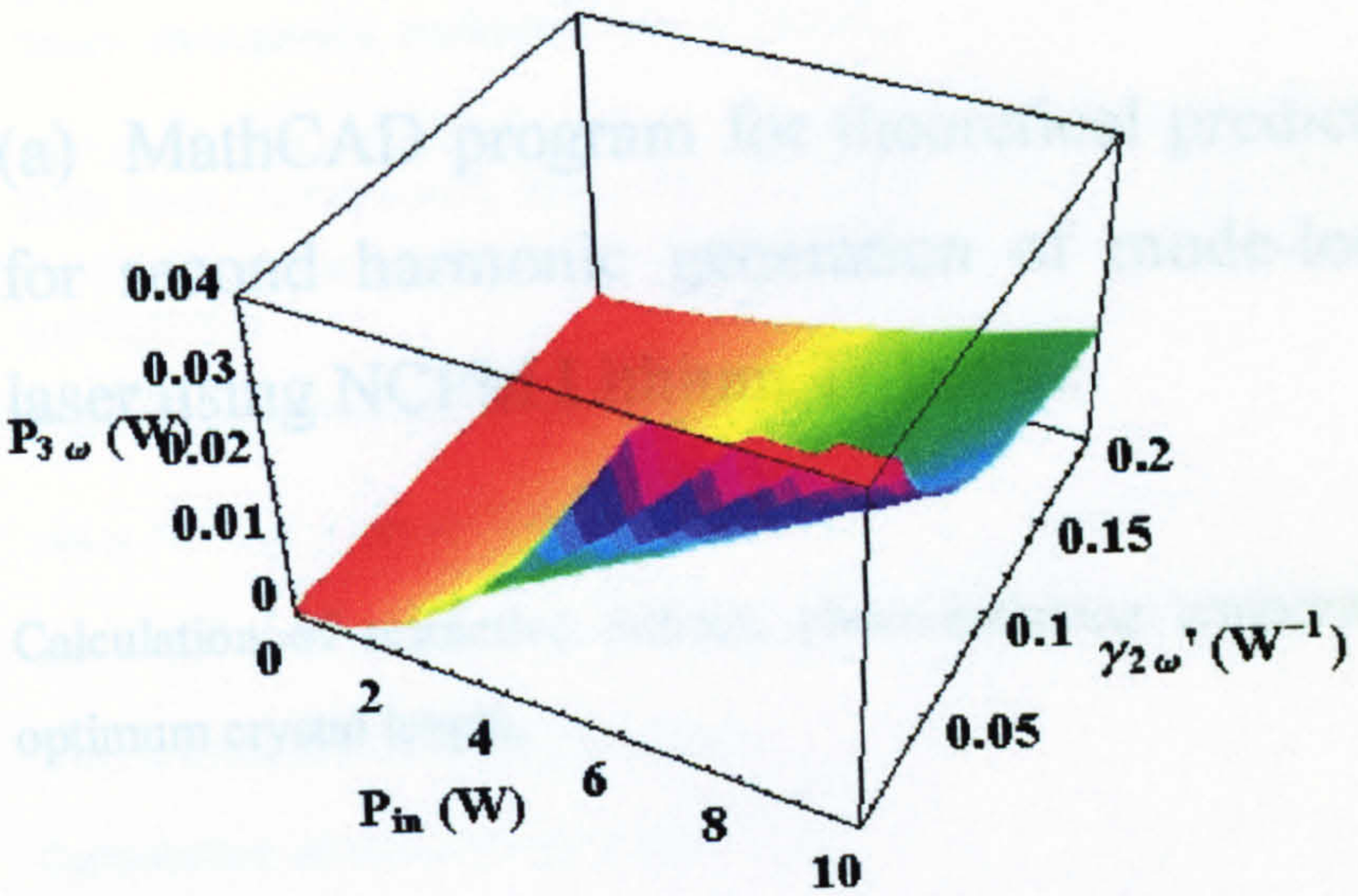

$\gamma'_{3\omega} = 0.0002, r = 0.96, t = 0.98$

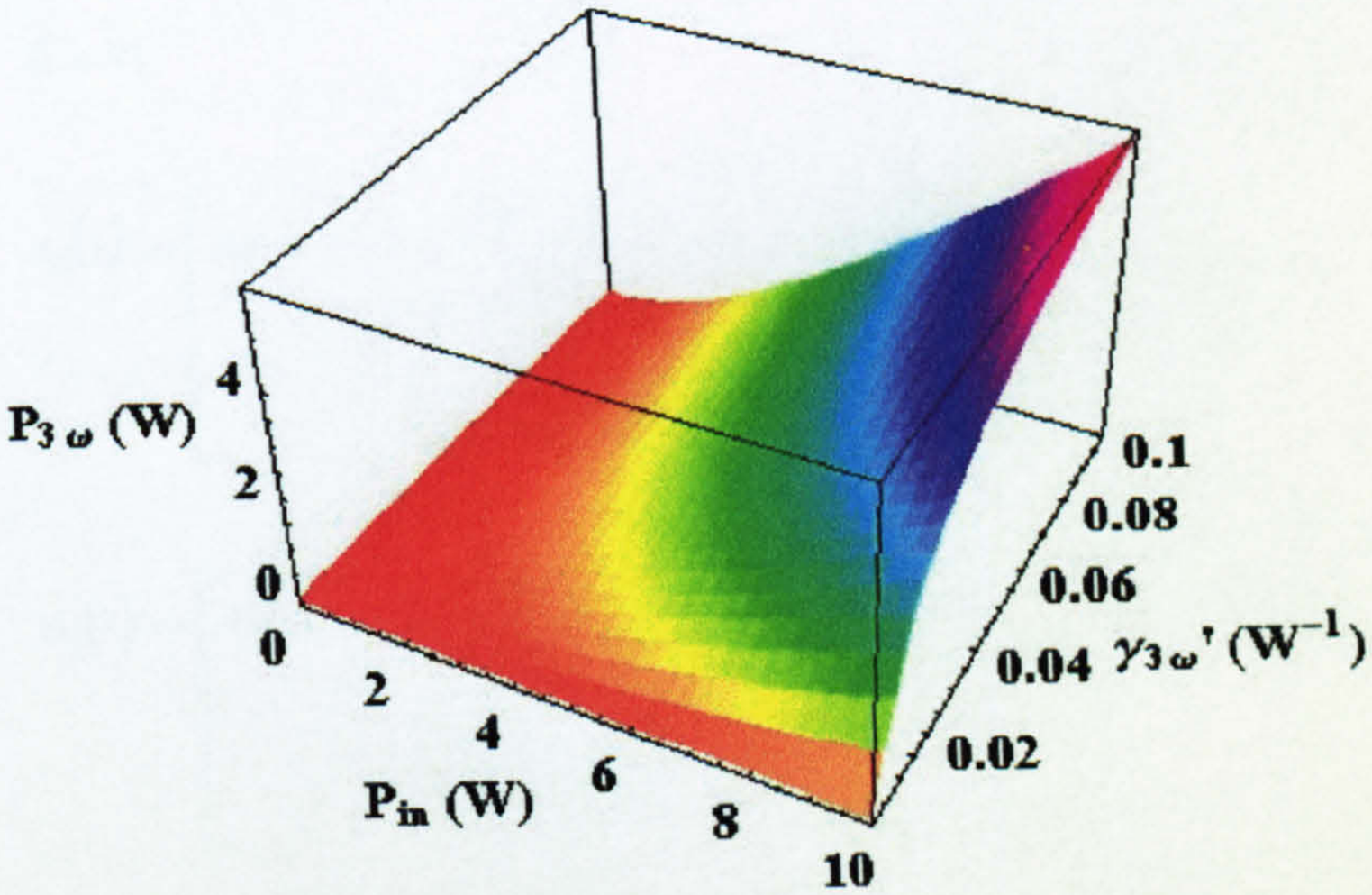

$\gamma'_{2\omega} = 0.0002, r = 0.96, t = 0.98$

Appendix Five.

(a) MathCAD program for theoretical prediction of properties for second harmonic generation of mode-locked Nd^{3+}:YVO_4 laser using NCPM Lithium Triborate

Calculation of refractive indices, phase-matching temperature, beam divergence, optimum crystal length.

Second harmonic generation in Lithium Triborate

Includes calculation of refractive indices, phasematching temperature, beam divergence, optimum crystal length.

Lithium Triborate (LBO): Sellmeier's, dispersion of thermo-optic coeffs.
Data from "Temperature dispersion of refractive indices inβ-BaB_2O_4 and LiB_3O_5 crystals for nonlinear optical devices", J. App. Phys., Vol. 78, No. 11, 1995 (pp52-6760)

Physical constants and units

$nm := 10^{-9} \cdot m \quad \mu m := 10^{-6} \cdot m \quad mm := 10^{-3} \cdot m \quad cm := 10^{-2} \cdot m \quad A \equiv 10^{-10} \cdot m$

$c := 3 \cdot 10^{8} \cdot \left(m \cdot sec^{-1}\right) \quad \varepsilon_0 := 8.854 \cdot 10^{-12} \cdot \frac{farad}{m} \quad ps := 10^{-12} \cdot sec$

$TOL := 0.00000000000000000000001$

Calculation of refractive indices

Wavelength range (Transparency region) $\lambda := 2000 \cdot A, 2010 \cdot A .. 12000 \cdot A$

The room Temperature Sellmeier coeffs.

$Ax := 1.4426279 \quad Bx := 1.0109932 \quad Cx := 1.1210197 \cdot 10^{-2} \quad Dx := 1.2363218$

$Ay := 1.5014015 \quad By := 1.0388217 \quad Cy := 1.2157100 \cdot 10^{-2} \quad Dy := 1.7567133$

$Az := 1.4489240 \quad Bz := 1.1365228 \quad Cz := 1.1676746 \cdot 10^{-2} \quad Dz := 1.5830069$

$E := 91$

$$n_x(\lambda) := \left[Ax + \frac{Bx}{1 - \frac{Cx}{\left(\frac{\lambda}{A \cdot 10000}\right)^2}} + \frac{Dx}{1 - \frac{E}{\left(\frac{\lambda}{A \cdot 10000}\right)^2}} \right]^{\frac{1}{2}}$$

$$n_y(\lambda) := \left[Ay + \frac{By}{1 - \frac{Cy}{\left(\frac{\lambda}{A \cdot 10000}\right)^2}} + \frac{Dy}{1 - \frac{E}{\left(\frac{\lambda}{A \cdot 10000}\right)^2}} \right]^{\frac{1}{2}}$$

$$n_z(\lambda) := \left[Az + \frac{Bz}{1 - \frac{Cz}{\left(\frac{\lambda}{A \cdot 10000}\right)^2}} + \frac{Dz}{1 - \frac{E}{\left(\frac{\lambda}{A \cdot 10000}\right)^2}} \right]^{\frac{1}{2}}$$

Temperature Range (deg. C) $T := 20, 20.1 .. 300$

$\lambda_{igx} := 0.053 \cdot \mu m$

Isentropic Band Gaps /μm $\lambda_{igy} := 0.0327 \cdot \mu m$

$\lambda_{igz} := 0.0435 \cdot \mu m$

Normalised Dispersive Wavelengths $R_x(\lambda) := \dfrac{\lambda^2}{\lambda^2 - \lambda_{igx}^2}$

$$R_y(\lambda) := \frac{\lambda^2}{\lambda^2 - \lambda_{igy}^2}$$

$$R_z(\lambda) := \frac{\lambda^2}{\lambda^2 - \lambda_{igz}^2}$$

Fitting Coeffs.

$G_x := -127.70167 \cdot 10^{-6}$

$G_y(T) := \left[\left(372.170 - 2.199 \cdot 10^{-1} \cdot T\right) + 1.1748 \cdot 10^{-3} \cdot T^2 - 2.05077 \cdot 10^{-6} \cdot T^3\right] \cdot 10^{-6}$

$G_z := -446.95031 \cdot 10^{-6}$

$H_x := 122.13435\ 10^{-6}$

$H_y := -415.10435\ 10^{-6}$

$H_z := 419.33410\ 10^{-6}$

Thermo-optic coeffs (dn/dT) $\delta n_{Tx}(\lambda) := \dfrac{G_x \cdot R_x(\lambda) + H_x \cdot R_x(\lambda)^2}{2 \cdot n_x(\lambda)}$

$$\delta n_{Ty}(T, \lambda) := \frac{G_y(T) \cdot R_y(\lambda) + H_y \cdot R_y(\lambda)^2}{2 \cdot n_y(\lambda)}$$

$$\delta n_{Tz}(T, \lambda) := \frac{G_z \cdot R_z(\lambda) + H_z \cdot R_z(\lambda)^2}{2 \cdot n_z(\lambda)}$$

Wavelength of $Nd:YVO_4$ $\lambda_1 := 1.064 \cdot \mu m$

Refractive indices at T

$$n_{Tx}(\lambda_1, T) := n_x(\lambda_1) + (T - 20) \cdot \delta n_{Tx}(\lambda_1)$$

$$n_{Ty}(\lambda_1, T) := n_y(\lambda_1) + (T - 20) \cdot \delta n_{Ty}(T, \lambda_1)$$

$$n_{Tz}(\lambda_1, T) := n_z(\lambda_1) + (T - 20) \cdot \delta n_{Tz}(T, \lambda_1)$$

Frequency Doubled wavelength $\lambda_2 := 0.532 \cdot \mu m$

Refractive indices at T

$$n_{Tx}(\lambda_2, T) := n_x(\lambda_2) + (T - 20) \cdot \delta n_{Tx}(\lambda_2)$$

$$n_{Ty}(\lambda_2, T) := n_y(\lambda_2) + (T - 20) \cdot \delta n_{Ty}(T, \lambda_2)$$

$$n_{Tz}(\lambda_2, T) := n_z(\lambda_2) + (T - 20) \cdot \delta n_{Tz}(T, \lambda_2)$$

90 degree PM: θ=90, ϕ=0, propagates along the y axis with fundamental along the z axis.

$$n_2(\lambda_2, T) := n_{Ty}(\lambda_2, T) \qquad n_1(\lambda_1, T) := n_{Tz}(\lambda_1, T)$$

$$\Delta K(T) := 2 \cdot \pi \cdot \left(\frac{n_2(\lambda_2, T)}{\lambda_2} - \frac{2 n_1(\lambda_1, T)}{\lambda_1} \right)$$

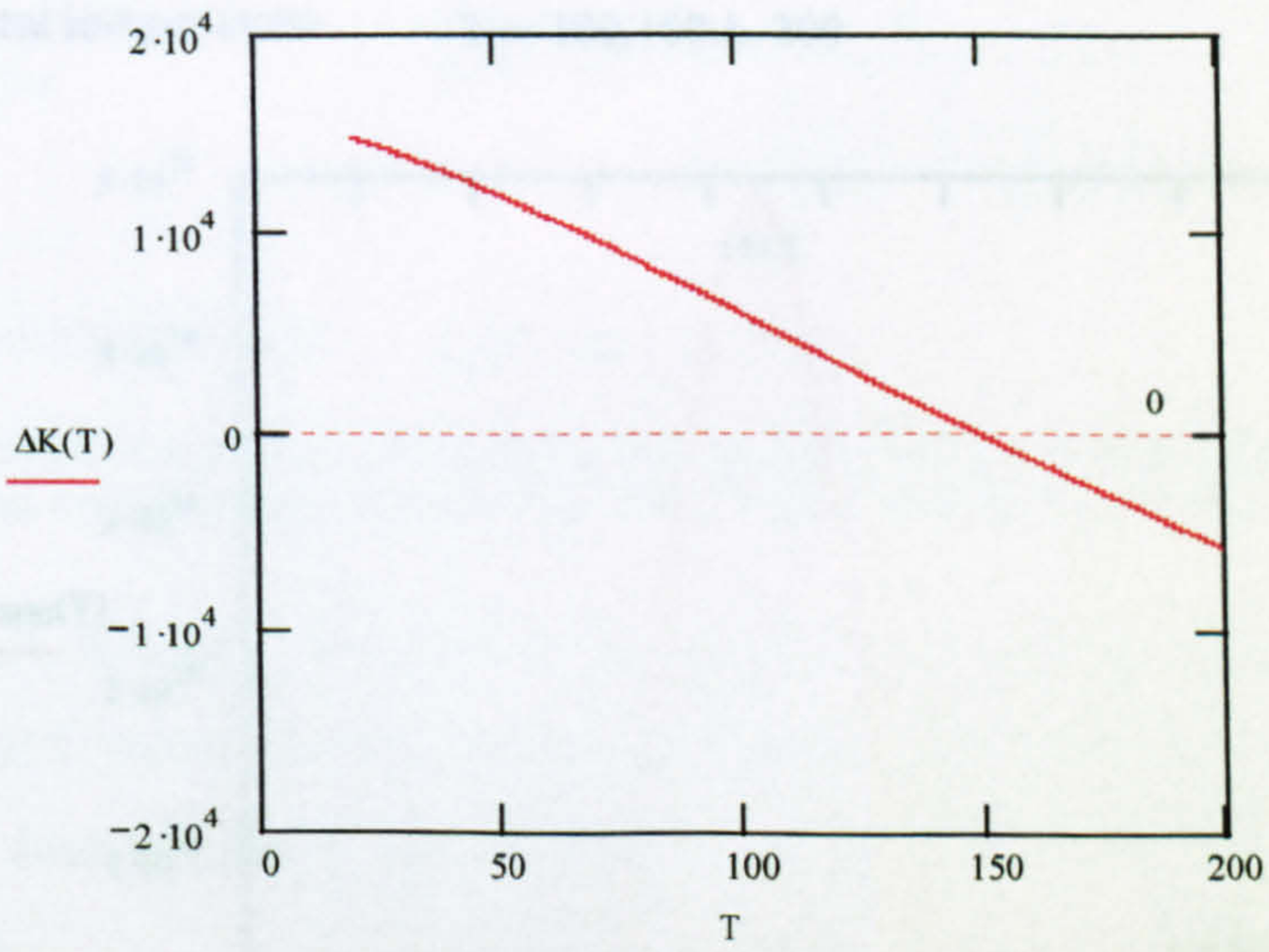

Since we are working with fundamental wavelength of 1064nm (frequency doubling to 532nm) and the phase-matching temperature is established as 148 degrees, we can express the refractive indices as

$$n_\omega := n_1(\lambda_1, 148.8)$$

$$n_{2\omega} := n_2(\lambda_2, 148.8)$$

$$n_\omega = 1.604 \qquad n_{2\omega} = 1.604$$

Calculation of phasematching temperature

Average laser power $P_\omega := 4.4 \cdot \text{watt}$

Crystal length $L := 15 \cdot \text{mm}$

Plane wave impedance $\eta := \frac{377 \cdot \text{ohm}}{n_\omega}$

Effective nonlinear coefficient $\text{deff} := 0.85 \cdot 10^{-12} \cdot \left(\frac{\text{m}}{\text{volt}}\right)$

Fundamental parameters $\omega_x(\lambda_1) := \frac{2 \cdot \pi \cdot c \cdot n_\omega}{\lambda_1}$

$$K := 2 \cdot \eta^3 \cdot \omega_x(\lambda_1)^2 \cdot \text{deff}^2$$

Area of beam $A := 2 \cdot \pi \cdot (70 \cdot 10^{-6} \cdot \text{m})^2$

SHG efficiency $$\eta_{SHG}(T) := L^2 \cdot K \cdot \frac{P_\omega}{A} \cdot \frac{\sin\left(\frac{\Delta K(T) \cdot L}{2}\right)^2}{\left(\frac{\Delta K(T) \cdot L}{2}\right)^2}$$

Crystal temperature $T := 100, 100.1 .. 200$

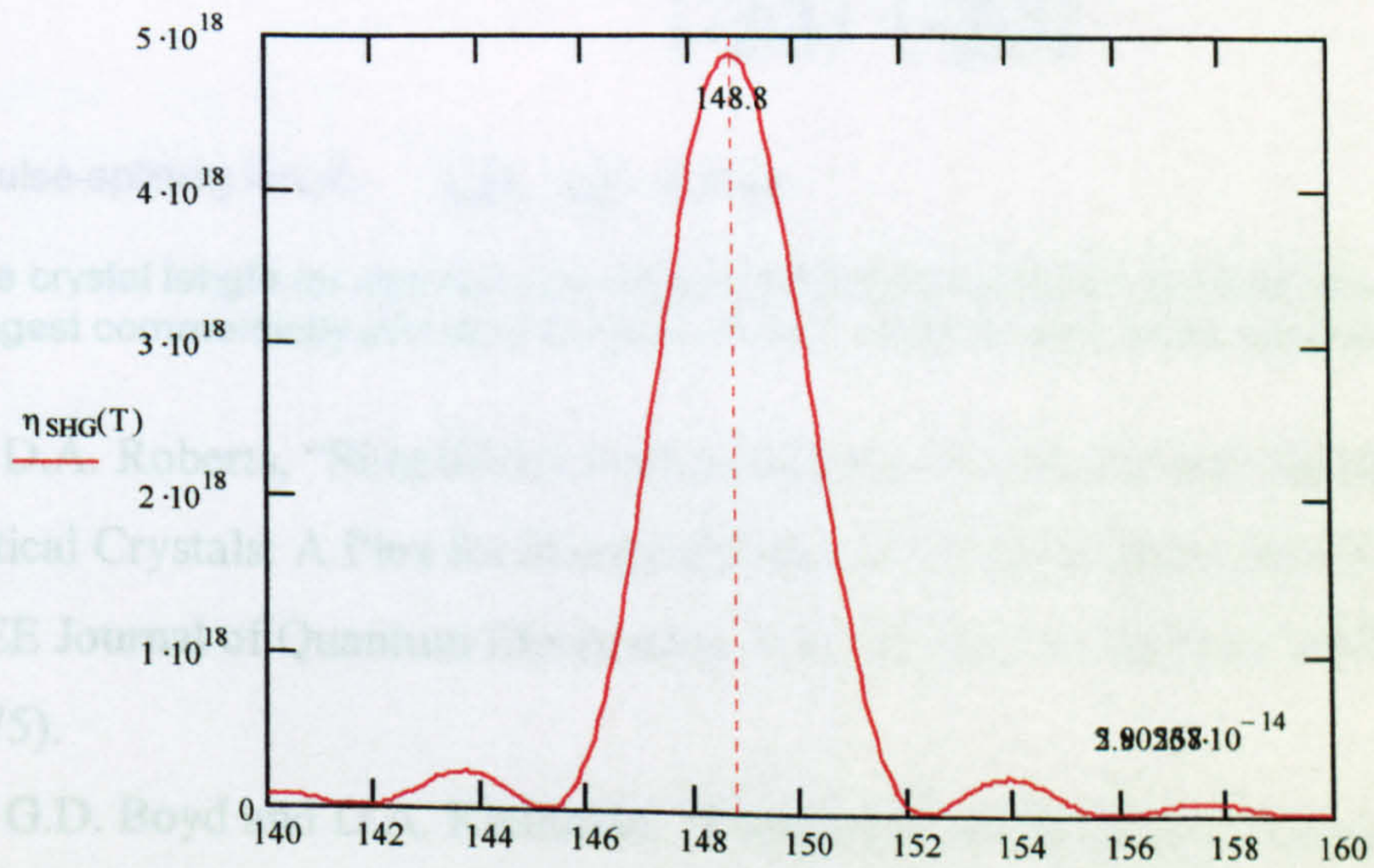

Phase-matching temperature is therefore 148.8 degrees.

Calculation of beam divergence

$$\Delta\theta := \left[\frac{0.44 \cdot \frac{\lambda_1}{L}}{\left(n_y(\lambda_2) - n_z(\lambda_1)\right)} \right]^{\frac{1}{2}} \cdot n_z(\lambda_1)$$

$$\Delta\theta = 0.254$$

Pulse walk-off

Angular frequency $\omega_z(\lambda_1) := 2 \cdot \pi \cdot \frac{c \cdot n_\omega}{\lambda_1}$

Group velocity $G(\lambda) := \frac{n_\omega}{c} - 2\left(\frac{\pi}{\omega_z(\lambda_1)}\right) \cdot \frac{d}{d\lambda} n_z(\lambda)$

$$v_g(\lambda) := \frac{1}{G(\lambda)}$$

Pulse duration $\tau_p := 33 \cdot ps$

Pulse-splitting lengths $l_{ps}(\lambda_1, \lambda_2) := \frac{\tau_p}{\left(\frac{1}{v_g(\lambda_2)}\right) - \left(\frac{1}{v_g(\lambda_1)}\right)}$

Pulse-splitting length $l_{ps}(\lambda_1, \lambda_2) = 0.324m$

The crystal length for optimum conversion is therefore 324mm, however the longest commercially available length is 15mm, which is used in the experiment.

[1] D.A. Roberts, "Simplified Characterization of Uniaxial and Biaxial Nonlinear Optical Crystals: A Plea for Standardization of Nomenclature and Conventions", IEEE Journal of Quantum Electronics, Vol. 28, No. 10, October 1992 (pp2057-2075).

[2] G.D. Boyd and D.A. Kleinman, "Parametric Interaction of Focussed Gaussian Light Beams", Journal of Applied Physics, Vol. 39, No. 8, July 1968 (pp3597-3639)

Appendix Five.

(b) MathCAD program for theoretical prediction of properties for third harmonic generation of mode-locked Nd^{3+}:YVO_4 laser using Lithium Triborate

Calculation of refractive indices, phase-matching angle, beam divergence, optimum crystal length.

Third harmonic generation in Lithium Triborate

Includes calculation of refractive indices, phasematching angle, beam divergence, optimum crystal length.

Lithium Triborate (LBO): Sellmeier's, dispersion of thermo-optic coeffs.
Data from "Temperature dispersion of refractive indices in β-BaB_2O_4 and LiB_3O_5 crystals for nonlinear optical devices", J. App. Phys., Vol. 78, No. 11, 1995 (pp6752-6760)

Physical constants and units

$nm := 10^{-9}\cdot m \quad \mu m := 10^{-6}\cdot m \quad mm := 10^{-3}\cdot m \quad cm := 10^{-2}\cdot m \quad A \equiv 10^{-10}\cdot m$

$c := 3\cdot 10^{8}\cdot\left(m\cdot sec^{-1}\right) \quad \varepsilon_0 := 8.854\,10^{-12}\cdot\frac{farad}{m} \quad ps := 10^{-12}\cdot sec$

$TOL := 0.00000000000000000000001$

Crystal transparency range $\lambda := 2000A, 2010A .. 12000A$

The room Temperature
Sellmeier coeffs.

$Ax := 1.4426279 \quad Bx := 1.0109932 \quad Cx := 1.121019710^{-2} \quad Dx := 1.2363218$

$Ay := 1.5014015 \quad By := 1.0388217 \quad Cy := 1.215710010^{-2} \quad Dy := 1.7567133$

$Az := 1.4489240 \quad Bz := 1.1365228 \quad Cz := 1.167674610^{-2} \quad Dz := 1.5830069$

$E := 91$

Sellmeier expression for calculation of refractive indices.

$$n_x(\lambda) := \left[Ax + \frac{Bx}{1 - \frac{Cx}{\left(\frac{\lambda}{A\cdot 10000}\right)^2}} + \frac{Dx}{1 - \frac{E}{\left(\frac{\lambda}{A\cdot 10000}\right)^2}} \right]^{\frac{1}{2}}$$

Sellmeier expression for calculation of refractive indices.

$$n_y(\lambda) := \left[Ay + \frac{By}{1 - \frac{Cy}{\left(\frac{\lambda}{A\cdot 10000}\right)^2}} + \frac{Dy}{1 - \frac{E}{\left(\frac{\lambda}{A\cdot 10000}\right)^2}} \right]^{\frac{1}{2}}$$

Sellmeier expression for calculation of refractive indices.

$$n_z(\lambda) := \left[Az + \frac{Bz}{1 - \frac{Cz}{\left(\frac{\lambda}{A\cdot 10000}\right)^2}} + \frac{Dz}{1 - \frac{E}{\left(\frac{\lambda}{A\cdot 10000}\right)^2}} \right]^{\frac{1}{2}}$$

Operational wavelengths

Fundamental wavelength $\lambda_{IR} := 1.064\,\mu m$

Second harmonic wavelength $\lambda_G := 0.532\,\mu m$

SFM expression $\lambda_B(\lambda_{IR}, \lambda_G) := \lambda_{IR} \cdot \frac{\lambda_G}{\lambda_G + \lambda_{IR}}$

Third harmonic wavelength $\lambda_B(\lambda_{IR}, \lambda_G) = 3.547 \times 10^{-7}\,m$

Temperature Range $T := 22$

Isentropic Band Gaps /μm $\lambda_{igx} := 0.053\,\mu m$

$\lambda_{igy} := 0.0327\,\mu m$

$\lambda_{igz} := 0.0435\,\mu m$

Normalised Dispersive Wavelengths $R_x(\lambda) := \frac{\lambda^2}{\lambda^2 - \lambda_{igx}^2}$

$R_y(\lambda) := \frac{\lambda^2}{\lambda^2 - \lambda_{igy}^2}$

$R_z(\lambda) := \frac{\lambda^2}{\lambda^2 - \lambda_{igz}^2}$

Fitting Coeffs.

$G_x := -127.701671 10^{-6}$

$G_y(T) := \left[\left(372.170 - 2.19910^{-1} \cdot T\right) + 1.17481 10^{-3} \cdot T^2 - 2.050771 10^{-6} \cdot T^3\right] \cdot 10^{-6}$

$G_z := -446.950311 10^{-6}$

$H_x := 122.134351 10^{-6}$

$H_y := -415.104351 10^{-6}$

$H_z := 419.334101 10^{-6}$

Thermo-optic coeffs (dn/dT)

$$\delta n_{Tx}(\lambda) := \frac{G_x \cdot R_x(\lambda) + H_x \cdot R_x(\lambda)^2}{2 \cdot n_x(\lambda)}$$

$$\delta n_{Ty}(T,\lambda) := \frac{G_y(T) \cdot R_y(\lambda) + H_y \cdot R_y(\lambda)^2}{2 \cdot n_y(\lambda)}$$

$$\delta n_{Tz}(T,\lambda) := \frac{G_z \cdot R_z(\lambda) + H_z \cdot R_z(\lambda)^2}{2 \cdot n_z(\lambda)}$$

Angular range

$$\theta_1 := 0 \cdot \frac{\pi}{180}, 1 \cdot \frac{\pi}{180} .. 90 \cdot \frac{\pi}{180}$$

Refractive indices at fixed temperature for fundamental wavelength

$$n_{Tx}(\lambda_{IR}, T) := n_x(\lambda_{IR}) + (T - 20) \cdot \delta n_{Tx}(\lambda_{IR})$$

$$n_{Ty}(\lambda_{IR}, T) := n_y(\lambda_{IR}) + (T - 20) \cdot \delta n_{Ty}(T, \lambda_{IR})$$

$$n_{Tz}(\lambda_{IR}, T) := n_z(\lambda_{IR}) + (T - 20) \cdot \delta n_{Tz}(T, \lambda_{IR})$$

Refractive indices at fixed temperature for second harmonic wavelength

$$n_{Tx}(\lambda_G, T) := n_x(\lambda_G) + (T - 20) \cdot \delta n_{Tx}(\lambda_G)$$

$$n_{Ty}(\lambda_G, T) := n_y(\lambda_G) + (T - 20) \cdot \delta n_{Ty}(T, \lambda_G)$$

$$n_{Tz}(\lambda_G, T) := n_z(\lambda_G) + (T - 20) \cdot \delta n_{Tz}(T, \lambda_G)$$

Angular dependence of extraordinary refractive index

$$n_{e\theta}(\lambda, \theta, T) := \frac{n_{Tx}(\lambda, T) \cdot n_{Tz}(\lambda, T)}{\left(n_{Tz}(\lambda, T)^2 \cdot \cos(\theta)^2 + n_{Tx}(\lambda, T)^2 \cdot \sin(\theta)^2\right)^{\frac{1}{2}}}$$

$$n_2(\lambda_G, T) := n_{Tx}(\lambda_G, T) \qquad n_1(\lambda_{IR}, T) := n_{Tz}(\lambda_{IR}, T)$$

$$\Delta K(\theta_1) := 2 \cdot \pi \cdot \left(\frac{n_{e\theta}(\lambda_B(\lambda_{IR}, \lambda_G), \theta_1, T)}{\lambda_B(\lambda_{IR}, \lambda_G)} - \frac{n_{Tz}(\lambda_G, T)}{\lambda_G} - \frac{n_{Tx}(\lambda_{IR}, T)}{\lambda_{IR}} \right)$$

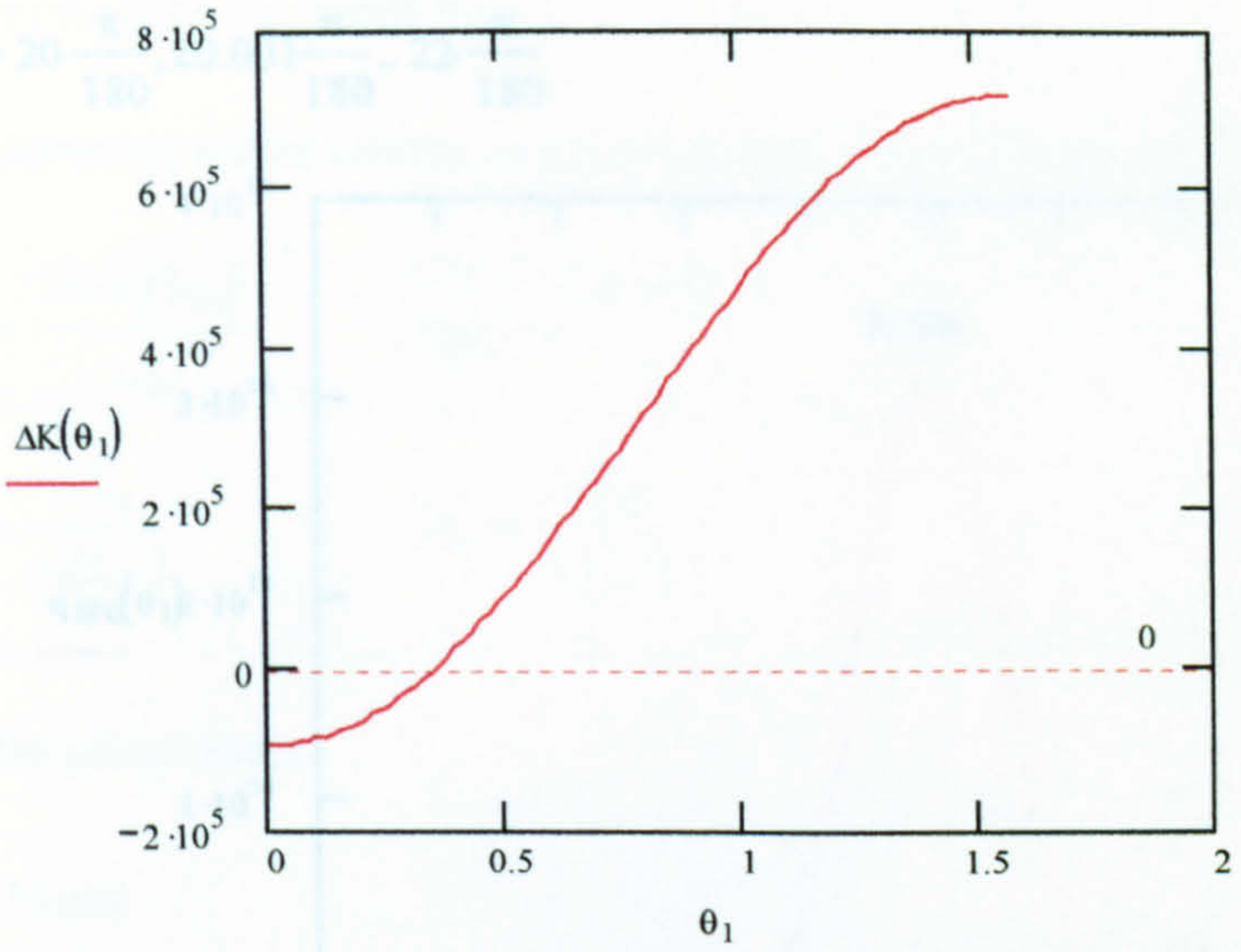

Average laser power $P_\omega := 4.4 \cdot watt$

Crystal length $L := 10 \cdot mm$

Plane wave impedance $\eta := \frac{377 \cdot ohm}{n_1(\lambda_{IR}, 2)}$

Effective nonlinear coefficient $deff := 1.16\,10^{-12}\left(\frac{m}{volt}\right)$

$\omega_1 := \frac{2 \cdot \pi \cdot c}{\lambda_{IR}}$

$K := 2 \cdot \eta^3 \cdot \omega_1^2 \cdot deff^2$

Area of beam $A := 2 \cdot \pi \cdot (50 \cdot 10^{-6} \cdot m)^2$

SFG efficiency $\eta_{SFG}(\theta_1) := L^2 \cdot K \cdot \frac{P_\omega}{A} \cdot \frac{\sin\left(\frac{\Delta K(\theta_1) \cdot L}{2}\right)^2}{\left(\frac{\Delta K(\theta_1) \cdot L}{2}\right)^2}$

$$\theta_1 := 20\cdot\frac{\pi}{180}, 20.001\frac{\pi}{180} .. 22\cdot\frac{\pi}{180}$$

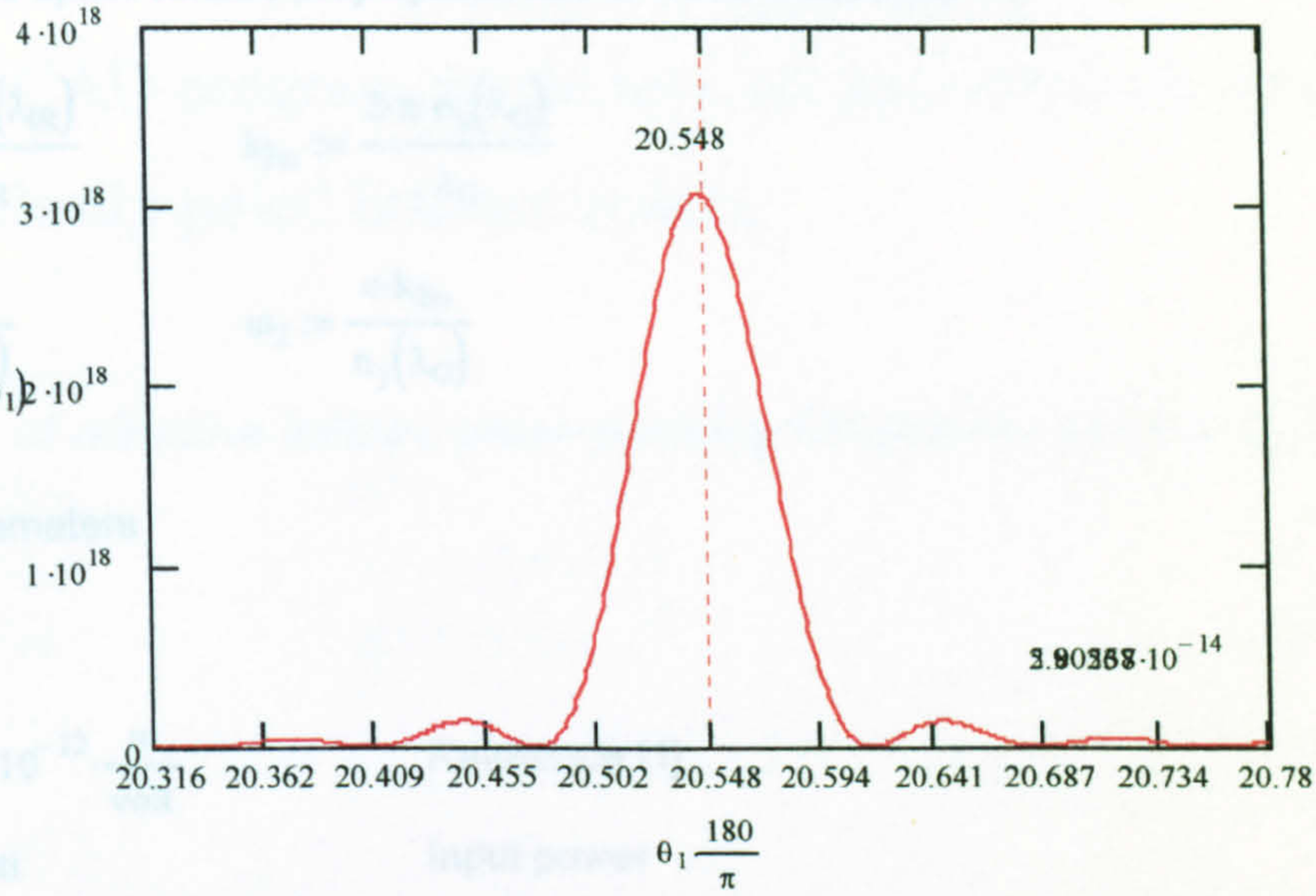

Since this is the "half-angle", this agrees with the angle of 42 deg. produced by the SNLO program. The phase-matching angle is therefore 42 degrees.

Pulse walk-off

Angular frequency

$$\omega(\lambda) := 2\cdot\pi\cdot\frac{c\cdot n_z(\lambda)}{\lambda_{IR}}$$

Group velocity

$$G(\lambda) := \frac{n_z(\lambda)}{c} - 2\left(\frac{\pi}{\omega(\lambda)}\right)\cdot\frac{d}{d\lambda}n_z(\lambda)$$

$$v_g(\lambda) := \frac{1}{G(\lambda)}$$

Pulse duration

$$\tau_p := 33\cdot ps$$

Pulse-splitting lengths

$$l_{ps}(\lambda_{IR}, \lambda_G) := \frac{\tau_p}{\left(\frac{1}{v_g(\lambda_G)}\right) - \left(\frac{1}{v_g(\lambda_{IR})}\right)}$$

pulse-splitting length

$$l_{ps}(\lambda_{IR}, \lambda_G) = 0.214m$$

Calculation of $\gamma_{2\omega}$ from d_{eff}

Fundamental optics relates propagation vector k and frequency w a:

$$k_\omega := \frac{2\cdot\pi\cdot n_z(\lambda_{IR})}{\lambda_{IR}} \qquad k_{2\omega} := \frac{2\cdot\pi\cdot n_y(\lambda_G)}{\lambda_G}$$

$$\omega_1 := \frac{c\cdot k_\omega}{n_z(\lambda_{IR})} \qquad \omega_2 := \frac{c\cdot k_{2\omega}}{n_y(\lambda_G)}$$

Crystal parameters

$L := 15\cdot mm$

$d_{eff} := 0.496\,10^{-12}\cdot\frac{m}{volt}$ Reference [1]

$P_1 := 4.4\cdot watt$ Input power

$h_m := 1$ Reference [2]

$$\gamma_{2\omega} := \left(\frac{2\cdot\omega_1^{\,2}\cdot d_{eff}^{\,2}}{\pi\cdot n_z(\lambda_{IR})^2\cdot n_y(\lambda_G)\cdot\varepsilon_0\cdot c^3}\right)\cdot P_1\cdot L\cdot k_\omega\cdot h_m$$

$\gamma_{2\omega} = 3.107\times 10^{-4}$

For cw third harmonic generation, $\gamma_{3\omega}\sim 10^{-4}\,W^{-1}$.

[1] D.A. Roberts, "Simplified Characterization of Uniaxial and Biaxial Nonlinear Optical Crystals: A Plea for Standardization of Nomenclature and Conventions", IEEE Journal of Quantum Electronics, Vol. 28, No. 10, October 1992 (pp2057-2075).

[2] G.D. Boyd and D.A. Kleinman, "Parametric Interaction of Focussed Gaussian Light Beams", Journal of Applied Physics, Vol. 39, No. 8, July 1968 (pp3597-3639).

Appendix Five.

(c) MathCAD program for theoretical prediction of properties of periodically poled lithium niobate

Calculation of refractive indices, phase-matching temperature and acceptance parameters.

Calculations for Periodically poled lithium niobate optical parametric oscillator

Optical parameters

$c := 3 \cdot 10^{8}$ m/s $\quad \varepsilon o := 8.85 \cdot 10^{-12}$ F/m

Interaction type

eee

Sellmeier coefficients

$A1e := 4.5820$ $\quad B1e := 5.271610^{-8}$

$A2e := 0.09921$ $\quad B2e := -4.914310^{-8}$

$A3e := 0.21090$ $\quad B3e := 2.297110^{-7}$

$A4e := 0.021940$

Room temperature

$To := 24.5$

Fitting coefficient

$F(T) := (T - To) \cdot (T + To + 546)$

Sellmeier equation for $LiNbO_3$

$$ne(\lambda, T) := \sqrt{A1e + \frac{A2e + B1e \cdot F(T)}{\lambda^2 - (A3e + B2e \cdot F(T))^2} + B3e \cdot F(T) - A4e \cdot \lambda^2}$$

Temperature of PPLN crystal

$T := 150$

Pump (p), signal (s) and idler (i) wavelengths (μm)

$\lambda p := 1.064$ $\quad \lambda s := 1.52$

$$\lambda i := \frac{\lambda s \cdot \lambda p}{\lambda s - \lambda p} \qquad \lambda i = 3.547$$

Length of PPLN crystal (m)

$L := 50 \cdot 10^{-3}$

Refractive indices at p,s and i wavelengths

$np := ne(\lambda p, T)$ $\quad np = 2.1618$

$ns := ne(\lambda s, T)$ $\quad ns = 2.1443$

$ni := ne(\lambda i, T)$ $\quad ni = 2.0821$

Dispersion relations and values

$$ne'(\lambda s, T) := \frac{d}{d\lambda s} ne(\lambda s, T)$$

$$ne'(\lambda s, T) = -0.0299$$

$$ne''(\lambda s, T) := \frac{d}{d\lambda s} ne'(\lambda s, T)$$

$$ne''(\lambda s, T) = 0.0183$$

Group velocities.

$$vgz(\lambda, T) := c \cdot \left(\frac{1}{ne(\lambda, T) - \lambda \cdot ne'(\lambda, T)} \right)$$

Pump, signal and idler group velocities (m/s)

$$vgz(\lambda p, T) = 1.351862 \times 10^8$$

$$vgz(\lambda s, T) = 1.370049 \times 10^8$$

$$vgz(\lambda i, T) = 1.352184 \times 10^8$$

Group Velocity mismatch.

$$vsp := \frac{1}{vgz(\lambda s, T)} - \frac{1}{vgz(\lambda p, T)}$$

Coherence length of crystal

$$lc := \frac{\lambda s}{4(ne(\lambda s, T) - ne(\lambda p, T))}$$

$vsp \cdot 10^{12} = -98.199$ fs/mm $vsp \cdot lc \cdot 10^{12} = 2.13 \times 10^3$ ps

$$vip := \frac{1}{vgz(\lambda i, T)} - \frac{1}{vgz(\lambda p, T)}$$

$vip \cdot 10^{12} = -1.7623$ fs/mm $vip \cdot lc \cdot 10^{12} = 38.2252$ ps

$$vis := \frac{1}{vgz(\lambda s, T)} - \frac{1}{vgz(\lambda i, T)}$$

$vis \cdot 10^{12} = -96.4367$ fs/mm $vis \cdot lc \cdot 10^{12} = 2.0917 \times 10^3$ ps

Beam waist radius (m)

$wzs := 86 \cdot 10^{-6}$ $\quad wys := wzs$ $\quad wys = 8.6 \times 10^{-5}$

$wzp := 80 \cdot 10^{-6}$ $\quad wyp := wzp$ $\quad wyp = 8 \times 10^{-5}$

Pump / signal pulse 1/e duration

$\tau pi := 33 \cdot 10^{-12}$

$$\tau s := \frac{\tau pi}{\sqrt{2 \cdot \ln(2)}}$$

$\tau s = 2.8028 \times 10^{-11}$

Laser repetition rate (MHz)

$RL := 235 \cdot 10^{6}$

Average power (W)

$P := 4.4$

Peak Power (W)

$$PP := \frac{P}{RL \cdot \tau pi}$$

$PP = 567.3759$

Pump beam peak intensity (W/m)

$$Ip := \frac{2 \cdot PP}{\pi \cdot \left(\frac{wzp}{2} \right)^2}$$

$Ip \cdot 10^{-10} = 22.5752$ MW/cm^2

Pump signal and idler frequencies

$$\omega p := \frac{2 \cdot \pi \cdot c \cdot 10^{6}}{\lambda p} \qquad \omega s := \frac{2 \cdot \pi \cdot c \cdot 10^{6}}{\lambda s} \qquad \omega i := \frac{2 \cdot \pi \cdot c \cdot 10^{6}}{\lambda i}$$

d coefficient (m/V)

$d := 16 \cdot 10^{-12}$

Miller's Delta Function

$$deff := d \cdot \frac{\left(ne(\lambda p, T)^2 - 1\right) \cdot \left(ne(\lambda s, T)^2 - 1\right) \cdot \left(ne(\lambda i, T)^2 - 1\right)}{\left(ne(\lambda p, T)^2 - 1\right) \cdot \left(ne(\lambda p \cdot 2, T)^2 - 1\right) \cdot \left(ne(\lambda p \cdot 2, T)^2 - 1\right)}$$

Effective nonlinear coefficient (m/V)

$deff = 1.5437 \times 10^{-11}$

Single pass parametric gain

$$\Gamma := \sqrt{\frac{2 \cdot \omega s \cdot \omega i \cdot deff^2}{np \cdot ns \cdot ni \cdot \varepsilon o \cdot c^3} \cdot Ip} \qquad \Gamma = 175.3543$$

Cavity losses (All high reflectors, excluding output coupler)

Output coupler transmission

$$Tout := .05$$

Other cavity losses

$$L := 0.01$$

$$T := Tout + L$$

Threshold calculation (W)

$$Pthres := P \cdot \frac{T}{\Gamma^2 \cdot lc^2}$$

$$Pthres = 1.8249 \times 10^{-8}$$

Output power calculation

pump depletion (%)

$$dep := 0.78$$

$$\Delta P := dep \cdot P$$

Converted pump power

$$\Delta P = 3.432\,W$$

Signal output power (W)

$$Ps := Tout \cdot \Delta P \cdot \frac{\omega s}{\omega s + \omega i}$$

$$Ps = 0.1201$$

Idler output power (W)

$$Pi := \frac{\omega i}{\omega s} \cdot Ps$$

$$Pi = 0.0515$$

Spectral acceptance for SROPO (signal resonant)

Signal wavelengths

$\lambda s := 1.2, 1.21 .. 1.8$

$$\delta\lambda(\lambda s) := \frac{0.4429\lambda s}{L} \cdot \left(\left| \frac{ne(\lambda s, T) - ne(\lambda p, T)}{\lambda s} + \frac{d}{d\lambda s} ne(\lambda s, T) - 0.5 \cdot \frac{d}{d\lambda s} ne(\lambda s, T) \right| \right)^{-1}$$

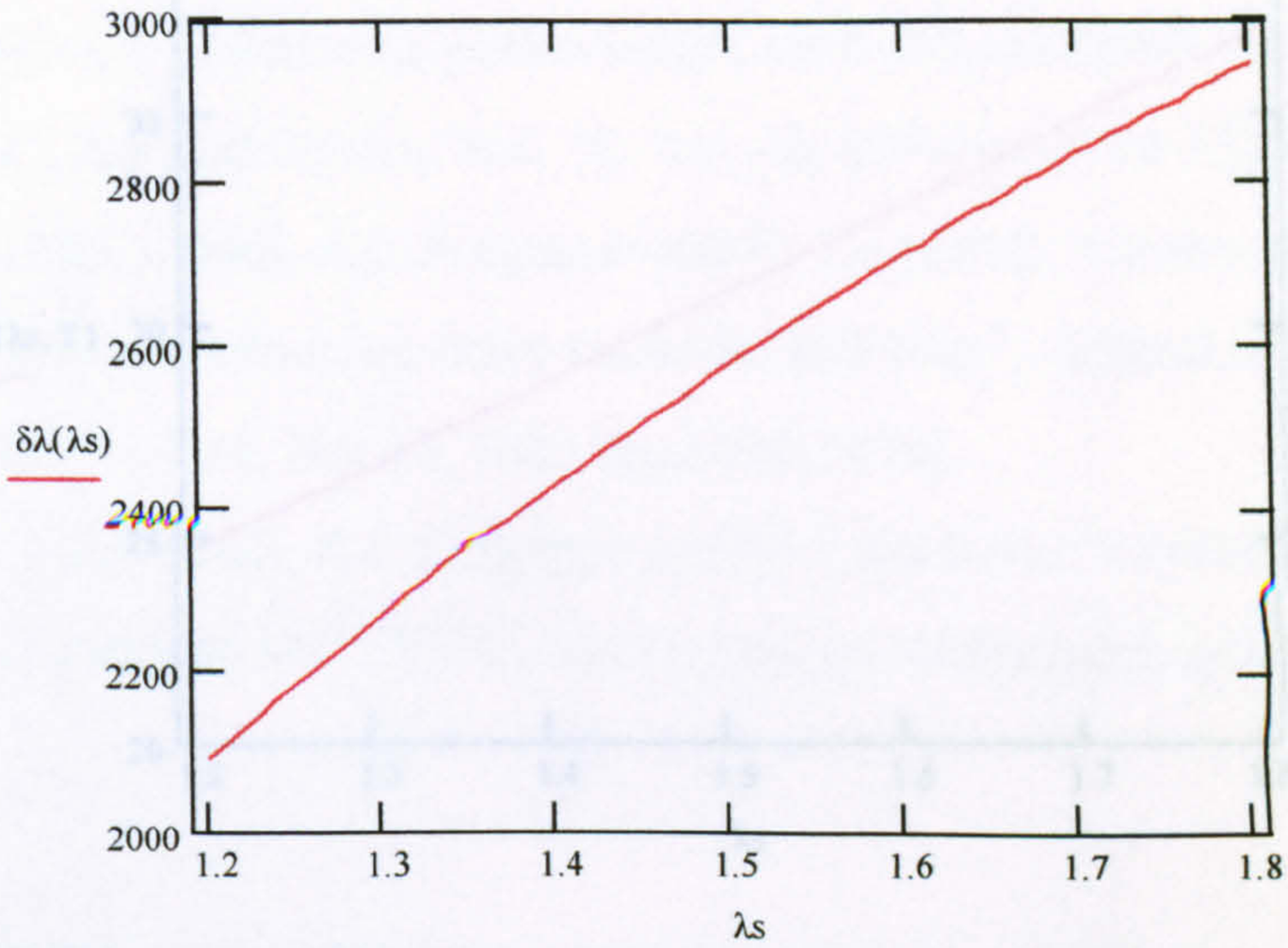

Angular acceptance for SROPO (signal resonant) (mrad)

$l_c := 129$ $\nu := 0$

$$\delta\nu(\lambda s, \nu) := 2 \cdot \left(1.772 \frac{ne(\lambda s, T)}{ne(\lambda p, T)} \cdot \frac{l_c}{L} \cdot \cos(\nu) \right)^{0.5}$$

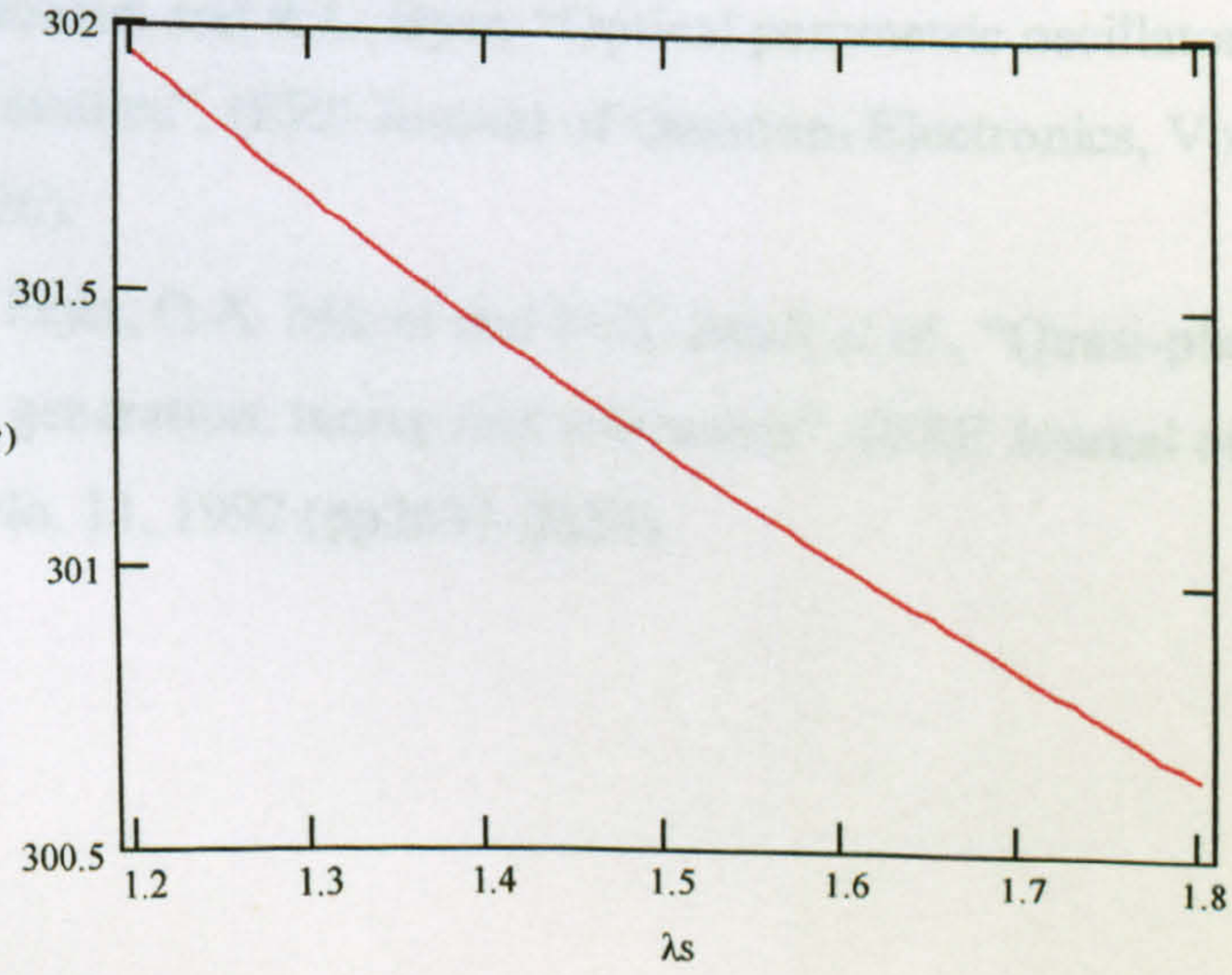

Temperature acceptance bandwidth (K)

$$\alpha := 4.43 \cdot 10^{-6}\ /K$$

$$\Delta T(\lambda s, T) := \frac{0.4429\lambda s}{L} \cdot \left[\left| \frac{d}{dT} ne(\lambda s, T) - ne(\lambda p, T) + \alpha \cdot (ne(\lambda s, T) - ne(\lambda p, T)) \right| \right]^{-1}$$

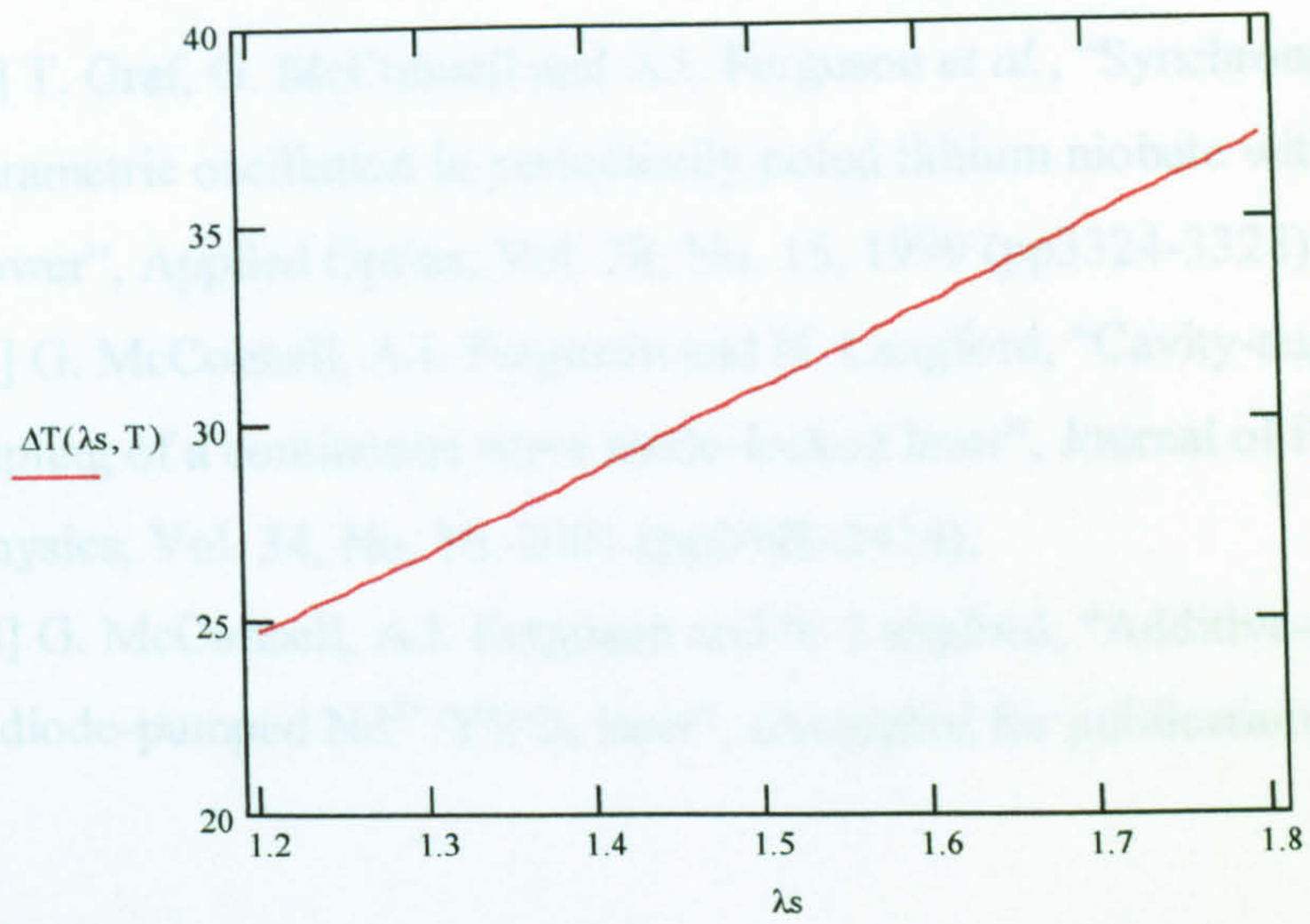

[1] G.J. Edwards and M. Lawrence, "A temperature-dependent dispersion equation for congruently grown lithium niobate" Optical and Quantum Electronics. Vol. 16, 1984 (pp373-375).

[2] G.A. Massey and J.C. Johnson, "Gain limitations in optical parametric amplifiers", IEEE Journal of Quantum Electronics, Vol. QE-15, No. 4, 1979 (pp201-203).

[3] S.J. Brosnan and R.L. Byer, "Optical parametric oscillator threshold and linewidth studies", IEEE Journal of Quantum Electronics, Vol. QE-15, No. 6, 1979 (pp415-426).

[4] M.M. Fejer, G.A. Magel and D.H. Jundt *et al.*, "Quasi-phase-matched second harmonic generation: tuning and tolerances", IEEE Journal of Quantum Electronics, Vol. 28, No. 11, 1992 (pp2631-2654).

Appendix Six.

Publications

[1] T. Graf, G. McConnell and A.I. Ferguson *et al.*, "Synchronously pumped optical parametric oscillation in periodically poled lithium niobate with 1-W average output power", Applied Optics, Vol. 38, No. 15, 1999 (pp3324-3328).

[2] G. McConnell, A.I. Ferguson and N. Langford, "Cavity-augmented frequency tripling of a continuous wave mode-locked laser", Journal of Physics D: Applied Physics, Vol. 34, No. 16, 2001 (pp2408-2414).

[3] G. McConnell, A.I. Ferguson and N. Langford, "Additive-pulse mode locking of a diode-pumped Nd^{3+}:YVO_4 laser", (Accepted for publication, Applied Physics B).